Urban, Kovac (2010) *3D drift diffusion and 3D Monte Carlo simulation of on-current variability due to random dopants.* PhD thesis.

University of Glasgow

3D Drift Diffusion and 3D Monte Carlo simulation of On-Current variability due to Random Dopants

by

Urban Kovac

A thesis submitted in fulfillment for the
degree of Doctor of Philosophy

in the
College of Science and Engineering, School of Engineering
Department of Electronics and Electrical Engineering

December 2010

Abstract

In this work Random Discrete Dopant induced on-current variations have been studied using the Glasgow 3D atomistic drift/diffusion simulator and Monte Carlo simulations. A methodology for incorporating quantum corrections into self-consistent atomistic Monte Carlo simulations via the density gradient effective potential is presented. Quantum corrections based on the density gradient formalism are used to simultaneously capture quantum confinement effects. The quantum corrections not only capture charge confinement effects, but accurately represent the electron impurity interaction used in previous *ab initio* atomistic MC simulations, showing agreement with bulk mobility simulation. The effect of quantum corrected transport variation in statistical atomistic MC simulation is then investigated using a series of realistic scaled devices nMOSFETs transistors with channel lengths 35 nm, 25 nm, 18nm, 13 nm and 9 nm. Such simulations result in an increased drain current variability when compared with drift diffusion simulation. The comprehensive statistical analysis of drain current variations is presented separately for each scaled transistor. The investigation has shown increased current variation compared with quantum corrected drift diffusion simulation and with previous classical MC results. Furthermore, it has been studied consistently the impact of transport variability due to scattering from random discrete dopants on the on-current variability in realistic nano CMOS transistors. For the first time, a hierarchic simulation strategy to accurately transfer the increased on-current variability obtained from the ab initio MC simulations to DD simulations is subsequently presented. The MC corrected DD simulations are used to produce target $I_D - V_G$ characteristics from which statistical compact models are extracted for use in preliminary design kits at the early stage of new technology development. The impact of transport variability on the accuracy of delay simulation are investigated in detail. Accurate compact models extraction methodology transferring results from accurate physical variability simulation into statistical compact models suitable for statistical circuit simulation is presented. In order to examine te size of this effect on circuits Monte Carlo SPICE simulations of inverter were carried out for 100 samples.

Contents

List of Tables **v**

List of Figures **viii**

Acknowledgements **xi**

Declaration of Authorship **xii**

Abbreviations **xv**

Physical Constants **xvii**

Symbols **xviii**

1 INTRODUCTION **1**
- 1.1 Aims and objectives . . . 3
- 1.2 Outline . . . 4

2 VARIABILITY **6**
- 2.1 Variability Classicfication . . . 8
- 2.2 Sources of Intrinsic Device Parameter Variation . . . 9
  - 2.2.1 Random Discrete Dopants . . . 11
  - 2.2.2 Other Sources of Variability . . . 16
- 2.3 Simulation of Intrinsic Variations . . . 17
- 2.4 Variability Impact on Circuits . . . 20
- 2.5 Summary . . . 22

3 DEVICE SIMULATORS **24**
- 3.1 The Drift Diffusion Simulator . . . 24
  - 3.1.1 Classical Drift Diffusion Simulations . . . 24
  - 3.1.2 Quantum Corrections . . . 26
  - 3.1.3 Solution Methodology . . . 28
    - 3.1.3.1 Random Discrete Dopants . . . 30
  - 3.1.4 Mobility Models . . . 32
    - 3.1.4.1 Concentration Dependent Mobility . . . 33
    - 3.1.4.2 Field Dependent Mobility . . . 34
    - 3.1.4.3 Atomistic Mobility . . . 36

3.2 Monte Carlo Simulator . . . 37
  3.2.1 Boltzman Transport Equation . . . 37
    3.2.1.1 Classical Boltzman Transport Equation . . . 37
    3.2.1.2 Semi-Classical Carrier Dynamics . . . 38
    3.2.1.3 Semi-Classical Boltzman Transport Equation . . . 40
  3.2.2 3D Monte Carlo Simulator . . . 41
    3.2.2.1 Band Structure . . . 42
    3.2.2.2 Analytic Band Approximations . . . 44
    3.2.2.3 Spherical Parabolic Band . . . 45
    3.2.2.4 Ellipsoidal Parabolic Band . . . 46
    3.2.2.5 Ellipsoidal Nonparabolic Band . . . 47
    3.2.2.6 Scattering Rate Calculation . . . 48
    3.2.2.7 Acoustic and Optical Phonon Scattering . . . 49
    3.2.2.8 Selection of Free Flight Time . . . 51
    3.2.2.9 Selection of Scattering Events . . . 52
    3.2.2.10 Carrier Dynamics . . . 53
    3.2.2.11 Bulk Calibration . . . 54
    3.2.2.12 *Ab Initio* Ionized Impurity Scattering . . . 55

4 ON-CURRENT VARIABILITY DUE TO RANDOM DOPANT DISTRIBUTIONS 60
4.1 Quantum Corrections in Monte Carlo . . . 61
  4.1.1 Density Gradient Quantum Corrections in Monte Carlo . . . 63
  4.1.2 The Effective Density Gradient Quantum Potential . . . 69
  4.1.3 Rutherford Scattering . . . 70
  4.1.4 The Concentration Dependent Bulk Mobility . . . 72
4.2 Drain Current Variability Simulation strategy . . . 76
  4.2.1 Scaled Devices Simulation Strategy . . . 76
  4.2.2 DD and MC Results and Discussion . . . 78
    4.2.2.1 Random Discrete Dopants Effects on Potential Distribution 78
    4.2.2.2 Random Discrete Dopants Effects on Electron and Current Density Distribution . . . 78
4.3 Conclusions . . . 82

5 DRAIN CURRENT VARIABILITY: STATISTICAL ANALYSIS 83
5.1 Statistical Analysis Strategy . . . 83
  5.1.1 Basic Statistics . . . 84
  5.1.2 Confidence Intervals . . . 84
  5.1.3 Normality Tests . . . 86
5.2 Results and Discussion Of On Current Variability of Scaled Devices . . . 88
  5.2.1 Descriptive Statistical Results at Low Drain Bias . . . 88
  5.2.2 Descriptive Statistical Results at High Drain Bias . . . 91
  5.2.3 DD versus MC : Percentage Change in Current . . . 93
5.3 Summary of Drain Current Variations of Scaled Devices . . . 96
  5.3.1 Summary of Low Drain Bias Results . . . 96
  5.3.2 Summary of High Drain Bias Results . . . 99
5.4 Electrostatic versus Transport Variations . . . 100

5.4.1 The Absolute Model of Electrostatic and Transport Variations . . 102
5.4.2 The Conditional Model of Electrostatic and Transport Variations . 103
5.4.3 Results of Electrostatic versus Transport Variations 108
5.5 Conclusions 115

6 Hierarchical simulation of statistical variability: from 3D MC with *ab initio* ionised impurity scattering to statistical compact models 117
6.1 Hierarchic Simulation Methodology 118
6.1.1 Stage One: Initial Variability Estimation 118
6.1.2 Stage Two: Calibration of DD Variability 120
6.1.3 Stage Three: 'enhanced' compact model extraction 121
6.1.4 Application to 35nm device 122
6.1.4.1 First Stage: Results of initial distributions 124
6.1.4.2 Second Stage: Calibration of DD mobility 126
6.1.4.3 Third Stage: compact model extraction 131
6.1.5 Simulation Strategy of the Variability in NANOCMOS Inverter . . 137
6.1.6 Results and Discussion 138
6.2 Conclusions 142

7 Conlucsion 143
7.1 Future Work 146

A Statistical Analysis of Drain Current Variability : 25 nm MOSFET 147
A.1 Descriptive Statistical Results at Low Drain Bias 147
A.2 Descriptive Statistical Results at High Drain Bias 149
A.3 DD versus MC : Percentage Change in Current 152

B Statistical Analysis of Drain Current Variability : 18 nm MOSFET 155
B.1 Descriptive Statistical Results at Low Drain Bias 155
B.2 Descriptive Statistical Results at High Drain Bias 157
B.3 DD versus MC : Percentage Change in Current 160

C Statistical Analysis of Drain Current Variability : 13 nm MOSFET 162
C.1 Descriptive Statistical Results at Low Drain Bias 162
C.2 Descriptive Statistical Results at High Drain Bias 164
C.3 DD versus MC : Percentage Change in Current 166

D Statistical Analysis of Drain Current Variability : 9 nm MOSFET 169
D.1 Descriptive Statistical Results at Low Drain Bias 169
D.2 Descriptive Statistical Results at High Drain Bias 171
D.3 DD versus MC : Percentage Change in Current 173

Bibliography 176

List of Tables

2.1 2009 ITRS Roadmap. * UTB FD device, ** MG device. 8

3.1 Band independent parameters and calibrated values for the minimum lying X-valley used in the MC simulation. These values govern the transport processes effecting the majority of electrons in silicon and are used consistently throughout this work. 58
3.2 Parameters for the L and Γ valleys. Though present within the simulation, little transport occurs in these valleys due to the large separation in energy from the X-valley. 59

4.1 Table of Device Design Characteristics including channel lengths, EOT and junction depth [26]. 76

5.1 95% nonparameric ABC confidence interval of mean value, standard deviation, skewness and kurtosis compute for 35 nm device at low drain bias. 90
5.2 95% nonparameric ABC confidence interval of mean value, standard deviation, skewness and kurtosis compute for 35 nm device at high drain bias. 92
5.3 Normality test for 35 nm device at high drain bias. 93
5.4 The standard deviation of the drain current variation obtained from both DD and MC simulations at low drain bias. 97
5.5 The standard deviation of the drain current variation obtained from both DD and MC simulations at high drain bias. 99
5.6 Regression results at low drain bias obtained from the absolute model. se is a standard error of the regression coefficient. R^2 or coefficient of determination is a measure of goodness-of-fit of linear regression. 109
5.7 Regression results at high drain bias obtained from the absolute model. se is a standard error of the regression coefficient. R^2 or coefficient of determination is a measure of goodness-of-fit of linear regression. 109
5.8 Ratios of electrostatic and transport variations at low drain bias obtained from the absolute model. 111
5.9 Ratios of electrostatic and transport variations at low drain bias obtained from the absolute model. 112
5.10 Ratios of electrostatic and transport variations at both high and low drain bias obtained from the approximated conditional model. 115

6.1 Mean and standard deviation of the threshold voltage at low and high drain bias for both original and enhanced DD. 130

6.2 Mean (μ), standard deviation (σ), skew (γ_1) and kurtosis (γ_2)of BSIM4 parameters for both original and enhanced statistical compact models. . . 135

A.1 The values of the mean, standard deviation, skewness and kurtosis of drain currents results obtained from both DD and MC simulations at low drain bias of 25 nm device. 147
A.2 95% nonparameric ABC confidence interval of mean value, standard deviation, skewness and kurtosis compute for 25 nm device at low drain bias. 148
A.3 Normality test for 25 nm device at low drain bias. 149
A.4 The values of the mean, standard deviation, skewness and kurtosis of drain currents results obtained from both DD and MC simulations at high drain bias of 25 nm device. 150
A.5 95% nonparameric ABC confidence interval of mean value, standard deviation, skewness and kurtosis compute for 25 nm device at high drain bias. 151
A.6 Normality test for 25 nm device at high drain bias. 152
A.7 Uniform currents obtained from DD and MC simulations of 25 nm device. 152

B.1 The values of the mean, standard deviation, skewness and kurtosis of drain currents results obtained from both DD and MC simulations at low drain bias of 18 nm device. 155
B.2 95% nonparameric ABC confidence interval of mean value, standard deviation, skewness and kurtosis compute for 18 nm device at low drain bias. 156
B.3 Normality test for 18 nm device at low drain bias. 157
B.4 The values of the mean, standard deviation, skewness and kurtosis of drain currents results obtained from both DD and MC simulations at high drain bias of 18 nm device. 158
B.5 95% nonparameric ABC confidence interval of mean value, standard deviation, skewness and kurtosis compute for 18 nm device at high drain bias. 158
B.6 Normality test for 18 nm device at high drain bias. 159
B.7 Uniform currents obtained from DD and MC simulations of 18 nm device. 160

C.1 The values of the mean, standard deviation, skewness and kurtosis of drain currents results obtained from both DD and MC simulations at low drain bias of 13 nm device. 162
C.2 95% nonparameric ABC confidence interval of mean value, standard deviation, skewness and kurtosis compute for 13 nm device at low drain bias. 163
C.3 Normality test for 13 nm device at low drain bias. 164
C.4 The values of the mean, standard deviation, skewness and kurtosis of drain currents results obtained from both DD and MC simulations at high drain bias of 13 nm device. 165
C.5 95% nonparameric ABC confidence interval of mean value, standard deviation, skewness and kurtosis compute for 13 nm device at high drain bias. 165
C.6 Normality test for 13 nm device at high drain bias. 166

C.7 Uniform currents obtained from DD and MC simulations of 13 nm device. 167

D.1 The values of the mean, standard deviation, skewness and kurtosis of drain currents results obtained from both DD and MC simulations at low drain bias of 9 nm device. 169
D.2 95% nonparameric ABC confidence interval of mean value, standard deviation, skewness and kurtosis compute for 9 nm device at low drain bias. 170
D.3 Normality test for 9 nm device at low drain bias. 171
D.4 The values of the mean, standard deviation, skewness and kurtosis of drain currents results obtained from both DD and MC simulations at high drain bias of 9 nm device. 171
D.5 95% nonparameric ABC confidence interval of mean value, standard deviation, skewness and kurtosis compute for 9 nm device at high drain bias. 172
D.6 Normality test for 9 nm device at high drain bias. 173
D.7 Uniform currents obtained from DD and MC simulations of 9 nm device. 174

List of Figures

2.1 The major scaling challanges 7
2.2 Variability matrix 9
2.3 Transition from continuous towards atomistic device 10
2.4 Representation of 10nm MOSFET 11
2.5 KMC simulation of RDD (DADOS, Synopsys) 12
2.6 Typical 3D potential distribution reflecting the impact of RDD 13
2.7 Percentage drain current variation as a function of channel length 15
2.8 Line Edge Roughness 16
2.9 Polysilicon Gate granuality 17
2.10 Granularity in HfON high-κ dielectrics 17
2.11 Metal granularity causing gate work-function variation 18
2.12 Interface roughness 18
2.13 SRAM cell 21
2.14 Static transfer characteristics 21

3.1 Silicon Lattice structure 31
3.2 Comparison between classical and quantum corrected elelectron concentrations 33
3.3 Concentration dependent mobility 34
3.4 Bulk field dependent velocity 35
3.5 Monte Carlo flow chart. 42
3.6 The First Brillouin zone in Si 43
3.7 The Si band structure 44
3.8 Calibration of MC simulator 55
3.9 Concentration dependent mobility 56

4.1 Agreement between NEGF and DD 64
4.2 Agreement between NEGF and DD for different gate voltages 65
4.3 Flowchart showing atps needed for quantum correction in MC 67
4.4 Poorly maintained electron density in the x-direction at the source and drain regions 68
4.5 Box plot at low drain bias 68
4.6 DG potential 69
4.7 Rutheford simulation domain 71
4.8 Rutheford model 71
4.9 Schematic 3D atomistic simulation structure of N+NN+ diode 73
4.10 Potential of 3D atomistic simulation structure of N+NN+ diode 73
4.11 Simulated bulk mobility 74

4.12 Scaled devices . . . 76
4.13 $I_D - V_G$ characteristics experimental versus simulated and Simulated $I_D - V_G$ characteristic of the scaled devices . . . 77
4.14 Potential distribution of 35 nm device . . . 79
4.15 Potential distribution of 18 nm device . . . 79
4.16 Potential distribution of 9 nm device . . . 80
4.17 Electron concentration and current density of 35 nm device. . . . 80
4.18 Electron concentration and current density of 18 nm device. . . . 81
4.19 Electron concentration and current density of 9 nm device. . . . 81

5.1 Q-Q plots 35nm at low drain bias . . . 91
5.2 Q-Q plots 35nm at high drain bias . . . 93
5.3 Scatter plot of 35 nm device. . . . 94
5.4 Box plot at low drain bias . . . 97
5.5 Standard deviation of drain current variation at low drain bias. . . . 98
5.6 Box plot at high drain bias . . . 99
5.7 Standard deviation of drain current variation at high drain bias. . . . 100
5.8 The linear regression of MC v DD percentage drain-current variation at low drain bias . . . 109
5.9 The linear regression of MC v DD percentage drain-current variation at high drain bias . . . 110
5.10 95% confidence intervals of β_1 regression coefficient . . . 110
5.11 Electrostatic versus Transport variation at low drain bias . . . 112
5.12 Electrostatic versus Transport variation at high drain bias . . . 112
5.13 Percentage of total variation attributed to electrostatic effects . . . 113
5.14 Percentage contribution of transport variation to the total variation in MC 114
5.15 Electrostatic versus Transport variation at both low and high drain bias . 115

6.1 Flow chart of hierarchic simulation methodology . . . 119
6.2 $I_D - V_G$ characteristics of the 35-nm MOSFET . . . 123
6.3 $I_D - V_G$ characteristics of the uniform 35-nm MOSFET obtained from MC simulations at both low and high drain bias. . . . 124
6.4 Electrostatic potential distribution of 35-nm atomistic nMOSFETs. . . . 125
6.5 Electron concentration and current density of 35-nm atomistic nMOSFETs. 125
6.6 Percentage drain-current variation of 35-nm atomistic nMOSFETs from quantum corrected MC simulation against quantum corrected DD simulation. . . . 126
6.7 Original $I_D - V_G$ curves of 35-nm atomistic nMOSFETs obtained from quantum corrected DD. . . . 127
6.8 Enhanced $I_D - V_G$ curves of 35-nm atomistic nMOSFETs obtained from quantum corrected DD. . . . 127
6.9 The mean of original and enhanced on-current of 35-nm atomistic nMOSFETs obtained from original and quantum corrected DD. . . . 128
6.10 Distribution of on-current at high gate voltage at both low and high drain bias. . . . 128
6.11 Standard deviation of drain-current variation of 35-nm atomistic nMOSFETs as a function of gate voltage. . . . 129

6.12 Coefficient of variation of drain current of 35-nm atomistic nMOSFETs as a function of gate voltage. 129
6.13 Original and enhanced V_T distribution at both low and high drain bias. . 130
6.14 Original and enhanced Ioff distribution at both low and high drain bias. . 131
6.15 Original and enhanced subthreshold slope distribution at both low and high drain bias. 131
6.16 Original and enhanced DIBL distribution 132
6.17 Distribution of RMS error. 133
6.18 Original and enhanced scatters plot of key electrical parameter. 134
6.19 Distribution of BSIM parameters. 136
6.20 Schematic inverter. 137
6.21 Mean values of t_{dHL} and E versus different input rise times. 139
6.22 Normalized values of σ/μ of t_{dHL} versus different input rise times. 139
6.23 Normalized values of σ/μ of t_{dHL} versus various load capacitances 140
6.24 Mean values of E versus different input rise times. 141
6.25 Normalized values of σ/μ of dissipated energy E versus different input rise times. 141
6.26 Normalized values of σ/μ of E versus various load capacitances 142

A.1 Q-Q plots 25 nm at high drain bias 149
A.2 Q-Q plots 35nm at high drain bias 151
A.3 Scatter plot of 25 nm device. 153

B.1 Q-Q plots 18 nm at low drain bias 157
B.2 Q-Q plots 18nm at high drain bias 159
B.3 Scatter plot of 18 nm device. 160

C.1 Q-Q plots 13 nm at low drain bias 164
C.2 Q-Q plots 13nm at high drain bias 166
C.3 Scatter plot of 13 nm device. 167

D.1 Q-Q plots 9nm at low drain bias 171
D.2 Q-Q plots 9nm at high drain bias 173
D.3 Scatter plot of 9 nm device. 174

Acknowledgements

I would like to thank my family for all of the aid and support that they have offered me as I have worked to complete this thesis, without their love and strength I would never have gotten finished. A great deal of thanks goes to my supervisors, Prof. Asen Asenov and Dr. Scott Roy for their patience and guidance over the duration of my studies. I would also like to thank to the various members of the Device Modelling Group (too numerous to mention) for all their aid and support, who have been on hand to answer the many questions Ive asked over the last few years. In particular, I would like to thank Craig Alexander for his help with and guidance through the Monte Carlo and drift diffusion algorithms and simulations.

Declaration of Authorship

I, Urban Kovac, declare that this thesis titled, '3D Drift Diffusion and 3D Monte Carlo simulation of On-Current variability due to Random Dopants' and the work presented in it are my own. I confirm that:

- This work was done wholly or mainly while in candidature for a research degree at University of Glasgow.
- Where any part of this thesis has previously been submitted for a degree or any other qualification at University of Glasgow or any other institution, this has been clearly stated.
- Where I have consulted the published work of others, this is always clearly attributed.
- Where I have quoted from the work of others, the source is always given. With the exception of such quotations, this thesis is entirely my own work.
- I have acknowledged all main sources of help.
- Where the thesis is based on work done by myself jointly with others, I have made clear exactly what was done by others and what I have contributed myself.

Signed: ____

Date: ____

Publications

Urban Kovac, Craig Alexander, and Asen Asenov,Statistical Estimation of Electrostatic and Transport Contributions to Device Parameter Variation, 14th International Workshop on Computational Electronics, October 27th-29th, 2010.

Urban Kovac, Craig Alexander, Gareth Roy, Binjie Cheng, and Asen Asenov, Compact Model Extraction from Quantum Corrected Statistical Monte Carlo Simulation of Random Dopant Induced Drain Current Variability, 8th International Conference on Advanced Semiconductor Devices and Microsystems, pp. 317-320, October 25-27, 2010.

Urban Kovac, Craig Alexander, Gareth Roy, C. Riddet, Binjie Cheng, Asen Asenov, Hierachrical simulation of statistical variability: from 3D MC with ab initio ionised impurity scattering to statistical compact models,IEEE Trans. Electron Dev.,Vol.57, Issue 10, pp. 2418-2426, Oct.2010.

A. Asenov, B. Cheng, D. Dideban, **Urban Kovac**, N. Moezi, C. Millar, G. Roy, A. R. Brown, S. Roy, Modeling and Simulation of Transistor and Circuit Variability and Reliability, IEEE Custom Integrated Circuits Conference, September 19 - 22, accepted.

Urban Kovac, D. Dideban, B. Cheng, N. Moezi, G. Roy and A. Asenov, A Novel Approach to the Statistical Generation of Non-normal Distributed PSP Compact Model Parameters using a Nonlinear Power Method, in Proc. Simulation of Semiconductor Processes and Devices (SISPAD), Bologna, Italy, Sept. 6-8, 2010, pp. 125128.

A. Asenov, A. R. Brown, G. Roy, B. Cheng, C. L. Alexander, C. Riddet, **Urban Kovac**, A. Martinez, N. Seoane and S. Roy, "Simulation of statistical variability in nano-CMOS transistors using drift-diffusion, Monte Carlo and non-equilibrium Greens function techniques," Journal of Computational Electronics, vol. 8, iss. 3-4, pp. 349-373, 2009.

C. Alexander, **Urban Kovac**, G. Roy, S. Roy and A. Asenov, A unified density gradient approach to ab-initio ionised impurity scattering in 3D MC simulations of nano-CMOS variability In: Ultimate Integration of Silicon, pp.43-46, 2009.

A. Asenov, S. Roy, A. R. Brown, G. Roy, C. L. Alexander, C. Riddet, C. Millar, B. Cheng, A. Martinez, N. Seoane, D. Reid, M. Faiz. Bukhori, X. Wang and **Urban Kovac**, "Advanced simulation of statistical variability and reliability in nano CMOS transistors," in Proc. IEDM, USA, Dec. 2008, p. 421.

Urban Kovac, D. Reid, C. Millar, G. Roy, S. Roy and A. Asenov, Statistical simulation of random dopant induced threshold voltage fluctuations for 35 nm channel length MOSFET,Microelectronics Reliability, vol. 48, iss. 8-9, pp. 1572-1575, 2008.

Urban Kovac, Reid, D., Millar, C., Roy, G., Roy, S.,Asenov,A., Statistical Simulation of Random Dopant induced treshold Voltage Fluctuactions for 35nm Channel Length MOSFET, 19th European Symposium on Reliability of Electron Devices, Failure Physics and Analysis, 29th September - 2nd October , 2008.

Abbreviations

BSIM	Berkeley Short-channel IGFET Model
BTE	Boltzman Transport Equation
BZ	Brillouin Zone
CMOS	Complementary Metal Oxide Semiconductor
DD	Drift Diffusion
EOT	Equivalent Oxide Thickness
FinFeT	Fin Field Effect Transistor
FQMC	Frozen Quantum Monte Carlo
HP	High Performance
HVT	Herring-Vogt transformation
IC	Integrated Circuits
ITRS	International Technology Roadmap for Semiconductors
LAH	**L**ist **A**bbreviations **H**ere
LER	Line Edge Roughness
LP	Low Performance
MC	Monte Carlo
MG	Multi-Gate
MOSFET	Metal Oxide Field Effect Transistor
NBTI	Negative Bias Temperature Instability
NEGF	Non-Eequlibrium Greens Functions
OPC	Optical Proximity Correction
OTV	Oxide Thicknes Variations
PDK	Preliminary Design Kit
PSG	Polysilicon Gate Granuality
RDD	Random Discrete Dopants

RTS	Random Telegraph Signal
SCE	Short Channel Effects
SCQMC	Self-Consistent Quantum Monte Carlo
Si	Silicon
SNM	Static Noise Margin
SOR	Successive Over-Relaxation
SRAM	Static Random Access Memory
TCAD	Technology Computer-Aided Design
UTB FD SOI	Ultra-Thin Body Fully Depleted Silicon on Insulator
WNM	Write Noise Margin

Physical Constants

Reduced Plancks constant	$\hbar$	$=$	$1.054571628 \times 10^{-34}$ Js
Vacuum permittivity	ϵ_0	$=$	$8.85418782 \times 10^{-14}$ F/cm
Boltzmanns constant	k_B	$=$	1.38×10^{-23} J/K
Electron rest mass	m_0	$=$	9.11×10^{-31} kg
Elementary (unit) charge	q	$=$	1.60×10^{-19} C
Silicon Lattice Constant	a	$=$	0.543 nm

Symbols

a	distance	m
b_n	Density Gradient Parameter	
$C[f]$	The collision term	
D_n	Diffusion Constant of Electrons	
E	Electric Field	Vm^{-1}
E_{cn}	Constant Field Fitting Parameter	Vm^{-1}
E_g	Band Gap	eV
$E_{\parallel n}$	Parallel Applied Electric Field	Vm^{-1}
$E_{\perp}$	Normal Component of The Electric Field at The Interface	Vm^{-1}
$\boldsymbol{F}$	Force	N
$\widehat{F}$	Empirical Distribution Function	
F_{q}	Quantum Force	Vm^{-1}
F_{cl}	Classical Force	Vm^{-1}
F_{qc}	Quantum Correction Force	Vm^{-1}
$f(\boldsymbol{r}, \boldsymbol{k}, t)$	Distribution Function	
$G_{surf,n}$	Parameter that Reflects The Rate of Surface Roughness Scattering	
H	Hamiltonian	
H_0,	Null Hypothesis	
H_1	Alternative Hypothesis	
I_d	Drive Current	A
I_{off}	leakage current	A
$\boldsymbol{J}_n$	Electron Current Density	Am^{-2}
$\boldsymbol{K}$	Reciprocal Lattice Vector	m^{-1}
$\boldsymbol{k}$	Electron Wavevector	m^{-1}
m_d^*	Density of States Effective Mass	kg

m_l	Longitudinal Mass Component	kg
m_n^*	carrier's effective mass	kg
m_t	Transverse Mass Component	kg
$\mathcal{N}$	Family of Univariate Normal Distributions	
N_A	Acceptor Doping Concentration	m^{-3}
N_D	Donor Doping Concentration	m^{-3}
N_P	Polysilicon Doping Concentration	m^{-3}
N_{refn}	Reference Concentration Parameter	m^{-3}
n	Electron Carrier Densities	m^{-3}
n_i	Intrinsic Carrier Concentration	m^{-3}
n_{mc}	Electron Distribution from MC	m^{-3}
P	power	W (Js^{-1})
$\boldsymbol{P}$	Crystal Momentum	kgms^{-}1
p	Hole Carrier Densities	m^{-3}
$\boldsymbol{r}$	Position	m
r_c	Cut-Off Radius	m
$S_l(\boldsymbol{k'}, \boldsymbol{k})$	The Transition Probability per Unit Time	
T_n	Electron Temperature	K
$\boldsymbol{U}$	Herring-Vogt Transformation Matrix	
$U_C(\boldsymbol{r})$	Crystal Lattice Potential Energy	eV
$u_{n\boldsymbol{k}}(\boldsymbol{r})$	The Corresponding Bloch Function	
V_D	Drain Voltage	V
V_G	Gate Voltage	V
$V_{t,sat}$	Saturation Threshold Voltage	V
$V(\boldsymbol{r}(t))$	The Position Dependent Electrostatic Potential	V
$\boldsymbol{v}_g$	Electron Group Velocity	ms^{-1}
v_{inj}	Equivalent injection velocity	ms^{-1}
v_n	Electron Velocity	ms^{-1}
v_n^{sat}	Saturation Velocity	ms^{-1}

α_n	Fitting Parameter
α	Significance Level
β_n	Dimensionless Fitting Parameter

β_0	Constant Parameter of Linear Regression Model	
β_1	Slope Parameter of Linear Regression Model	
γ_1	Skewness	
γ_2	Kurtosis	
Γ_S	Area of The Source Terminal	
Γ_D	Area of The Drain Terminal	
Γ_G	Area of The Gate Terminal	
Γ_{SUBS}	Area of The Back Substrate Contact	
$\varepsilon_n(\boldsymbol{k})$	Eigen Energy Values	eV
μ_n	Electron Mobility	$\mathrm{m^2V^{-1}s^{-1}}$
μ	Mean Value	
$\mu_{n_{min}}$	Minimum of The Range of Experimental Mobilities	$\mathrm{m^2V^{-1}s^{-1}}$
$\mu_{n_{max}}$	Maximum of The Range of Experimental Mobilities	$\mathrm{m^2V^{-1}s^{-1}}$
μ_{0n}	Concentration Dependent Mobility	$\mathrm{m^2V^{-1}s^{-1}}$
σ	Standard Deviation	
τ	Intrinsic Delay	s
ϕ_n	Electron Quasi-Fermi Level	V
ϕ_p	Hole Quasi-Fermi Level	V
ψ_{eff}	Effective Quantum-Corrected Potential	V
ψ	Electrostatic Potential	V
ψ_{qc}	Quantum Potential Correction Term	V
ψ_{DG}	Density Gradient Effective Quantum Potential	V
ψ_{CL}	Classical Potential	V
$\psi_{\boldsymbol{k}}$	Bloch Wave	
Ω	Damping Parameter in SOR method	
θ	Statistical Parameter of Interest	
Ξ_{ac}	Acoustic Deformation Potential	eV

Chapter 1

INTRODUCTION

Currently 45 nm and, very recently, 32 nm technology conventional Si MOSFETs are present in personal computer devices [1]. The progressive scaling of CMOS transistors to achieve faster devices and higher circuit density has fuelled the phenomenal success of the semiconductor industry, as captured by Moore's famous law [2, 3]. According to the International Technology Roadmap for Semiconductors (ITRS), devices with channel lengths of 17 nm are predicted to be in mass production around 2015 [4]. At such small dimensions, physical variations introduced between devices due to the discreteness of charge and granularity of matter will have significant effects on device characteristics [5]. Such statistical variation is in addition to systematic on-wafer variation but, unlike it, cannot be reduced by tightening process control.

It is widely recognised that increased statistical variability associated with reduced device dimensions is among the major challenges to the scaling of the next generation CMOS transistors and their integration in digital circuits [6, 7]. Statistical variability already critically effects SRAM scaling and introduces leakage and statistical timing issues in digital logic circuits which increasingly lead to hard digital faults. Variability is also the main factor restricting the scaling of the supply voltage, which contributes to the looming power crisis. The power crisis refers to the increase of the power density on chip that accompanies the increase of transistor density and that can not be alleviated as device variation limits the ability to scale supply voltage.

Experimental evaluation of statistical variability is complicated by the number of independent sources that contribute to it and by the contribution of additional systematic sources. Some of the most important sources of statistical variation include random discrete dopants (RDD) [5, 8, 9], gate line edge roughness (LER) [10, 11], oxide-thickness variations (OTV) [12–14], polysilicon gate granularity PSG [7, 15, 16], high-κ granularity [17, 18] and metal gate granularity [19, 20]. In contrast, statistical simulation studies of device parameter variation provides a valuable opportunity to investigate the influence of individual sources of variability and to do so early in the design stage. Such simulation studies can provide a vital description of the complex statistical distribution of device parameters and help to estimate the first few moments of the distributions as an industrial gold standard in order to be able to build reliable and stable future technology generations of circuits and systems.

In conventional MOSFETs RDD variation is the dominant source of variability for near-future scaling. LER becomes dominant in very short channel double gate devices with undoped channels [10, 11]. OTV arises from the microscopic irregularity of Si/SiO_2 and gate/dielectric interfaces [12] and contributes to the local variations in surface roughness scattering [13]. Localised states associated with the PSG grain boundaries and corresponding carriers trapping result is surface potential pinning and localized threshold voltage variation [7]. Similarly, high-κ insulator materials with different dielectric constants due to crystalline grain orientation contributes to variations in the surface potential which affects fluctuations in charge density and carrier transport at the interface. Metal gate granularity results in carrier density and transport variations via local variations in work-function [21].

A significant amount of work has been done in examining intrinsic parameter variability experimentally and using numerical simulations in both idealised [5, 10, 13, 14, 22–24] and more realistic devices [9, 25]. Several simulation techniques may be employed to these ends, such as Drift Diffusion (DD), Monte Carlo (MC) and quantum transport models. For many years drift diffusion simulations have been driving statistical variability simulations. DD captures well the electrostatic impact of the statistical variability sources and provides accurate and reliable results in respect of threshold voltage [26] and leakage variability [27, 28]. However, for the estimation of on-current variability, DD simulations are inaccurate and unreliable. DD cannot describe the nonequilibrium quasiballistic transport in modern nano CMOS transistors and, most importantly, variations in transport due to scattering from the Coulomb potential of random configurations of discrete dopants and from channel potential and quantisation variation associated with other variability sources. With respect to this, MC simulation is well suited to capture transport variation and resultant on-current variability. However, MC simulation is computationally expensive and prohibitive for the simulation of a very large statistical ensemble of device characteristics required for compact model extraction and circuit design analysis.

The focus of this work is to resolve transport variation in MC and accurately study on-current variability induced by random discrete dopants in conventional CMOS devices. This work then aims to bridge the gap between DD and MC simulation by establishing a reliable framework for incorporating the accuracy of MC in transport simulation with the efficiency of DD in resolving electrostatic variation. This will enable accurate statistical scale device simulation of on-current variability in nano-scale MOSFETs and its transfer to industry standard compact models.

1.1 Aims and objectives

Quantum corrections within DD are vital for the accurate simulation of nano-CMOS transistors and for the accurate inclusion of discrete dopant effects, mediating the trapping of carriers in the sharply resolved Coulomb wells of the individual impurities [29, 30]. The introduction of quantum corrections in MC simulation is similarly essential in order to incorporate confinement effects in nano scale devices [31]. Efficient quantum mechanical corrections have been demonstrated previously in self-consistent ensemble MC device simulation [32]. Previous MC simulation studies of RDD induced drain current variability [33, 34] however omitted any such corrections relying upon a short-range correction to account for carrier-impurity interactions. A major aim of this work will be the implementation of quantum corrections as a consistent approach to the treatment of confinement effects and the resolution of scattering from random discrete dopants in self-consistent *ab initio* MC simulations.

Further, a methodology to accurately propagate the MC simulated device variability into compact models, which serve as a proxy between physical models and circuit simulations, is required in order that the variability may be transferred to complex circuit analysis. Due to the huge computational cost of MC simulation with respect to obtaining full $I_D - V_G$ characteristics for an ensemble of nanoscale devices, there is a need to develop a reliable simulation strategy to propagate on-current variability from MC into efficient DD simulations. Based upon this methodology, sets of $I_D - V_G$ characteristics may be simulated which in turn serves as an input to statistical compact modelling.

In light of the above considerations, this work proposes to develop an economical and computationally efficient hierarchical simulation strategy that allows the accurate on-current variability resulting from self-consistent quantum corrected *ab initio* MC simulation to be transferred into efficient statistical 3D DD simulations. MC will be limited to device simulation above threshold, where DD omits additional variation from transport effects. DD simulations subsequently calibrated through mobility model parameters to be consistent with MC will then in turn be used to obtain full target $I_D - V_G$ characteristics for the extraction of statistical compact models, suitable for comprehensive statistical circuit analysis. To the best of our knowledge, this represents the most comprehensive, efficient and accurate approach for predictive simulation of RDD variability and its incorporation in industry standard compact models for use in statistical circuit design.

1.2 Outline

This work is organised as follows. In chapter 2 the important device scaling challenges are reviewed with focus on intrinsic parameter fluctuations. Furthermore, the classification of variability is discussed with a brief description of the most important sources of intrinsic parameter fluctuations. The hierarchy of the most comprehensive currently available 3D tools for statistical simulation of variability in contemporary and future nano-CMOS transistors, including DD and MC techniques, is presented. Finally, the variability impact on circuits is briefly discussed.

Chapter 3 comprises a review of the DD and MC simulations techniques. A detailed summary of the fundamentals and equations used by DD simulation with quantum corrections is followed by a description of the Glasgow statistical 3D DD atomistic simulator with an emphasis on the implementation of the RDD. Furthermore, the mobility models used by the 3D DD simulator are reviewed. DD simulations are chosen as the benchmark for subsequent MC simulation. In the second part of chapter 3, the 3D MC simulator is discussed in greater detailes. This is preceded by a brief discussion of the semi-classical carrier dynamics and semi-calssical Boltzmann Transport Equation followed by a detailed description of the non-parabolic and ellipsoidal approximation of the band structure, scattering mechanisms, carrier dynamics, and *ab initio* ionised impurity scattering. The last section is dedicated to the calibration of bulk Si where fundamental physical values and calibration parameters are summarised.

Chapter 4 presents details of the study of an accurate description of bulk carrier-ion interactions via the density gradient effective quantum potential within finely discretized 3D self-consistent Monte Carlo simulation. Further, the density gradient method is compared to previously reported methods based upon a classical potential with short-range correction. The impact of individual acceptors on drain current variability is examined in a variety of scaled bulk n-channel MOSFETs.

Chapter 5 describes an extensive statistical enhancement methodology for studying RDD induced on-current variability in a range of well scaled MOSFETs. The accuracy of this approach and its results are validated by a comprehensive statistical analysis. Results are presented to devices with different channel lengths. A comprehensive statistical model is built to accurately separate the impact of the random discrete dopants on the drain current variations into their relative electrostatic and transport contributions.

Chapter 6 is dedicated to the detailed description of the hierarchic simulation methodology which propagates on-current variability obtained by MC simulation at high gate bias at both low and high drain bias to the DD simulations by suitable calibration of the DD mobility models. Furthermore, the complex compact model extraction strategy is described. Based upon this overall simulation strategy, inverter circuit simulations are carried out to demonstrate the impact of the proposed methodology on subsequent circuit analysis.

Finally, the conclusions for this research project are drawn in Chapter 7, where suggestions for future work are also made.

Chapter 2

VARIABILITY

Conventional silicon MOSFETs are still the workhorse of the semiconductor industry and continue to drive CMOS technological advance. They have developed rapidly over the last three decades following Moore's law [2, 3] - the continuous developmental goal the semiconductor industry. The corresponding scaling of the CMOS transistors to smaller dimensions, allowing increased speed as well as higher density and lower cost per function. However, the industry is now facing major technology and design challenges [35, 36], illustrated in figure 2.1 [37]. These challenges brought to an end the period of so-called "happy scaling". Figure 2.1 illustrates the market bifurcation in the cumulative interdependent challenges as a function of time and technology generation. Currently, maximizing yield is the major challenge to chip fabrication and this is comprised of a series of independent challenges. Power consumption is one important factor, subthreshold drain and gate leakage also affects CMOS scaling and integration since they are linked closely to threshold voltage variability. Increasing CMOS device variability has become one of the most acute problems facing the semiconductor manufacturing and design industries at, and beyond, the 45 nm technology generation. New applications of current and future technology generations necessitate a new set of performance metrics. We will discuss briefly each challenge further.

Of the major design challenges that needed to be addressed, in the middle of this decade was the high gate leakage current associated with the reduced oxide thickness required to maintain electrostatic integrity and high gate capacitance [27, 28]. This leakage

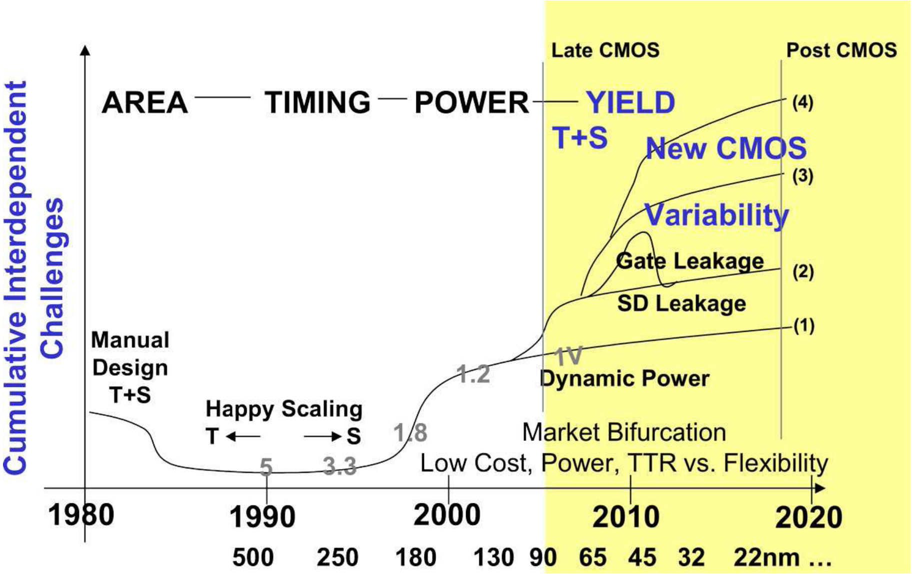

FIGURE 2.1: The major scalling challanges [37].

significantly impacts static power dissipation and is mitigated by introducing a high-κ gate dielectric in place of the traditional SiO_2 in the 45 nm technology generation [38, 39]. This maintains gate capacitance while allowing a physically thicker dielectric and resistance to tunnelling. Current leading high-κ materials are HfO_2 [38] ($\epsilon_k \sim 22$ [40]) and $HfSiO_x$ [38] ($\epsilon_k \sim 12-16$). Additionally, polysilicon gate depletion reduces the gate capacitance and significantly reduces on-current. This was initially combated through increased poly doping to reduce depletion effects, but this is limited by the solid solubility of the relevant dopants in silicon. Metal gates effectively remove gate depletion and in combination with high-κ dielectrics are essential in next generation devices [39, 41–43], demonstrating higher drive currents [44] and improved subthreshold slope [39]. Strain engineering in order to obtain higher channel mobility to improve device performance is also necessary in order to meet device requirements [44].

However, intrinsic device parameter fluctuations associated with the discreteness of charge and granularity of matter have emerged in the past decade [5] as one of the major challenges to scaling and integration for the present and next generation of nano-CMOS transistors and circuits [6, 7, 36]. Statistical variability has a significant impact on SRAM (Static Random Access Memory) scaling [45, 46] and the associated increase in leakage current and timing has become a major issue in logic circuits with a detrimental effect on subsequent circuit performance [47]. Variability is also the main factor restricting the scaling of the supply voltage, which for the last four technology generations has remained virtually constant, adding to the looming power crisis [36]. The 2008 update of ITRS relaxed the speed of introducing new technology generations with the current, 2009, edition extending the life for high performance planar bulk MOSFET until the year 2015. A restricted set of ITRS 2009 device dimensions and design parameters forecast is listed in table 2.1. After 2015, an industry shift to ultra-thin body fully depleted silicon on insulator (UTB FD SOI) CMOS with 11.7 nm final physical gate length in 2019 is expected, which should be replaced latter by multi-gate (MG) CMOS continuing through to the projected end of the current edition of the Roadmap in 2024 [4]. As this work focuses on the effects of variability, some time is devoted to describing it in detail and in particular defining the difference between statistical and systematic sources of variability. This is discussed next.

	Year of Production				
	2010	2013	2015	2019	2024
MPU/ASIC Metal 1 (M1) 1/2 Pitch $[nm]$	45	27	21	13.4	7.5
Physical Gate Length $[nm]$	27	20	17	11.7	7.4
Equivalent Oxide Thickness $[nm]$	0.95	0.65	0.53	0.5^{*}	0.5^{**}
Eletrical Equivalent Oxide Thickness [nm]	1.26	0.95	0.82	0.9^{*}	0.9^{**}
Channel Doping $[10^{18}cm^{-3}]$	4	5.7	7.5	0.1	0.1
Power Supply Voltage $[V]$	0.97	0.87	0.81	0.71	0.6
Saturation Threshold Voltage $V_{t,sat}[mV]$	289	295	302	235^{*}	231^{**}
NMOS Drive Current $I_{d,sat}[\mu A/\mu m]$	1200	1450	1680	1970^{*}	2170^{**}
Equivalent injection velocity $v_{inj}10^{7}[cm/s]$	0.77	0.84	0.98	1.41^{*}	2.32^{**}
Intrinsic delay $\tau = CV/I[ps]$	0.78	0.57	0.45	0.22^{*}	0.13^{**}

TABLE 2.1: 2009 ITRS Roadmap. * UTB FD device, ** MG device.

2.1 Variability Classicfication

Several approaches exist to categorise device variability. Bernstein et al. [6] categorised the variability by means of the variability matrix, shown in figure 2.2. The spatial extent to which device variability correlates defines the separation of the matrix rows. Global variation refers to variation between wafers, from chip to chip on single wafer, and slow variations across chip. Local variation refer to variations between adjacent devices in a chip. The matrix columns separate process, operational environment and temporal factors that influence device variation [6].

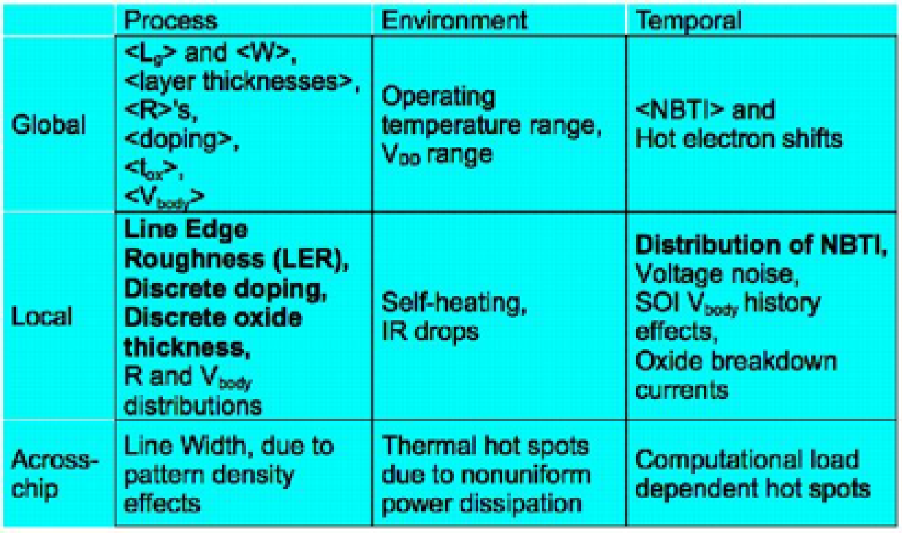

	Process	Environment	Temporal
Global	$<L_g>$ and $<W>$, $<$layer thicknesses$>$, $<R>$'s, $<$doping$>$, $<t_{ox}>$, $<V_{body}>$	Operating temperature range, V_{DD} range	$<$NBTI$>$ and Hot electron shifts
Local	**Line Edge Roughness (LER),** **Discrete doping,** **Discrete oxide thickness,** R and V_{body} distributions	Self-heating, IR drops	**Distribution of NBTI,** Voltage noise, SOI V_{body} history effects, Oxide breakdown currents
Across-chip	Line Width, due to pattern density effects	Thermal hot spots due to nonuniform power dissipation	Computational load dependent hot spots

FIGURE 2.2: The variability matrix in which the local random variability is a major source of concern [6].

Further, Bernstein et al. separate device variability into intrinsic device variability and extrinsic process variability [6]. Extrinsic process variability is associated with the operating dynamics of contemporary changes in the fabrication process conditions. Generally, it is present in different levels from lot to lot; from wafer to wafer within a lot; across wafer; from chip to chip and across chip [6]. The main focus of this work is not on extrinsic process variability but rather focuses on intrinsic statistical variability, highlighted in the local row and process column in the variability matrix.

Intrinsic statistical device variability is introduced by the discreteness of matter and charge and, unlike local systematic variation, cannot be eliminated by tightening of process controls [5, 25]. Statistical variability may result in adjacent macroscopically identical transistors having characteristics that are from opposite ends of some statistical distribution. At the 45 nm technology generation the statistical variability account for more than 50% of total variability [48, 49]. It is expected that the impact of statistical variability will significantly increase in the following 32nm technology node [50] and on future scaling and integration [51]

2.2 Sources of Intrinsic Device Parameter Variation

As transistors are scaled to nanometre dimensions, uncontrollable random variations in their atomic structure independent of the quality of the fabrication process result in stochastic variations in their electrical characteristics. These atomic scale differences make each device unique and effect their operation, leading to a distribution of key device parameters such as threshold voltage and on/off current [5, 22, 25, 26]. Figure 2.3 [36] represents an idealised archetypal device, highlighting straight lithographic edges, ideal material interfaces and continuous doping profiles. This is contrasted with a more 'realistic' looking representation of a 20nm MOSFET in which there will be fewer than 50 Silicon atoms along the channel. The scale of the Silicon lattice is suggested in the figure, lithographic gate edges show variation about a mean, material interfaces reveal discontinuities on the order of the atomic separation and individual dopant atoms are randomly distributed according to the nominal doping profile.

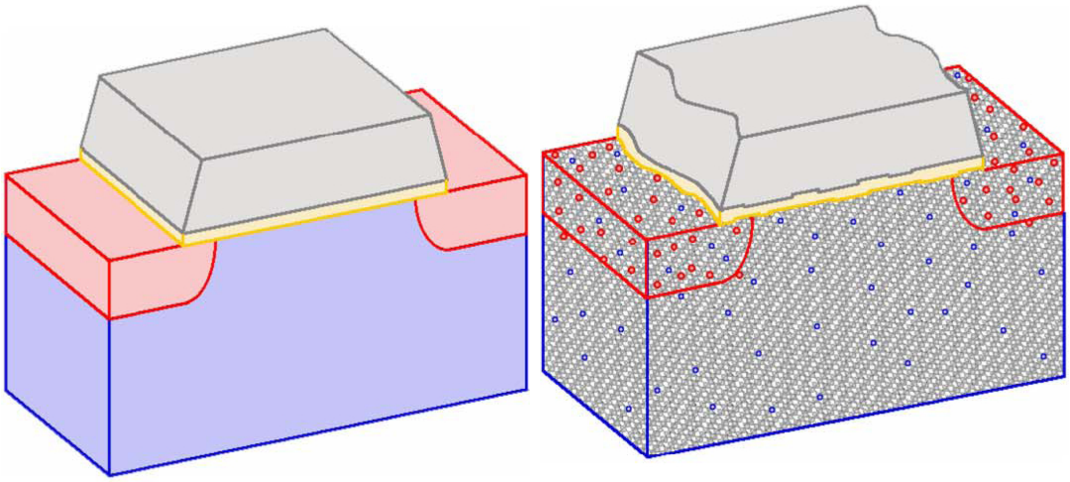

FIGURE 2.3: Traditional continuous device description (left), assuming a continuous doping distributions and smooth boundaries and interfaces, compared with a realistic atomistic description (right) highlighting discrete changes [36].

Continued scaling to sub10nm channel length MOSFETs is similarly illustrated in figure 2.4. In such devices, even at the high levels of doping required, there are few substrate and source/drain dopants and variation in their position and number have the potential to significantly effect individual device characteristics.

In addition, the gate oxide thickness has become equivalent to only few atomic layers with a typical interface roughness on the order of 1/2 atomic layers. This will introduce a localised variation in the oxide thickness resulting in each transistor having a microscopically different oxide thickness or body thickness pattern in the case of SOI and multigate device architectures [13]. The granularity of the photoresist, together with other factors, will introduce unavoidable line edge roughness (LER) in the gate pattern

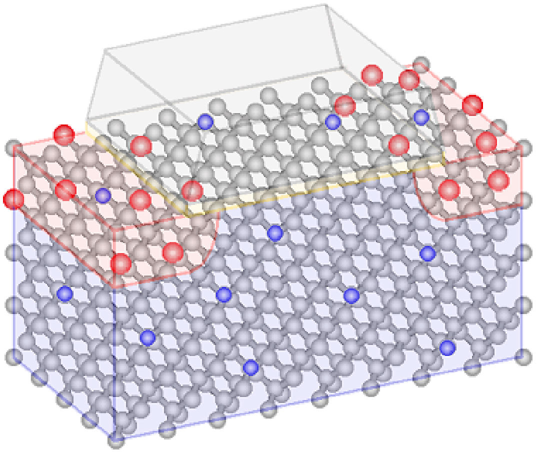

Figure 2.4: Representation of a sub 10 nm MOSFET. There are only a handful of Si atoms along the channel and variation in number/position of the few dopants expected will be statistically significant [36].

definition and statistical variations in geometry between devices [10, 11, 52]. Granularity of the poly-silicon gate [7] and, as devices move to high-κ/metal gate stacks in the 45 nm technology generation [1], the granularity of the high-κ dielectric [17, 40] and metal gate [19–21, 53] become further prominent sources of statistical variability.

In current conventional bulk MOSFETs, statistical variation in random discrete dopants within the channel plays the prominent role in device parameter variation, with simulations at the 45 nm technology node demonstrating that RDD contributes 65% of the total variability [54]. This could be overshadowed by line edge roughness in future technologies if LER cannot be scaled below the currently achievable magnitude and in novel device architectures like SOI which tolerate low channel doping concentrations. Random dopant fluctuations will however still play a role via variation in the source/drain doping, correlated with the LER pattern, and play a significant role in RTS noise and device performance degradation. As they currently represent the greatest source of concern and are of great importance in future technologies, random discrete dopants are the focus of the work in this thesis. As such, a description of RDD is given next.

2.2.1 Random Discrete Dopants

Random dopants are introduced predominantly by ion implantation and redistributed during high temperature annealing. Figure 2.5 illustrates the dopant distribution obtained by the atomistic process simulator DADOS by Synopsys [36]. Despite the high doping concentrations, nanoscale devices contains a few tens of dopants within the active region. The distribution of RDD follows a Poisson distribution [55, 56]. This implies that for an average of N dopants within an arbitrary volume, the number of dopants varies with $\sqrt{N}$. According to the 2009 edition of the ITRS, the average number of dopant atoms will decrease with scaling technology, however the ratio between the standard deviation and the average number of dopants within active region of device will increase rapidly ($1/\sqrt{N} \uparrow$, if $N \downarrow$).

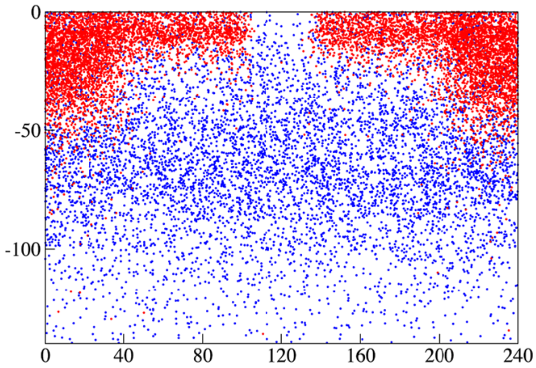

FIGURE 2.5: Kinetic Monte Carlo (KMC) simulation of RDD (DADOS, Synopsys). The position of discrete random dopants obtained from the output of an atomic scale process simulation [36].

The random position of each dopant atom creates a unique charge distribution within each device and alters significantly a single device's electrostatic operation and the transport of carriers due to the associated fluctuations in the potential landscape. These potential fluctuations are illustrated in Figure 2.6 which is the result of a drift diffusion simulation of an atomistic doped 35 nm n-channel MOSFET. The variations result in a significant distribution of threshold voltage compared with the threshold voltage of the ideal device [5]. In such a potential landscape, current flows predominantly through percolation paths formed by local potential energy minima between channel dopants. Trapping and de-trapping of carriers at interface states has some probability of occurring along such a percolation path, raising the local potential minima. This blocks the current path, consequently having a greater impact than if current flowed uniformly across the channel. This effect results in the observed very high amplitudes of random telegraph signal (RTS) [57, 58].

The adverse effects of RDD variation on device parameter distributions in aggressively scaled devices were predicted in the early seventies of the last century [55, 59] and have

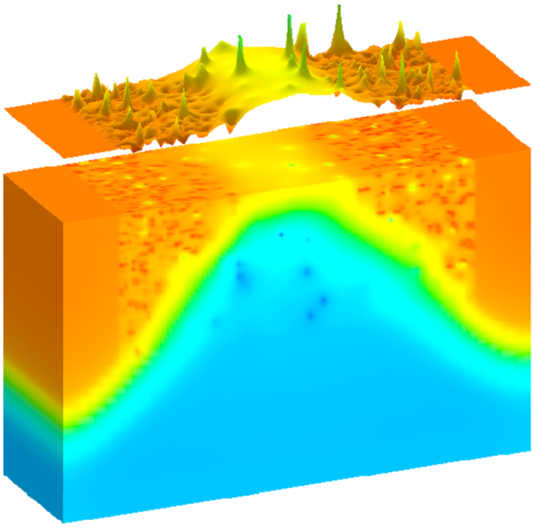

Figure 2.6: Typical 3D potential distribution reflecting the impact of random discrete dopants in a typical 35 nm n-channel MOSFET [36].

been experimentally verified [8, 56, 60, 61]. A significant amount of work has been done in examining the effects of random dopant variation on MOSFET characteristics analytically [56, 62–65]. Initial simulation studies were performed in 2D [9, 66] and were based upon a continuous doping profile [66, 67]. However, since the variation is inherently three dimensional and discrete, 3D simulations with individual dopants were necessarily developed [5, 22, 68]. Several methods for determining the random distribution of dopant atoms within the simulated devices were also developed, varying from simple models based upon assigning dopants directly to a mesh node, through assigning a dopant to the underlying crystal lattice before applying a charge assignment scheme, to kinetic Monte Carlo simulation of dopant implantation and diffusion [5, 23, 66, 69]. In order to construct a reliable estimate of a particular parameter's distribution, simulation of a large statistical ensemble is required. This is computationally expensive and until recently had restricted such simulation studies to relatively small samples of typically 200 microscopically different devices [26, 30]. Results of such studies revealed a lowering of the average threshold voltage with respect to the ideal, uniform, device [5] and showed that the threshold voltage distribution is close to normally distributed. Critically, it has been shown that the effect of RDD on the standard deviation of threshold voltage distribution increases with decreasing device dimensions [26]. This is as a result of the above mentioned increased statistical variation in the number of dopants and of the size of the impurity potential affecting a larger relative area of the active region within smaller devices. Further, it has been demonstrated that the position of the channel dopants plays a key role in determining the magnitude of the threshold voltage variations [24, 70], with dopants nearer the interface having significantly greater impact on device parameters [71]. Transitioning to SOI [72] and FinFeT [73] devices will consequently reduce the impact of RDD induced variation since such devices have superior electrostatic integrity and tolerate low channel doping. However, the design implications of variability requires an accurate knowledge of parameter distributions well into the tails and this demands the simulation of a very large populations of devices. With modern computing facilities such truly large scale statistical studies have become practical and have led to the simulation study with sample size in the range of 10^5 [70, 74–77]. These studies revealed for the first time that the distribution of the threshold voltage variations caused by random dopants is not a Gaussian, revealing significant skew and kurtosis.

In addition to threshold voltage variation, on current variability has been investigated experimentally [78] in which 44 pairs of n/p MOSFET were measured, and the standard deviation of the saturation current was derived based on the α power law which states that the saturation current is proportional to $(V_G - V_{th})^\alpha$. The constant α defines the slope between the standard deviation of the threshold voltage and the standard deviation of the saturation current. It was reported that the saturation current variability might be reduced by minimising the threshold voltage variability [78].

As with simulation of threshold voltage variation above, drain current variation associated with RDD has been estimated via statistical drift diffusion simulations [26]. While DD accurately captures the electrostatic variation and its impact on device performance arising from the variability sources discussed previously, thus accurately capturing threshold voltage and off-current variation, it is insensitive to 'transport variation' arising from differences in position dependent scattering from device to device. The accurate investigation of drain current variation demands the accurate resolution of transport variation. It is in this regard that Monte Carlo (MC) simulation capable of capturing deterministic, position dependent scattering and associated transport variation is indispensable for a complete estimate of device parameter variation. Such 'ab initio' approaches to scattering in MC simulations have been presented, with the focus on resolving the carrier-impurity interaction [33, 34, 79–81]. These models all attempt to incorporate ionised impurity scattering directly via carrier propagation, removing the traditional stochastic ionised impurities scattering rate mechanism. Few, however, have been applied to large scale statistical simulations.

One such statistical 'ab initio' MC simulation of transport variation has been presented in [33, 34] and applied to the study of RDD induced drain current variation in a series of realistic scaled devices at both low and high drain bias. Results for each device dimension consistently show a significant increase in the standard deviation of the drain current distribution compared with DD estimates. This is shown in figure 2.7 [33]. Results were consistent with previously published results [26] and those obtained using the commercial simulator TMA MEDICI [82]. MC simulation highlighted the importance of transport variation in estimating drain current variation, with the relative contribution of transport variation to the total drain current variation, shown inset in figure 2.7, accounting for as much as 60%.

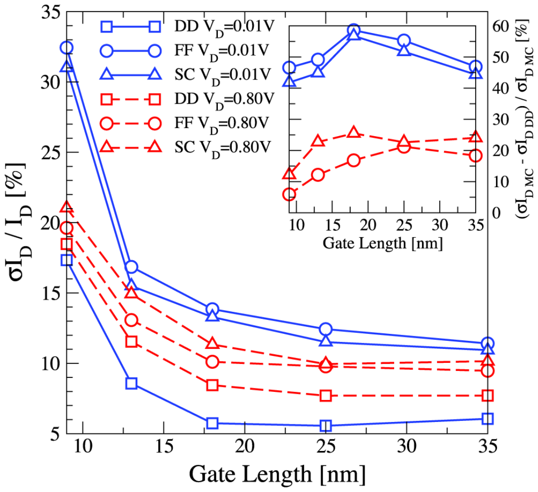

FIGURE 2.7: Percentage drain current variation as a function of channel length from DD simulation and frozen field and self-consistent *ab initio* MC. The contribution from transport variation within MC is shown inset [33].

However, the results in [33, 34] were obtained in the absence of any quantum mechanical corrections. Density gradient quantum corrections have however recently been included in the self-consistent MC simulations of on-current variation in double gate MOSFETs [32]. They are applied via a pre-defined correction to the classical potential derived from drift diffusion simulation. It has been shown to accurately reproduce carrier densities in inversion layers as well as the body thickness dependence of mobility in ulta-thin silicon layers [83].

2.2.2 Other Sources of Variability

Line edge roughness, illustrated in figure 2.8, caused by tolerances inherent to materials and tools used in the lithography processes is yet another source of fluctuation that needs close attention. It will be increasingly difficult to reduce LER below the current level of approximately 5 nm, which is limited by the molecular dimensions in the photoresist used in the 193 nm lithography systems, and therefore will be an increasingly important source of intrinsic parameter fluctuations in the future [10, 11, 52].

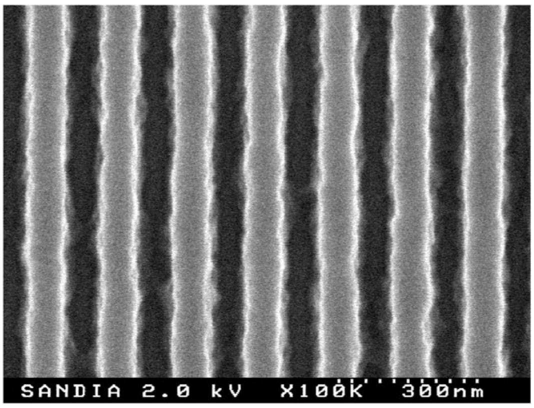

FIGURE 2.8: Typical LER in photoresist (Sandia Labs.) [36].

The polycrystalline granular structure of the polysilicon gate (PSG), illustrated in figure 2.9, has also been identified as an important source of intrinsic parameter fluctuation [7, 16]. Enhanced diffusion along the grain boundaries and localised penetration of dopants through the gate oxide into the channel from the high doping regions in the gate are potential sources of variability [15]. However, the most significant source of fluctuations within polysilicon gates is likely to be Fermi level pinning at the boundaries between grains due to the high density of defect states [84]. This pinning directly affects the surface potential resulting in a local increase in the potential barrier coincident with the grain boundary. The exact nature of grain boundary alignment above the channel will then determine the effect on drain current.

The introduction of high-κ/metal gate technology improves the RDD-induced variability due to the reduction in the equivalent oxide thickness and removal of the PSG effects. However, at the same time it introduces high-κ granularity illustrated in figure 2.10 and variability associated with work-function variation due to the metal gate granularity illustrated in figure 2.11 [18]. In extremely scaled transistors, atomic scale interface

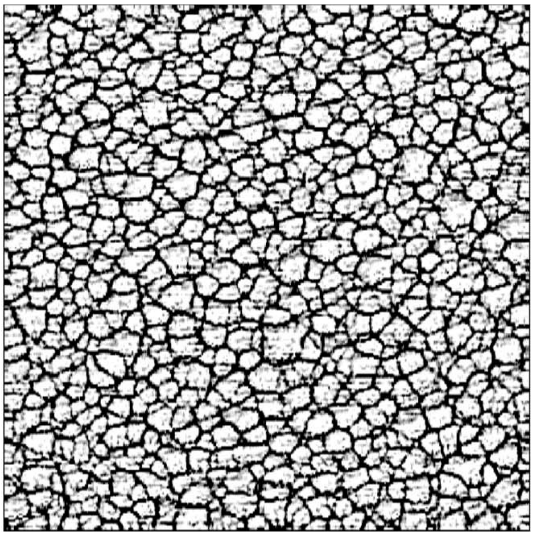

FIGURE 2.9: An SEM micrograph of typical PSG [36].

roughness illustrated in figure 2.12 [13] and corresponding body thickness variations [85] can become an additional important source of statistical variability.

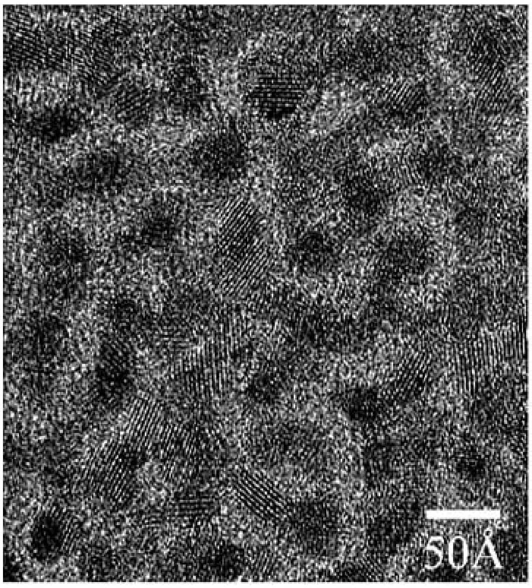

FIGURE 2.10: Granularity in HfON high-κ dielectrics (Sematech) [18, 36].

2.3 Simulation of Intrinsic Variations

The requirement for statistical simulations transforms the traditional device simulation problem into a four-dimensional space where the fourth dimension is considered as the

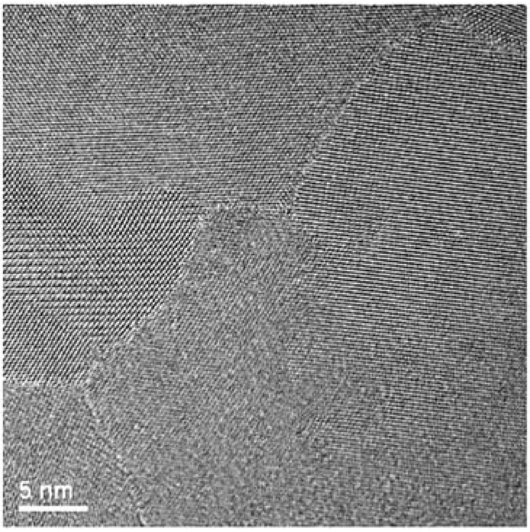

FIGURE 2.11: Metal granularity causing gate work-function variation [36].

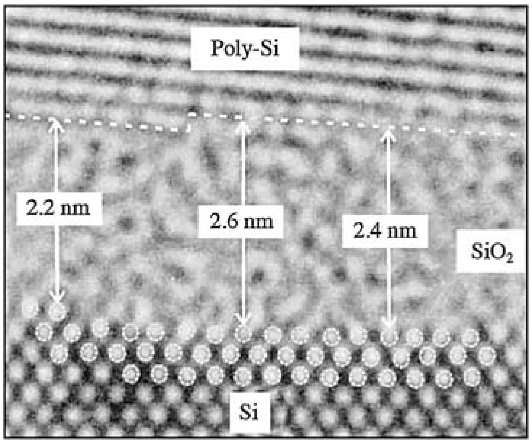

FIGURE 2.12: Scanning electron microscope image of interface roughness (IBM) [13, 36].

size of the statistical sample. This is in order to estimate the mean values, variance and higher moments of the distribution of basic design parameters such as threshold voltage, subthreshold slope, transconductance and on-current for the ensemble of microscopically different devices [86]. It must be emphasised that even the mean values obtained from, for example, statistical atomistic simulations are not identical to the values corresponding to continuous charge simulation [23].

In a typical modern chip there are over one billion transistors, hence there is a need to assess up to 6σ or 7σ of the statistical distribution. This requires the simulation of a large ensemble of devices in order to make reliable estimates of the distribution and to accurately infer the implications of sources of variability. It is important to understand how large the statistical samples need to be in order to obtain sufficient accuracy of the true distribution; how present tools might be used together to produce sufficient accuracy for a single device and the number of results that properly examine the tails of the distributions of a large ensemble of devices. It is recognised that this poses significant simulation challenges and that the successful approach to this problem will make the most efficient use of the currently available simulation tools.

A hierarchy of simulation techniques can be constructed according to their relative computational complexity and accuracy [87, 88]. Compact model simulations are the most efficient due to the phenomenological physical models employed, but can not be used independently of other simulation methods for estimating the effects of device parameter variation as the models are insensitive to microscopic device details. Compact model parameters may however be calibrated to describe individual random instances of a device given device characteristics obtained from more comprehensive simulation techniques. Drift Diffusion (DD) simulation is an example of one such technique. It solves an approximation of the Boltzmann Transport Equation (BTE) using the first two moments. It is the most efficient method of 3D device simulation, capable of accurately describing the electrostatic effects associated with discrete variations.

As such, DD is suitable to study threshold and sub-threshold variation as they are dominated by device electrostatics. Including the third moment of the BTE, representing energy conservation, results in the Hydrodynamic model. The solution of this model, while computationally more demanding than DD, increases the accuracy of simulation results in the drive-current regime due to the partial incorporation of non-equilibrium velocity overshoot effects. While this extension is an improvement over DD it falls short of an complete description of carrier transport, omitting possible carrier backscattering and the effects of multiple independent scattering mechanisms. Ensemble Monte Carlo (MC) simulation is a solution of the BTE via the direct simulation of carrier transport in the presence of multiple scattering mechanisms and represents a considerable increase in accuracy but also in computational effort compared to both the DD and Hydrodynamic models. It can accurately describe non-local and non-equilibrium carrier transport and so accurately estimate on-currents. The MC technique is described in detail in section 3.2 and is used extensively within this work. While modifications of the traditional, semi-classical, MC algorithm allow quantum mechanical tunnelling effects to be simulated, dedicated quantum modelling approaches to the solution of the coupled Poisson Schrodinger, Wigner distribution function, and Non-Eequlibrium Green's Functions (NEGF) exist as advanced quantum transport models. Such quantum transport modelling approaches are however computationally prohibitive for large devices and large statistical ensembles.

DD simulation therefore represents the most efficient and flexible predictive technique for the accurate estimation of threshold/sub-threshold device characteristics, while MC, although slow, is the most efficient and accurate predictive method for estimating on-current characteristics.

2.4 Variability Impact on Circuits

Statistical variability of transistor characteristics already critically affects SRAM scaling [45, 46], and introduces leakage and timing issues in digital logic circuits [47]. Intrinsic parameter fluctuations crucially affect the yield and performance of SRAM circuits, forcing the use of redundancy and flexible powering and are responsible for the different stability and performance of SRAM cells. A schematic of an SRAM cell is shown in figure 2.13 with the static transfer curves for an ensemble of 200 SRAM cells, considering parameter variations associated only with RDD, shown in figure 2.14. Accurate investigation of the tails of key parameter distributions is of fundamental importance to SRAM design as, due to the millions of cells in modern memory arrays, devices that populate the tails are to be expected. Currently SRAM design tolerates devices within 7σ or 8σ of the mean, though a Gaussian distribution is typically assumed. Asymmetry of distributions, already observed in very large scale statistical simulations, could very strongly affect the outcome of SRAM design.

Compact models form a key design component and interface between technology and design. The first step towards variability aware design is to develop statistical compact modelling approaches that can reliably capture statistical variability information and that will enable designers to confidently take full advantage of advanced technologies. Historically, the importance of device matching in the analogue domain drove the statistical compact modelling efforts [89]. For a semiconductor technology to be economically viable in the analog domain the devices require well controlled variance behaviour.

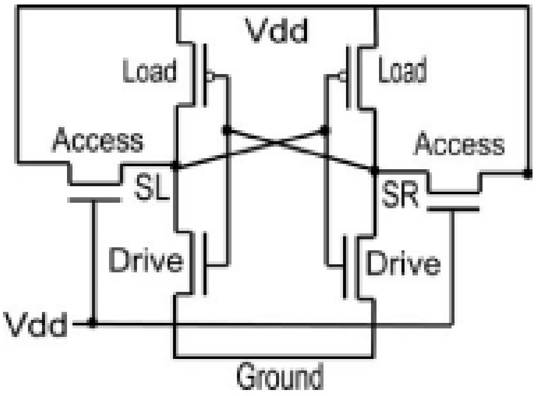

FIGURE 2.13: SRAM cell bias configuration for Static Noise Margin calculation. [45, 77].

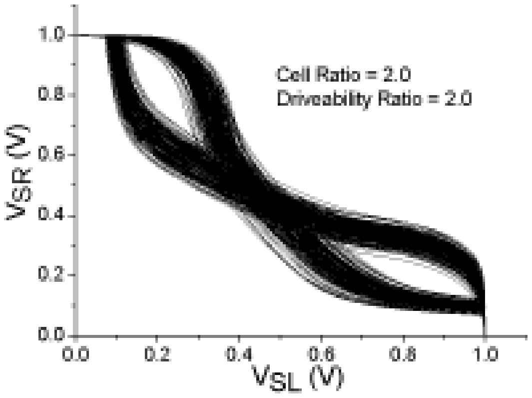

FIGURE 2.14: Static transfer characteristics from an ensemble of 200 SRAM cells. [45, 77].

CMOS digital logic circuits are by contrast more resistant to statistical device variation [90], although it can cause concern in timing and power dissipation. However, the magnitude of statistical parameter variation within the current device technology is now such that it may introduce faults even in digital logic circuits. Consequently, accurate statistical compact models able to capture the simulated or measured statistical device variability are required since this is the only way to communicate this information to designers.

Previous variability research using statistical compact models was restricted to identify only variability associated with process variation [91]. In addition, most statistical compact model approaches developed for the analog domain were based upon the assumption that the compact model parameters were uncorrelated and normally distributed [92].

Unfortunately, the current industrial standard compact models do not have natural parameters designed to incorporate seamlessly the truly statistical variability associated with RDD, LER, PSG, metal gate and high-κ and other relevant variability sources. Representative sets of current-voltage characteristics for each microscopically different device from simulated ensembles are required in order to extract statistical compact models [45, 93].

Based on the statistical compact model libraries built from the above mentioned direct statistical compact modelling results, the impact of RDD variation on 6T and 8T SRAM stability for the next generations of bulk CMOS technology can be investigated [94]. Currently, 6T SRAM is the dominant SRAM cell architecture in SoC and microprocessors. The functionality of SRAM is determined by both static noise margin (SNM) and the write noise margin (WNM). By using write assist technology [95], WNM can be dramatically improved.

More and more, the strategic technology decisions that the industry will be making in the future will be motivated by the desire to reduce statistical variability. SRAM is the most sensitive IC component in respect of statistical variability and needs special care and creative design solutions in order to take full advantage from scaling in present and future technology generations. Statistical compact modelling plays a vital role in variability aware design.

2.5 Summary

In this chapter the main sources of variability in modern nano-CMOS transistors, such as RDD, LER, PSG, metal gate, and high-κ, were presented with regards to the most comprehensive currently available 3D tool for statistical simulation of variability including DD and Monte Carlo. DD results accurately reproduce the measured threshold voltage variability in real devices. MC simulations with *ab initio* ionised impurity scattering are needed to capture properly the transport variability introduced by the random configuration of scatterers in the devices.

The useful life of bulk MOSFETs, from a statistical variability point of view, can be extended below the 20 nm technology mark only if the LER and the equivalent oxide thickness could be successfully scaled to the required values. The introduction of fully-depleted SOI MOSFETs, and perhaps FinFETs, will mainly be motivated by the necessity to reduce the statistical variability. In SOI devices and FinFET technology the statistical variability induced by RDD is suppressed since these technologies benefit from undoped channels, have improved electrostatics integrity and better performance compared with bulk MOSFET. This, however, might be jeopardised by other sources of variability associated with the introduction of the high-κ/metal gate stack and increased statistical reliability problems. It is vital to capture the simulated or measured statistical variability in statistical compact models since this is the only way to propagate this information into subsequent circuit analysis.

Chapter 3

DEVICE SIMULATORS

In this chapter the DD and MC device simulators used in our studies are described, paying particular attention to their abilities to resolve the discrete random dopant effects in details that are the focus of this work. In the first section we briefly describe the quantum corrected, atomistic 3D drift diffusion (DD) simulator, before describing the quantum corrected, *ab initio* atomistic 3D Monte Carlo (MC) simulator in the second section. Particular attention is payed to the *ab initio* treatment of ionised impurity scattering within MC and of the implementation of quantum corrections therein.

3.1 The Drift Diffusion Simulator

3.1.1 Classical Drift Diffusion Simulations

The Glasgow atomistic 3D DD simulator has been developed over the course of ten years with the specific aim of accurately estimating statistical device parameter variation in ultra-small semiconductor devices. It is a generalised, fully three dimensional (3D) drft-diffusion device simulator tailored to accurately capture the effects of the inherently 3D statistical variations in a range of device structure. It has the capability of simulating variation associated with Random Discrete Dopants (RDD), Line Edge Roughness (LER), Oxide Thickness Variations (OTV), polysilicon granularity and random grain orientation within high-k dielectrics within MOSFET, SOI MOSFET and DG MOSFET devices [26, 29, 30]. It captures the electrostatic impact of the above sources of variation and results in accurate estimation of the statistical variability of threshold voltage, subtreshold slope and off current [7, 10, 13, 22, 26], all of which are dominated by device electrostatics.

The DD simulator numerically solves the fundamental system of drift-diffusion equations governing the electrostatic behavior of semiconductor devices in [96]. This involves the numerical solution of Poisson's equation coupled with the solution of the current continuity equation. Poisson's equation may be stated as,

$$\nabla . \epsilon \nabla \psi = -q(p - n + N_D - N_A) \tag{3.1}$$

where ψ is the electrostatic potential which is unknown, ϵ is the position dependent dielectric permittivity, q the electronic charge, n and p are the negative (electron) and positive (hole) charge carrier densities obtained from the solution of the current continuity equation and N_D and N_A are the donor and acceptor doping concentrations. Only unipolar MOSFETs are simulated, as an integral part of CMOS technology and therefore one type of charge carrier is considered in the solution of the current continuity. Additionally, generation and recombination are ignored as these play little role in the MOSFET operation. Considering this, and from now on assuming electrons as the majority charge carriers, current continutity is expressed as,

$$\boldsymbol{\nabla} \cdot \boldsymbol{J}_n = 0 \tag{3.2}$$

with the current density $\boldsymbol{J}_n$ in the drift-diffusion approximation given by,

$$\boldsymbol{J}_n = -qn\mu_n \boldsymbol{\nabla}\psi + qD_n \boldsymbol{\nabla} n \tag{3.3}$$

where μ_n is the carrier mobility and D_n the diffusion constant. In all simulations Boltzmann statistics is considered leading to the Einstein relationship

$$D_n = \mu_n \frac{k_B T_n}{q} \tag{3.4}$$

where k_B is Boltzmann's constant and T_n is the carrier temperature which is assumed to be equal to the lattice temperature [97].

The electron and hole concentrations, n and p respectively, are given by a Maxwell-Boltzmann distribution [98],

$$n = n_i \exp\left(-\frac{q(\phi_n - \psi)}{k_B T}\right) \tag{3.5}$$

$$p = n_i \exp\left(\frac{q(\phi_p - \psi)}{k_B T}\right) \tag{3.6}$$

where n_i is the intrinsic carrier concentration and ϕ_n and ϕ_p are the electron and hole quasi-fermi levels respectively. The dependence of the above carrier concentrations upon the electrostatic potential ψ makes Poisson's equation (3.1) non-linear.

3.1.2 Quantum Corrections

In modern, ultra-small, MOSFETs the large electric field normal to the interface in the channel depletion layer results in a quantum well and inversion layer carrier confinement. This quantum confinement alters the distribution of carriers, shifting the peak concentration away from the interface and reducing the effective oxide capacitance. This in combination with the energy quantisation has a significant impact on the device operation, increasing the threshold voltage and reducing the device performance, capturing these effects is essential for the accuracy of the device simulator [5, 26, 31]. Quantum effects are included within the 3D DD by means of the Density Gradient (DG) quantum correction [99, 100], which has similarities with the Bohm interpretation of quantum mechanics [101]. The DG approach can be as a correction to the classical potential and can be derived from the modified Boltzmann Transport Equation using the Wigner distribution function. It may be thought of as the inclusion of an additional driving term for the carriers that is associated with the additional, quantum, potential. The incorporation of DG modifies the carrier distribution so that, instead of being described by the simple Maxwell-Boltzmann distribution (3.5), it must be obtained as the solution of

$$2b_n \frac{\nabla^2\sqrt{n}}{\sqrt{n}} = \phi_n - \psi + \frac{k_B T}{q} ln(\frac{n}{n_i}) \tag{3.7}$$

where the term $b_n = \hbar^2/12qm_n^*$ is a function of the carrier's effective mass m_n^* and is treated as a fitting parameter. The additional driving term (at the left hand side of equation (3.7)) modifies the classical current continuity equation (3.2) such that [102],

$$\boldsymbol{J}_n = -qn\mu_n \boldsymbol{\nabla}\psi_{\text{eff}} + qD_n\boldsymbol{\nabla}n \tag{3.8}$$

where the term ψ_{eff} represents the effective quantum-corrected potential, which is calculated from (3.7) as

$$\psi_{\text{eff}} = \psi + 2b_n \frac{\nabla^2\sqrt{n}}{\sqrt{n}} = \phi_n + \frac{k_B T}{q} ln(\frac{n}{n_i}) \tag{3.9}$$

The additional driving term forces carriers away from the interface. The DG formalism has been shown to accurately reproduce the carrier distribution for a range of confining potential distributions when compared with fully quantum mechanical solutions [29, 68, 103] and accurately reproduce their impact of the quantum confinement on device characteristics [26, 30, 104].

Another method widely used to include quantum corrections within device simulation is the Effective Potential approach (EP) [105, 106]. In this case, the classical potential from the solution of Poisson's equation is convolved with an electron wavepacket to produce a smoothed 'effective' potential that has the desired effect of forcing carriers away from sharp changes in the potential. It is implemented simply as a Gaussian smoothing kernel applied over the classical potential. However, it suffers from the deficiency that the calibration of the Gaussian, is somewhat empirical and has to be performed for each individual device [105]. It has been also shown that the EP provides a less satisfactory fit to the inversion layer distribution when compared with DG and fully quantum solutions [104].

3.1.3 Solution Methodology

In order to numerically solve the fundamental system of coupled partial differential equations 3.1, 3.2 and 3.7, the continuous equations need to be suitably discretized. Since individual discrete dopant resolution requires regular dense meshes, cartesian grids on a finite differences discretisation is adopted. This is also beneficial for avoiding self force effect in the MC simulations that uses the same grid. To prevent the impact of self-forces in particle propagation the use of orthogonal uniform meshes is necessary [107–109] where the self-force is zero when the charge assignment and force interpolation schemes are the same. The advantage of orthogonal uniform grids is the simple calculation of the charge assignment and electric field interpolation obtained directly from grid points. The treatment of self-forces on unstructured grids has been investigated only by a few studies [107, 108] . In [108] reasonable results were obtained only for equilateral triangular elements. The higher computational effort which is needed to eliminate the self-forces on unstructured tetrahedral meshes has been investigated in the study [107]. This study has shown that the accuracy of the interpolation of the electric field is degraded on unstructured meshes. The complexity of the charge assignment and electric field interpolation schemes in the unstructured nonuniform meshes has a higher computational cost compared with orthogonal uniform meshes [107].

Following a finite differences discretisation method, the Poisson, DG and current continuity equations are rewritten in their integral forms and, in turn, the box volume method is applied to obtain their full 3D discretization [110]. This leads to a large system of nonlinear equations, since the Poisson and DG equations are nonlinear. The Newton-Raphson method is introduced in order to linearize the system of equations [110], enabling the solution via classical iterative matrix methods. The one dimensional solution of this set of coupled equations was first presented by Scharfeteer-Gummel [111] and this forms the basis of our solution.

Boundary conditions are applied to the discretized equation such that at the edge of the simulation domain the normal derivative of the electrostatic potential is zero (Neumann boundary condition). This ensures that the current flux through the edge of the simulation domain is zero. This condition is default unless the boundary represents an external contact, in which case a fixed value potential boundary condition is imposed

(Dirichlet boundary condition). Similar boundary conditions are applied to the quantum corrected carrier concentrations. A finite penetration of the carriers in the gate insulator is assumed, which corresponds to a finite value of the normal derivative of the carrier concentration at the interface [112]. Otherwise, the normal derivative of carrier concentrations are assumed to be zero. To summarize the above, the Dirichlet boundary conditions may be stated as

$$\begin{aligned}
\psi|_{\Gamma_S} &= 0, \\
\psi|_{\Gamma_D} &= V_D, \\
\psi|_{\Gamma_G} &= V_G + \frac{k_B T}{q}\ln(\frac{N_P}{N_D}), \\
\psi|_{\Gamma_{SUBS}} &= -\frac{k_B T}{q}\ln(\frac{N_A N_D}{n_i^2})
\end{aligned} \tag{3.10}$$

where Γ_S is the area of the source ohmic contact, Γ_D is the area of the drain ohmic contact, Γ_G is the area of the gate, Γ_{SUBS} is the area of the back substrate contact, V_G is applied voltage between the source and gate contacts, V_D is applied voltage between the source and drain contacts, and finally N_P is n^+-polysilicon concentration in the polysilicon gate. Neumann boundary conditions may be expressed as

$$\begin{aligned}
\frac{\partial \psi}{\partial \vec{\boldsymbol{n}}}|_{\Gamma_N} &= 0, \\
\frac{\partial n}{\partial \vec{\boldsymbol{n}}}|_{\Gamma_N} &= 0, \\
\frac{\partial \boldsymbol{J}_n}{\partial \vec{\boldsymbol{n}}}|_{\Gamma_N} &= 0,
\end{aligned} \tag{3.11}$$

where Γ_N is the edge of the simulation domain where the Neumann conidtions are applied.

Following this method, the discretized system of simultaneous equations is solved via a two step process that is iterated until convergence. Therefore, this process is a modified Gummel procedure [111] and can be described as follows. In the first step, the electrostatic potential and the quantum corrected carrier densities are solved iteratively and self-consistently. A Red-Black Successive Over-Relaxation (SOR) method is used where the damping parameter Ω (within the interval range 0 and 2) regulates the speed of convergence. The convergence criteria for potential and current density is defined as difference between two consecutive iterations of potential and carrier density. The convergence is met for SOR method when difference is less than given tolerance level. Solution of the linear discretized current continuity equation (3.2) follows using an efficient Bi-Conjugate Gradient Stabilized method. This process is repeated until the current converges. The convergence requirements are met when the difference between two consecutive iterations of Gummel cycle [111] is less than defined tolerance level.

3.1.3.1 Random Discrete Dopants

Here we describe the inclusion of RDD within the DD simulator as this forms an important part of this work. The creation of RDD distributions, the assignment of the associated charge and the resolution of the classical Coulomb potential will be addressed.

With aggressive scaling to sub-nanometer dimensions, and simulation domains discretized on the order of inter-atomic separations, it becomes not only computationally manageable but essential to consider the underlying crystal lattice comprising the device and the probability of random dopants positioned at its sites. The Silicon crystal lattice is described by the diamond structure - a face centered cubic (fcc) lattice with a basis of two silicon atoms. Thus the lattice may be equivalently described by a simple cubic lattice with a basis of 8 silicon atoms with basis vectors $(0,0,0)$, $(0,\frac{1}{2},\frac{1}{2})$, $(\frac{1}{2},0,\frac{1}{2})$, $(\frac{1}{2},\frac{1}{2},0)$, $(\frac{1}{4},\frac{1}{4},\frac{1}{4})$, $(\frac{1}{4},\frac{3}{4},\frac{3}{4})$, $(\frac{3}{4},\frac{1}{4},\frac{3}{4})$ and $(\frac{3}{4},\frac{3}{4},\frac{1}{4})$, normalised with respect to the silicon lattice constant $a = 0.543$nm. The basis atoms are presented in figure 3.1. By starting at a point within the simulation domain and translating over all lattice vectors and subsequent basis vectors that fall within the domain, the entire Silicon lattice structure of the transistor may be accurately traversed.

Having defined a means of traversing all silicon lattice sites, the next step in the RDD generation process is to make a decision for each lattice site as whether or not to place a dopant in it. This is determined by a rejection technique first described in [25] in which the probability of a dopant occupying a lattice site is calculated based upon the local continuous doping concentration typically obtained from TCAD simulation and the site volume. This probability necessarily lies between 0 and 1. A random number

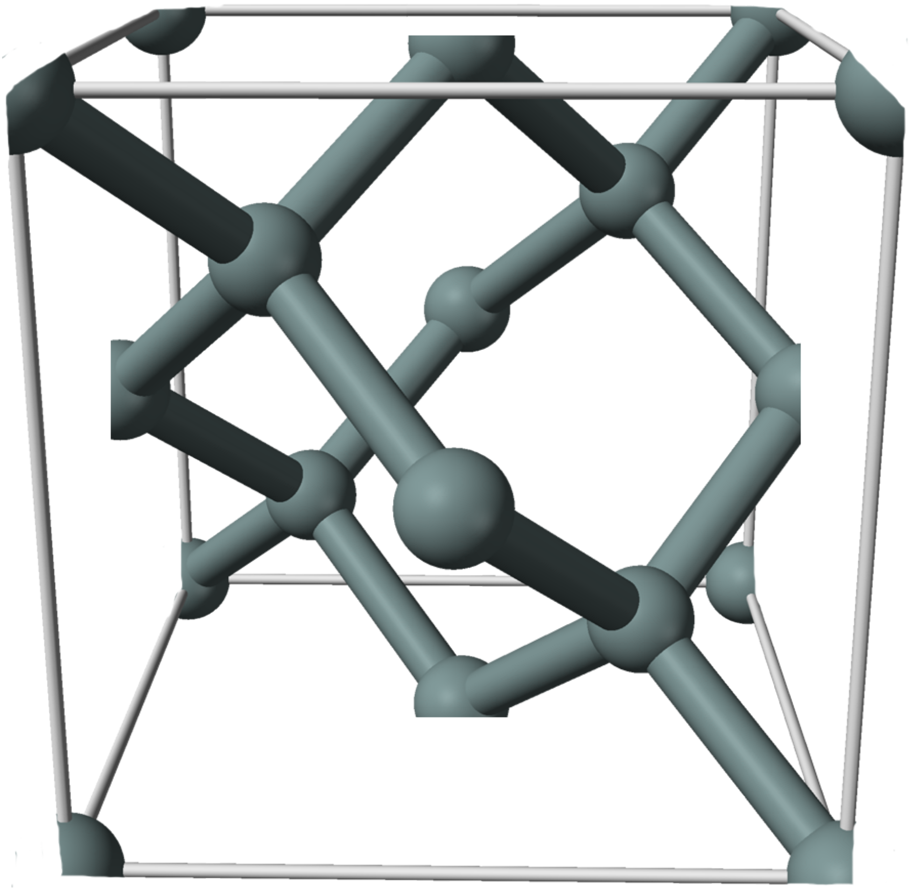

FIGURE 3.1: Equivalent Silicon basis consisting of 8 silicon atoms within a cubic lattice unit cell.

is then generated between 0 and 1 and a dopant is accepted at this site if this number is smaller than the prior probability. The number of dopants generated following this method follows a Poisson distribution with a mean equal to the expected number of dopants consistent with a continuous charge density [87].

Since the lattice sites generally differ from the nodes of the discretization mesh, dopants will in general lie between mesh points. The cloud-in-cell (CIC) [109] charge assignment scheme is used to assign their charge to the mesh as it retains information for the actual position of the within the mesh cell while localising the charge so that the discrete nature of the dopant is retained an accurately as possible. In this scheme, the charge associated with a single dopant is assigned to the surrounding eight mesh points. The ratio of the charge assigned to each mesh point is inversely proportional to the distance between the mesh point and dopant - thus the closest grid node acquires the largest fraction of the dopant charge density.

At this point it is important to clarify the role of the density gradient quantum corrections for the accurate treatment of localised discrete dopants within DD simulations. On a fine grained discretization mesh, the solution of Poisson's equation with a discrete dopant will result in a sharply resolved Coulomb potential well. The depth of this well will increase with reduced mesh spacing approximating better singular point charge Coulomb potential. The Boltzmann statistics 3.5 relates the carrier concentration to the almost singular electrostatic potential around the dopants which results in artificial carrier trapping on dopants which reduces the free carrier concentration and increases resistance in simulations [30, 113]. Quantum confinement prevents this in reality. The inclusion of the DG quantum corrections mediates the trapping of carriers in the sharply resolved Coulomb wells of the individual impurities, yielding a quantum mechanically consistent approach to resolving individual discrete dopants in atomistic drift diffusion simulations [5, 29, 30]. A comparison between the classical and the quantum corrected electron concentration surrounding a discrete impurity distribution is illustrated in figure 3.2 where the local reduction in carrier concentration in the DG case is clearly seen. This also eliminates the mesh sensitivity of the solution.

3.1.4 Mobility Models

In order to solve the current continuity equation (3.2), the mobility μ_n, and by consequence the diffusion constant D_n, must be specified. The mobility is defined generally as a macroscopic constant of proportionality that relates the equilibrium carrier velocity v_n to a constant electric field E

$$v_n = \mu_n E \tag{3.12}$$

The mobility however depends on the underlying doping concentration, temperature and electric field. It is also in general not a scaler value, reflecting the anisotropy of the discrete crystal lattice, and is properly expressed as a tensor. However, the anisotropy in silicon at the temperatures concerned is small and may be neglected by taking a suitably calibrated average scalar value. The dependence of doping concentration and electric field are taken into account through the following empirical models [114].

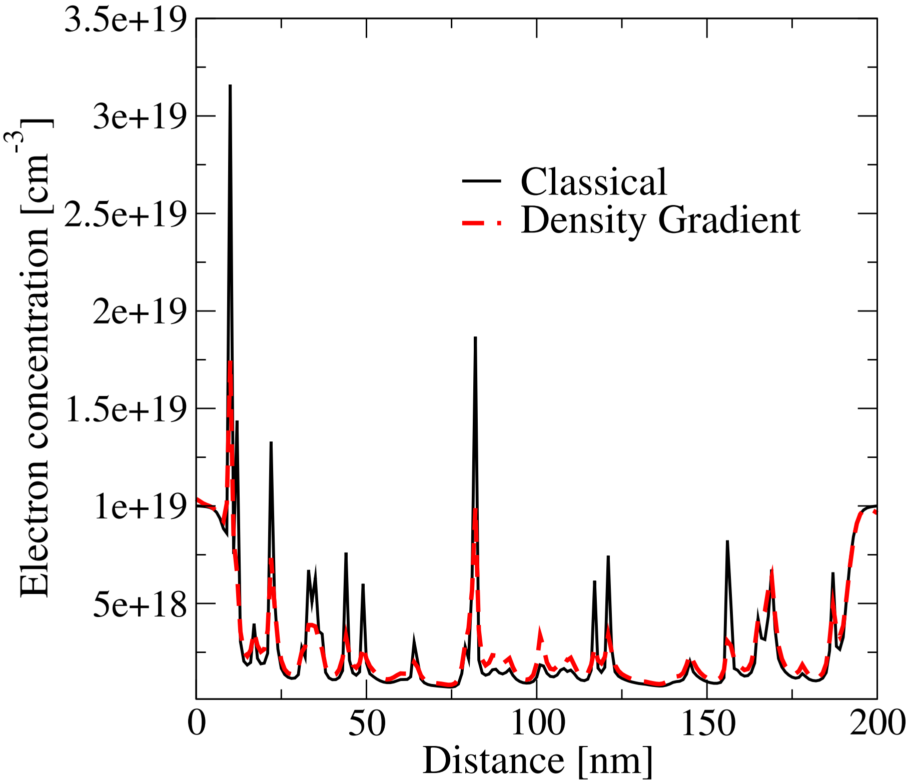

FIGURE 3.2: Electron Concentrations within a 200 × 25 × 25 nm resistor, showing both the classical electron concentration due to Boltzmann statistics and the quantum electron concentration generated by the inclusion of Density Gradient quantum corrections.

3.1.4.1 Concentration Dependent Mobility

The experimentally mobility measurements show strong doping concentration dependence [115]. A good fit to the measured data provides so-called ”min-max” expression:

$$\mu_{0n}(N_{total}) = \mu_{n_{min}} + \frac{\mu_{n_{max}} - \mu_{n_{min}}}{1 + (\frac{N_{total}}{N_{refn}})^{\alpha_n}} \tag{3.13}$$

where N_{total} is the doping concentration, $\mu_{n_{min}}$ and $\mu_{n_{max}}$ are parameters specifying the minimum and maximum of the range of experimental mobilities, N_{refn} is a reference concentration that affects the onset of the mobility degradation of high doping concentrations and α_n is a fitting parameter describing the rate of degradation. A good fit is shown in figure 3.3.

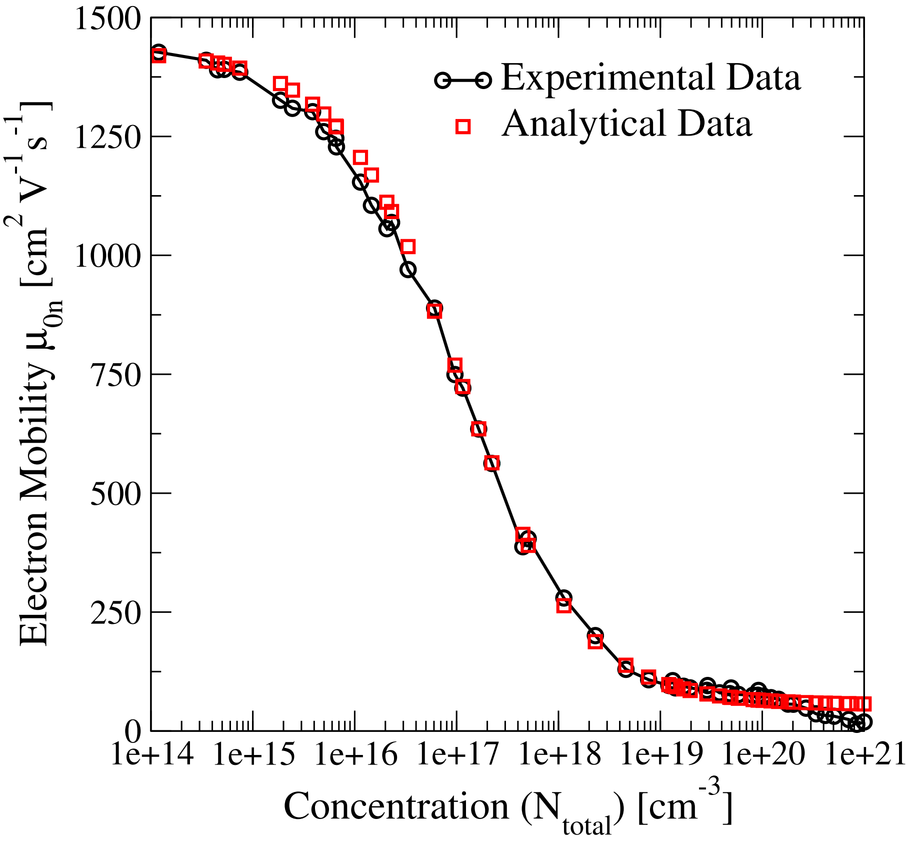

FIGURE 3.3: Comparison of experimentally measured mobility [115] and empirical mobility model (3.13) where $N_{refn} = 1.072 \times 10^{17}\mathrm{cm}^{-3}$, $\mu_{n_{min}} = 55.24\mathrm{cm}^2\mathrm{V}^{-1}\mathrm{s}^{-1}$, $\mu_{n_{max}} = 1429.23\mathrm{cm}^2\mathrm{V}^{-1}\mathrm{s}^{-1}$ and $\alpha_n = 0.73$.

3.1.4.2 Field Dependent Mobility

Futher to the concentration mobility dependance, the carrier velocities in bulk saturates with the increase of the electric field. The velocity saturation is typically modelled using empirically fitted expression. One of the most popular expressions is given below

$$\mu_n = \frac{\mu_{0n}}{[1 + (\frac{\mu_{0n}E_{\parallel n}}{v_n^{sat}})^{\beta_n}]^{\frac{1}{\beta_n}}} \tag{3.14}$$

where μ_{0n} is the concentration dependent mobility obtained from equation (3.13), $E_{\parallel n}$ is the electric field in the direction of the current flow, v_n^{sat} is the experimentally observed saturation velocity and β_n is a dimensionless fitting parameter. The fit with experimentally observed velocities in undoped bulk silicon is shown in figure 3.4. However, the mobility can vary due to the device orientation and under the influence of strain [116, 117]. These effects are not directly accounted for in this model.

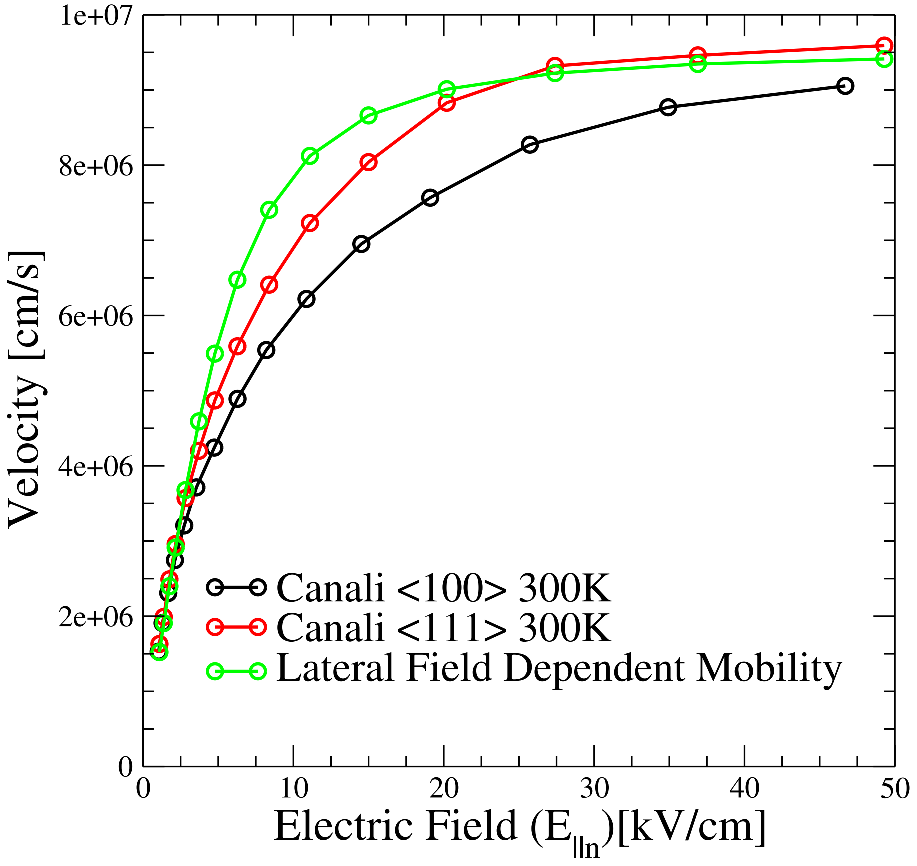

FIGURE 3.4: Comparison of experimentally measured velocity-field characteristics in undoped silicon at 300K with the empirical mobility model (3.14) where $\mu_{0n} = 1410\text{cm}^2\text{V}^{-1}\text{s}^{-1}$, $v_n^{sat} = 0.95 \times 10^7\text{cms}^{-1}$, $\beta_n = 2$ and subsequently the velocity is obtained from (3.12) as $v = \frac{E_{\|n}}{\mu_n}$.

In MOSFETs however, an additional field dependent mobility degredation factor associated with the surface scattering of confined carriers from the rough interface along the channel must be considered. This so-called vertical field dependent mobility is parameterised depending on the field component normal to the interface and is often modelled using the expression as

$$\mu_{S,n} = G_{surfn} \frac{\mu_{0n}}{\sqrt{1 + \frac{E_\perp}{E_{cn}}}} \tag{3.15}$$

where μ_{0n} is again the concentration dependent mobility obtained from equation (3.13), $G_{surf,n}$ is a parameter between 0 and 1 that reflects the rate of surface roughness scattering, $E_\perp$ is the normal to the interface component of the electric field at the interface and E_{cn} is a field fitting parameter.

In device simulations, the concentration dependent mobility (3.13) is first determined at each mesh point based on the local doping concentration assigned there. This is then modified to account for the local vertical field dependence following equation (3.15) before being modified again to account for the local lateral field dependence following equation (3.14). The fields are determined from the current Poisson and density gradient solution in order to maintain self-consistency.

3.1.4.3 Atomistic Mobility

The use of the mobility model described above becomes problematic in the presence of RDD due to the large and localized charge densities associated with dopants and the correspondingly large Coulomb fields in fine grained discretization meshes. The unphysically large and localised charge densities result in discontinuous jumps in mobility from the extremes of too high a mobility in regions where no doping is assigned, to unphysically low mobility in regions where it is. Similarly, the large short-range field surrounding dopants, even when applying quantum corrections, unphysically saturates carrier velocities. A solution to this problem is to use in the atomistic simulations mobility taken from a prior solution of an identical, but continuously doped, device at equivalent bias conditions. The continuous doping solutions provide the mobility at every mesh point for a simulation under specific bias conditions. These are stored as separate mobility files which may be re-used in the simulation of microscopically different devicies.

This highlights a major limitation of the DD simulations; that while the device electrostatics may be accurately incorporated, the carrier transport models rely upon an idealised local relation between the mobility and electric field. Therefore DD cannot describe nonequilibrium transport phenomena to rapid electric field changes in time or position as a result at which the carrier distribution may momentarily or locally be driven out of equilibrium. Nonequilibrium, near ballistic transport however plays a very important role in determining the performance of contemporary MOSFETs. This calls upon the use of ensemble Monte Carlo (MC) simulations suitable to accurate physical description of effects.

3.2 Monte Carlo Simulator

The in house 3D Monte Carlo (MC) simulator has been developed over the course of the last eight years with the specific goal of capturing carrier transport variability due to random discrete doping configurations employing also efficient quantum corrections techniques [32, 33, 118]. As the basis of this work, the 3D MC simulator is discussed in detail in this section. A brief introduction to the MC method is first given before details of band structure and scattering mechanisms specific to the simulator are presented.

3.2.1 Boltzman Transport Equation

3.2.1.1 Classical Boltzman Transport Equation

Monte Carlo device simulation seeks to solve the Boltzmann Transport Equation (BTE); a general continuity equation that expresses the evolution of the carrier distribution function in six dimensional position-velocity phase space. The classical BTE is universally derived from the Liouville-von Neumann master equation [119] under given approximations frequently presented in the following form

$$\frac{\partial f}{\partial t} + \boldsymbol{v} \cdot \nabla_r f + \frac{\boldsymbol{F}}{m} \cdot \nabla_v f = \left(\frac{\delta f}{\delta t} \right)_{Coll} \tag{3.16}$$

$f(\boldsymbol{r}, \boldsymbol{k}, t)$ is the carrier distribution function and is defined as the probability of finding a carrier within $\delta \boldsymbol{r}$ of position $\boldsymbol{r}$ and with velocity within $\delta \boldsymbol{v}$ of $\boldsymbol{v}$. The BTE describes the time evolution of the distribution function due to the deterministic motion and acceleration of carriers and due to the stochastic velocity changes due to collision events. The deterministic motion is expressed in the second and third terms on the left hand side of (3.16), frequently called drift terms, which respectively express the conservation of the flux of particles with velocity $\boldsymbol{v}$ within an elemental volume in real space and a similar flux of particles with acceleration $\frac{\boldsymbol{F}}{m}$ in an elemental volume in velocity space, where $\boldsymbol{F}$ is external force. The right hand side of (3.16) is the general stochastic collision term that describes all possible processes other than external fields that effects a particle's velocity. If the distribution function can be obtained, all quantities of interest ranging from charge densities, energies and velocities to device terminal currents may be derived.

3.2.1.2 Semi-Classical Carrier Dynamics

The detailed dynamics of particles within a semiconductor is inherently a many-body problem and as such is impossible to solve directly for practical purposes. In order to overcome this it is necessary to impose some simplifying assumptions. To reduce the order of the problem, electron-electron interactions are ignored in the so-called 'independent single electron' approximation and only the interaction between a single electron and an infinite and perfectly periodic, static, crystal lattice is considered. Solutions to the following time independent Schrodinger equation are then sought [120]

$$[-\frac{\hbar^2}{2m_0}\nabla^2 + U_C(\boldsymbol{r})]\psi = \varepsilon\psi \tag{3.17}$$

where ψ is the independent electron wavefuntion, $U_C(\boldsymbol{r})$ is the crystal lattice potential energy and m_0 is the free electron mass. The periodicity of the crystal lattice is such that $U_C(\boldsymbol{r}) = U_C(\boldsymbol{r}+\boldsymbol{R})$, where $\boldsymbol{R}$ is any Bravais lattice vector. Quantum mechanical solutions of (3.17) for the electron wavefunction exists in the form of Bloch waves [120]. These have the form of a plane wave multiplied by a function with the periodicity of the Bravais lattice

$$\psi_{n\boldsymbol{k}} = u_{n\boldsymbol{k}}(\boldsymbol{r})e^{i\boldsymbol{k}\cdot\boldsymbol{r}} \tag{3.18}$$

where $e^{i\boldsymbol{k}\cdot\boldsymbol{r}}$ is a plane wave with electron wavevector $\boldsymbol{k}$ and $u_{n\boldsymbol{k}}(\boldsymbol{r})$ is the corresponding Bloch function satisfying the periodic condition

$$u_{n\boldsymbol{k}}(\boldsymbol{r}) = u_{n\boldsymbol{k}}(\boldsymbol{r}+\boldsymbol{R}) \tag{3.19}$$

The subscript n denotes different solutions and is termed the band index. Inserting equation (3.19) into (3.17) results in the following equation

$$[-\frac{\hbar^2}{2m_0}(\nabla^2 + 2i\boldsymbol{k}\cdot\nabla - \boldsymbol{k}^2) + U_C(\boldsymbol{r})]u_{n\boldsymbol{k}}(\boldsymbol{r}) = \varepsilon_n(\boldsymbol{k})u_{n\boldsymbol{k}}(\boldsymbol{r}) \tag{3.20}$$

The periodic boundary condition, spanning the finite volume of the crystal lattice unit cell, allows the solution of the eigenvalue problem given the Hamiltonian in (3.20). The constraint of the solution to the finite volume leads to a set of discrete eigenvalues in the wavevector $\boldsymbol{k}$. For each wavevector there exists a family of eigenfunctions $u_{n\boldsymbol{k}}(\boldsymbol{r})$ belonging to the eigenenergy values $\varepsilon_n(\boldsymbol{k})$. This family of the quasi-continuous functions $\varepsilon_n(\boldsymbol{k})$ creates the so called band structure associated with the crystal lattice. Given the band structure, the independent electron Hamiltonian may be written as

$$H(\boldsymbol{k}(t), \boldsymbol{r}(t)) = \varepsilon(\boldsymbol{k}(t)) + eV(\boldsymbol{r}(t)) \tag{3.21}$$

The Hamiltonian is decomposed into two parts; the first part is the above band structure while the second is the position dependent electrostatic potential $V(\boldsymbol{r}(t))$. Both parts are generally time dependent. From energy conservation, the following relation is obtained [120]

$$\frac{dH(\boldsymbol{k}(t), \boldsymbol{r}(t))}{dt} = [\nabla_{\boldsymbol{k}}\varepsilon(\boldsymbol{k})]\frac{d\boldsymbol{k}}{dt} + [\nabla_{\boldsymbol{r}}eV(\boldsymbol{r}(t))]\frac{d\boldsymbol{r}(t)}{dt} = 0 \tag{3.22}$$

Analogously with the de Broglie relationship for free electrons, a crystal momentum $\boldsymbol{P}$ associated with an electron with wavevector $\boldsymbol{k}$ may be defined as [120, 121]

$$\boldsymbol{P} = \hbar\boldsymbol{k} = m^*\boldsymbol{v}_g \tag{3.23}$$

where m^* is a mass-like term, not equal to the free electron mass, termed the effective mass and $\boldsymbol{v}_g$ is the electron's velocity within the crystal and is defined analogously with a group velocity as

$$\boldsymbol{v}_g = \frac{d\boldsymbol{r}(t)}{dt} = \frac{1}{\hbar}\nabla_{\boldsymbol{k}}\varepsilon(\boldsymbol{k}) \tag{3.24}$$

Substituting (3.24) into (3.22) yields

$$\boldsymbol{v}_g \cdot \frac{d(\hbar\boldsymbol{k})}{dt} + [\nabla_{\boldsymbol{r}}eV(\boldsymbol{r}(t))] \cdot \boldsymbol{v}_g = 0 \tag{3.25}$$

from which the fundamental expression for the rate of change of momentum may be obtained as [122]

$$\frac{d(\hbar \boldsymbol{k})}{dt} = -\nabla_{\boldsymbol{r}} eV(\boldsymbol{r}(t)) \tag{3.26}$$

This is recognisable as Newton's law when considering an electron in an electric field where now the crystal momentum replaces the electron's real momentum. Equations (3.24) and (3.26) then define the semi-classical equations of motion for the electron within the crystal lattice.

3.2.1.3 Semi-Classical Boltzman Transport Equation

Substituting (3.24) and (3.26) into (3.16) results in the semi-classical BTE

$$\frac{\partial f}{\partial t} + \frac{1}{\hbar}\nabla_{\boldsymbol{k}}\varepsilon(\boldsymbol{k}) \cdot \nabla_{r} f - \frac{1}{\hbar}\nabla_{\boldsymbol{r}} eV(\boldsymbol{r}(t)) \cdot \nabla_{k} f = C[f] \tag{3.27}$$

The collision term $C[f]$ expresses the net rate of change of f due to all possible scattering processes that instantaneously alter the crystal momentum $\hbar\boldsymbol{k}$. It may be expressed as

$$C[f] = \sum_{\boldsymbol{k'},l} [S_l(\boldsymbol{k'},\boldsymbol{k}) f(c,\boldsymbol{k'},t)[1 - f(\boldsymbol{r},\boldsymbol{k},t)] - S_l(\boldsymbol{k},\boldsymbol{k'}) f(\boldsymbol{r},\boldsymbol{k},t)[1 - f(\boldsymbol{r},\boldsymbol{k'},t)]] \tag{3.28}$$

where $S_l(\boldsymbol{k'},\boldsymbol{k})$ is the transition probability per unit time that a carrier in state $\boldsymbol{k'}$ scatters into the new state $\boldsymbol{k}$, where it is required that $\boldsymbol{k}$ is empty. $S_l(\boldsymbol{k},\boldsymbol{k'})$ is similarly the rate at which a carrier in state $\boldsymbol{k}$ scatters into state $\boldsymbol{k'}$. The subscript l ranges over all possible scattering mechanism and the terms $[1 - f(\boldsymbol{r},\boldsymbol{k},t)]$ and $[1 - f(\boldsymbol{r},\boldsymbol{k'},t)]$ represent the probability of the respective states being empty.

The quantum mechanical nature of (3.27) is incorporated in two ways. Firstly in the use of band structure to describe the interaction between electrons and the crystal lattice, and secondly in the scattering rates as expressed through perturbation theory using Fermi's Golden Rule. The scattering rates will be discussed later in section 3.2.2.6. All the above defines the semi-classical approach to transport within the BTE.

Monte Carlo simulation is a stochastic approach to the solution of the BTE (3.27) in which the distribution function is evaluated by an iterative process of repeated carrier propagation and self-consistent scattering, representing the drift and collision terms respectively. Propagation treats carriers as classical point particles, obeying newtonian dynamics and defining an exact position and velocity in contrast with the uncertainty principle. The stochastic nature of the solution enters through the evaluation of carrier free flight times and in the evaluation of the scattering mechanisms included within 3.28. The scattering rates are calculated within the Born-Openheimer approximation using Fermi's Golden Rule (see section 3.2.2.6) and, along with the band structure, exerting the quantum mechanical nature of the problem.

The general MC method is presented as a flowchart in figure 3.5. Propagation and scattering is punctuated with regular statistics gathering form which the distribution function is estimated. The MC simulations can be performed in two regimes. The first regime is called a 'frozen field' approximation [123–125], which is valid for drain biases typically lower than 50 mV [125]. The second regime is the self-consistent MC simulation [126–128], as shown in figure 3.5, where the classical potential is updated at the end of each field adjusting time step using new carrier concentrations in the Poisson's equation (3.1) in order to properly capture the changes in the electron distribution and velocity at higher drain bias where the current and field are strongly coupled and the potential must be regularly updated. For the purpose of this project, all MC simulations were carried out self-consistently. Accuracy is obtained after averaging over a sufficiently large number of iterations [129]. The proof that MC method leads to the distribution function for a single particle obeying the BTE can be found in [130] where the BTE was transformed into iteration of the path integral.

3.2.2 3D Monte Carlo Simulator

Having briefly outlined the basic theory behind Monte Carlo simulation including the repeated propagation and scattering of carriers, in this section the details of the band structure, scattering mechanisms and propagation methods specific to the Monte Carlo simulator used will be presented.

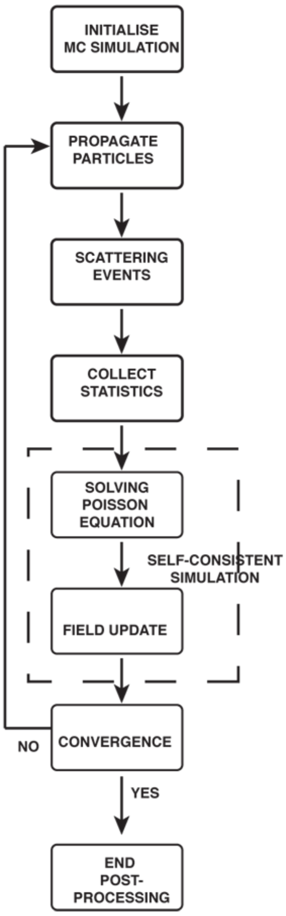

FIGURE 3.5: Monte Carlo flow chart.

3.2.2.1 Band Structure

According to equation (3.24), the band structure $\varepsilon_n(\boldsymbol{k})$ must be defined in order to describe carrier dynamics. The band structure is intimately linked to the periodic potential of the crystal lattice such that the wave solutions of (3.20) are similarly periodic, within the reciprocal space of the real space lattice [131]. This periodicity is expressed analogously to the periodic potential as

$$\varepsilon_n(\boldsymbol{k}) = \varepsilon_n(\boldsymbol{k} + \boldsymbol{K}) \tag{3.29}$$

where $\boldsymbol{K}$ is a reciprocal lattice vector. All information regarding the band structure is contained within the primitive (Wigner-Seitz) cell of the reciprocal lattice called the first Brillouin zone (BZ) [120, 121]. This is shown for Silicon in figure 3.6. Due to the symmetry of the BZ it is convenient to refer to only a unique volume within it, the irreducible wedge [132], when discussing the band structure in absence of strain. The Silicon band structure is illustrated in figure 3.7 along the symmetry axes of the irreducible wedge including a family of solutions, each defining a band. The band with maxima at the Γ point, shown here with reference energy 0 eV, is the valence band and represents bound states of electrons within the crystal lattice. At higher energy, separated by the so-called band gap E_g of 1.12 eV [121], is the family of conduction bands representing unbound electron states allowing conduction. As this work is only concerned with the transport of unbound electrons, the conduction band will be focus of the remainder of this discussion.

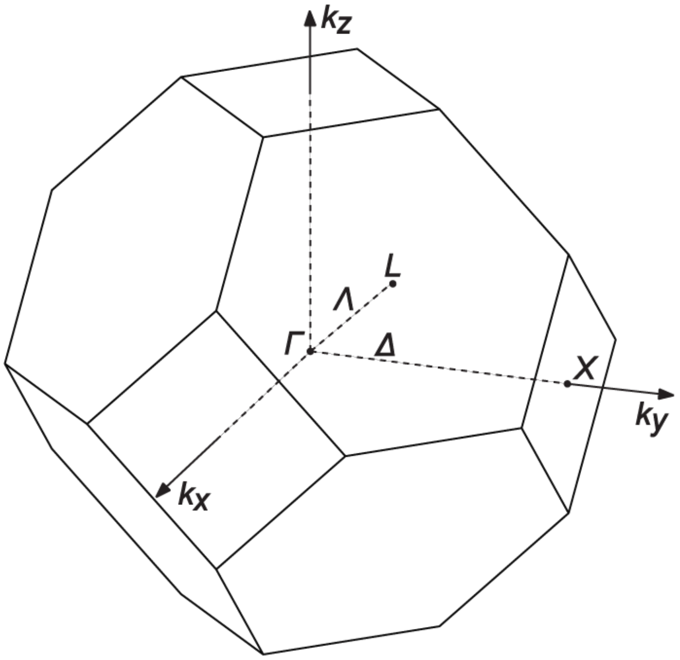

FIGURE 3.6: The first Brillouin zone of the Silicon lattice. Some important points of high symmetry are shown X and L. The point $X = \frac{2\pi}{a}(1,0,0)$ lies on the surface in center of BZ rectangular face along symmetry line $\Delta = (1,0,0)$. The point $L = \frac{\pi}{a}(1,1,1)$ is located on the surface in the center of BZ hexagonal face along symmetry line $\Lambda = (1,1,1)$.The point $\Gamma = (0,0,0)$ lies in the center of BZ.

The Conduction band minima is located at $\boldsymbol{k}_{min} = \frac{2\pi}{a}(0,0,0.85)$ along the Δ line near the X point [133]. Due to the symmetry of the BZ, there are six equivalent X valley minima. Higher energy minima are seen at the eight equivalent L points and at the central Γ point [134]. As can be seen, the band structure is complicated and approximations are required in order to describe it. As the majority of conduction band electrons reside near the band minima at room temperature, it is sufficient only to describe the band structure locally about this point. This is the aim of the analytical band models

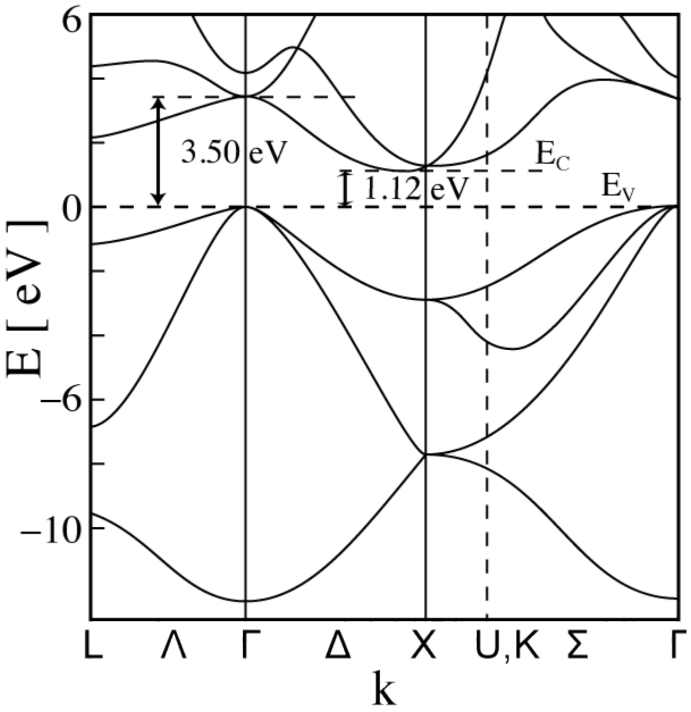

FIGURE 3.7: Illustration of the real silicon band structure within the first BZ. Three conduction band minima near points of high symmetry at X, Γ and L are highlighted with their separations in energy from the valence band maxima.

described below. If the accurate dynamics of high energy electrons is required, a description of the full band structure is necessary which is significantly more complicated. This relies upon the calculation and interpolation of the band structure discretised in $\boldsymbol{k}$-space and obtained from semi-empirical methods such as $k \cdot p$ [135–139], pseudopotential [140–143] or tight-binding [144–146]. As this work does not focus on the transport phenomena associated with high energy carriers an analytic band model is adopted for efficiency.

3.2.2.2 Analytic Band Approximations

There are several analytic band approximations that may be employed, each involving trades off between benefits and costs [129, 147]. Each approximates the conduction band minima $\varepsilon(\boldsymbol{k}_{min})$ near the X point, which can be expanded by a Taylor series in the vicinity of $\boldsymbol{k}_{min}$ as [120]

$$\varepsilon(\boldsymbol{k}_{min} + \boldsymbol{k}) = \varepsilon(\boldsymbol{k}_{min}) + \nabla_{\boldsymbol{k}}\varepsilon(\boldsymbol{k}_{min}) \cdot \boldsymbol{k} + \frac{1}{2}\boldsymbol{k}^T \nabla^2_{\boldsymbol{k}}\varepsilon(\boldsymbol{k}_{min})\boldsymbol{k} + \cdots \tag{3.30}$$

Since the band reaches a local minima at $\boldsymbol{k}_{min}$, $\nabla\varepsilon(\boldsymbol{k}_{min})$ vanishes. Equienergetic surfaces are then given by the third term of the expansion as $\frac{1}{2}\boldsymbol{k}^T\nabla^2_{\boldsymbol{k}}\varepsilon(\boldsymbol{k}_{min})\boldsymbol{k}$ which defines the local curvature of the band edge at the minima. This curvature has a quadratic algebraic form where the expression $\nabla^2_{\boldsymbol{k}}\varepsilon(\boldsymbol{k}_{min})$ represents a second rank tensor. By analogy with the energy of a free electron with momentum $\boldsymbol{P}$ as $\varepsilon = \frac{\boldsymbol{P}^2}{2m}$ and the definition of the crystal momentum in equation (3.23), associated terms define the effective mass as the second rank tensor

$$\boldsymbol{m}^* = \hbar^2[\nabla^2_{\boldsymbol{k}}\varepsilon(\boldsymbol{k})]^{-1} = \hbar^2[\frac{\partial^2\varepsilon(\boldsymbol{k})}{\partial k_i \partial k_j}]^{-1} \tag{3.31}$$

The tensor components in (3.31) depend upon the chosen coordinate system in $\boldsymbol{k}$ space, although the tensor may be diagonalised by a suitable rotation. This rotated $\boldsymbol{k}$ coordinate system is called a principle coordinate system. In the principal coordinate system, the effective mass tensor has the form of a diagonal matrix.

3.2.2.3 Spherical Parabolic Band

Given the diagonalised effective mass, the simplest approximation assumes identical mass m^* for all main diagonal elements. This removes any dependence of the orientation of $\boldsymbol{k}$ with respect to the principal axis on the energy $\varepsilon(\boldsymbol{k})$, and defines spherical equienergetic surfaces, giving rise to the spherical parabolic band approximation. Written with reference to the local minima, this is given by

$$\varepsilon(\boldsymbol{k} - \boldsymbol{k_{min}}) = \varepsilon(\boldsymbol{k}) = \frac{\hbar^2|\boldsymbol{k}|^2}{2m^*} \tag{3.32}$$

analogous to the free electron energy. (3.32) is a first order approximation of the carrier energy in the vicinity of the band minima and is widely used for the conduction band at Γ point or for the split-off valence band when the approximation is sufficient for most simulation [120].

3.2.2.4 Ellipsoidal Parabolic Band

However, the above isotropic band approximation results in an isotropic description of carrier dynamics that is only valid in Silicon at low electric fields and associated carrier energies and in absence of strain. Anisotropic carrier dynamics is experimentally observed though the velocity-field characteristics in response to electric field applied along different crystallographic orientations [120, 129]. In order to capture this effect, an anisotropic band structure is required instead of the spherical band approximation.

This anisotropy is obtained with a reference to the diagonalised effective mass tensor now assuming different mass components on the main diagonal. In this case the band structure, with reference to the local minima, can be represented as

$$\varepsilon(\boldsymbol{k}-\boldsymbol{k_{min}})=\varepsilon(\boldsymbol{k})=\frac{\hbar^2}{2}[\frac{k_x^2}{m_x}+\frac{k_y^2}{m_y}+\frac{k_z^2}{m_z}] \tag{3.33}$$

Owing to the symmetry of the Silicon band structure, two of the mass components are identical and (3.33) may be written as

$$\varepsilon(\boldsymbol{k}-\boldsymbol{k_{min}})=\varepsilon(\boldsymbol{k})=\frac{\hbar^2}{2}[\frac{k_x^2}{m_l}+\frac{k_y^2+k_z^2}{m_t}] \tag{3.34}$$

where the effective mass has been separated into a longitudinal component m_l and a transverse component m_t with respect to the axis of symmetry of the local minima where it is assumed the longitudinal direction is aligned along the x direction in $\boldsymbol{k}$ space. This describes an ellipsoidal equi-energetic surface and is a better approximation to the local minima in the Silicon conduction band [129, 134, 147]. The introduced anisotropy to the band structure more accurately recovers the conduction band transport in silicon [148].

The introduction of this anisotropic band however complicates the calculation of carrier scattering rates (see 3.2.2.6) owing to conservation of momentum that is now dependent upon orientation. In order to simplify this, the anisotropic equi-energy surfaces of the ellipsoidal band model are transformed into the isotropic equi-energy surfaces of the spherical band model via the Herring-Vogt transformation (HVT) [147, 149]. The transformed momentum space is defined by the following matrix equation [129]

$$\boldsymbol{k}^* = \boldsymbol{U}\boldsymbol{k} \tag{3.35}$$

where $\boldsymbol{k}^*$ is the transformed wave vector and $\boldsymbol{U}$ is the Herring-Vogt transformation matrix

$$U = \sqrt{m_d^*}\begin{bmatrix} \sqrt{\frac{1}{m_l}} & 0 & 0 \\ 0 & \sqrt{\frac{1}{m_t}} & 0 \\ 0 & 0 & \sqrt{\frac{1}{m_t}} \end{bmatrix} \tag{3.36}$$

written in the valley frame of reference which is centred in the valley aligned along the x axis in $\boldsymbol{k}$ space. m_d^* represents the density of states effective mass obtained from the relation $m_d^* = (m_l m_t^2)^{1/3}$ [129]. The components of transformed vector $\boldsymbol{k}^*$ are written in terms of the components of the original $\boldsymbol{k}$ vector as

$$k_x^* = \sqrt{\frac{m_d^*}{m_l}}k_x, k_y^* = \sqrt{\frac{m_d^*}{m_t}}k_y, k_z^* = \sqrt{\frac{m_d^*}{m_t}}k_z \tag{3.37}$$

and the energy is represented as in the case of an isotropic band as

$$\varepsilon(\boldsymbol{k}^*) = \frac{\hbar^2}{2m_d^*}\boldsymbol{k}^{*T}\boldsymbol{k}^* = \frac{\hbar^2}{2m_d^*}(\boldsymbol{U}\boldsymbol{k})^T\boldsymbol{U}\boldsymbol{k} = \frac{\hbar^2}{2m_d^*}\boldsymbol{k}^T\boldsymbol{U}^T\boldsymbol{U}\boldsymbol{k} = \frac{\hbar^2}{2}[\frac{k_x^2}{m_l} + \frac{k_y^2 + k_z^2}{m_t}] = \varepsilon(\boldsymbol{k}) \tag{3.38}$$

where (3.35) has been substituted for $\boldsymbol{k}^*$. From (3.38) it is clear that the HVT preserves the energy. Applying this transformation allows the treatment of the band as isotropic in momentum space, given that the transformation is applied consistently to all other vector quantities, while the inverse transformation returns the correct anisotropic result.

3.2.2.5 Ellipsoidal Nonparabolic Band

For energies above the conduction band minima the parabolic band approximation of the above two models is inaccurate. The accuracy may be improved by accounting for the variation in curvature of the band within the so-called nonparabolic band approximation. The local conduction band minima may then be written as [129, 150]

$$\varepsilon(\boldsymbol{k})(1+\alpha\varepsilon(\boldsymbol{k}))=\gamma(\boldsymbol{k})=\frac{\hbar^2}{2}[\frac{k_x^2}{m_l}+\frac{k_y^2+k_z^2}{m_t}] \tag{3.39}$$

where α is the nonparabolicity parameter. $\varepsilon(\boldsymbol{k})$ is explicitly given by

$$\varepsilon(\boldsymbol{k})=\frac{-1+\sqrt{1+4\alpha\gamma}}{2\alpha}=\frac{2\gamma}{1+\sqrt{1+4\alpha\gamma}} \tag{3.40}$$

Equation (3.40) is the classic solution of the quadratic equation (3.39) while the algebraic form of the second term reduces loss of precision in numerical calculation. The nonparabolic model approximates the silicon conduction band minima accurately to energies of around 200 meV [151].

Due to its simplicity and suitable accuracy within the range of energy important to this work, the ellipsoidal nonparabolic model in conjunction with the Herring-Vogt transformation above is the approximation to the band structure used throughout. The entire conduction band is then modelled as a set of discrete minima, each described by equation (3.39).

3.2.2.6 Scattering Rate Calculation

Having described the implemented band structure that defines the semi-classical electron transport governing the drift terms of BTE (3.27), it is left to describe the representation of the collision term $C[f]$ (equation (3.28)) that comprises the right hand side.

Scattering between states occurs due to perturbations of the ideal periodic lattice potential. It is typically treated via first order perturbation theory by considering the effect of an additional scattering potential $U_S(\boldsymbol{r})$ on the unperturbed Hamiltonian. The transition rate from an initial state $\boldsymbol{k}$ to final state $\boldsymbol{k}^{'}$ is determined from the scattering matrix element, defined within the Born approximation as [120]

$$H_{\boldsymbol{k}',\boldsymbol{k}}=\frac{1}{\Omega}\int_{-\infty}^{\infty}\psi^*_{\boldsymbol{k}'}U_S(\boldsymbol{r})\psi_{\boldsymbol{k}}d^3\boldsymbol{r} \tag{3.41}$$

where Ω is the volume in real space, $\psi_{\boldsymbol{k}}$ is Bloch wave and $\psi^*_{\boldsymbol{k}'}$ is a conjugate Bloch wave. The transition rate is thus obtained from Fermi's Golden Rule as [120, 129]

$$S(\boldsymbol{k},\boldsymbol{k}^{'}) = \frac{2\pi}{\hbar}|H_{\boldsymbol{k}^{'},\boldsymbol{k}}|^{2}\delta(\varepsilon(\boldsymbol{k}^{'}) - \varepsilon(\boldsymbol{k}) \pm \Delta\varepsilon)\delta_{\boldsymbol{k}^{'},\boldsymbol{k}\pm\beta} \tag{3.42}$$

The above δ-function expresses conservation of energy given that an amount of energy $\Delta\varepsilon$ may in general be absorbed or emitted as a result of scattering, determined by the plus and minus sign respectively. The Kronecker δ similarly expresses momentum conservation where $\hbar\beta$ is the change in momentum due to scattering and where plus and minus represent absorption and emission respectively. The final scattering rate for a given initial state $\boldsymbol{k}$ is then the sum of the above transition rates over all possible final states, given as [120]

$$\Gamma(\boldsymbol{k}) = \frac{1}{\tau(\boldsymbol{k})} = \sum_{\boldsymbol{k}^{'}} S(\boldsymbol{k},\boldsymbol{k}^{'})[1 - f(\boldsymbol{k}^{'})] \tag{3.43}$$

where $\tau(\boldsymbol{k}_0)$, the reciprocal of the scattering rate, is the average time between collisions and $f(\boldsymbol{k}^{'})$ is the probability that the final state $\boldsymbol{k}^{'}$ is unoccupied.

At this point the band structure $\varepsilon(\boldsymbol{k})$ again enters the discussion. As it determines the energy-momentum relationship, it strongly effects the energy and momentum conservation in equation (3.42) and the number of allowed final states in the subsequent summation in equation (3.43). The number of states within a given energy range at a given energy per unit volume is termed the density of states and, for the ellipsoidal nonparabolic band used here, is sufficiently well approximated for states with energy up to 2 eV [120].

It is now left to detail the scattering mechanism included within this work.

3.2.2.7 Acoustic and Optical Phonon Scattering

Phonons are discrete coupled modes of oscillation of the crystal lattice, driven by the thermal motion of its atoms, which are described by a plane wave propagating in the periodic lattice with properties similar to the Bloch wave [120, 121]. Similar to the electron band structure, phonon modes have unique energy-momentum relationships (dispersion relations) that defines their interaction with carriers through energy and momentum conservation similarly to equation (3.42). There are a number of important modes that are considered here:

Acoustic phonons are associated with oscillations of adjacent atoms in the same directions. In reality there are multiple branches representing longitudinal and transverse wave solutions of the coupled modes with an anisotropic dependence on the momentum. This anisotropy is small however and the acoustic modes are averaged into a single, isotropic mode for efficient calculation. Only intravalley carrier scattering is considered as the probability of large momentum transfers, necessary for intervalley transition, is negligible. Acoustic phonons are treated inelastically following [120, 129, 147] in order to properly account for energy relaxation at low energies and are described by a general phonon dispersion given by [152]. Calibration of the scattering rate is obtained via altering the acoustic deformation potential Ξ_{ac}.

Optical phonons, by contrast, are associated with oscillations of adjacent atoms in opposite directions. Both intravalley and intervalley scattering by optical phonons is considered. Following the common approach described in [129], three g-type and three f-type intervalley optical phonon transitions are considered. Each optical phonon transition is considered as a dispersionless mode due to the small range in phonon momentum allowed in transitions and the relatively flat dispersion relation over the Brillouin Zone. Calibration is achieved via their respective coupling constants. The calibration of the phonon model is discussed later in section 3.2.2.11.

Ionised impurity scattering, relevant in modern highly doped devices, is included via the Brooks-Herring formalism [153] including Ridley's Third Body screening [154, 155]. This model effectively limits the scattering rate in regions of low screening and improves the efficiency of the simulation, although it may be less accurate in regions of extremely low screening where it asymptotically approaches the Conwell-Weisskopf model [156].

Additional scattering mechanisms such as carrier-carrier scattering, electron-plasmon scattering and impact ionisation are not considered in this work. These mechanisms are important for investigating the high energy electron distribution and energy exchange and play little role in this work.

3.2.2.8 Selection of Free Flight Time

The total scattering rate defines the average number of collisions per unit time and is equal to the sum of all scattering rates associated with the individual mechanisms considered

$$\Gamma(\boldsymbol{k}) = \sum_{i=1}^{l} \Gamma_i(\boldsymbol{k}) \tag{3.44}$$

The reciprocal of the total scattering rate defines the the average free flight time between collision

$$\tau(\boldsymbol{k}) = \frac{1}{\Gamma(\boldsymbol{k})} \tag{3.45}$$

The free flight times are random but follow a probability distribution function $F(t)$, where $F(t)dt$ defines the probability that a collision occurs between times t and $t + dt$ and is expressed as

$$F(t) = \Gamma(\boldsymbol{k}) e^{-\Gamma(\boldsymbol{k})t} \tag{3.46}$$

Unfortunately, a direct evaluation of (3.46) for each electron at every time step is a cumbersome and time-consuming task since the total scattering rate $\Gamma(\boldsymbol{k})$ varies in the time dependent upon carrier propagation. In order to overcome this, the total scattering rate $\Gamma(\boldsymbol{k})$ is replaced with a constant $\Gamma_0 = \Gamma(\boldsymbol{k}) + \Gamma_{self}(\boldsymbol{k})$ where $\Gamma_{self}(\boldsymbol{k})$ is the rate associated with a fictitious scattering mechanism, termed self-scattering [157, 158], which does not change the state of the electron. This simplifies the mathematics such that the total scattering rate is now energy independent and allows (3.46) to be re-written as

$$F = \Gamma_0 e^{-\Gamma_0 t} \tag{3.47}$$

Integrating the left hand side of (3.47) over the interval $[0, t_{ff}]$ gives the probability that the electron undergoes its first collision at time t_{ff} and this may be used in connection with a uniformly distributed random number to sample the probability distribution [120]. We have the following expression

$$P(x < r) = \int_0^r dx = \Gamma_0 \int_0^{t_{ff}} e^{-\Gamma_0 t} dt = 1 - e^{-\Gamma_0 t_{ff}} \tag{3.48}$$

where x is the uniformly distributed random variable in the intreval $[0, 1]$, r is a random number draw between $[0, 1]$ from uniform distribution, expressing the probability that the electron undergoes its first collision until time t_{ff} and P represents the probability that the random variable x is less than the random number r. Therefore, the expression $r_{ff} = 1 - r$ defines the probability that electron survives without collision until time t_{ff} and also is drawn from uniform distribution between 0 and 1. Thus, using this formulation, the free flight can be generated by following formula

$$t_{ff} = -\frac{1}{\Gamma_0} \ln r_{ff} \tag{3.49}$$

This method is commonly used for selecting free flight times and is the method adopted in this work.

3.2.2.9 Selection of Scattering Events

Having determined the free flight time, it is necessary to select the appropriate scattering mechanism responsible for its termination. The scattering mechanism selection must properly account for the relative probabilities of each considered mechanism dependent upon the carrier's energy. The ith relative probability of the ith scattering mechanism corresponds to the rate of this mechanism with respect to the constant Γ_0. The condition for selecting the ith scattering mechanism can be expressed as [120]

$$\sum_{j=1}^{i-1} \Gamma_j(\varepsilon) \leq r\Gamma_0 \leq \sum_{j=1}^{i} \Gamma_j(\varepsilon) \tag{3.50}$$

where r is a random number drawn from uniform distribution, $1 \leq i \leq l$ and the last lth mechanism is reserved for the self-scattering Γ_{self}. The introduction of the self-scattering rate into the selection process significantly enhances the efficiency and speed of the simulation [129]. Further enhancement of the selection process is achieved through the construction of a scattering table, discretised over a range of energy limited to the maximum expected energy. During the course of a simulation, selection of a scattering mechanism is done with reference to this look-up table for a given carrier energy.

3.2.2.10 Carrier Dynamics

Having determined the new wavevector after a scattering event and generated the new free flight, integration of the carrier's equations of motion is performed. It is assumed that the ellipsoidal equienergetic surfaces are transformed into spherical equienergetic surfaces by (3.35) prior to the updating of the carrier momentum and coordinates. In turn, the transformed wavevector is used to determine the new wavevector, the new position vector and the new velocity vector of carrier. Following this and using (3.26) and the Velocity-Verlet algorithm [109, 118], the wavector is updated as

$$\begin{aligned}
k_x^{t+dt/2} &= k_x^t - \frac{e}{\hbar}\frac{\partial V(\boldsymbol{r}_t)}{\partial x}\frac{dt}{2} \\
k_y^{t+dt/2} &= k_y^t - \frac{e}{\hbar}\frac{\partial V(\boldsymbol{r}_t)}{\partial y}\frac{dt}{2} \\
k_z^{t+dt/2} &= k_z^t - \frac{e}{\hbar}\frac{\partial V(\boldsymbol{r}_t)}{\partial z}\frac{dt}{2}
\end{aligned} \tag{3.51}$$

where dt is a duration of the free flight. Thereafter, for nonparabolic band structure defined by (3.39) the following relation for velocity at time $t + dt/2$ can be obtained

$$\boldsymbol{v}_{t+dt/2} = \frac{\hbar \boldsymbol{k}_{t+dt/2}}{m_d^*(1 + 2\alpha\varepsilon(\boldsymbol{k}_{t+dt/2}))} \tag{3.52}$$

where $\boldsymbol{k}_{t+dt/2}$ is wavector in the spherical space obtained from the relation (3.51). Using (3.24) and (3.52) the spatial coordinates of the electron at time $t + dt$ is updated as

$$
\begin{aligned}
x^{t+dt} &= x^{t} + \frac{\hbar k_x^{t+dt/2}}{m_d^*(1+2\alpha\varepsilon(\boldsymbol{k}_{t+dt/2}))}dt \\
y^{t+dt} &= y^{t} + \frac{\hbar k_y^{t+dt/2}}{m_d^*(1+2\alpha\varepsilon(\boldsymbol{k}_{t+dt/2}))}dt \\
z^{t+dt} &= z^{t} + \frac{\hbar k_z^{t+dt/2}}{m_d^*(1+2\alpha\varepsilon(\boldsymbol{k}_{t+dt/2}))}dt
\end{aligned}
\tag{3.53}
$$

In turn, the new wavevecctor at time $t + dt$ may be expressed as

$$
\begin{aligned}
k_x^{t} &= k_x^{t+dt/2} - \frac{e}{\hbar}\frac{\partial V(\boldsymbol{r}_{t+dt})}{\partial x}\frac{dt}{2} \\
k_y^{t} &= k_y^{t+dt/2} - \frac{e}{\hbar}\frac{\partial V(\boldsymbol{r}_{t+dt})}{\partial y}\frac{dt}{2} \\
k_z^{t} &= k_z^{t+dt/2} - \frac{e}{\hbar}\frac{\partial V(\boldsymbol{r}_{t+dt})}{\partial z}\frac{dt}{2}
\end{aligned}
\tag{3.54}
$$

where $\boldsymbol{r}_{t+dt}$ is given by (3.53). Finally, the new wavevector is transformed back to the ellipsoidal form by using the inverse transformation to (3.35).

3.2.2.11 Bulk Calibration

Calibration of the phonon scattering rates specific to the band model adopted is necessary to ensure good agreement with experimentally observed results. This was achieved through initial bulk simulation and comparison with theoretical mobility field dependence [159]. The acoustic phonon deformation potential was first calibrated at low temperatures in order to freeze out the higher energy optical phonons. The simulation temperature was gradually increased to bring in higher energy acoustic phonons which were then calibrated. This was further refined with comparison to experimental velocity-field measurements at both 77K and 300K and in different crystal orientations [148] in which the dominant phonon was adjusted for a best fit. The final calibration is shown in the reproduction of the velocity-field characteristics in silicon in figure 3.8. Recovery of the anisotropic behaviour is noted.

The calibrated values of the acoustic phonon deformation potential and optical phonon coupling constants are tabulated in table 3.1 and 3.2.

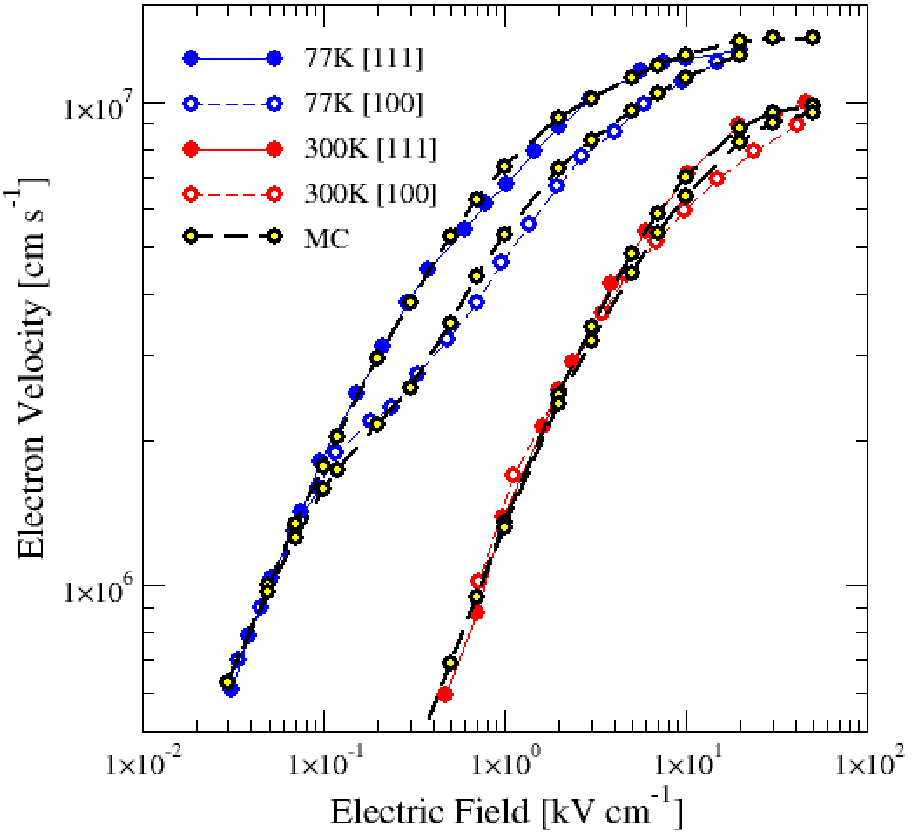

FIGURE 3.8: The acoustic deformation potential as well as the optical phonon coupling constants have been calibrated to reproduce the experimantally obtained anisotropic bulk velocity-field characteristics of Silicon at 77K and 300K.

Reproduction of bulk concentration dependent mobility in Silicon using the Brooks-Herring formalism is shown in figure 3.3 showing typical agreement with overestimation at higher doping densities.

3.2.2.12 *Ab Initio* Ionized Impurity Scattering

This work is concerned with random dopant distributions in modern nano-scale MOSFETs and their impact on current variation through position dependent variation in ionised impurity scattering. For such purpose, the treatment of ionised impurity scattering via the above mentioned scattering rate is unsuitable as it is an inherently random process defined within a conceptual homogeneously doped and infinite volume. Further, it assumes a two-body interaction which ignores multi-ion contributions to the scattering potential [160] and treats scattering events as localised instantaneous interactions rather than extended in the space and time. For these reasons it is unable to properly

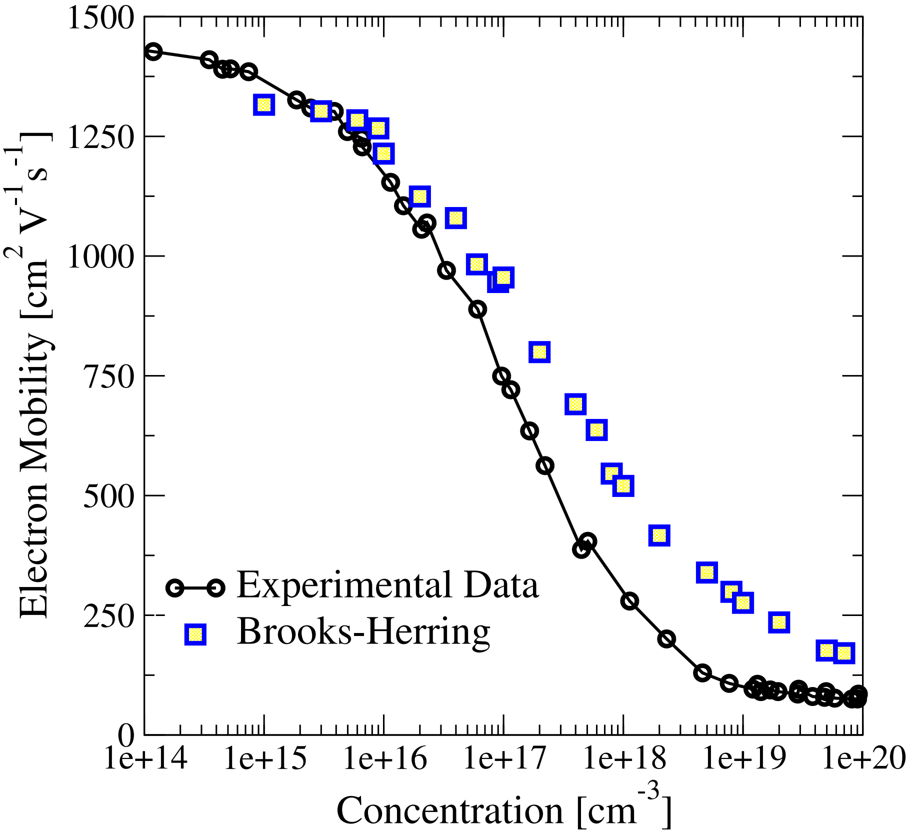

FIGURE 3.9: Simulated low field concentration dependent bulk electron mobility in Silicon at 300 K using the Brooks-Herring scattering rate [153]. Comparison with experimental data [115] is also shown.

account for transport variation due to the random configuration of a small number of dopants [161]. The proper treatment of random dopant induced transport variations requires the unique potential associated with 3D dopant configurations to be taken into account and for a deterministic treatment of carrier interaction. This is achieved within MC through an *ab initio* treatment of ionised impurity scattering [33, 161] in which the carrier-impurity interaction is explicitly included within the propagation step. Ionised impurity scattering rates are removed from the scattering rate table and transport variations are then naturally included via the real-space trajectories of electrons propagating through the electric field associated with a random configuration of dopants. This approach additionally automatically accounts for multi-ion interactions, dynamic screening and removes the necessity to make any assumptions about the local dependance of the distribution and screening length [79].

Ab initio ionised impurity scattering has previously been introduced to the MC simulator [33, 118] via the P^3M method [109, 161] which includes the full electron-ion interaction via the mesh based potential with an additional short range correction over neighbouring particles. The mesh based solution of Poisson's equation accurately recovers long range interactions while the short range corrections account for the aliasing in the solution. To suppress errors associated with the numerical integration of particle trajectories, and to prevent the artificial carrier trapping in the case of an attractive impurity potential, [33, 162, 163] the short range interaction was assumed not to follow the Coulomb law, but instead a modified form which limited the interaction at close separation was used. This modified force is an analytical model defined as

$$F_{SR} = \frac{qr}{4\pi\varepsilon(r^2 + \frac{1}{2}r_c^2)^{\frac{3}{2}}} \tag{3.55}$$

where r is the carrier-impurity separation and r_c defines a cut-off radius at which the force reaches a maximum. F_{SR} recovers the Coulomb law at large distances while limiting the interaction at close-range [33, 161]. The accuracy of this method was demonstrated with the reproduction of the concentration dependence of mobility in bulk silicon [33] in which propagation within a large number of donor atoms was simulated. The number of donors, around 15,000, were large enough to be self-averaging.

This previous work however omitted quantum corrections that are essential to the accurate simulation of nano-scale devices. Such quantum corrections have since been included within MC simulations via the density gradient framework in order to account for the inversion layer carrier distribution [32]. This has been shown to be in excellent agreement with the equivalent drift diffusion solution. Within this work, quantum corrections are novelly applied to the impurity potential from the classical solution of Poisson's equation to unify *ab initio* scattering and quantum corrections. This will be discussed in detail in the following chapter.

BAND INDEPENDENT PARAMETER	**SYMBOL**	**VALUE**
Transverse sound velocity	u_t	5340 ms^{-1}
Longitudinal sound velocity	u_l	9040 ms^{-1}
Acoustic deformation potential	Ξ_{ac}	6.30 eV
Density	ρ	2329 kgm^{-3}
Static dielectric constant	ε	11.90
X-Valley Parameters	**SYMBOL**	**VALUE**
Energy of band X relative to the valence band edge	E_g	1.12 eV
Transverse effective mass	m_t	0.190 m_e
Longitudinal effective mass	m_l	0.916 m_e
Non-parabolicity parameter	α	0.5 eV^{-1}
Optical Coupling Constant		
g_1 phonon process	$D_tK_{g_1}$	0.500×10^{10} eVm^{-1}
g_2 phonon process	$D_tK_{g_2}$	0.800×10^{10} eVm^{-1}
g_3 phonon process	$D_tK_{g_3}$	3.000×10^{10} eVm^{-1}
f_1 phonon process	$D_tK_{f_1}$	0.150×10^{10} eVm^{-1}
f_2 phonon process	$D_tK_{f_2}$	3.400×10^{10} eVm^{-1}
f_3 phonon process	$D_tK_{f_3}$	4.000×10^{10} eVm^{-1}
Optical Phonon Energies		
g_1 phonon process	$\hbar\omega_{g_1}$	1.206×10^{-2} eV
g_2 phonon process	$\hbar\omega_{g_2}$	1.853×10^{-2} eV
g_3 phonon process	$\hbar\omega_{g_3}$	6.300×10^{-2} eV
f_1 phonon process	$\hbar\omega_{f_1}$	1.896×10^{-2} eV
f_2 phonon process	$\hbar\omega_{f_2}$	4.740×10^{-2} eV
f_3 phonon process	$\hbar\omega_{f_3}$	5.903×10^{-2} eV
Inter-valley Optical Coupling Constants		
$X \rightleftarrows X$	$D_tK_{X \rightleftarrows X}$	1.750×10^{10} eVm^{-1}
$X \rightleftarrows L$	$D_tK_{X \rightleftarrows L}$	2.340×10^{10} eVm^{-1}
$X \rightleftarrows \Gamma$	$D_tK_{X \rightleftarrows \Gamma}$	5.480×10^{10} eVm^{-1}
Inter-valley Optical Phonon Energies		
$X \rightleftarrows X$	$\hbar\omega_{X \rightleftarrows X}$	4.300×10^{-2} eV
$X \rightleftarrows L$	$\hbar\omega_{X \rightleftarrows L}$	3.716×10^{-2} eV
$X \rightleftarrows \Gamma$	$\hbar\omega_{X \rightleftarrows \Gamma}$	2.189×10^{-2} eV

TABLE 3.1: Band independent parameters and calibrated values for the minimum lying X-valley used in the MC simulation. These values govern the transport processes effecting the majority of electrons in silicon and are used consistently throughout this work.

L-Valley and Γ-Valley Parameters	**SYMBOL**	**VALUE**
Bandgap L-Valley	E_{gL}	$2.169\ eV$
Bandgap Γ-Valley	$E_{g\Gamma}$	$3.495\ eV$
Transverse effective mass L-Valley	m_{tL}	$0.126\ m_e$
Longitudinal effective mass L-Valley	m_{lL}	$1.634\ m_e$
Transverse effective mass Γ-Valley	$m_{t\Gamma}$	$1.000\ m_e$
Longitudinal effective mass Γ-Valley	$m_{l\Gamma}$	$1.000\ m_e$
Non-parabolicity parameter L-Valley	α_L	$0.3\ eV^{-1}$
Non-parabolicity parameter Γ-Valley	α_Γ	$0.0\ eV^{-1}$
Inter-valley Optical Coupling Constants		
$L \rightleftarrows L$	$D_tK_{L\rightleftarrows L}$	$2.630 \times 10^{10}\ eVm^{-1}$
$L \rightleftarrows \Gamma$	$D_tK_{L\rightleftarrows \Gamma}$	$2.090 \times 10^{10}\ eVm^{-1}$
$\Gamma \rightleftarrows \Gamma$	$D_tK_{\Gamma\rightleftarrows \Gamma}$	$2.990 \times 10^{10}\ eVm^{-1}$
Inter-valley Optical Phonon Energies		
$L \rightleftarrows L$	$\hbar\omega_{L\rightleftarrows L}$	$3.887 \times 10^{-2}\ eV$
$X \rightleftarrows \Gamma$	$\hbar\omega_{X\rightleftarrows \Gamma}$	$2.090 \times 10^{-2}\ eV$
$\Gamma \rightleftarrows \Gamma$	$\hbar\omega_{\Gamma\rightleftarrows \Gamma}$	$2.568 \times 10^{-2}\ eV$

TABLE 3.2: Parameters for the L and Γ valleys. Though present within the simulation, little transport occurs in these valleys due to the large separation in energy from the X-valley.

Chapter 4

ON-CURRENT VARIABILITY DUE TO RANDOM DOPANT DISTRIBUTIONS

Monte Carlo simulation with the careful inclusion of an *ab initio* treatment of ionized impurity scattering has in the past been shown to accurately describe concentration dependent bulk mobility [33], position dependent scattering in nano-scale devices [33, 79–81] and the corresponding transport variation [33, 34]. Statistical device simulations focusing on discrete dopant induced drain current variability has also since been reported using such *ab initio* MC simulation and have been shown to capture significant additional current variability when compared with equivalent statistical DD simulation [33, 34]. The increased variation is associated with additional transport variation in MC, due to position dependent impurity scattering, over and above the electrostatic variation captured in DD. It was therefore concluded that any complete study of variability requires careful consideration of transport variation.

However,previous studies omitted quantum mechanical corrections that are vital for accurate simulation of nano-scale devices. When such corrections are included, they can accurately reproduced the impact of the quantum confinement on the inversion layer carrier distribution. The difference between the classical and quantum mechanical inversion layer distribution results in significant differences in the electrostatic screening of discrete dopants. Specifically, the large interface carrier concentration in the classical case is more effective at screening impurity potentials compared to the more smeared quantum carrier distribution. Significantly increased transport variation may therefore be expected when quantum mechanical corrections are considered within *ab initio* MC, owing to stronger scattering potentials. Quantum corrections have been applied accurately to MC simulation recently [32] but have yet to be applied to and tested in respect of *ab initio* impurity scattering in the presence of statistical dopant distributions.

Additionally the *ab initio* force resolution within the earlier classical version of the Glasgow MC code was based upon a short-range correction to the mesh resolved Coulomb potential. Although this correction was treated efficiently, it represents an additional computational overhead. It has also conceptual problems at boundaries and interfaces where image charge effects are present. It is also not possible to guarantee the short-range force exactly matches the mesh-resolved force in the transition between the two regimes and this results in an unsatisfactory discontinuity. In this chapter, a unique method to overcome these limitations is presented by means of a solely mesh-based force evaluation that captures *ab initio* carrier-impurity scattering in addition to quantum confinement effects. This force is obtained from the self-consistent inclusion of the Density Gradient (DG) effective quantum potential solution within MC.

This chapter is structured as follows. The quantum corrected MC methodology is discussed and verified in section 4.1, highlighting the use of the DG quantum potential as applied to discrete dopant scattering. Section 4.2 details the implementation of this new method for the simulation of on-current variability in a series of realistically scaled devices. The developed approach is then applied to accurately study random discrete dopant induced drain current variability in a series of realistic, well-scaled bulk MOSFETs with results presented in section 4.2 before conclusions are finally drawn.

4.1 Quantum Corrections in Monte Carlo

The most widely used alternative techniques to quantum corrections in MC simulations are based upon the approximation to the Wigner transport equation [164, 165], effective conduction band edge (ECBE) method [166], Effective Potential method [105, 106] and self-consistent Schr"odinger-Poisson calculations [167].

The Wigner transport equation, derived from the BTE, gives a quantum correction term in the following form $\psi_{\mathrm{qc}} = -\frac{\hbar^2}{12m^*}\nabla^2 ln(n)$ [168], which is applied in 4.4. This method has the capability to mimic tunneling effects [168]. The use of this approach in MC simulation has shown a significant sensitivity to noise due to noise in the electron concentration within the simulation domain which can be overcome by time averaging and spatially smoothing [165, 169]. The need to calibrate the fitting parameter m^* is an other clear drawback of this approach. 2D MC simulations with this approach [170] have shown good agreement with Posison-Schrodinger [169] and NEGF [171] results.

This method can be further extended from the Bohmian interpretation of quantum mechanics [101] leading to the ECBE method [166] where the quantum potential is given in the form $\psi_{\mathrm{q}} = \psi_{\mathrm{cl}} + \frac{\hbar^2}{4m^* r k_B T}[\nabla^2\psi_{\mathrm{q}} - \frac{1}{2k_B T}(\nabla\psi_{\mathrm{q}})^2]$. The ECBE approach is strongly non-linear due to term $(\nabla\psi_{\mathrm{q}})^2$ which complicates the solution. This approach has been successfully employed in $2D$ MC simulations [172, 173].

The Effective potential method smooths the classical potential using a Guassian kernel [105], resulting in the reduction of the electron concentration in the inversion layer and moving the charge away from the interface, both of which lead to current degradation [174]. The smoothed conduction band edge is shifted further from Fermi energy which results in the increase of threshold voltage [105], further, the inversion layer produces the quantum capacitance. This method with Gaussian kernel has been used in 2D MC simulation in [175] and 3D MC simulation in [105]. Alternatively, Pearson kernel can be used in the smoothing procedure in place of a Gaussian and has been applied to MC simulation in [176].

Another approach to quantum corrections is a self-consistent Schrodinger-Poisson solver within MC simulation which accounts for the size quantization effects [167]. In order to capture these effects the 1D Schrodinger equation is solved along the normal direction to the interface as follows [167]

$$-\frac{\hbar^2}{2}\frac{\partial}{\partial z}(\frac{1}{m_z^*}\frac{\partial}{\partial z}\psi) + V_p(z)\psi = \varepsilon\psi \tag{4.1}$$

where $V_p(z)$ is slowly varying potential along the normal direction to interface. The quantum density $n_q(z)$ along the normal direction to interface is used to feed the Poisson equation in a self-consistent loop. The quantum potential term is $\psi_{\mathrm{q}} = -k_B T_z ln(n_q(z)) -$

$V_p(z) + V_0$, and $V_0 = k_B T_z ln(N_{eff}) + E_F$ where N_{eff} is effective density of states and E_F is Fermi level. From equation 4.1 the system of energy eigenvalues with wave eigen functions is obtained and, in turn, they are used to calculate the quantum density as follows [177] $n_q = \frac{1}{\pi}(\frac{2m^* k_B T}{\hbar})^2 \sum_j |\psi_j|^2 \mathcal{F}_{-1/2}(\frac{E_F - \varepsilon_j}{k_B T})$, where ψ_j is jth wave eigen function belonging to jth energy eigen value ε_j. The computational efficiency and accuracy depends on the number of eigen values taken into account in the simulations. This method does not need to calibrate the fitting parameter since it uses a physical value for effective mass m^*. This is one clear difference from the Wigner transport and Effective potential method which both of are required the fitting parameters m^*, and a_0, respectively. This approach has been successfully used in 2D [167, 178] and 3D MC simulations [179] capturing accurately the size quantization, but it poorly mimics the tunneling effects [180].

The NEGF formalism represents the complex approach to the simulation of the quantum transport [181]. In order to accurately capture the size of quantization and tunneling effects the NEGF approach has to be self-consistently coupled with the Poisson equation. The NEGF method provides the open boundary solution to the Schrodinger equation. The methods to solving of NEFG and scattering mechanisms used in NEGF approach are described in [181–184]. Within this work, NEGF approach is used to calibrate and validate the above mentioned DG quantum corrected model [36] since DD and MC simulation with quantum corrections by means of mentioned approaches cannot properly capture the coherent quantum transport and tunneling effects [184].

The common drawback of the above mentioned methods are the considerable amount of computational cost needed to be used [167]. This enormous computational inefficiency prohibits the use of these methods for 3D to the large scale statistical simulations of CMOS devices, particularly NEGF method and self-cosistent Poisson-Schrodinger solver. For this reason DG quantum corrections are employed in the MC simulations in large scale statistical simulations of CMOS devices, as the computational overhead associated with them is considerably smaller.

4.1.1 Density Gradient Quantum Corrections in Monte Carlo

DG quantum corrections have been commonly included in DD simulators (see section 3.1.2) and accurately reproduce the carrier density in regions of strong confinement

[26, 30]. Next to full scale quantum transport simulations, DG corrected statistical DD simulation represents the most economic and accurate way to resolve the impact of individual dopants [26]. Importantly, it also accurately reproduces the charge distribution around individual impurities [30], as shown in figure 4.1 in the extreme case of an n-channel nanowire MOSFET with 3×3 nm^2 cross section in the presence of a single donor in the middle of the channel. DD simulation with DG quantum corrections accurately reproduces the complex inversion layer charge distribution when compared with NEGF simulations in the effective mass approximation [185]. Confinement effects are clearly seen in figure 4.1 through the greatly reduced electron concentration at both top and bottom interfaces. Figure 4.2 [102] shows that DG corrections also accurately reproduce the complex inversion layer electron distribution over a range of gate biases, again even in the presence of a strongly localized attractive impurity potential.

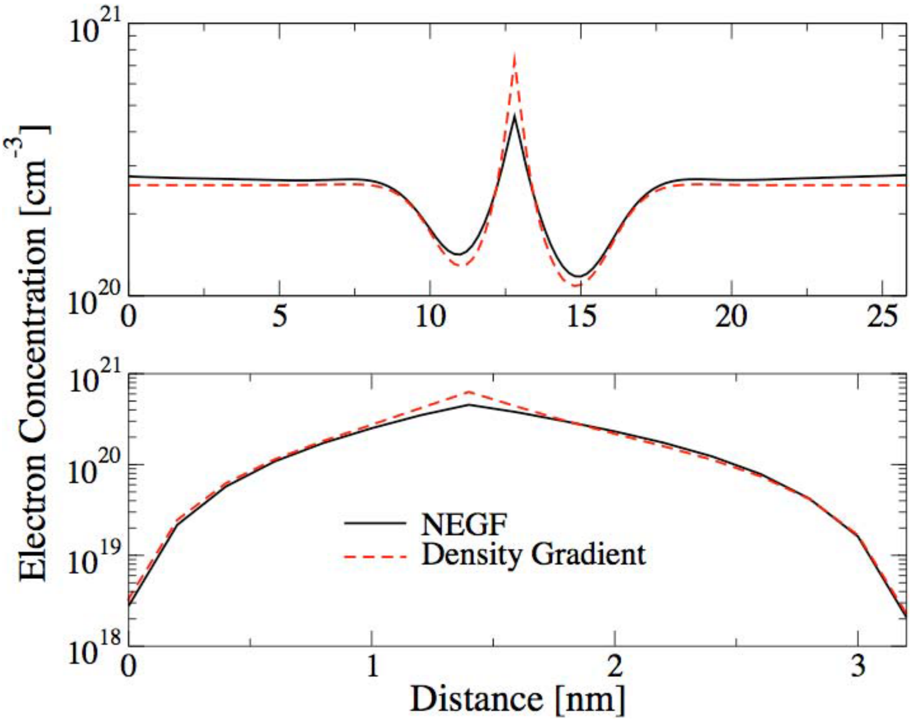

FIGURE 4.1: Agreement between NEGF and DD from (top) source to drain and (bottom) top interface to bottom interface.

As mentioned in section 3.2.2.12, DG quantum corrections have been previously introduced into self-consistent MC simulations of body thickness variation in double gate devices and have accurately reproduced the electron distribution from identical DD simulation [32]. This was achieved by defining an effective quantum potential used to derive the driving force in the MC particle propagation step. The effective quantum potential

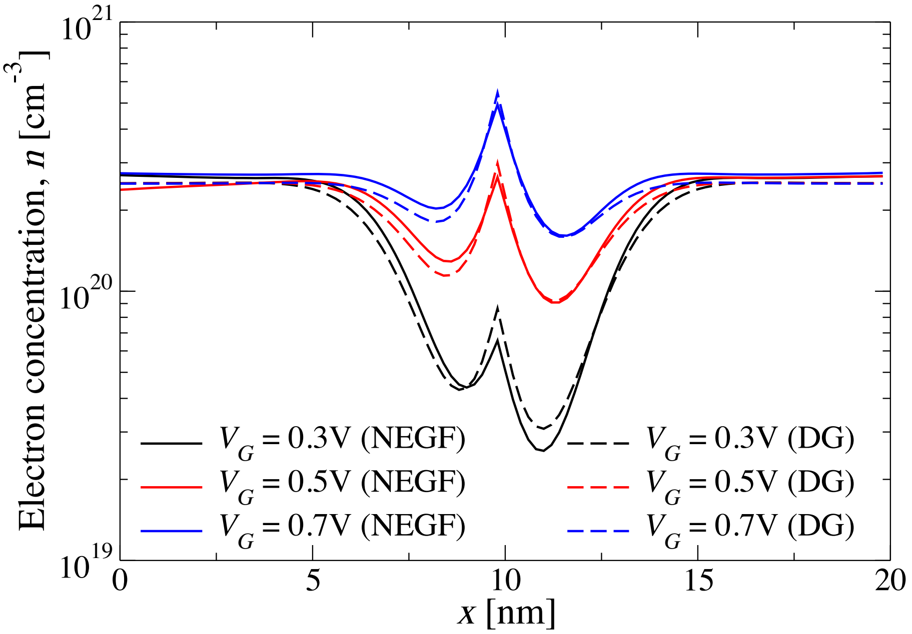

FIGURE 4.2: Comparison of the electron distribution within an n-channel nanowire MOSFET obtained from NEGF and density gradient corrected DD for different gate voltages [102] ($m_x = 0.1$, $m_y = m_z = 0.22$). Agreement is seen even around a strong impurity potential.

was itself defined from a constant mesh-based correction applied to the classical potential solution. The correction term ψ_{qc} was obtained as the difference between the effective quantum and classical potentials from an equivalent prior DD solution, explicitly stated as [180]

$$\psi_{\mathrm{qc}} = \psi_{\mathrm{DG}} - \psi_{\mathrm{CL}} \tag{4.2}$$

where ψ_{DG} is the effective quantum potential from DD solution with DG quantum corrections as described in [32, 68, 100, 104] and ψ_{CL} is the classical potential consistent with the quantum corrected solution. This approach to quantum corrections obtained from DG effective potential is denoted as FQMC (Frozen Quantum Monte Carlo) [36].

When applied within self-consistent MC simulation, the quantum correction term updates the classical potential obtained from solution of Poisson's equation at each field adjusting time step as follows

$$\psi_{\mathrm{q}} = \psi_{\mathrm{cl}} + \psi_{\mathrm{qc}} \tag{4.3}$$

where ψ_{cl} is the classical potential solution within MC and ψ_{q} is a quantum corrected potential. The driving force acting upon carriers is then defined in the usual way as

$$F_{\text{q}} = F_{\text{cl}} + F_{\text{qc}} = -(\nabla\psi_{\text{cl}} + \nabla\psi_{\text{qc}}) \tag{4.4}$$

where F_{q} is a quantum force, which is divided into the classical F_{cl} and quantum correction F_{qc} forces. This method is more efficient than solving either $1D$ or $2D$ coupled Poisson-Schrodinger equations [186], though it gives no information about sub-band structure and 2D transport in the inversion layer.

The additional approach to DG quantum corrections that might be incorporated within the 3D MC simulation is a fully self-consistent approach (Self-Consistent Quantum Monte Carlo-SCQMC), which accounts for a certain degree of self-consistency between transport, field and the quantum corrections, as shown in blue region of figure 4.3 [36]. In SCQMC the ψ_{qc} term is updated regularly during the course of the simulation by solving the modified DG equation [187] for quantum density n_q [36]

$$\frac{2b_n}{S_n}\left(\frac{1}{m_{nx}}\frac{\partial^2 S_n}{\partial x^2} + \frac{1}{m_{ny}}\frac{\partial^2 S_n}{\partial y^2} + \frac{1}{m_{nz}}\frac{\partial^2 S_n}{\partial z^2}\right) = \phi_n - \langle\psi\rangle_t + \frac{k_BT}{q}ln(S_n^2) \tag{4.5}$$

where $S_n = \sqrt{n_q/n_i}$, ϕ_n is the quasi-Fermi level, $\langle ... \rangle_t$ denotes a time averaged value, the other symbols have their usual meaning. Time averaging of statistic is necessary here due to the inherent noise of the MC carrier distribution. Equation 4.5 is discretized using a finite box method; the corresponding system of equations is linearized and solved using a Red-Black SOR iterative scheme. We assume a Maxwell-Boltzmann equation of state [167], and ϕ_n might be updated as

$$\phi_n = \langle\psi_{cl} + \psi_{qc}\rangle_t - \frac{k_BT}{q}ln\left(\frac{\langle n_{mc}\rangle_t}{n_i}\right) \tag{4.6}$$

where n_{mc} is the electron distribution obtained from MC simulation. A new quantum correction term is obtained as

$$\psi_{qc} = \phi_n + \frac{k_BT}{q}ln\left(\frac{\langle n_{mc}\rangle_t}{n_i}\right) - \langle\psi_{cl}\rangle_t \tag{4.7}$$

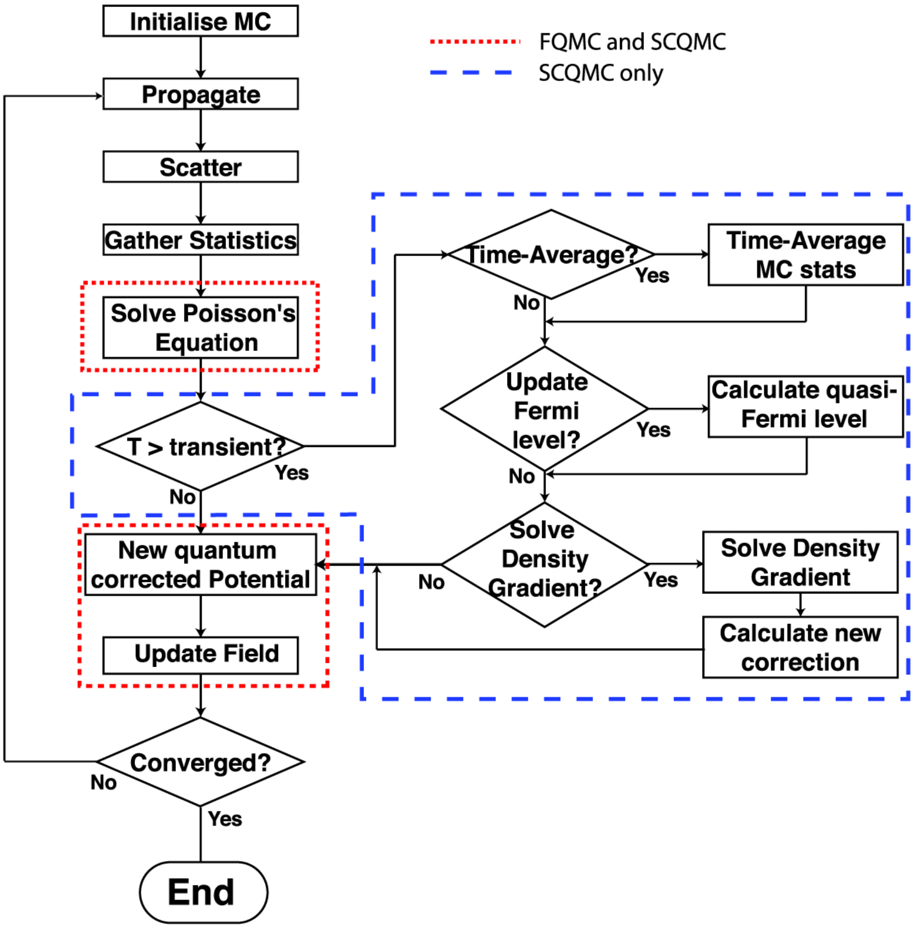

FIGURE 4.3: Flowchart showing the computational steps needed for FQMC (Frozen Quantum Monte Carlo) and SCQMC (Self-Consistent Quantum Monte Carlo) [36].

The update of ψ_{qc} is coupled self-consistently with Poisson's equation using similar approach as Schrodinger based quantum correction scheme in [167]. Due to high noise sensitivity of the SCQMC approach during initial transient part of simulation the quantum correction term is not updated.

The accurate implementation of boundary conditions (BCs) at Si/SiO_2 interface and source and drain regions is highly important [188, 189] as they account for a smooth transition of the carrier density towards the interface and for the penetration of the electrons wavefunction into the oxide layer [36, 188, 189]. In order to prevent inconsistencies which can disrupt simulation, the appropriate incorporation of BCs at the Ohmic contacts in the source and drain regions is extremely crucial [36, 188]. The local charge neutrality is managed by removing and replacing carriers after reaching contact boundaries and the difference in ϕ_n between the source and drain contacts (the applied drain bias) is maintained by this careful management of carriers in the contact regions.

The classical approach of fixing the potential and carrier concentration (Dirichlet BCs) at the Ohmic contacts results in significant depletion of carriers in the source and drain regions, as shown in figure 4.4, since insufficient numbers of carriers are injected. This treatment of BCs does not match the carrier distribution consistent with that introduced by the quantum concentrations [36]. In order to fix this issue, Neumann BCs [112, 188] are implemented at the Ohmic contact regions. In this treatment the quasi Fermi level ϕ_n is fixed, while potential ψ_n and carrier concentration are altered so that it matches the proper quantum carrier distribution, as illustrated at the left picture in figure 4.5. The right picture in figure 4.5 shows and compares electron concentration distribution obtained from different approaches to DG quantum corrections within MC simulation in the middle of the channel of a double gate MOSFET at low drain voltage [188].

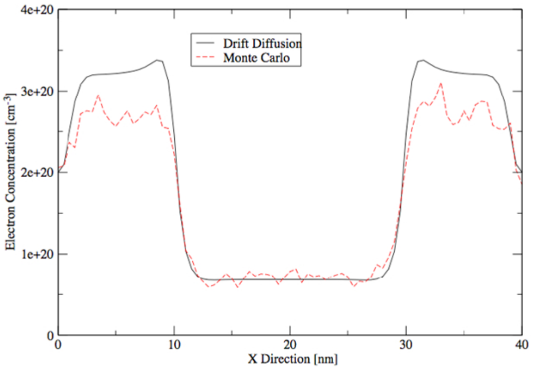

FIGURE 4.4: Electron density in the x-direction showing the depletion resulting from the contacts being poorly maintained [188].

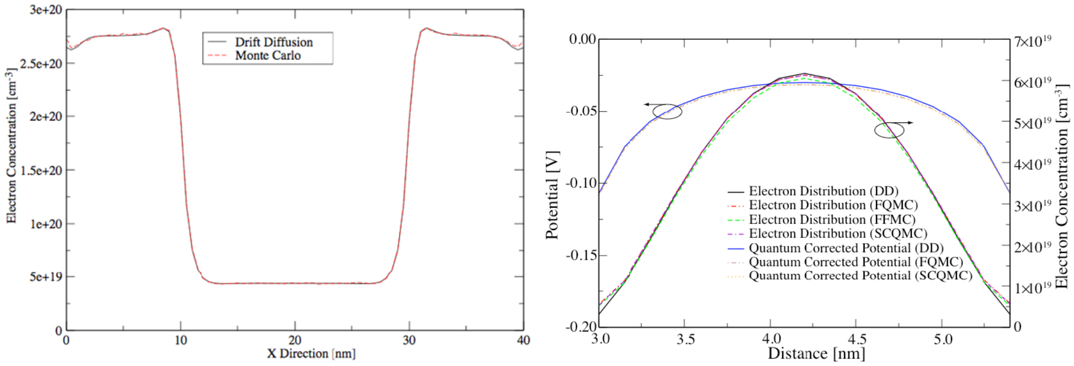

FIGURE 4.5: Electron density (left) in the x-direction with properly maintained contacts as a result of the use of Neumann BCs [36, 188]. Electron density and Quantum corrected potential in the z-direction (right) with Neumann BCs for double gate MOSFET [36, 188].

Within this work FQMC is used (red dashed line in figure 4.3) since the previously demonstrated good agreement between FQMC and SCQMC suggests that the self-consistency of the quantum corrections is not vital [36, 190].

4.1.2 The Effective Density Gradient Quantum Potential

The effective quantum potential obtained from the density gradient solution surrounding a single attractive impurity potential is shown in figure 4.6. Solutions corresponding to cubic discretization meshes with different mesh spacings are shown. Compared to a strong mesh spacing dependence of the classical Coulomb potential near a localized impurity [26, 30], the effective DG quantum potential has only a weak mesh spacing dependence and shows convergence of the potential solution for mesh spacings of 1 nm and smaller.

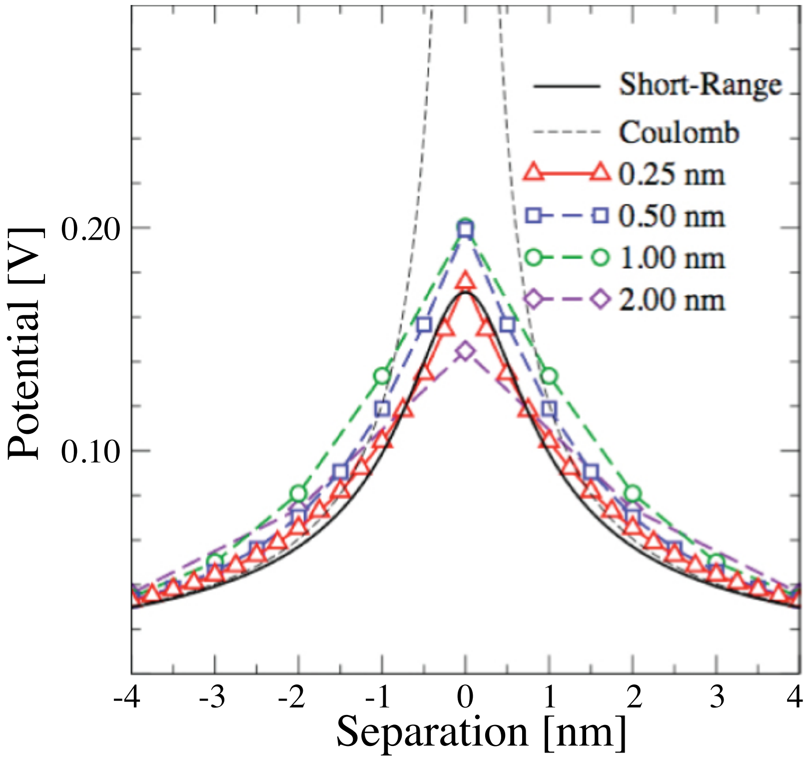

Figure 4.6: Comparison of analytic short-range correction applied in [33] to density gradient solution around a point charge. It can be seen that a mesh spacing of 2 nm underestimates the potential while mesh spacings of 1 nm and below show better agreement. The potential for a mesh spacing of 0.25 nm agrees very well, but has a lower potential than that of 1 nm or 0.5 nm mesh. Mesh spacings of 1 nm or less are good.

Also shown in figure 4.6 is the analytic Coulomb potential and short-range correction model applied within previous *ab initio* MC [33]. It is clear that the analytic short-range model closely agrees with the converged DG effective quantum potential. The similarity hints at the suitability to simultaneously include quantum corrections and short-range electron-impurity interactions from the mesh resolved quantum potential when treating *ab initio* impurity scattering in MC. This would provide an efficient and consistent mesh based treatment that would automatically include confinement effects as well as *ab initio* Coulomb interactions and would accurately define boundary and image-charge effects. However, the application of this approach needs to be verified.

Validation of the effective quantum potential short-range interaction model follows two stages, analogous to the previous verification of the analytic short-range model [33]. First the Rutherford dependence of scattering angle upon impact parameter is reproduced and, second, the bulk mobility dependence upon doping concentration is reproduced .

4.1.3 Rutherford Scattering

For the purposes of simulating Rutheford scattering, a sufficiently large circular simulation domain is used such that the initial and final carrier velocities approximate the asymptotic velocities before and after the collision. The simulation domain has a radius of 5000 nm and a singly negative or positive ion, which represent the interactions with an acceptor or donor respectively, is placed at its centre. The DG effective quantum potential solution for such a point charge has been obtained on a $20 \times 20 \times 20nm^3$ mesh with uniform spacing of $0.5nm$ and boundary conditions set to match the analytic short-range model in figure 4.6. Within this domain the interaction is obtained by interpolating the mesh based solution, while outside the analytical short range model is used, as shown in figure 4.7. The analytic model was chosen as it tends to the Coulomb interaction at large separation but limits discontinuity in the force during the transition between the two domains.

Electrons are considered with an initial energy of 40 meV and are set at the boundary of the outer, circular, domain to cover a range in impact parameters of 200 nm. Having been propagated within the analytic and mesh based potential and upon leaving the simulation domain, the corresponding angle of deflection is determined. The resulting scattering angle dependence is compared with the original analytic short-range model

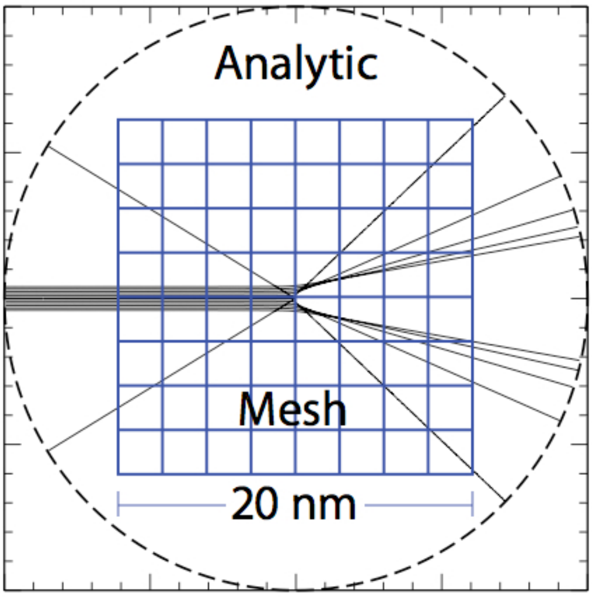

FIGURE 4.7: Picture shows transition from analytical to mesh interpolation for the case of Density Gradient potential.

and the exact Rutherford model in figure 4.8 for the cases of a positive and negative central ion.

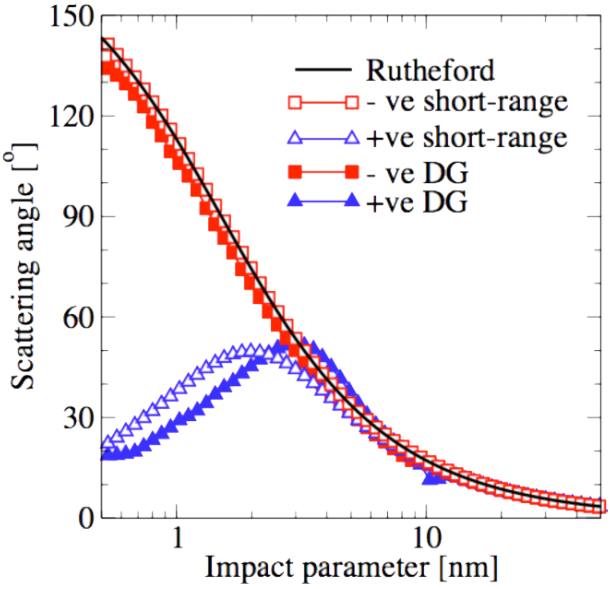

FIGURE 4.8: Comparison of scattering angle dependence upon impact parameter using analytical short-range model and mesh-based interpolation from density gradient solution.

Close agreement between the new effective quantum potential and the old analytical short-range model is obtained. The good agreement between the new model and the old one gives confidence as bulk concentration dependent mobility was well reproduced with the old model. Additionally, in both models the scattering angle closely agrees with Rutherford's result over the complete range of impact parameters in the case of a repulsive interaction with a negative ion. For attractive interactions, significant underestimation of the scattering angle is seen at small impact parameters. This is as a result of the limited interaction at close range that reduces the artificial carrier trapping in DD and MC simulations. This reduced interaction also results in more accurate integration of the equation of motion of carriers in attractive potentials by reducing the variation of the field over each propagation step. It is clear that the *ab initio* interaction with a single charge is well reproduced when using the mesh resolved DG effective quantum potential, so long as the mesh spacing is of the order of $1nm$ or below.

4.1.4 The Concentration Dependent Bulk Mobility

The second stage in the validation involves the reproduction of experimental concentration dependent bulk mobility. This was previously achieved through the simulation of a series of atomistically doped resistor structures [33]. These covered a wide range of doping concentrations in simulation domains containing approximately 15,000 discrete dopants to ensure self-averaging and bulk-like properties. However, such simulations using the effective quantum potential are limited by practicality to small, highly doped simulation domains due to the upper limit of $1nm$ on the mesh spacing.

Following the methodology described in [33] self-consistent simulations of a series of atomistic N+NN+ resistors, illustrated in figure 4.9, with bulk doping of 2×10^{18} cm^{-3}, 5×10^{18} cm^{-3} and 8×10^{18} cm^{-3} have been performed. These doping concentrations are relevant to the channel doping in modern nanoscale bulk MOSFETs. These resistors are simulated with contact regions with doping of 10^{19} cm^{-3}. The numerically affordable volume of the simulation domain contains on average only 250, 625 and 1000 dopant atoms for each level of doping.

Drift diffusion simulations with density gradient quantum corrections were initially performed for each resistor in order to obtain the quantum correction term necessary for MC simulation. A bias was applied across each resistor such that a field of approximately $1kV/cm$ accelerated carriers in the central region. The DD simulation results

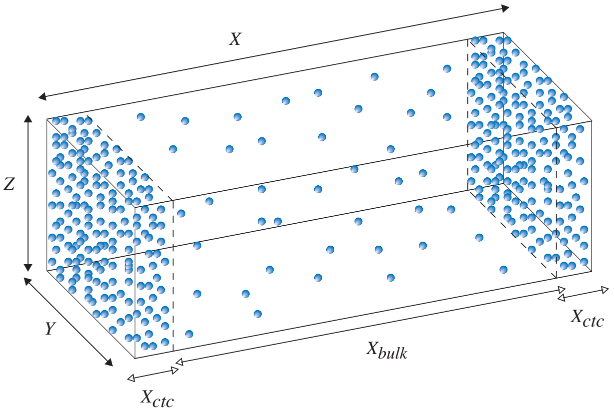

FIGURE 4.9: Schematic 3D atomistic simulation structure for recovery of bulk mobility. The central doped region (three cases : 2×10^{18} cm^{-3}, 5×10^{18} cm^{-3} and 8×10^{18} cm^{-3}), length $X_{bulk} = 200$ nm, is the concentration under investigation and is situated between two more heavily doped contact regions (10^{19} cm^{-3}), length $X_{ctc} = 10$ nm.

were transferred into the 3D MC simulator and the quantum corrected MC simulation with *ab initio* impurity scattering were performed.

The classical electrostatic potential obtained from DD is compared with the effective DG quantum potential for one such simulated structure in figure 4.10. It can be clearly seen that the effective quantum potential reduces the peaks associated with the donor impurities and limit their interaction with electrons as expected.

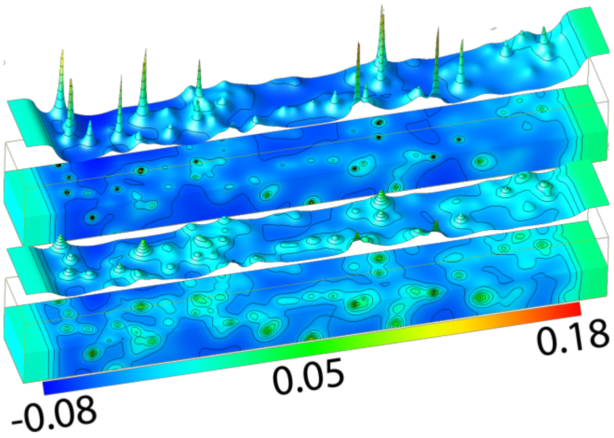

FIGURE 4.10: Classical (top) and effective quantum (bottom) potential in an atomistic resistor with central doping of $2 \times 10^{18} cm^{-3}$.

Due to the small number of dopant atoms in each simulated device, bulk mobility was estimated by averaging 10 different MC simulations with unique random dopant configurations for each level of 'bulk' doping. Values for the average field and average velocity within the central region were extracted for each device over the range of 'bulk' doping concentrations. The average mobility was obtained as the ratio of velocity and field of different of doping levels using equation (3.12).

The simulated mobility is plotted in figure 4.11 and compared with experimental data and *ab initio* results [33] obtained using the short-range correction approach. Good agreement is achieved with experimental data and with the trend of the prior simulation results. The simulated mobility shows the correct trend of a reduction in mobility with increasing doping concentration. This gives confidence in the DG effective potential approach for treating position dependent scattering from discrete random dopants. Still the estimated mobility does not fall off rapidly enough with increasing doping concentration when compared with experimental data. This may be associated with the limited size of the simulated structures restricting the number of dopant atoms and making the comparison with bulk properties difficult.

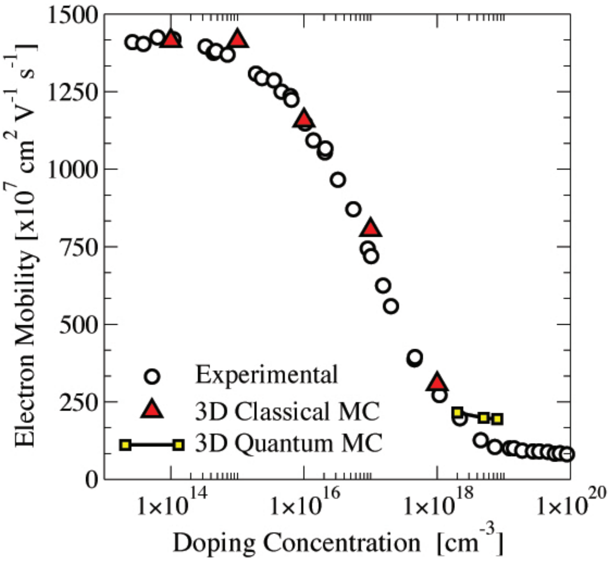

FIGURE 4.11: Simulated bulk mobility at $2 \times 10^{18} cm^{-3}$ using the mesh-based effective quantum potential from density gradient. Agreement with experimental data [115] is seen and extends the original *ab initio* 3D MC Classical results of [33].

This simulation of bulk concentration dependent mobility is limited by the size of the solution domain it is practical to simulate. Accurate results require as large a solution domain as possible in order to include as many dopants as possible to recover the self-averaged scattering that defines the bulk problem. The solution domain here has been chosen to maximise the number of dopants and the carrier trajectory in order to best approximate a bulk material. However, it is noted that the cross section of the simulated resistors is therefore limited to only 20×20 nm^2. As seen from the simulated results of

Rutherford scattering using both classical short-range corrected and quantum potentials, the scattering angle of attractive interactions is significantly underestimated for impact parameters below around 5nm. Concentration dependent mobility was nonetheless well reproduced with the classical potential and short-range corrections up to concentrations of 1×10^{18} cm^{-3} [33], suggesting that the longer interactions were dominant. The same would be expected here, except that such long range interactions are almost ruled out in two of the three dimensions by the solution domain. Additionally, the imposed Neumann boundary conditions will effect the local Coulomb potential near the boundaries. Despite this, mobility results are close to experimental results and prior classical simulation. Taken together with the agreement of the simulated Rutherford scattering, this provides additional credibility to the quantum potential interaction.

4.2 Drain Current Variability Simulation strategy

4.2.1 Scaled Devices Simulation Strategy

Having been satisfied that the unified quantum potential approach to ionized impurity scattering accurately reproduces experimental bulk mobility in the doping concentration range of interest, we apply it to the *ab initio* MC simulations of random dopant induced drain current variability in a series of realistically well-scaled n-channel bulk MOSFETs.

The scaling process was based on a 35-nm MOSFET reported by Toshiba in 2001 [191]. The continuous doping profile was obtained from carefully calibrated and comprehensive process simulation using Taurus Process [192]. This device was scaled to gate lengths of 25, 18, 13, and 9 nm,as shown in figure 4.12. The scaling process carefully followed the prescription of the ITRS [193] in order to meet the requirements for oxide thickness, junction depth, doping, and supply voltage. The resulting realistically well-scaled devices have been used in previous DD simulation studies and are described in detail elsewhere [26]. The corresponding basic device parameters including the channel length, equivalent oxide thickness and junction depths x_j of the extensions are summarized in table 4.1 [26]. The comparison betweeen experimental and simulated $I_D - V_G$ characteristics at $V_G = 850mV$ is presented in 4.13 [26].

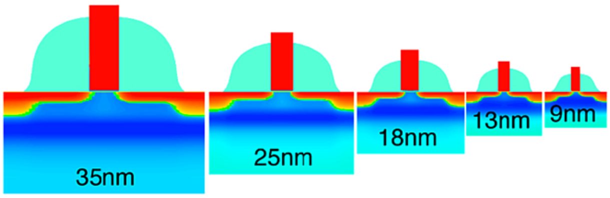

Figure 4.12: Examples of realistic conventional MOSFETs scaled from a template 35 nm device according to the ITRS requirements for the 90 nm, 65 nm, 45 nm, 32 nm and 22 nm technology generations, obtained from process simulation with Taurus Process [36].

Channel Length $[nm]$	35	25	18	13	9
Equivalent Oxide Thickness $[nm]$	0.88	0.65	0.5	0.43	0.35
Junction depth, x_j $[nm]$	20	13	9	8	6

Table 4.1: Table of Device Design Characteristics including channel lengths, EOT and junction depth [26].

For each of the scaled devices described above, ensembles of 50 atomistic devices with randomly configured substrate doping were generated. For the purpose of this work, the

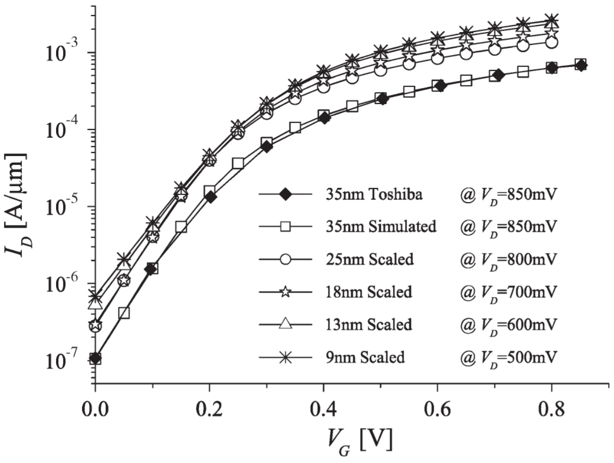

FIGURE 4.13: Simulated $I_D - V_G$ characteristic of the well scaled devices at drain voltages and measured $I_D - V_G$ characteristics of the 35 nm MOSFET [26].

effect of variation within the channel doping was of key interest and so in all simulated devices the source/drain doping was treated as continuous.

Simulations were performed at a high gate bias of 0.80V and at both low and high drain biases of 0.01V and 0.80V respectively. An initial DD solution with DG quantum corrections was performed to obtain the quantum correction term, defined as the difference between the classical quantum potential, applied throughout MC simulation (see section 4.1). The DD solution was also used as an initial solution from which the MC proceeded. A uniformly doped reference device was similarly simulated for each ensemble to allow the percentage variation in drain current to be determined as follows

$$\Delta I_D^i = \frac{I_D^i - I_D^u}{I_D^u} \times 100\% \tag{4.8}$$

where $I_{D\ DD}^i$ is the drain-current obtained from simulation of the ith atomistic device and I_D^u denotes the drain-current obtained from simulation of the uniformly doped device.

Self-consistent 3D MC simulations were then performed for the same ensembles of devices, including the continuously doped reference devices. As described above in section 4.1, the quantum correction was applied to the classical potential solution at every time step in order to recover a quantum corrected mesh potential. Interpolation of the field derived from this potential was used as the sole driving force within MC simulation in order to account for both confinement effects and the full electron-acceptor interaction.

Ridley's third-body interference scattering rate [154, 155] was applied for the simulation of the continuously doped reference devices and for the continuously doped source/drain regions in the atomistic ensembles.

The variation in drain-current for each device in each ensemble, estimated from MC with respect to the uniformly doped reference devices, is then determined identically to the DD case using 4.8.

The standard deviation of the drain-current variation for physical and percentage values obtained from both DD and MC simulations were then determined for each of the scaled devices at each drain bias. The comprehensive statistical analysis of on current variations is reported in the next chapter.

4.2.2 DD and MC Results and Discussion

4.2.2.1 Random Discrete Dopants Effects on Potential Distribution

Potential distributions illustrative of the self-consistent 3D MC simulation are shown for the 35 nm devices with the greatest and least currents within the ensemble in figure 4.14. Individual acceptors are represented by blue spheres and the localised reduction in potential is evident around them. The variation in potential within the peak of the inversion layer is illustrated using the 2D surface plot accompanying each figure. Similar potential profiles for the 18-nm and 9-nm devices are shown in figures 4.15 and 4.16 respectively.

4.2.2.2 Random Discrete Dopants Effects on Electron and Current Density Distribution

Figure 4.17 shows the simulated electron concentration from source to drain (left-right) and the corresponding current density within the peak of the inversion layer from MC simulation. The reduction in electron concentration principally around acceptors and otherwise extended throughout the channel is seen in the low current device (right) when compared with the highest current device (left) where few acceptors are present. The electron concentration within channel of the highest current device is on average ten times higher than in the low current case.

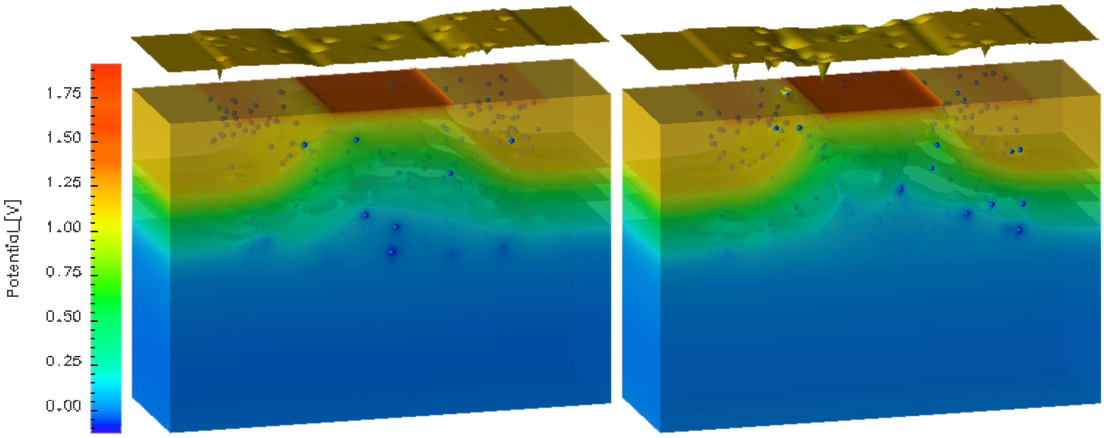

FIGURE 4.14: Potential distribution within the channel and substrate for 35 nm atomistic devices with (left) highest, and (right) lowest current. Variation in the channel potential due to the unique atomistic dopant distributions is clearly seen.

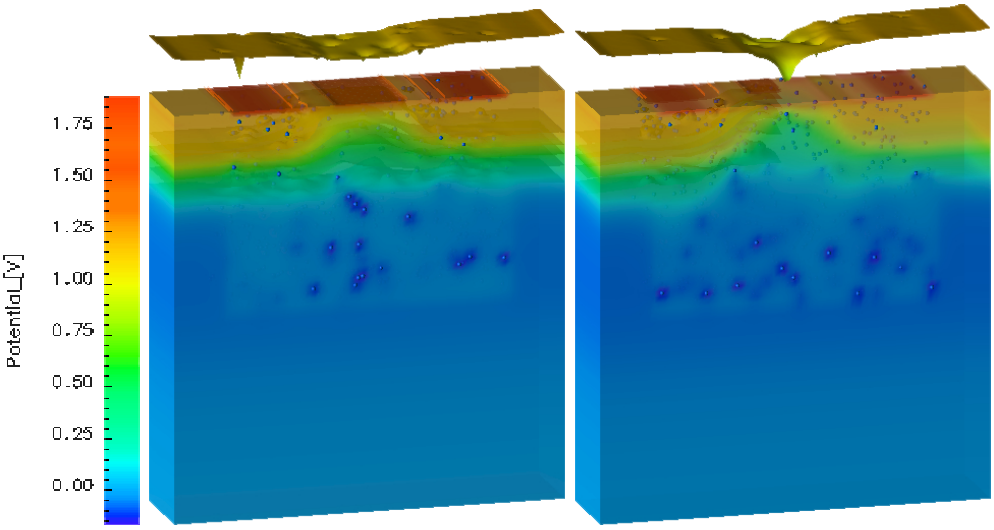

FIGURE 4.15: Potential distribution within the channel and substrate for 18 nm atomistic devices with with (left) highest, and (right) lowest current.

The literature has shown [33, 194] that acceptors lying near the source/channel edge play a significant role in current reduction due to the increased scattering of low energy carriers there. The potential variations within the inversion layer of the lowest current device, presented at the top of the right picture in figure 4.14, clearly shows a crowd of dopants near the source region. This line of dopants across the width of the device efficiently impede current flow and is responsible for the greatly reduced current. The effect however is extended, reaching out with the screened impurity potential. In particular, the acceptors near the source and lying close to the inversion layer backscatter electrons into the source region and impact on the current far greater than the localised

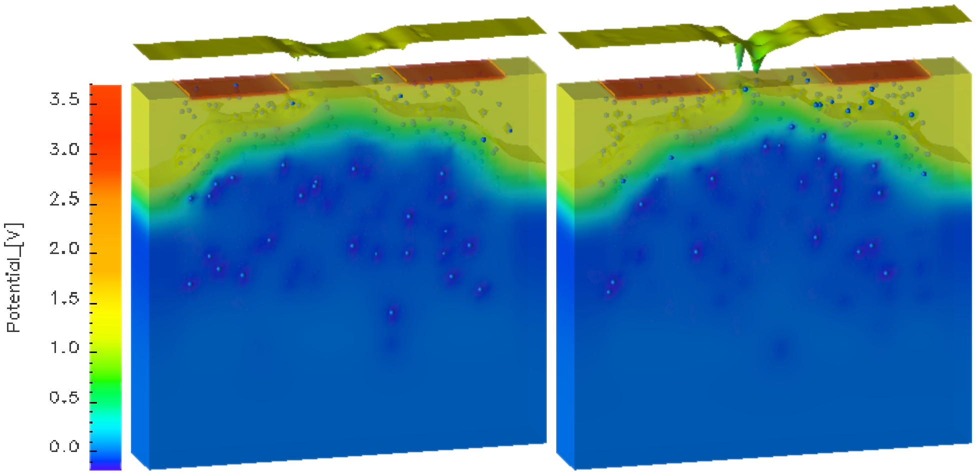

FIGURE 4.16: Potential distribution within the channel and substrate for 9 nm atomistic devices with (left) highest, and (right) lowest current.

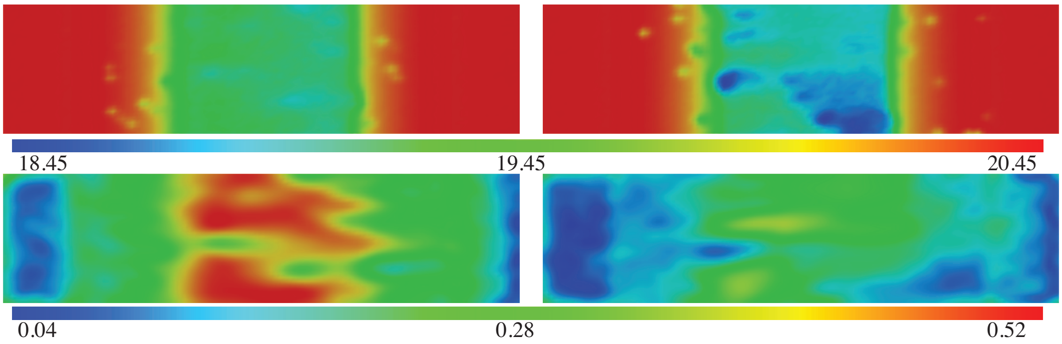

FIGURE 4.17: Electron concentration (top) [$\log_{10}(\mathrm{cm}^{-3})$] and current density (bottom) [$\mathrm{mA}\mu\mathrm{m}^{-2}$] within the inversion layer of devices with the highest (left) and lowest (right) current. Clearly seen are the effects of individual acceptors.

potential reduction. In this case the positioning of the dopants as well as their number effect the current in MC. This is contrasted with the lack of acceptors near the source within the high current device which creates large 'un-doped' regions. The impact of this on current flow can be seen through the greatly increased current density in figure 4.17. Local reductions in current density associated with individual acceptors can still be seen.

Figures 4.18 and 4.19 similarly show results for the 18-nm and 9-nm devices. Within the 18-nm device, current is largely impeded within the lowest current device by a number of acceptors directly within the peak inversion layer concentration. They are responsible for a large potential barrier in figure 4.15 and the associated reduction in electron concentration is clearly seen in figure 4.18. Current is then forced to flow through a greatly narrowed channel. Similar observations are made in the 18-nm device with highest current, but in this case the acceptors that effect the current are somewhat displaced from the peak inversion layer concentration and their effect on the potential barrier, electron concentration and, ultimately, current is reduced.

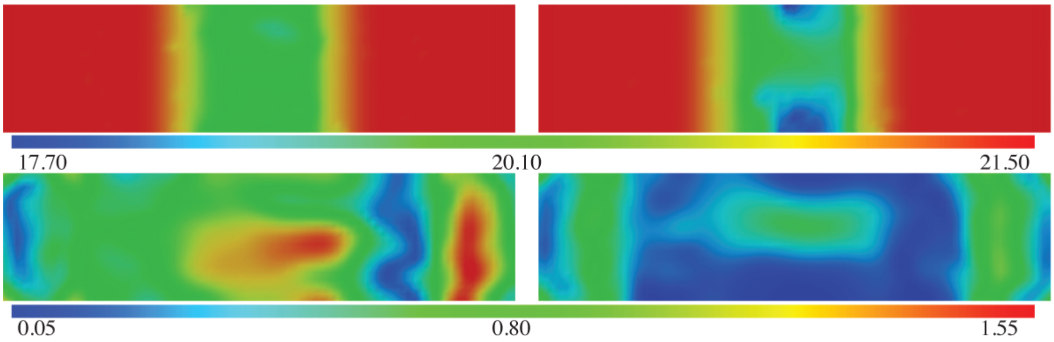

FIGURE 4.18: Electron concentration (top) [$\log_{10}(\text{cm}^{-3})$] and current density (bottom) [mAμm^{-2}] within the inversion layer of devices with the highest (left) and lowest (right) current. Clearly seen are the effects of individual acceptors.

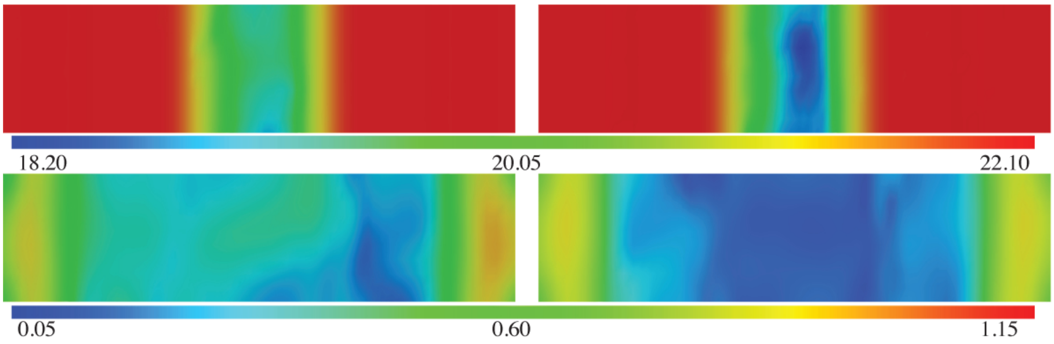

FIGURE 4.19: Electron concentration (top) [$\log_{10}(\text{cm}^{-3})$] and current density (bottom) [mAμm^{-2}] within the inversion layer of devices with the highest (left) and lowest (right) current.

4.3 Conclusions

An efficient method to unify quantum corrections with an accurate description of bulk carrier-ion interactions via the density gradient quantum potential has been presented for use within finely discretized 3D selfconsistent Monte Carlo simulation. The carrier-ion treatment was shown to be analogous to previously reported methods based upon a classical potential with short-range correction and yielded consistent results. The method was applied to realistically study random dopant induced drain current variations in a series of scaled devices, highlighting additional variation due to reduced screening when quantum effects are taken into account.

The impact of individual acceptors within the channel is clearly demonstrated through reduced carrier concentration and modulated current density. This effect is more evident in quantum corrected simulations compared with previous classical results. The effect of quantum corrections increases the current variation in both DD and MC. This is attributed to reduced screening of the channel impurities due in part to reduced inversion layer density compared with classical simulations and importantly to the inherently reduced screening density associated with the density gradient solution surrounding a point charge. The reduced screening significantly effects ionized impurity scattering and thus transport variation. This is seen in the significant increase in variation from quantum corrected MC compared with classical results [33].

Chapter 5

DRAIN CURRENT VARIABILITY: STATISTICAL ANALYSIS

The first section of this chapter discusses the comprehensive statistical analysis of the results from the simulation of the MOSFET set describe in chapter 4. In the second section the comprehensive statistical results of on current variability of scaled devices is presented. The following section presents the summary of drain current variability results. The fourth section describes theoretical models which separate the overall drain current variations into the electrostatic and transport variation components. Finally, the conclusions are drawn in the last section.

5.1 Statistical Analysis Strategy

The comprehensive statistical analysis strategy is applied separately to each scaled device at both high and low drain bias. Initially, the statistical analysis is performed at low drain bias and divided into the following steps: In the first step, we investigate the basic statistical parameters such as mean, standard deviation, skew and kurtosis. Secondly, we introduce the statistical confidential intervals to assess the accuracy of simulation results, and, finally, we perform one graphical and two analytical normality tests.

The same analysis is carried out at high drain conditions. The statistical analysis of each device concludes with the statistical investigation of the percentage drain current variations.

5.1.1 Basic Statistics

We start with a basic statistical parameters calculation. The mean (μ) and standard deviation (σ) values are computed with corresponding error terms. In order to better define the distribution of drain current variations for both DD and MC results, the higher moments of the distributions are calculated. Knowledge of the higher moments is equivalent to more accurate knowledge of the distribution function and allows the distribution function to be expressed in terms of these moments [195].

The skew (γ_1) and kurtosis (γ_2) [195] which are related to as the third and the fourth order normalized moments of the distribution respectively are calculated. The skewness gives indication of the extent of departure from symmetry. Its positive values indicate that the distribution is shifted to the right of the mean, while its negative values imply that the distribution is shifted left of the mean. The kurtosis provide indication for the shape of distribution around its mode or peak. Positive values of kurtosis indicate the more sharply peaked, so-called leptokurtic, distribution, while its negative values imply the more flat-topped distributions, termed as platykurtic. A normal distribution has zero skewness and a kurtosis of three which is sometimes normalized by subtracting three, therefore, its value is zero, hereafter we will refer to its normalized value. The skew and kurtosis of DD and MC results are compared with the moments of a univariate standard normal distribution in order to find the resemblance between simulation results and a normal distribution.

5.1.2 Confidence Intervals

Estimation of statistical parameters bears some amount of uncertainty which may be expressed in terms of the sampling variance or the standard error of the estimator. For this purpose, the construction of the confidence interval θ of a statistical parameter is added to the comprehensive statistical analysis in order to indicate reliability. Within this work, the statistical parameter θ is determined for the sample mean, sample standard deviation, sample skewness and sample kurtosis. The confidence interval of a given statistical parameter provides additional information about the distribution function since they rely only on the frequency theory of probability [196].

In practice, the construction of confidence intervals requires two quantities t_0 and t_1, such that for all θ it holds that

$$P(t_0 \leq \theta \leq t_1) = 1 - \alpha \tag{5.1}$$

where α is the chosen significance level [196]. Within this work a value of $\alpha = 0.05$ is used unless it is stated otherwise. This asserts that θ lies in the interval between t_0 and t_1, which are the lower and upper bound of a confidence interval for parameter θ, respectively. The procedure for the construction of the standard approximate interval that will be used for the comparison is described next.

The standard approximate interval may be expressed as

$$\theta \in [\widehat{\theta} + \widehat{\sigma} z^{(\alpha)}, \widehat{\theta} + \widehat{\sigma} z^{(1-\alpha)}] \tag{5.2}$$

where θ is some real-valued parameter, $\widehat{\theta}$ is its maximum likelihood estimate (MLE), $\widehat{\sigma}$ is the above mentioned uncertainty of $\widehat{\theta}$ expressed as an estimate of its sample standard deviation, $z^{(\alpha)}$ is the $100.\alpha$ percentile of the standard normal distribution, which for $\alpha = 0.05$ gives $z^{(\alpha)} = -z^{(1-\alpha)} = -1.645$.

It should be noted that the small sample size of 50 simulation results for each set may cast doubt on the statistical analysis used to invoke asymptotic results [197, 198]. A reliable analysis of the confidence intervals for the simulation results necessitates that accurate statistical techniques are used, owing to the small sample sizes. To this end, accurate nonparametric methods, which are capable of handling small sample sizes, are used throughout this analysis and discussed next.

The confidence interval is constructed by using the concept of the bootstrap introduced by Efron [199–201]. The bootstrap requires almost no assumptions about the statistical cumulative distribution function of the simulation results and their estimated parameters. This assigns the bootstrap to the family of nonparametric methods. The general concept may be briefly described with respect to the simulation results specific to this work as follows.

It is assumed that the simulated drain current data are independent observations from some unknown probability distribution denoted as F. $\widehat{F}$ may be estimated by an empirical probability distribution giving a mass $1/n$ to each observed data point. For example, we make 50 random draws with replacement from the sample of 50 simulated drain currents and recompute the statistics of interest. In doing so the observations from the simulation sample are randomly reassigned and, thereafter, a new estimate for the statistics obtained. This process is repeated to yield a distribution in the original observed statistic, collectively termed the bootstrap replication statistics [200]. Using the above process, for each simulation sample a distribution size of 1000 for each statistic of interest is obtained from which the nonparametric confidence intervals can be derived.

The nonparametric ABC method (”ABC” standing for approximate bootstrap confidence intervals) [197] is deployed to obtain sufficient accurate nonparametric confidence intervals. This method corrects the deficiency of the standard method, making the nonparametric ABC intervals second-order accurate as well as second-order correct [197, 198]. The nonparametric ABC algorithm is described in [197] and will not be discussed here. Simultaneously with the calculation of the nonparametric confidence interval the $R\backslash L$ ratio, defined as the ratio of the right side of the interval, measured from the estimated parameter, to the left side, is calculated. The $R\backslash L$ ratio of the nonparametric confidence interval is compared to the standard normal approximate which produces symmetric confidence intervals. This gives some indication of the extent to which the observed distribution of the simulation results differs from the normal distribution.

5.1.3 Normality Tests

Firstly, the nonparametric confidence intervals might be used to assess the naive normality test which would determine whether the simulation results come from a univariate normal distribution. Secondly, the proper tests for univariate normality of simulation results are carried out using one graphical and two analytical tests. The general test of normality may be described as follows.

Let $\mathcal{N}$ denote the family of univariate normal distributions and $\widehat{F}$ represents the empirical distribution of simulation results. The hypotheses of interest are $H_0 : \widehat{F} \in \mathcal{N}$, the so-called null hypothesis, and $H_1 : \widehat{F} \notin \mathcal{N}$, termed the alternative hypothesis. Two types of error can occur in statistical testing; a Type I error occurs if the null hypothesis is rejected when in fact it is true, a Type II error occurs if the null hypothesis is not rejected when in fact it is false. An upper bound on the probability of Type I error is called α and denotes the significance level of a test. Within this work, we set the significance level $\alpha = 0.05$ for normality tests.

In order to test normality within the above confidence interval, the following hypothesis structure is constructed. The null hypothesis is $H_0 : \widehat{\theta} = 0$ and the alternative hypothesis is $H_1 : \widehat{\theta} \neq 0$, where $\widehat{\theta}$ represents the sample estimated skew and kurtosis. The null hypothesis states that if the skew and kurtosis of the simulated results is zero, the sample data may have come from a normal distribution. The confidence interval $100.(1 - \alpha)\%$ defines the interval containing of all those value $\widehat{\theta}$ for which the null hypothesis is not rejected at given significance level of $100.\alpha\%$. If the zero value of skewness and kurtosis lies in the 95% confidence interval, then we accept the null hypothesis for both estimated statistics.

For the graphical normality test the Q-Q plot is used, which is obtained as follows. Firstly, the drain current values are ordered in ascending order such that $I_D^1 < I_D^2 < ... < I_D^{50}$. Secondly, the proportions of observations that are the less than I_D^i is estimated by $(i - 0.5)/50$, where 0.5 is subtracted to correct for continuity. These proportions are assumed to be percentiles or probability levels for the cumulative standard normal distribution. Subsequently, the corresponding theoretical quantiles of the normal distribution are computed. Finally, we plot theoretical quantiles against ordered drain current values in order to construct the Q-Q plot. A linear plot indicates normal distribution of observations and a nonlinear plot shows their non-normal distribution.

The graphical normality test using Q-Q plot is, however, subjective as the plot has to be visually inspected in order to establish whether it is linear or not. In order to accurately confirm the graphical and the confidence interval normality test, two further analytical tests, the Shapiro-Wilk [203] and Jarque-Bera [204] tests, are preformed. In order to accept or reject the null hypothesis in these tests the chosen α to p-value, which is the probability computed by the test, is compared. If the p-value is less than the chosen α then the H_0 is rejected otherwise it is accepted.

5.2 Results and Discussion Of On Current Variability of Scaled Devices

Here we present the comprehensive statistical analysis of the simulation results for the 35 nm tansistor. To avoid repetition the equivalent analysis of the results for the 25 nm, 18 nm, 13 nm, and 9 nm transistors are given in appendices.

5.2.1 Descriptive Statistical Results at Low Drain Bias

For all devices, the DD simulations at low drain bias result in larger currents when compared with the equivalent MC results. This is associated with calibration of the mobility models within the DD to produce a physically realistic and optimally performing device that mimics the effects of strain. The effect of strain and the corresponding mobility enhancement are however not included within the MC simulation. The mean current (μ) over the 50 atomistic DD devices is approximately 50% higher compared the mean from MC. The values for the mean drain currents obtained from DD and MC at low drain bias are $\langle I_{D\ DD} \rangle = (9.17 \pm 0.06) \times 10^{-5} A\mu m^{-1}$ and $\langle I_{D\ MC} \rangle = (6.1 \pm 0.1) \times 10^{-5} A\mu m^{-1}$, respectively. However, the standard deviation (σ) in the drain current is of most interest in this study. The standard deviation associated with the DD simulated ensemble is $\sigma I_{D\ DD} = (4.6 \pm 0.5) \times 10^{-6} A\mu m^{-1}$ while that from MC is nearly twice as large, with a value of $\sigma I_{D\ MC} = (8.4 \pm 0.8) \times 10^{-6} A\mu m^{-1}$.

The higher DD on current value is due to the calibration of mobility models within the DD simulator against real device data [191] in order to obtain the desired set of device characteristics. The real device encompasses all physical phenomena including strain but the DD simulator can mimic how strain affects the current through the mobility models. The lower values of on-current produced by the MC simulator is due to the omission of strain effects, as mentioned above. The impact of the simplest strain in MC simulations can be included through the band structure via a lowering of the two-fold valleys consistent with the application of strain and a recalibration of the deformation potentials. [117, 202]. These, in turn, affect the scattering (through shifts in band energies and phonon scattering rates) and propagation (through the change in masses) of electrons and ultimately the current.

MC captures significantly larger variation in the drain current compared with DD. This additional variation is associated with variations in position dependent scattering between devices and is an effect in addition to the electrostatic modulation of carrier density that is alone responsible for the variation in DD.

33 and 32 of the 50 devices from DD simulations and from MC simulations, respectively, have drain current values within the range of σ from the mean. Almost all devices from both DD and MC simulations lie within the range of 2σ, which corresponds approximately to a 95% confidence interval, while only two from DD and one from MC simulations fall far outside the range of 2σ. Thus, both DD and MC results at low drain bias show moderate variability across the sample.

It is noted however that since the values of drain currents obtained from DD significantly differs from those of MC, the standard deviation normalised by their respective mean values should be comapred. These values hereafter referred to as the coefficient of variation, are obtained as $CV = (\sigma \setminus \mu) \times 100\%$. The coefficient of variation for MC is obtained as $CV = 13.8\%$, while DD only has $CV = 5.0\%$. CV coefficient indicates the higher variations in MC results than in DD. This is important as it highlights the relative variability increase associated with transport variation over and above electrostatic variation.

The distribution of DD results is negatively skewed ($\gamma_{1\ DD} = -0.38$) while the distribution of MC data is positively skewed ($\gamma_{1\ MC} = 0.06$). Both distributions of DD and MC results are platykurtic ($\gamma_{2\ DD} = -0.27$ and $\gamma_{2\ MC} = -0.74$). In both cases, the skewness indicates little departure from symmetry and kurtosis shows small flat-topped shape.

95% confidence intervals of mean, standard deviation, skewness and kurtosis of the drain current obtained from both DD and MC simulations at low drain bias are presented in table 5.1. The confidence interval of $\langle I_{D\ MC} \rangle$ (μ in table) indicates very little departure from asymmetry compared with the standard normal approximation since its $R \setminus L$ ratio is close to one. The confidence interval of $\langle I_{D\ DD} \rangle$ has modest asymmetry of the interval since $R\backslash L$ value is modestly less than one. Both DD and MC nonparametric confidence intervals of their mean values show very little departure from the standard normal approximation.

The confidence interval of $\sigma I_{D\ MC}$ (σ in table) indicates modest departure from the asymmetry compared with the standard normal approximation. This is also seen in the confidence interval of $\sigma I_{D\ DD}$. The above mentioned indications and observations might lead to the inference that the true population distributions for DD and MC simulation results come from the normal distribution. From the table 5.1, it is clearly seen that the zero value of skewness and kurtosis for both DD and MC simulation results lie within the range of the 95% confidence interval. This is in favour of accepting the null hypothesis for both skewness and kurtosis.

	35 nm Device : Simulations at Low Drain Bias			
	DD		MC	
	95% Confidence Interval	$R\backslash L$	95% Confidence Interval	$R\backslash L$
$\mu\ [A\mu m^{-1}]$	$[9.04, 9.29] \times 10^{-5}$	0.93	$[5.85, 6.31] \times 10^{-5}$	1.01
$\sigma\ [A\mu m^{-1}]$	$[3.81, 5.43] \times 10^{-6}$	1.25	$[7.17, 9.73] \times 10^{-6}$	1.23
γ_1	$[-1.09, 0.45]$	1.14	$[-0.63, 0.82]$	1.11
γ_2	$[-0.92, 0.62]$	1.75	$[-1.18, -0.03]$	1.89

TABLE 5.1: 95% nonparameric ABC confidence interval of mean value, standard deviation, skewness and kurtosis compute for 35 nm device at low drain bias.

Q-Q plots for DD and MC simulation results at low drain bias are illustrated in figure 5.1. In the DD plot (left) of figure 5.1, two outliers are evident at the low end of the range. In the MC plot (right) of figure 5.1, one outlier is evident at the high end of the range. Both plots are to a very good approximation linear, suggesting that the data are normally distributed. However, the plots deviate from true linear behaviour due to small sample size.

DD results have the Shapiro-Wilk test statistics $W = 0.97$ and its p-value $= 0.28$ while the Jarque-Bera test statistics $JB = 1.40$ and its p-value$= 0.50$. For MC results, the Shapiro-Wilk test statistics $W = 0.98$ and its p-value$= 0.64$ while the Jarque-Bera test statistics $JB = 1.31$ and its p-value $= 0.52$. In all cases, the p-values are greater than the chosen significance level $\alpha = 0.05$ so we finally accept the null hypothesis that DD and MC simulations results come from a normally distributed population.

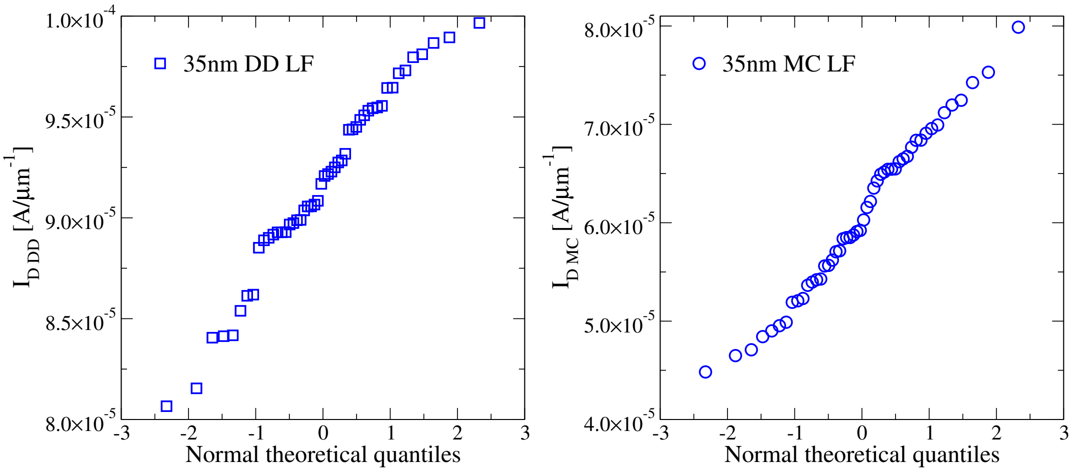

FIGURE 5.1: Q-Q plot for DD (left) and MC (right) simulation results at low drain bias for the 35nm scaled device.

5.2.2 Descriptive Statistical Results at High Drain Bias

Analysis of the results at high drain bias follows analogously to those presented above for low drain bias. In general it is noted that, for all devices, the DD simulations at high drain bias result in larger currents when compared with the equivalent MC results. This is again due to calibration of the DD mobility models and the desire to reflect strain induced mobility enhancements not captured within the MC simulator. The mean current associated with DD over the 50 devices is approximately 3.5 times greater than that from MC, with values of $\langle I_{D\ DD}\rangle = (3.78 \pm 0.05) \times 10^{-3} A\mu m^{-1}$ and $\langle I_{D\ MC}\rangle = (1.03 \pm 0.02) \times 10^{-3} A\mu m^{-1}$, respectively. The standard deviation in the drain current calculated from DD is $\sigma I_{D\ DD} = (3.2 \pm 0.3) \times 10^{-4} A\mu m^{-1}$, while that from MC is $\sigma I_{D\ MC} = (1.4 \pm 0.1) \times 10^{-4} A\mu m^{-1}$. The coefficient of variation for MC is obtained as $CV = 13.3\%$, while DD only has $CV = 8.6\%$. The CV coefficient indicates the higher variations in MC results than in DD.

33 and 30 of the 50 devices from DD and MC simulations respectively have drain current values within the range of σ from the mean. Almost all devices from both DD and MC simulations lie within the range of 2σ, which corresponds approximately 95% confidence interval, while only one from both DD and MC simulations fall far outside the range of 2σ. Thus, both DD and MC results at high drain bias show moderate variability across the sample.

Both DD and MC distribution of drain currents are negatively skewed ($\gamma_{1\ DD} = -0.25$ and $\gamma_{1\ MC} = -0.26$), and both distributions are platykurtic ($\gamma_{2\ DD} = -0.48$ and $\gamma_{2\ MC} = -0.35$). In both cases, the skewness indicates little departure from symmetry and kurtosis shows a small flat-topped shape.

Table 5.2 presented the confidence intervals of the estimated statistical parameters obtained from DD and MC simulation results at high drain bias. The confidence intervals of $\langle I_{D\ MC}\rangle$ and $\langle I_{D\ DD}\rangle$ indicates very little departure from asymmetry compared with the standard normal approximation since $R\backslash L$ ratio values are somewhat less than one. The confidence intervals of $\sigma I_{D\ MC}$ and $\sigma I_{D\ DD}$ indicate moderate departure from asymmetry compared with the standard normal approximation since $R\backslash L$ ratios are moderately higher than one.

	35 nm Device : Simulations at High Drain Bias			
	DD		MC	
	95% Confidence Interval	$R\backslash L$	95% Confidence Interval	$R\backslash L$
μ $[A\mu m^{-1}]$	$[3.68, 3.86] \times 10^{-3}$	0.95	$[0.99, 1.06] \times 10^{-3}$	0.95
σ $[A\mu m^{-1}]$	$[2.74, 3.83] \times 10^{-4}$	1.37	$[1.14, 1.62] \times 10^{-4}$	1.32
γ_1	$[-1.06, 0.51]$	0.92	$[-1.06, 0.60]$	1.11
γ_2	$[-1.11, 0.54]$	1.96	$[-0.95, 0.55]$	1.88

Table 5.2: 95% nonparameric ABC confidence interval of mean value, standard deviation, skewness and kurtosis compute for 35 nm device at high drain bias.

Further, the table 5.2 shows that the zero value of skewness and kurtosis of DD and MC simulation results lie within the range of the 95% confidence interval. This leads to acceptance of the null hypothesis of the confidence interval normality test for both skewness and kurtosis. This in turn means that data may be drawn from a normally distributed population.

Further, and analogous with the previous low bias case, the normality of data from DD and MC simulation results at high drain bias was investigated using Q-Q plots. These are illustrated in figure 5.2. In the DD (left) plot of figure 5.2, one outlier is evident at the low end of the range while in the MC (right) plot one outlier is evident at the high end and one at the low end of the range. Both plots are approximating linear, suggesting that the data are normally distributed. The plots are not completely linear, again due to small sample size.

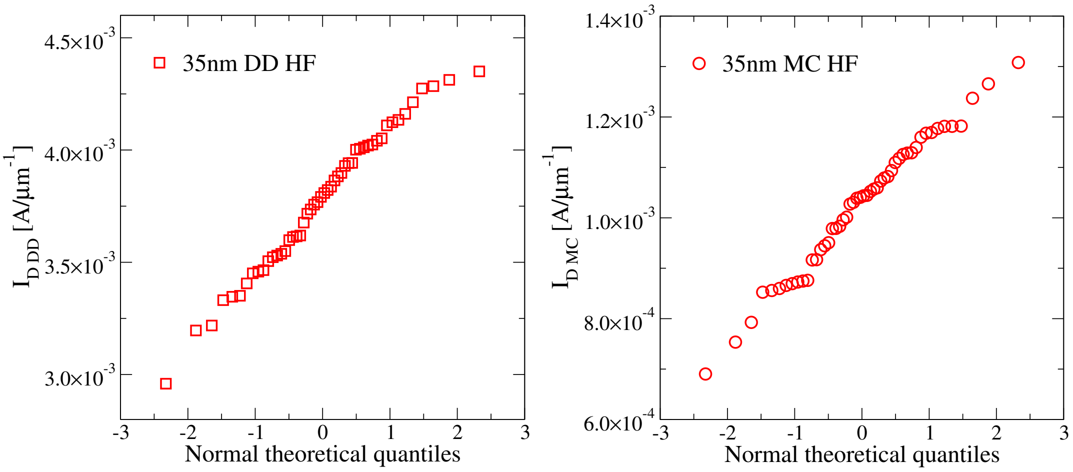

FIGURE 5.2: Q-Q plot for DD (left) and MC (right) simulation results at high drain bias of 35nm device.

Table 5.3 presents the normality test results from the Shapiro-Wilk and Jarque-Bera tests. DD results have the Shapiro-Wilk test statistics $W = 0.9822$ and its p-value $=$ 0.6493 and the Jarque-Bera test statistics $JB = 1.13848$ and its p-value= 0.566. MC results have the Shapiro-Wilk test statistics $W = 0.9831$ and its p-value= 0.6887 and the Jarque-Bera test statistics $JB = 0.9351$ and its p-value= 0.6265. For all cases, the p-values are greater than the chosen significance level $\alpha = 0.05$ so we again accept the null hypothesis that DD and MC simulations results come from a normally distributed population.

	35 nm Device : Simulations at High Drain Bias			
	Normality test			
	DD		MC	
	Test Statistics	p-value	Test Statistics	p-value
Shapiro-Wilk	0.98	0.65	0.98	0.69
Jarque-Bera	1.14	0.57	0.94	0.63

TABLE 5.3: Normality test for 35 nm device at high drain bias.

5.2.3 DD versus MC : Percentage Change in Current

The percentage change in current from the uniform device for both DD and MC at both low and high drain biases is next determined. $I^u_{D\ DD}$ in equation (4.8) is substituted with the uniform drain current value $9.30 \times 10^{-5} A\mu m^{-1}$ obtained from DD simulation at low drain bias, and with value $3.88 \times 10^{-3} A\mu m^{-1}$ at high drain bias. Similarly $I^u_{D\ MC}$

in equation (4.8) is substituted with the uniform drain current value $6.04 \times 10^{-5} A\mu m^{-1}$ obtained from MC simulation at low drain bias, and with value $1.12 \times 10^{-3} A\mu m^{-1}$ at high drain bias. From this it can be seen that DD simulation of the atomistic devices results in an average current that is less than that obtained from the uniform device in both cases, while MC simulation shows a reduction in the average current only at low drain bias. Despite this difference, the variation in current between devices is largely reproduced between both simulation models. This is clearly seen in the scatter plots, presented in figure 5.3, of the percentage change in current with respect to the uniform device for both DD and MC at both low and high drain bias for all 50 devices. Higher correlation ($\rho = 0.86$) at high drain bias reflects the greater importance of electrostatic effects, common to both MC and DD, while at low drain bias the lesser correlation ($\rho = 0.72$) reflects the importance of transport variation imposed by the random dopants that is alone captured within MC.

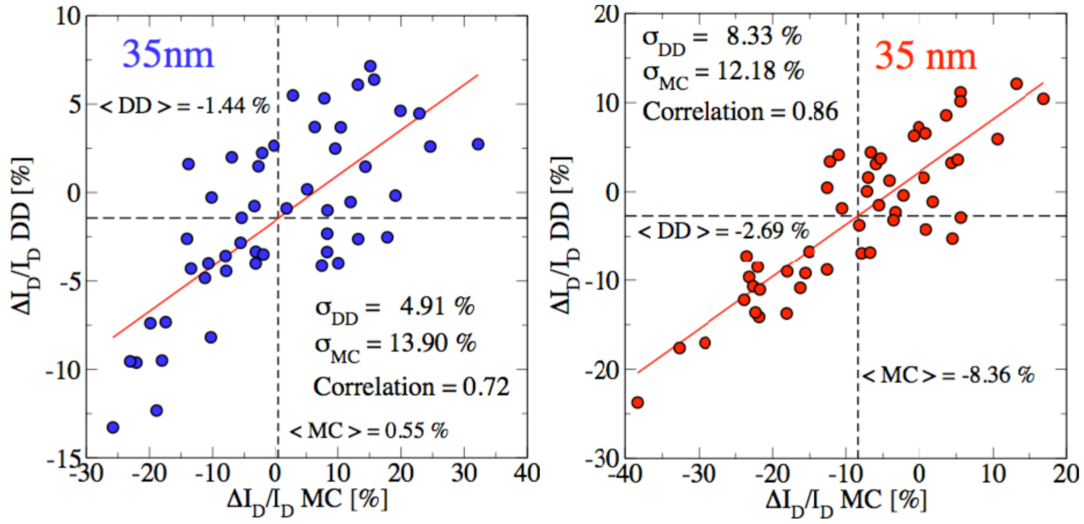

FIGURE 5.3: Scatter plots of percentage drain-current variation from MC simulation against DD simulation, both including quantum corrections.The statistical ensemble is shown along with a linear regression line.The correlation at high (red) and low (blue) drain is seen.

29 of the 50 devices from MC simulation at low drain bias show reduced current while the corresponding number of devices in DD simulation increases slightly to 31. 14 of the 50 devices from MC simulation at low drain bias show a greater, or approximately similar, reduction in current compared with the device with maximum reduction in current from corresponding DD simulation. Similarly, 19 of the 50 devices from MC simulation at low drain bias show a greater, or approximately similar, increase in current compared with

the device with maximum increase in current from DD simulation. The absolute value of the largest increase in current in MC at low drain bias is seen to be modestly larger (approximetly 24%) than the absolute value of the largest reductions in current seen in MC, while the highest reductions in current in DD is moderately larger (approximately 85%) than the largest increase in current seen in DD. These indications result in the larger percentage change in current variations in MC than DD. The standard deviation of the percentage change in current variation calculated from DD at low drain bias is $\sigma\Delta I_{D\ DD} = 4.91\%$ while the standard deviation from MC is $\sigma\Delta I_{D\ MC} = 13.90\%$, as illustrated in figure 5.3.

36 of the 50 devices from MC simulation at high drain bias show reduced current, while the number of devices fairly decrease to 26 at low drain bias. 11 of the 50 devices from MC simulation at high drain bias show greater or approximately similar reduction in current compared with the device with maximum reduction in current from DD. The increase in current in MC and DD simulations at high drain bias are seen to be comparable. The absolute value of the largest reductions in current in MC at high drain bias is seen to be significantly larger (approximately 126%) than the absolute value of the largest increase in current seen in DD, while the highest reductions in current in MC is moderately larger (approximetly 95%) than the largest increase in current seen in DD. The higher variations in MC compared with DD can again be clearly seen. The standard deviation of the percentage change in current variation calculated from DD at high drain bias is $\sigma\Delta I_{D\ DD} = 8.33\%$, while standard deviation from MC is $\sigma\Delta I_{D\ MC} = 12.18\%$, as presented in figure 5.3.

What is clear however, is that the magnitude of the MC percentage change in current variation is larger than compared to DD at both low drain and high drain biases. The MC percentage current variation in current at low drain bias is almost three times larger than in DD, while at high drain bias the percentage current variation in MC is only 50% larger than in DD. The significantly greater difference in standard deviation at low drain bias compared to that at high drain bias comes from the larger contribution from ionized impurity scattering at low drain bias. The different distribution of random dopants within device may contribute similar electrostatic effects in current while their impact on electron transport through ionized impurity scattering may vary dramatically [33]. The effects of individual dopants on the device current will be discussed later.

The comprehensive statistical analysis of the DD and MC simulation results for the 25 nm, 18 nm, 13 nm, and 9 nm are presented in appendices. In the next section, we summarize the results of this analysis.

5.3 Summary of Drain Current Variations of Scaled Devices

5.3.1 Summary of Low Drain Bias Results

Statistical theory was used to comprehensively analyse the results of drain current fluctuations obtained from DD and MC simulations. To begin the analysis, the drain current data is presented as box plots for each of the five well scaled MOSFET separately for each drain bias. The box plot displays the maximum value, upper quartile, median, lower quartile and minimum value. The rectangular box of the plot has edges defined by upper and lower quartile. This indicates where the middle 50% of results lie. The horizontal line inside the box represents the median. Upper and lower edges of the rectangular box continue with whiskers which represent the spread of the rest of values. The symmetry of the distribution of results may be interpreted through the symmetry about the median.

Box plots for each device at low drain bias are presented in figure 5.4. Standardized values of drain currents are compared since the magnitude of the drain currents vary significantly across device dimensions. The family of box plots presented in the left picture of figure 5.4 shows that 18-nm DD simulation results are more spread out than the rest. A substantial number of simulation results for DD simulation lie within the box for the case of 13-nm and 25-nm device, since the length of their boxes are slightly larger than other three boxes.

The box plots illustrated in the right picture of figure 5.4 indicates the larger spread of MC simulation results at low drain bias for 25 nm device. MC results show higher maximum values than DD. Both plots show that median values are nearly zero in all cases. This indicates that simulation results are almost symmetric about the median. These findings are in coincidence with the previous statistical analysis showing that both DD and MC simulation results at low drain bias show very little departure from a normal distribution. Both plots suggest that simulation results might be drawn from the normal distributed population.

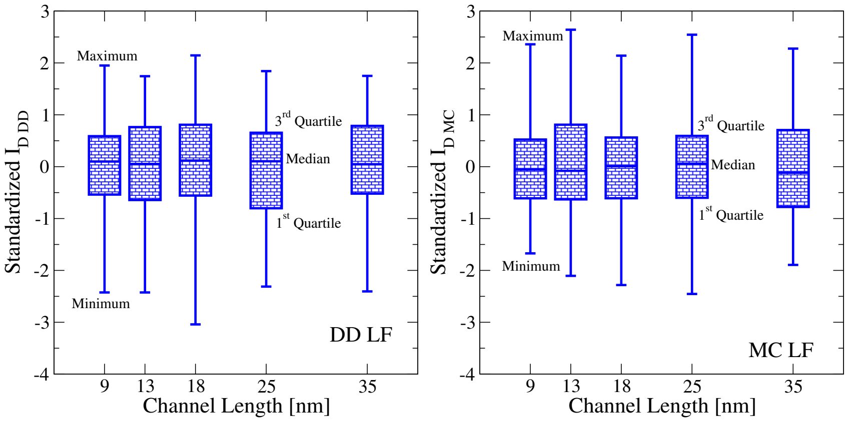

FIGURE 5.4: Box plots of standardized drain current values obtained from both DD (left) and MC (right) at low drain bias separately for each channel length.

The reliability of results was tested using the nonparametric confidence intervals. Further, the three different normality tests of the simulation results for both DD and MC simulations for each well scaled MOSFET suggest that data are drawn from normally distributed populations.

Table 5.4 summarises the data that has been collected throughout this chapter in respect of percentage change in drain current fluctuactions at low drain bias. It is clearly seen that the random dopants are a very important source of fluctuations in nano-scaled MOSFETs. It is also clear that MC simulations with *ab initio* impurity scattering show greatly increased variation compared with equivalent DD simulations. This is of great importance whenever accurate estimation of device parameter variation is required as it shows that commonly used DD simulation significantly underestimates variation by omission of transport variation.

	Standard Deviation at Low Drian Bias				
	Channel Length				
	35 nm	25 nm	18 nm	13 nm	9 nm
$\sigma_{I_{D\ DD}}$ [%]	4.92	6.33	9.38	12.71	24.11
$\sigma_{I_{D\ MC}}$ [%]	13.91	17.34	26.57	24.49	50.60

TABLE 5.4: The standard deviation of the drain current variation obtained from both DD and MC simulations at low drain bias.

The dependence of the standard deviation of the percentage change in drain current variation at low drain bias as a function of the channel length is presented in figure 5.5. Also shown for comparison are results from equivalent classical DD and self-consistent *ab initio* MC [33]. As it has been well observed before, variation increases consistently with reduction in device size. As mentioned above, the drain current significantly varies in magnitude from channel length to channel length. For this reason the coefficient of variation is also shown in figure 5.5 and confirms the standard deviation results. The plots of the coefficient of variation show a smoothly increasing trend in variations with decreasing channel length. It also smoothes the kink seen at standard deviation results for 13-nm device which might be caused by the presence of statistical noise in the simulations results.

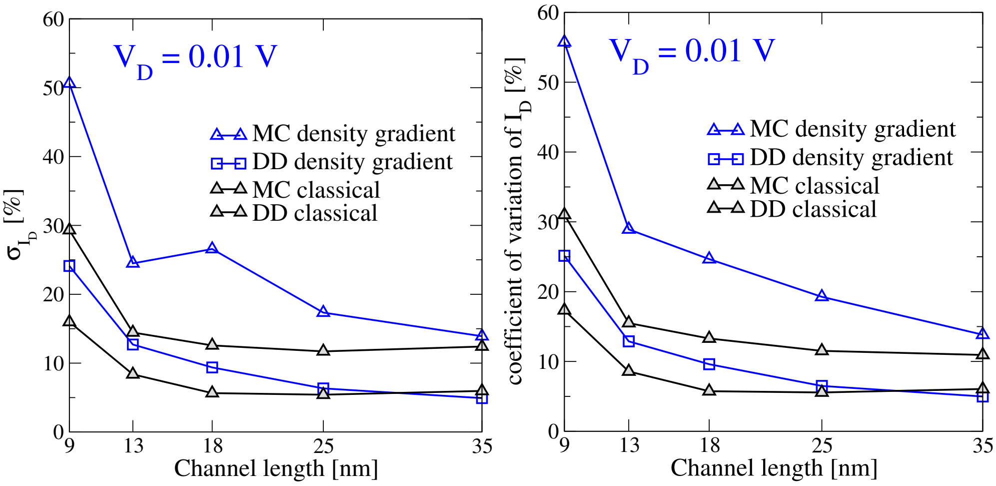

FIGURE 5.5: Standard deviation of drain current variation at low drain bias from DD and self-consistent MC.

In both classical and quantum MC simulations, with additional transport variation, significantly more variations are seen compared with DD. This effect is more pronounced in the larger devices where variations from MC are almost twice that seen in DD. With reduced channel length, and increased lateral field within the channel, the effect of transport variation compared with electrostatic variation is reduced due to increased ballisticity, although it is still significant.

5.3.2 Summary of High Drain Bias Results

Figure 5.6 shows the boxplots of the standardised drain current distribution at high drain bias. Both DD and MC simulations indicate the largest spread in results for the 18-nm device. Median values are nearly zero for all cases, while several boxes show that median lies a little off the middle of the box, indicating skew values that are modestly off zero. This implies similar symmetry compared with normal distribution. The close similarity of box lengths suggest that the most of results lie within middle 50% around the median. As has been mentioned in the statistical analysis of the low drain bias results, only a few devices fall far outside the region of 2σ. This implies compactness of the results.

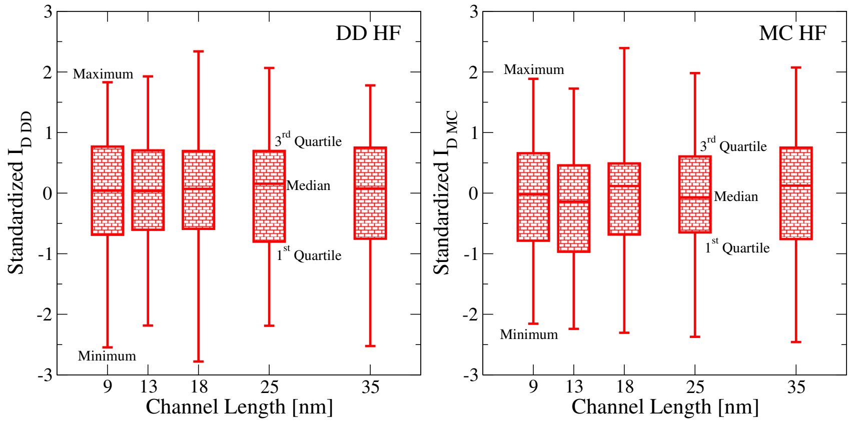

FIGURE 5.6: Box plots of standardized drain current values obtained from both DD (left) and MC (right) at high drain bias separately for each channel length..

The reliability of these results have been tested using the nonparametric intervals which accounts for the problem of the small sample sizes. Three normality tests all suggest that data come from a nearly normal distribution.

	Standard Deviation at High Drian Bias				
	Channel Length				
	35 nm	25 nm	18 nm	13 nm	9 nm
$\sigma_{I_{D\ DD}}$ [%]	8.33	10.77	15.68	18.84	30.14
$\sigma_{I_{D\ MC}}$ [%]	12.18	15.05	25.37	29.49	46.16

TABLE 5.5: The standard deviation of the drain current variation obtained from both DD and MC simulations at high drain bias.

Table 5.4 summarises the standard deviation of percentage change in drain current fluctuactions at high drain bias which are shown in figure 5.7 for both classical and quantum DD and MC. The coefficient of variation of drain current is also presented in this figure in the right graph. Again, variation increases with decreasing device size in all cases, and in both classical and quantum simulations MC yields greater variability than DD. Again the additional contribution from transport variation is comparatively greater at larger channel lengths, though compared with the low drain bias simulations the effect is somewhat reduced. This is attributed to the greater lateral field at high drain bias which accelerates carriers and reduces the Coulomb interaction with impurities. At smaller device dimensions, the screened potential associated with acceptors occupies a larger fraction of the device width, resulting in increased sensitivity to number and position of dopants within the source/channel where the lateral field is still modest.

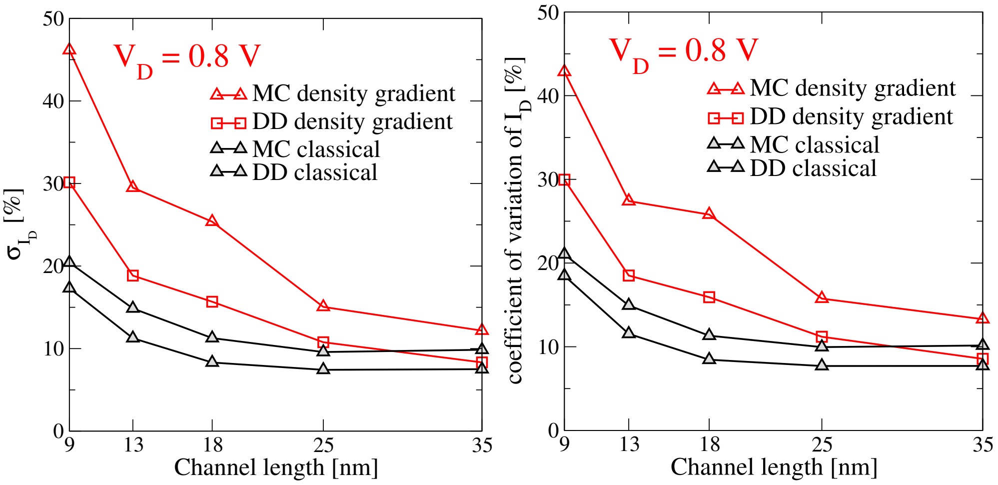

FIGURE 5.7: Standard deviation of drain current variation at high drain bias from DD and self-consistent MC.

Scatter plots illustrated in figures 5.3, A.3, B.3, C.3 and D.3 show significant correlation at both low and high drain bias, which is stronger at high drain. Reduced correlation implies variation in position dependent scattering. At high drain bias, larger correlation implies dominance of electrostatic effects. The near linear dependence of variations between MC and DD at high drain hints at a proper statistical model of the electrostatic and transport variation. This shall be discussed hereafter.

5.4 Electrostatic versus Transport Variations

In the previous sections, we have essentially constructed of two variables for the purpose of better understanding drain current variations. We have constructed the variable of electrostatic variations and the variable of transport variations. Hereafter these terms will be referred to as the electrostatic and transport variables.

The electrostatic variable is common to both DD and MC results. It is assumed that DD simulation only captures this electrostatic variable, and that within MC the same variable is well reproduced. That is to say that any effects associated with electrostatic variation are similarly captured, whether simulation precedes via DD or MC. This assumption may fail if dynamic screening of impurities by electrons in MC significantly varies from the static screening within DD [33]. Following this, it is therefore assumed that the electrostatic variable is entirely measured by $\sigma\Delta I_{D\ DD}$.

The transport variable is alone a result of MC simulation and it is assumed that it is not present in DD results. The transport variable is represented by the dynamic of ensemble of electrons within MC simulation, scattered by Coulomb potentials of the unique distribution of dopants within device. Although it is not directly measurable, its effects on the percentage change in current variations are observable, and hence subject to study.

The following additive model of the total variation in the percentage change in drain current is introduced

$$\text{total variations} = \text{electrostatic variations} + \text{transport variations} \tag{5.3}$$

where it is assumed that the total variation of the percentage change in drain current is completely resolved by MC simulation and measured by $\sigma\Delta I_{D\ MC}$. Previously presented correlations between DD and MC results (see figures 5.3, A.3, B.3, C.3 and D.3) indicate that the ratio of the electrostatic variations from DD simulation directly transforms to MC simulation. In order to properly measure the σ of the transport variable it is necessary to deploy an accurate statistical model.

Two concepts of the measurement of electrostatic and transport variables are proposed. The first concept is referred as the absolute drain current variation model. The second concept is referred to as the conditional drain current variation model. Each concept will be discussed separately.

5.4.1 The Absolute Model of Electrostatic and Transport Variations

The absolute drain current variation model may be expressed as

$$\Delta I_{D\ MC} = m(\Delta I_{D\ DD}) + \varepsilon \tag{5.4}$$

where $m(.)$ is an arbitrary function describing the relationship between the percentage change in drain current variations obtained from MC and DD simulations. ε is the random error within the model associated with the transport variable and shall be discussed shortly. The high positive correlation between MC and DD results suggests to substitute a linear function for $m(.)$. The model may then be expressed as

$$\Delta I_{D\ MC} = \beta_0 + \beta_1 \Delta I_{D\ DD} + \varepsilon \tag{5.5}$$

where β_0 and β_1 are parameters of the new linear model. If the correlation between MC and DD results is perfect, the drain current variations would lie on this line which would be only shifted by the intercept parameter β_0 from origin and have a slope β_1. Equation 5.5 is termed a linear regression model and is described in greater detailed in [196]. The total variation of the percentage change in drain current by using this model may be estimated as

$$Var(\Delta I_{D\ MC}) = Var(\beta_0 + \beta_1 \Delta I_{D\ DD} + \varepsilon) = \beta_1^2 Var(\Delta I_{D\ DD}) + Var(\varepsilon) \tag{5.6}$$

where it is assumed, consistent with a linear regression model, that $E[\Delta I_{D\ DD}\varepsilon] = 0$ [196]. This means that the electrostatic variations represented by $\Delta I_{D\ DD}$ are independent of the transport variations ε. The variance of the constant parameter β_0 is zero. Equation 5.6 may then be rewritten as

$$\underbrace{\sigma^2_{\Delta I_{D\ MC}}}_{\text{total variations}} = \underbrace{\beta_1^2 \sigma^2_{\Delta I_{D\ DD}}}_{\text{electrostatic variations}} + \underbrace{\sigma^2_{\varepsilon}}_{\text{transport variations}} \tag{5.7}$$

from which the transport variations σ^2_{ε} are

$$\sigma_{\varepsilon}^{2} = \sigma_{\Delta I_{D\ MC}}^{2} - \beta_1^2 \sigma_{\Delta I_{D\ DD}}^{2} \tag{5.8}$$

In order to determine the magnitude of the transport variation, the regression parameters β_0 and β_1 need to be estimated. These parameters from equation 5.5 are generally estimated using the familiar least square method [196]. After obtaining the regression parameters, the percentage ratio of the electrostatic variation and transport variation to the total variation may be computed as

$$\text{absolute ratio of electrostatic variations} = \frac{\beta_1^2 \sigma_{\Delta I_{D\ DD}}^{2}}{\sigma_{\Delta I_{D\ MC}}^{2}} \times 100\% \tag{5.9}$$

$$\text{absolute ratio of transport variations} = \frac{\sigma_{\varepsilon}^{2}}{\sigma_{\Delta I_{D\ MC}}^{2}} \times 100\% \tag{5.10}$$

Although the relationship may not be truly linear and that a nonlinear model might fit the data better, the assessment of the linear model given by equation 5.5 indicates enough statistical accuracy and reliability to allow its use.

5.4.2 The Conditional Model of Electrostatic and Transport Variations

Within the conditional drain current variation model, the common effects on the percentage change in drain current at both low and high drain bias are examined. The main difference with the model above is the lack of assumption that electrostatic and transport variations are independent. In the conditional model, endogeneity is assumed between these two variables. A dummy variable that splits the random variable into two terms, the first a dummy variable and the second a new random variable which is now uncorrelated with electrostatic variable, is applied. The dummy variable may be termed the fixed effect. Within this analysis, the fixed effect is related to the treatment of the simulation in terms of the applied bias. The dummy variable accounts for specific effects relating to the percentage change in current, subject whether the simulation is performed at low or high drain bias.

In order to proceed, a sample of 100 observations of the percentage change in drain current was compiled. This sample simply represents merging the high and low drain bias results for each device. Without loss of any generality, it is assumed that the first 50 of them belong to the simulations at high drain bias and the additional 50 from those at low drain bias. The conditional variation model introduces a dummy variable into equation (5.5) which may then be written as

$$\Delta I_{D\ MC} = \beta_1 \Delta I_{D\ DD} + \gamma d + \varepsilon \tag{5.11}$$

Here γ is the regression coefficient consistent with the dummy variable d. As opposed to equation (5.5), an intercept parameter β_0 is omitted, since it will be collinear with d. The dummy variable in equation (5.11) is expressed as

$$d_i = \begin{cases} 1 & \text{if } \Delta I_D^i \text{ is from high drain bias simulation} \\ 0 & \text{if } \Delta I_D^i \text{ is from low drain bias simulation} \end{cases} \tag{5.12}$$

where ΔI_D^i is the percentage change in drain current for the ith device, where the first 50 have value $d_i = 1$ and the remaining 50 have value $d_i = 0$. The mean value of the sample of d_i is $\mu_d = (50 \times 1 + 50 \times 0) \setminus 100 = 0.5$ and the variance σ_d^2 has a value 0.25.

The variance of the total variation of percentage change in drain current is determined in a similar fashion as in equation (5.6)

$$Var(\Delta I_{D\ MC}) = \beta_1^2 Var(\Delta I_{D\ DD}) + \gamma^2 Var(d) + 2\beta_1 \gamma Cov(\Delta I_{D\ DD}, d) + Var(\varepsilon) \tag{5.13}$$

where it is now assumed that $E[\varepsilon | \Delta I_{D\ DD}, d] = 0$, which is an assumption of the multivariate linear regression. Therefore, the total variance can be expressed in a form

$$\begin{aligned} \underbrace{\sigma^2_{\Delta I_{D\ MC}}}_{\text{total variations}} &= \underbrace{\beta_1^2 \sigma^2_{\Delta I_{D\ DD}}}_{\text{conditional electrostatic variations}} + \underbrace{\gamma^2 \sigma_d^2 + 2\beta_1 \gamma Cov(\Delta I_{D\ DD}, d)}_{\text{common effects}} \\ &+ \underbrace{\sigma_\varepsilon^2}_{\text{conditional transport variations}} \end{aligned} \tag{5.14}$$

where $Cov(\Delta I_{D\ DD}, d)$ stands for the covariance between the percentage change in current from DD simulation and the dummy variable. The term $\gamma^2\sigma_d^2$ is specific to whether or not the simulation was carried out at low or high drain bias. Even though, the variance of the dummy variable is fixed and its contribution to the total variation depends upon the regression coefficient γ. The σ_ε^2 is naturally incorporated in the MC simulation by its stochastic character.

The covariance term in the equation (5.14) is calculated as follows

$$Cov(\Delta I_{D\ DD}, d) = \frac{1}{100}\sum_{i=1}^{100}(\Delta I^i_{D\ DD} - \langle\Delta I_{D\ DD}\rangle)(d_i - \frac{1}{2}) \tag{5.15}$$

where the term $\Delta I_{D\ DD}$ may be split into two terms. The first term is the percentage change of drain current from high drain bias simulation, denoted $\Delta I^{HB}_{D\ DD}$, while the second term is related to simulation at low drain bias, denoted $\Delta I^{LB}_{D\ DD}$. Equation (5.15) may then be rewritten as

$$\begin{aligned} Cov(\Delta I_{D\ DD}, d) &= \frac{1}{100}[\sum_{i=1}^{50}\Delta I^{i\ HB}_{D\ DD} - \langle\Delta I_{D\ DD}\rangle)(d_i - \frac{1}{2}) \\ &+ \sum_{i=51}^{100}(\Delta I^{i\ LB}_{D\ DD} - \langle\Delta I_{D\ DD}\rangle)(d_i - \frac{1}{2})] \end{aligned} \tag{5.16}$$

The values for the d_i variables can be substituted as defined above. Thus, we write equation (5.16) as

$$\begin{aligned} Cov(\Delta I_{D\ DD}, d) &= \frac{1}{100}[\sum_{i=1}^{50}\Delta I^{i\ HB}_{D\ DD} - \langle\Delta I_{D\ DD}\rangle)\frac{1}{2} \\ &+ \sum_{i=51}^{100}(\Delta I^{i\ LB}_{D\ DD} - \langle\Delta I_{D\ DD}\rangle)(-\frac{1}{2})] \end{aligned} \tag{5.17}$$

and after the several algebraic operations, we have

$$Cov(\Delta I_{D\ DD}, d) = \frac{1}{200}[\sum_{i=1}^{50}\Delta I^{i\ HB}_{D\ DD} - \sum_{i=51}^{100}\Delta I^{i\ LB}_{D\ DD}] \tag{5.18}$$

Finally, the covariance term might be expressed as follows

$$Cov(\Delta I_{D\ DD}, d) = \frac{1}{4}[\langle \Delta I_{D\ DD}^{HB} \rangle - \langle \Delta I_{D\ DD}^{LB} \rangle] \tag{5.19}$$

where terms $\langle \Delta I_{D\ DD}^{HB} \rangle$ and $\langle \Delta I_{D\ DD}^{LB} \rangle$ stand for the mean values of the percentage change in drain current at high and low drain bias, respectively.

In a similar way, we can decompose the total variations as follows

$$\sigma^2_{\text{total variations}} = \frac{1}{100}\sum_{i=1}^{100}[\Delta I_{D\ MC}^{i} - \langle \Delta I_{D\ MC} \rangle]^2 \tag{5.20}$$

where $\langle \Delta I_{D\ MC} \rangle$ is the mean value of the percentage change in drain current across the entire sample of MC simulations at both low and high drain bias and may be expressed as

$$\begin{aligned} \langle \Delta I_{D\ MC} \rangle &= \frac{1}{100}\sum_{i=1}^{100} \Delta I_{D\ MC}^{i} \\ &= \frac{1}{2}[\frac{1}{50}\sum_{i=1}^{50} \Delta I_{D\ MC}^{i\ HB} + \frac{1}{50}\sum_{i=51}^{100} \Delta I_{D\ MC}^{i\ LB}] \\ &= \frac{1}{2}[\langle \Delta I_{D\ MC}^{HB} \rangle + \langle \Delta I_{D\ MC}^{LB} \rangle] \end{aligned} \tag{5.21}$$

where $\langle \Delta I_{D\ MC}^{HB} \rangle$ and $\langle \Delta I_{D\ MC}^{LB} \rangle$ are mean values of the MC simulation results at high and low drain bias, respectively. Substituting from (5.21) into (5.20) will give us the following decomposition of total variations

$$
\begin{aligned}
\sigma^2_{\text{total variations}} &= \frac{1}{100}\sum_{i=1}^{100}[\Delta I^{i}_{D\ MC} - \frac{1}{2}[\langle \Delta I^{HB}_{D\ MC}\rangle + \langle \Delta I^{LB}_{D\ MC}\rangle]]^2 \\
&= \frac{1}{2}[\frac{1}{50}\sum_{i=1}^{50}[\Delta I^{i\ HB}_{D\ MC} - \frac{1}{2}[\langle \Delta I^{HB}_{D\ MC}\rangle + \langle \Delta I^{LB}_{D\ MC}\rangle]]^2 \\
&+ \frac{1}{50}\sum_{i=51}^{100}[\Delta I^{i\ LB}_{D\ MC} - \frac{1}{2}[\langle \Delta I^{HB}_{D\ MC}\rangle + \langle \Delta I^{LB}_{D\ MC}\rangle]]^2 \\
&= \frac{1}{2}[\frac{1}{50}\sum_{i=1}^{50}[\Delta I^{i\ HB}_{D\ MC} - \langle \Delta I^{HB}_{D\ MC}\rangle]^2 \\
&- \frac{2}{50}(\frac{\langle \Delta I^{LB}_{D\ MC}\rangle - \langle \Delta I^{HB}_{D\ MC}\rangle}{2})\sum_{i=1}^{50}[\Delta I^{i\ HB}_{D\ MC} - \langle \Delta I^{HB}_{D\ MC}\rangle] \\
&+ \frac{1}{50}\sum_{i=1}^{50}(\frac{\langle \Delta I^{LB}_{D\ MC}\rangle - \langle \Delta I^{HB}_{D\ MC}\rangle}{2})^2 \\
&+ \frac{1}{50}\sum_{i=1}^{50}[\Delta I^{i\ LB}_{D\ MC} - \langle \Delta I^{LB}_{D\ MC}\rangle]^2 \\
&- \frac{2}{50}(\frac{\langle \Delta I^{HB}_{D\ MC}\rangle - \langle \Delta I^{LB}_{D\ MC}\rangle}{2})\sum_{i=1}^{50}[\Delta I^{i\ LB}_{D\ MC} - \langle \Delta I^{LB}_{D\ MC}\rangle] \\
&+ \frac{1}{50}\sum_{i=1}^{50}(\frac{\langle \Delta I^{HB}_{D\ MC}\rangle - \langle \Delta I^{LB}_{D\ MC}\rangle}{2})^2] \\
&= \frac{1}{2}[\sigma^{2\ HB}_{\Delta I_{D\ MC}} + \sigma^{2\ LB}_{\Delta I_{D\ MC}}] + (\frac{\langle \Delta I^{HB}_{D\ MC}\rangle - \langle \Delta I^{LB}_{D\ MC}\rangle}{2})^2 \qquad (5.22)
\end{aligned}
$$

where $\sigma^{2\ HB}_{\Delta I_{D\ MC}}$ and $\sigma^{2\ LB}_{\Delta I_{D\ MC}}$ are the variances of MC simulation results at high and low drain bias, respectively. The remaining term represents the contribution to total variations by merging two samples into one. In a similar way, the decomposition of electrostatic variations into low and high drain bias parts may be obtained and may be expressed as

$$
\begin{aligned}
\sigma^2_{\Delta I_{D\ DD}} &= \frac{1}{100}\sum_{i=1}^{100}[\Delta I^{i}_{D\ DD} - \frac{1}{2}[\langle \Delta I^{HB}_{D\ DD}\rangle + \langle \Delta I^{LB}_{D\ DD}\rangle]]^2 \\
&= \frac{1}{2}[\frac{1}{50}\sum_{i=1}^{50}[\Delta I^{i\ HB}_{D\ DD} - \frac{1}{2}[\langle \Delta I^{HB}_{D\ DD}\rangle + \langle \Delta I^{LB}_{D\ DD}\rangle]]^2 \\
&= \frac{1}{2}[\sigma^{2\ HB}_{\Delta I_{D\ DD}} + \sigma^{2\ LB}_{\Delta I_{D\ DD}}] + (\frac{\langle \Delta I^{HB}_{D\ DD}\rangle - \langle \Delta I^{LB}_{D\ DD}\rangle}{2})^2 \qquad (5.23)
\end{aligned}
$$

where $\sigma^{2\,HB}_{\Delta I_{D\,DD}}$ and $\sigma^{2\,HB}_{\Delta I_{D\,MC}}$ are the variances of DD simulation results at high and low drain bias, respectively. Substituting (5.19), (5.22) and (5.23) into (5.14) will give the decomposition of the transport variable as follows

$$\begin{aligned}
\underbrace{\sigma_{\varepsilon}^{2}}_{\text{conditional transport variations}} &= \underbrace{\frac{1}{2}[\sigma^{2\,HB}_{\Delta I_{D\,MC}} - \beta_1^2\sigma^{2\,HB}_{\Delta I_{D\,DD}}]}_{\text{high drain bias contributions to transport variations}} \\
&+ \underbrace{\frac{1}{2}[\sigma^{2\,LB}_{\Delta I_{D\,MC}} - \beta_1^2\sigma^{2\,LB}_{\Delta I_{D\,DD}}]}_{\text{low drain bias contributions to transport variations}} \\
&- \underbrace{\frac{1}{4}[\gamma^2 + \gamma\beta_1[\langle\Delta I^{HB}_{D\,DD}\rangle - \langle\Delta I^{LB}_{D\,DD}\rangle]]}_{\text{common effects correction term of transport variations}} \\
&+ \underbrace{\frac{1}{4}[(\langle\Delta I^{HB}_{D\,MC}\rangle - \langle\Delta I^{LB}_{D\,MC}\rangle)^2 - \beta_1^2(\langle\Delta I^{HB}_{D\,DD}\rangle - \langle\Delta I^{LB}_{D\,DD}\rangle)^2]}_{\text{general correction term of transport variations}}
\end{aligned} \tag{5.24}$$

In order to compute the transport variations from equation (5.24), the regression parameters β_1 and γ of equation (5.11) have to be determined. The regression parameters are again estimated by the familiar least square method. Further, the conditional ratios of electrostatic and transport variation are calculated in similar way as in equations (5.9) and (5.10).

5.4.3 Results of Electrostatic versus Transport Variations

The parameters β_0 and β_1 of equation (5.5) were estimated using the ordinary least square method. The parameters β_1 and models were significant at significance level 0.001 for all well-scaled MOSFETs. Results of the regression models with error estimation are presented in tables 5.6 and 5.7.

Scatter plots of the percentage drain current variation at both low and high drain bias are shown for the 35 nm device in Figure 5.8 and 5.9 respectively. The plots show significant correlation, with stronger correlation at high drain bias. The larger correlation implies the dominance of electrostatic effects contributing to the drain current variation at high drain. The near linear dependence between MC and DD at high drain hints at a

	Low Drian Bias: The Absolute Model				
	Channel Length				
	35 nm	25 nm	18 nm	13 nm	9 nm
β_1	2.0	2.1	2.2	1.6	1.9
se β_1	0.3	0.2	0.2	0.1	0.1
R^2	0.53	0.57	0.61	0.69	0.88
F statistics	53.1	65.7	74.7	106.9	344.8

TABLE 5.6: Regression results at low drain bias obtained from the absolute model. se is a standard error of the regression coefficient. R^2 or coefficient of determination is a measure of goodness-of-fit of linear regression.

	High Drian Bias: The Absolute Model				
	Channel Length				
	35 nm	25 nm	18 nm	13 nm	9 nm
β_1	1.3	1.3	1.4	1.4	1.5
se β_1	0.1	0.1	0.1	0.1	0.1
R^2	0.75	0.81	0.76	0.84	0.92
F statistics	142.6	209.8	152.8	244.0	545.3

TABLE 5.7: Regression results at high drain bias obtained from the absolute model. se is a standard error of the regression coefficient. R^2 or coefficient of determination is a measure of goodness-of-fit of linear regression.

proper statistical model of the electrostatic and transport variables. The linear regression lines following 5.5 are also shown in Figure 5.8 and 5.9. The average coefficient of determination for all channel lengths is roughly 80% at high drain bias and 60% at low drain bias respectively. The higher coefficient of determination at high drain bias is due to the stronger correlation between MC and DD results. The regression lines in both cases are presented along with 95% confidence intervals.

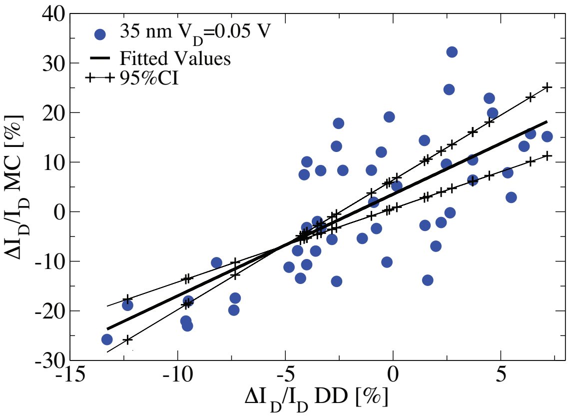

FIGURE 5.8: MC v DD percentage drain-current variation for the 35nm device ensemble at $V_D = 0.05$ V. The linear regression and its 95% confidence intervals are shown.

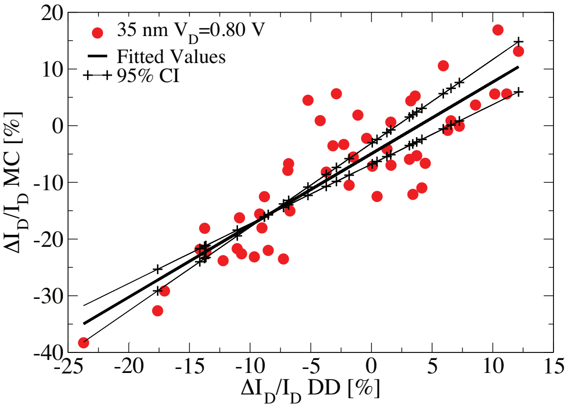

Figure 5.9: MC v DD percentage drain-current variation for the 35nm device ensemble at V_D = 1.0 V. The linear regression and its 95% confidence intervals are shown.

We estimate the 95% confidence interval of the β_1 coefficient of 5.5 for all channel lengths and for both low and high drain bias, the result of which is plotted in Figure 5.10. This result is used to estimate the electrostatic contribution from DD in MC. The confidence intervals are broader at low drain bias due to the greater influence of transport variation in reducing the correlation between DD and MC.

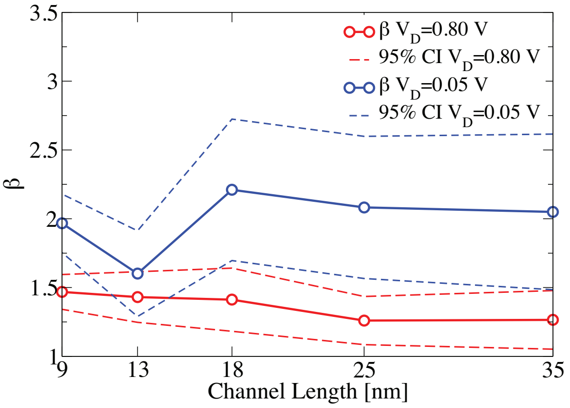

Figure 5.10: β_1 parameter extracted from the absolute model 5.5 for each scaled device and bias. 95% confidence intervals are shown.

Therefore the ratios of electrostatic and transport variations at low drain bias were determined and are presented in table 5.8. Figure 5.11 shows the contribution of transport variation to the total observed variation within MC at low drain bias. Again, results of previous classical simulation are shown for comparison. At large channel lengths it is seen that transport variations are comparable with electrostatic variations when quantum corrections are included, while in comparable classical simulations it is seen that the electrostatic effects are responsible for a greater share of the variation. This is most likely associated with increased screening of the discrete impurities by the inversion layer electrons. Within classical simulations, the high interface field induces a very large carrier concentration which effectively screens local impurities. Within quantum corrected simulation, the lower peak carrier concentration and its position away from the interface allows for more penetration of above lying potential fluctuations and for less screening within the inversion layer itself. In turn it is expected that more transport variation be revealed in simulations in which the interaction potential is more pronounced.

	Low Drian Bias: The Absolute Model				
	Channel Length				
	35 nm	25 nm	18 nm	13 nm	9 nm
Electrostatic variations[%]	52.5	57.8	60.9	69.0	87.8
Transport Variations [%]	47.5	42.2	39.1	31.0	12.2

Table 5.8: Ratios of electrostatic and transport variations at low drain bias obtained from the absolute model.

There is also a clear trend towards reduced transport variation with reduced device dimensions when quantum corrections are considered, while classical simulations show a general trend to increase. This is associated with the electrostatic reduction in carrier density associated with comparatively larger screening length in QM simulations occupying significantly larger areas of the active region of the devices. Thus electrostatic effects become more important. However, in classical simulations the strongly screened impurity potentials favour large angle scattering when carriers interact at short range. In smaller devices this becomes more likely thus the increased importance of transport variation.

Ratios of electrostatic and transport variations at high drain bias obtained from the absolute model are presented in table 5.9. Figure 5.12 plots these values, again showing results extracted from previous classical simulation. There can again be seen a general trend in which the ratio of electrostatic variation increases with reduced device dimensions and it can also be seen that electrostatic variation dominates over all devices. It is clear that the contribution of transport variation at high drain bias is less than that at low drain bias. It is also clear that reduced screening within the quantum corrected simulation leads to significantly more transport variation than in the classical case.

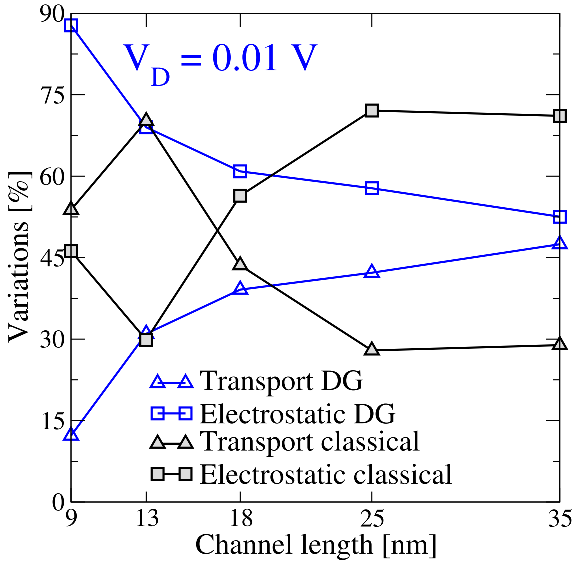

FIGURE 5.11: Electrostatic and transport variations at low drain bias estimated by the absolute model for each channel length.

	High Drian Bias: The Absolute Model				
	Channel Length				
	35 nm	25 nm	18 nm	13 nm	9 nm
Electrostatic variations [%]	74.8	81.4	76.1	83.6	91.9
Transport Variations [%]	25.2	18.6	23.9	16.4	8.1

TABLE 5.9: Ratios of electrostatic and transport variations at low drain bias obtained from the absolute model.

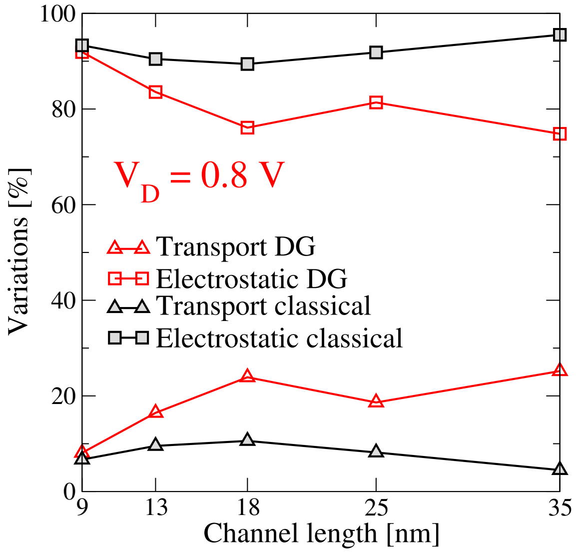

FIGURE 5.12: Electrostatic and transport variations at high drain bias estimated by the absolute model for each channel length.

Ratios of the electrostatic and transport variables at both low and high drain bias obtained from the absolute model 5.5 are presented in Figure 5.13. A general trend in which the ratio of electrostatic variation increases with reduced device dimensions is clearly established. It is also clear that the relative contribution of transport variation at high drain bias is less than that at low drain bias. The trend towards increased electrostatic variability at smaller device dimensions at high drain bias is associated with the increased ballisticity of these devices. High energy carriers, accelerated by the large drain bias, strongly favour small angle scattering when interacting with impurities and this does little to alter their momentum. Variation then becomes strongly effected by carrier injection, limited by the potential profile at the source/channel edge, which is purely an electrostatic effect.

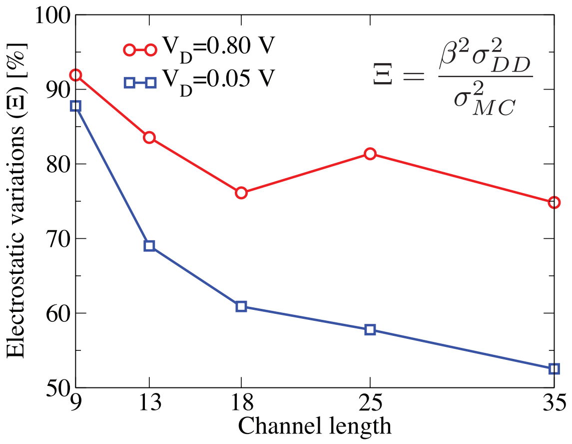

FIGURE 5.13: Percentage of total variation attributed to electrostatic effects as estimated by the absolute model at low and high drain bias.

As the alternative model to the absolute model a nave approach can be used to estimate the electrostatic and transport components. This nave approach assumes that DD simulations account for the electrostatic variation and that this is identically recovered within MC, so the percentage of the total variation observed in MC may be attributed in part to electrostatic variation and in part to transport variation. Figure 5.14 shows the contribution of transport variation to the total observed variation within MC at low and high drain bias. Results of previous classical simulation [33] are shown for comparison. The one major drawback of this approach is that it does not account for correlation between the DD and MC results, which can affect on estimated ratio of electrostatic and transport variation. The nave model overestimates significantly transport components compared with absolute model due to the lack of correlation between DD and

MC results. As mentioned before, the correlation coefficient changes the contribution of electrostatic component to the overall variation in MC.

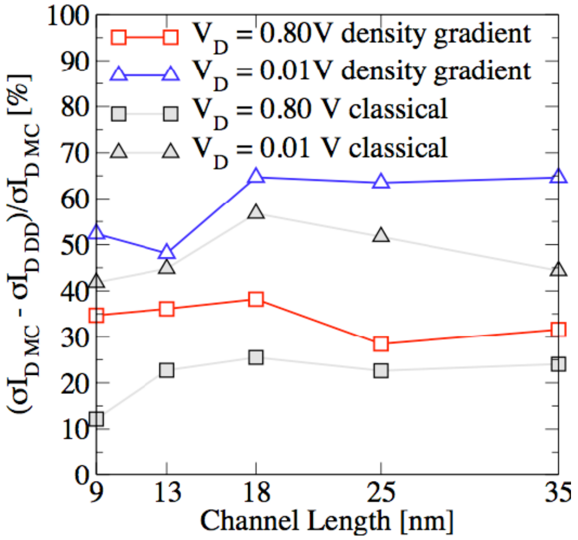

FIGURE 5.14: Percentage contribution of transport variation to the total variation in MC at low and high drain bias.

The results of the conditional model shows that the mixed third and fourth terms in equation (5.24) might be neglected. The conditional model can be approximated by the absolute model results as follows. We substitute β_1 into ((5.24) for the estimated values of the absolute model. Thereafter the conditional variation may be expressed as

$$\begin{aligned}\underbrace{\sigma^2_{\varepsilon}}_{\text{conditional transport variations}} &= \underbrace{\frac{1}{2}[\sigma^{2\ HB}_{\Delta I_{D\ MC}} - \beta_1^{2\ HB}\sigma^{2\ HB}_{\Delta I_{D\ DD}}]}_{\text{high drain bias contributions to transport variations}} \\ &+ \underbrace{\frac{1}{2}[\sigma^{2\ LB}_{\Delta I_{D\ MC}} - \beta_1^{2\ LB}\sigma^{2\ LB}_{\Delta I_{D\ DD}}]}_{\text{low drain bias contributions to transport variations}}\end{aligned} \tag{5.25}$$

Ratios values of this approximated model are presented in table 5.10 and illustrated in figure 5.15 where they are again compared with the previous classical simulation. The approximated conditional model clearly manifest the inclusion of quantum corrections which lessen the contribution of transport variations with decreasing channel length.

	the Approximated Conditional Model				
	Channel Length				
	35 nm	25 nm	18 nm	13 nm	9 nm
Electrostatic variations [%]	62.2	67.9	68.2	77.6	89.7
Transport Variations [%]	37.8	32.1	31.8	22.4	10.3

TABLE 5.10: Ratios of electrostatic and transport variations at both high and low drain bias obtained from the approximated conditional model.

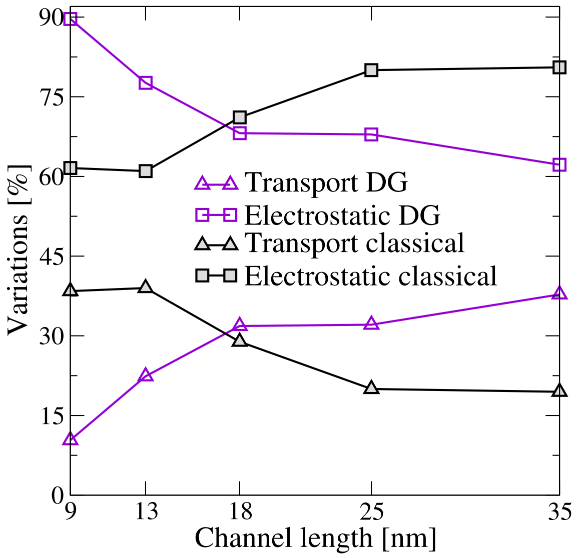

FIGURE 5.15: Electrostatic and transport variations at both low and high drain bias estimated by the approximated conditional model for each channel length.

5.5 Conclusions

It is clearly demonstrated that DD simulation underestimates the magnitude of the real current variation. The analysis has shown that transport variations play a significant role in determining the total drain current variation at all bias conditions, although as device dimensions are scaled it is clear that electrostatic effects have an increasing contribution. Transport variations are significantly more important at low drain bias owing to the inverse relationship between momentum transfer and incident carrier energy for the impurity scattering process. Consequently, electrostatic effects, most noticeably at the source p-n junction, significantly affect device current in this regime.

Two statistical models were constructed to accurately classify and assess the effects of the random discrete dopants on drain current fluctuations into their relative electrostatic and transport contributions. Their combined effects were estimated by absolute and conditional model assuming that DD simulation accounts for the entire electrostatic variation and that this is identically recovered within MC. The percentage of the total variation observed in MC may be attributed to in part electrostatic variation and in part transport variation. This analysis was a significant improvement over the previous estimation which did not account for the statistical dependence of the two sets of results.

Chapter 6

Hierarchical simulation of statistical variability: from 3D MC with *ab initio* ionised impurity scattering to statistical compact models

In the previous chapter, an efficient method to accurately capture quantum confinement effects as well as ab initio ionized impurity scattering based on the density gradient formalism was presented. This was then applied to study consistently the impact of transport variability due to scattering from random discrete dopants on the on-current variability in realistic nano CMOS transistors. Such simulations resulted in an increased drain current variability when compared with drift diffusion simulation.

Following from that work in this chapter, an efficient three-stage hierarchical simulation strategy is presented that propagates the increased on-current variability captured in 3D qunatum corrected ab initio MC into statistical 3D DD simulations that are in turn used to obtain target $I_D - V_G$ characteristics for the extraction of statistical compact models. Such a method is critical for the accurate modeling-based evaluation of statistical variability and its incorporation in statistical compact models, which is becoming an essential component of the preliminary design kit (PDK) development.

The first section describes the hierarchical simulation strategy that is further illustrated in the second section using a statistical ensemble of 100 devices, the results of which are presented with discussion. The benefits of this methodology are presented and highlighted in the third section when applied to circuit simulation of an inverter, before conclusions are drawn.

6.1 Hierarchic Simulation Methodology

The accurate modeling of statistical variability requires 3D simulation of a large ensemble of microscopically different transistors [26], from which representative sets of current-voltage characteristics are required in order to extract statistical compact models [45, 93]. The computational intensity of such a task favors the use DD simulations when studying the impact of RDD [8, 9] which have been identified as the major source of variability in bulk MOSFETs.

While DD simulations accurately capture the electrostatic impact of spatially resolved sources of variability, and related threshold voltage and sub-threshold variation, they underestimate variation associated with position dependent scattering from the corresponding potential fluctuations [205]. Monte Carlo simulation that incorporates position dependent scattering through real space trajectories of the particles within the resolved fluctuating potential landscape has been shown in the chapter 4 to capture this additional variation. However, MC simulations are so computationally expensive as to be impractical for the simulation of a complete set of target device characteristics for compact model extraction. In order to transfer the accurate information about current variability using MC into industrial strength compact models, the use of intermediate DD simulations are necessary in order to generate a full set of target $I_D - V_G$ characteristics for statistical compact model parameters extraction. To this end we have developed a three-stage hierarchic simulation strategy, illustrated in figure 6.1 and discussed below.

6.1.1 Stage One: Initial Variability Estimation

In the first stage, quantum corrected DD simulations are performed at a high gate bias and at both low and high drain biases for each device within the simulated statistical ensemble. Further, a device-specific, mesh-based, quantum correction term defined as

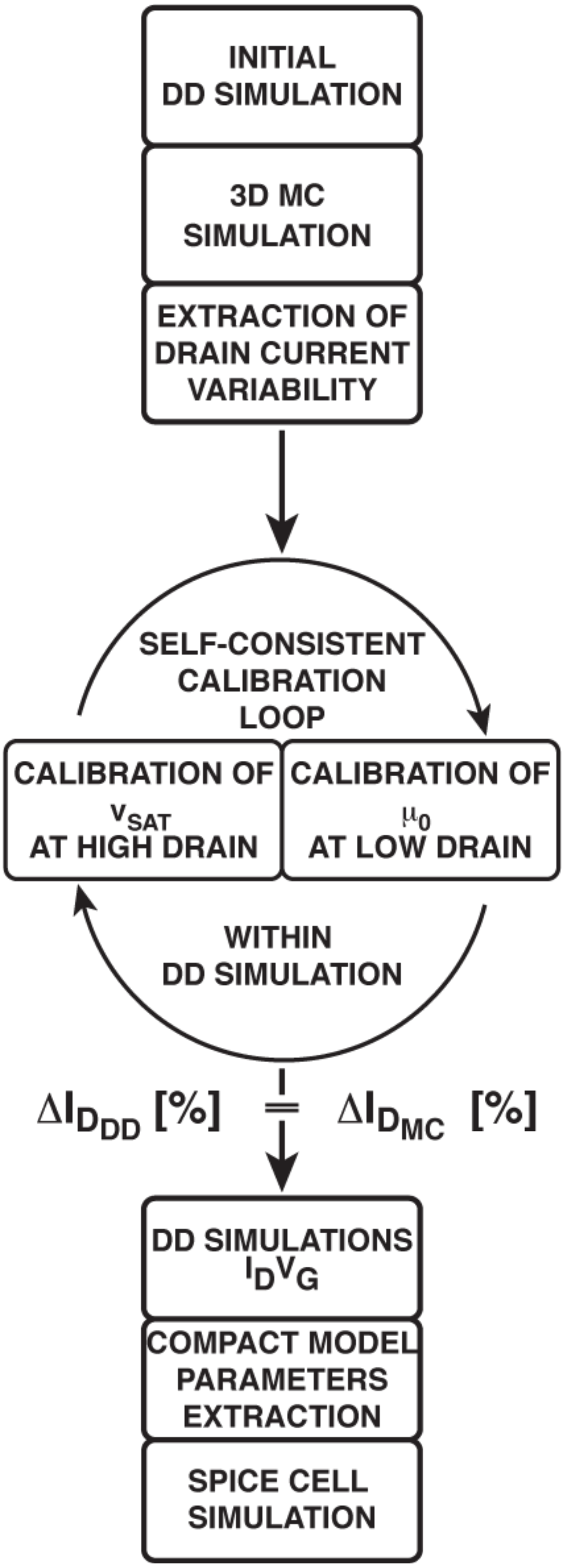

FIGURE 6.1: Flow chart depicting the three-stage hierarchic simulation strategy.

the difference between the classical and effective quantum potential solutions, is obtained from these initial DD results for use in self-consistent quantum corrected MC simulations.

MC simulations are then performed over the same ensemble and under the same bias conditions as DD simulation, utilizing the DD results as the initial solution for MC. In all cases a uniform device is similarly simulated as a reference from which to measure the percentage drain current variation for each transistor within each simulated ensemble. The percentage drain current variation may be expressed by equation (4.8). Results from MC simulation include additional transport variation and yield a greater percentage variation in drain current at both low and high drain bias.

6.1.2 Stage Two: Calibration of DD Variability

In chapter 4, it was shown that it may be possible to recover the total variations seen in MC simulations by using properly calibrated DD simulations. The strong linear dependence between DD and MC percentage drain current variations indicates that a proper adjustment of the mobility values may lead to the desired magnitude of percentage drain current variation from DD simulations. This is exploited in the second stage, during which DD simulations are calibrated device by device in order to obtain the same percentage variation in current as observed in MC for that device. This calibration is achieved through a self-consistent two-step iterative scheme in which low field mobility parameters are modified in the first step to match variation at low drain bias, followed by modification of saturation velocity to match variation at high drain bias.

Calibration of low-field mobility is achieved through adjustment of the parameter α which is used to scale the concentration dependent mobility (see equation (3.13)), while calibration of high-field mobility is similarly achieved through adjustment of the parameter β which is used to scale the saturation velocity in the lateral field dependent mobility model (see equation (3.14)) [192]. Application of the adjusted mobility models are here restricted to those regions in the device that are net p-type. This is because the adjusted mobility models are intended to reflect the variation in transport arising from variation in acceptor doping alone.

Given initial values of α and β, quantum corrected atomistic DD simulation is performed at low and high drain bias in order to extract the percentage current variation from uniform simulation. New values of α and β may then be derived as follows

$$\alpha_k = \frac{\Delta I^{*\mathrm{LB\ MC}}}{\Delta I_{k-1}^{\mathrm{LB}\ \mathrm{DD}}} \frac{\Delta I^{*\mathrm{HB\ MC}}}{\Delta I_{k-1}^{\mathrm{HB}\ DD}} \alpha_{k-1} \tag{6.1}$$

$$\beta_k = \frac{\Delta I^{*\mathrm{LB\ MC}}}{\Delta I_{k-1}^{\mathrm{LB}\ \mathrm{DD}}} \frac{\Delta I^{*\mathrm{HB\ MC}}}{\Delta I_{k-1}^{\mathrm{HB}\ DD}} \beta_{k-1} \tag{6.2}$$

where $\Delta I^{*\mathrm{LB\ MC}}$ and $\Delta I^{*\mathrm{HB\ MC}}$ represent the desired percentage drain current variations at low and high drian bias obtained from MC simulation and $\Delta I_{k-1}^{\mathrm{LB}\ \mathrm{DD}}$ and $\Delta I_{k-1}^{\mathrm{LB}\ \mathrm{DD}}$ are the percentage drain current variations at low and high drian bias obtained from $k-1$ loop of this two-step process. The new values are used as above and the process is iterated until a single set of mobility model parameters provides the defined accuracy at both low and high drain bias.

6.1.3 Stage Three: 'enhanced' compact model extraction

Upon calibration, a set of unique parameters α and β exist for each device within the original ensemble and allow matching of the percentage drain current variation for all devices at both low and high drain bias for a single gate bias. Quantum corrected atomistic DD simulation of the device ensemble may then be performed over a range of gate bias to obtain a complete set of 'enhanced' $I_D - V_G$ characteristics necessary for statistical compact model parameter extraction. Here the enhanced characteristics include additional variation due to acceptor impurity scattering obtained from MC simulations.

Compact model parameter extraction using the enhanced characteristics then follows a two-step procedure described in detail elsewhere [45]. In the first step, the complete set of BSIM4v4 [206] model parameters using Synopsis tool Aurora [207] are extracted from the simulated characteristics of transistors with continuous doping profiles and different channel lengths and widths. These account for the long channel behaviour, threshold voltage in the short channel regime and the behaviour of the drain current at high field. The second step is carried out in two sub-extraction loops and is based on the enhanced $I_D - V_G$ characteristics of each device from the simulated statistical ensemble. In this step, seven key BSIM4v4 model parameters are chosen and extracted that from a device operation point of view account for the effect of the unique distribution of dopants.

In the first sub-extraction loop, six of these parameters are extracted at low drain bias to properly take into account threshold and subthreshold slope variations and mobility variations. Firstly, $V\mathrm{th0}$ is the long channel device threshold voltage at zero substrate bias and is selected to take into account the threshold voltage variation induced by RDD. As the second parameter is selected $V\mathrm{off}$ which is an empirical parameter that describes the difference between the model V_T values used in subtreshold and strong inversion regime which has significant impact on subthreshold off-current variations. As the third parameter $N\mathrm{factor}$ is extracted that accounts for the depletion capacitance fluctuations due to unique distribution of random dopants and also maps subthreshold slope variance. $R\mathrm{dsw}$ is chosen as the fourth parameter and represents the basic S/D resistance. This parameter is selected to properly deal with the variation of RDD in the source/drain regions. Parameter $u0$ is extracted as the fifth parameter that represents low field mobility which is selected to account for current factor variation. The introduced extraction mechanism of $u0$ parameter takes into account the channel length, the width and the oxide definition shape. As the sixth parameter, we extract $M\mathrm{inv}$ which improves the accuracy of modelling transconductances in the moderate inversion regime.

The second extraction loop was performed for all seven parameters at high drain bias to account for short channel effects related to DIBL and body biasing. The threshold voltage is more sensitive as the channel length shrinks since the body bias less controls the depletion region. The additional effect on the threshold voltage is DIBL that increases with the drain bias. We introduce the extraction of $D\mathrm{sub}$ as the seventh parameter that calibrates the coefficient exponent of DIBL effect in the subthreshold region. After the extraction process, we generated the $I_D - V_G$ characteristics based on the results from direct statistical compact modeling of both original and enhanced physical set of characteristics using Spice simulator.

6.1.4 Application to 35nm device

To demonstrate the hierarchic simulation methodology, we study the RDD induced drain current variability of a realistic 35-nm physical gate length high performance bulk nMOSFET with n+ polysilicon gate [191] described in detail in [26]. The continuous doping profile for the simulated device was obtained from carefully calibrated and comprehensive process simulation using Taurus Process [192]. Calibration of the 3D atomistic DD simulator then gave good agreement with both experimentally reported $I_D - V_G$ characteristics and those obtained from Taurus device simulation. The calibration is shown in figure 6.2 in which the doping profile of the simulated device is also illustrated.

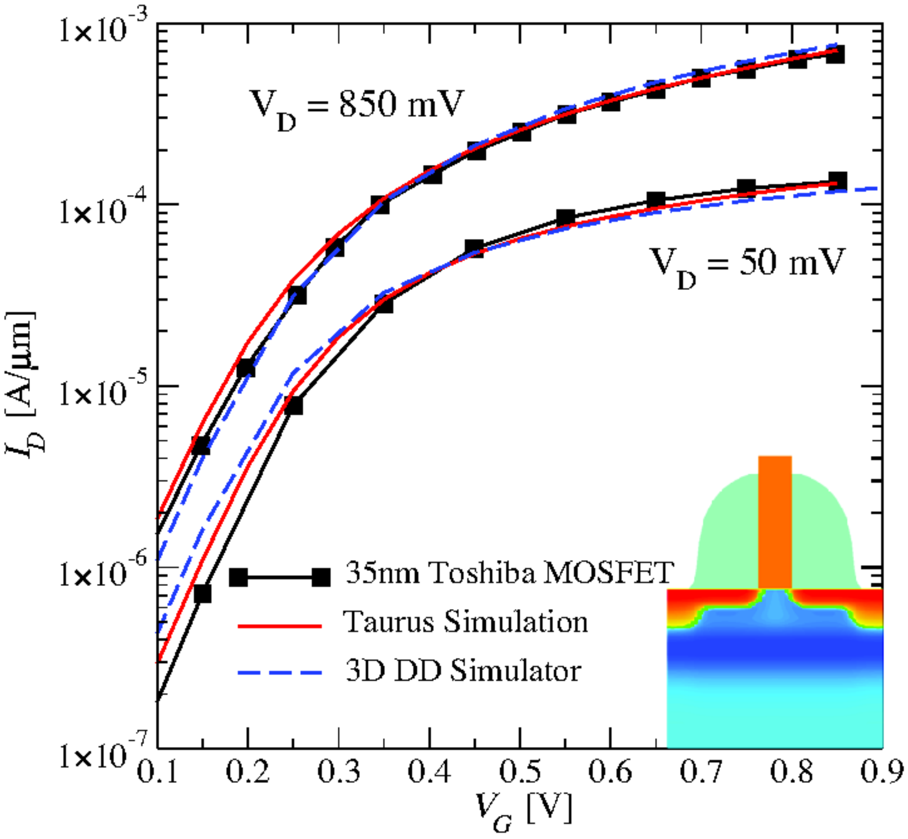

Figure 6.2: $I_D - V_G$ characteristics of the 35-nm MOSFET are shown. The doping profile of the device is shown inset.

$I_D - V_G$ characteristics obtained from self consistent MC simulation of the same uniform device are shown in figure 6.3 and show good agreement with 3D DD simulation. Within self consistent MC the coupled non-linear Poisson and density gradient solution is applied in the n+ polysicon gate in order to accurately account for polysilicon depletion in response to variation in carrier density in the substrate. Within the substrate, the solution to the linear Poisson equation is applied together with the quantum correction as described in the previous chapter.

The above described three-stage hierarchy is applied to study on-current variation due to substrate acceptor dopant distribution variation in an ensemble of 100 devices based

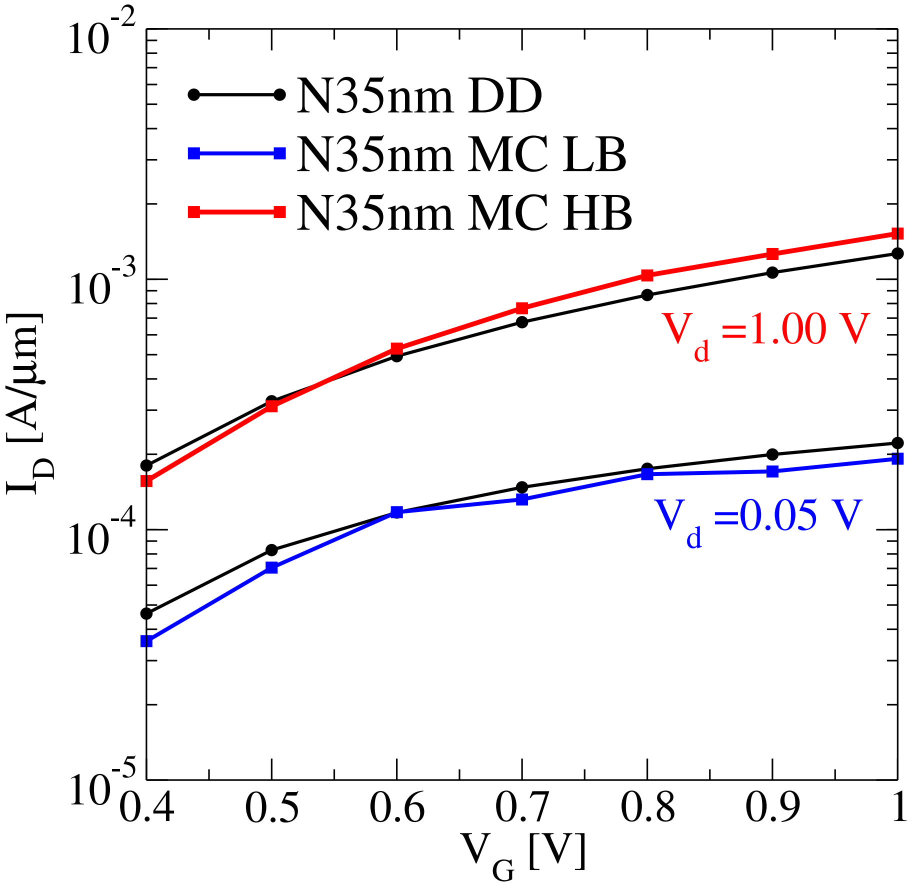

FIGURE 6.3: $I_D - V_G$ characteristics of the uniform 35-nm MOSFET obtained from MC simulation are compared to $I_D - V_G$ obtained from DD simulation at both low and high drain bias.

upon the uniform device. Discrete dopant variation within the channel was studied as it has been shown to have the greatest impact on variability at this device dimension. The large computational resources required for self-consistent statistical 3D MC simulations were provided based on the grid-computing methodology developed at the University of Glasgow in the framework of the NanoCMOS project [208]. Application and discussion of the three stages are given separately below.

6.1.4.1 First Stage: Results of initial distributions

DD simulation was initially performed at a high gate bias of 1.0 V and at both low and high drain biases of 0.05 V and 1.0 V respectively, followed by equivalent self-consistent MC simulation. The potential distributions of the devices with the highest and lowest drain currents obtained from MC simulation of the statistical sample at $V_G = 1.0V$ and

$V_D = 1.0V$ are presented in figure 6.4. The localised Coulomb potential associated with each acceptor is clearly resolved.

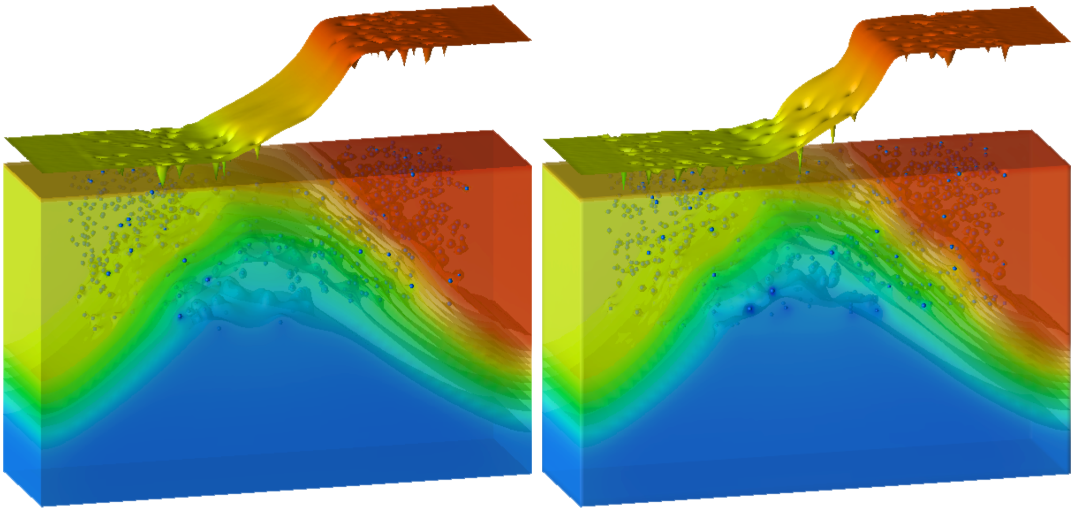

FIGURE 6.4: Electrostatic potential distribution within the channel and substrate for the 35-nm atomistic nMOSFETs with the highest (left) and lowest (right) currents.

The corresponding impact of the discrete impurities on the inversion layer electron concentration and current density is shown in figure 6.5. It is clear that in the lowest current case a crowd of dopants near the source region considerably reduces the carrier and current densities at the source, where the product of the local carrier concentration and their injection velocity determines the magnitude of the current.

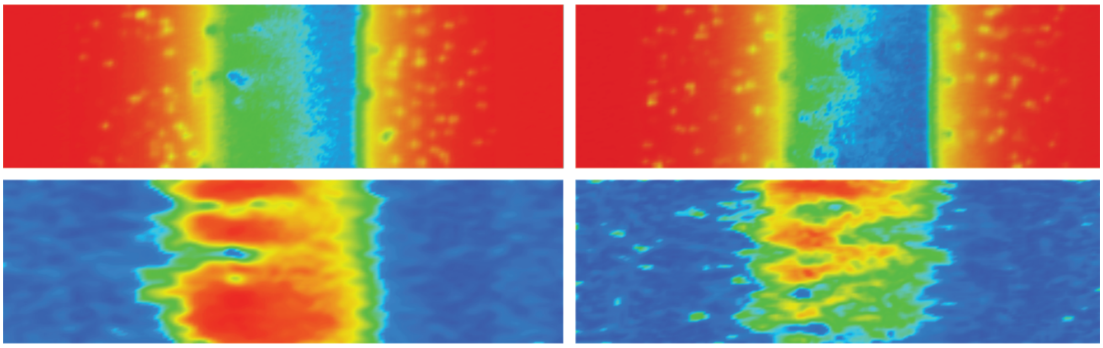

FIGURE 6.5: Electron concentration (top) and current density (bottom) within the inversion layer of devices with the highest (left) and lowest (right) current. Clearly seen are the effects of individual acceptors.

The correlation between the drain current obtained from the MC and the DD simulations at both low and high drain bias is illustrated in figure 6.6. Significantly greater variation resulting from MC simulation is observed in both cases. At low drain bias, the incorporation of transport variation in MC simulation results in an increase in the standard deviation of the on-current of roughly 100% compared with the electrostatic variation alone captured in the DD simulations. At high drain bias, the transport related increase in the variability is approximately 35%. A positive correlation between the MC and DD data is also observed in both cases, with the data points almost contained within a compact ellipse and well represented by a simple linear regression curve. The correlation highlights the underlying shared electrostatic variation, while the spread and the difference in the standard deviation at both low and high drain bias highlights the differing contributions from ionized impurity scattering. At low drain bias, within the Ohmic regime, scattering from acceptor impurities plays a dominant role and leads to the greater observed increase in current variability. While at high drain bias, in the presence of high lateral fields, ballistic transport becomes more apparent and the dominance of impurity scattering is reduced.

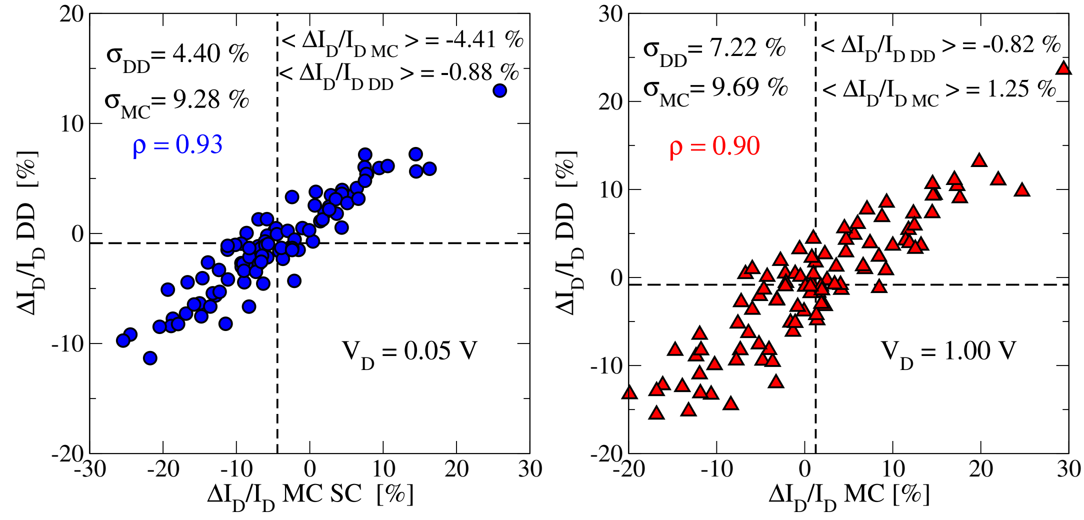

FIGURE 6.6: Percentage drain-current variation from quantum corrected MC simulation against quantum corrected DD simulation. Strong correlation at both low drain bias (left) and at high drain bias (right) is seen.

6.1.4.2 Second Stage: Calibration of DD mobility

Device by device calibration of the mobility parameters within DD simulation followed using the two-step iterative procedure outlined previously. Excellent agreement with the on-current variability obtained from MC simulation was achieved, thus allowing the simulation of enhanced $I_D - V_G$ characteristics for each device. Current-voltage characteristics obtained from the DD simulation at both low and high drain bias, before and after calibration to MC simulation, are shown in figures 6.7 and 6.8 respectively. Despite the increased on current variability, the mean drain current is preserved in the proposed calibration procedure, as shown in figure 6.9.

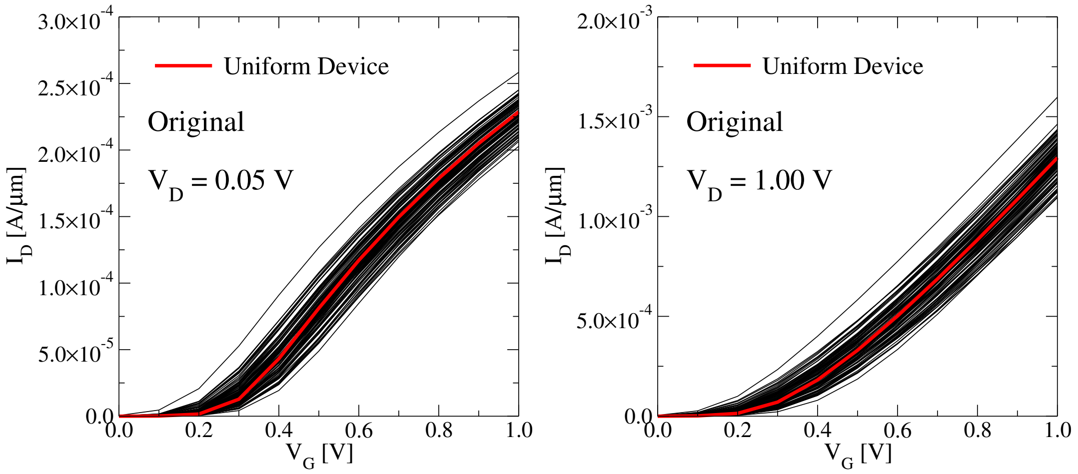

FIGURE 6.7: Original $I_D - V_G$ curves obtained from quantum corrected DD at both low drain bias (left) and high drain bias (right).

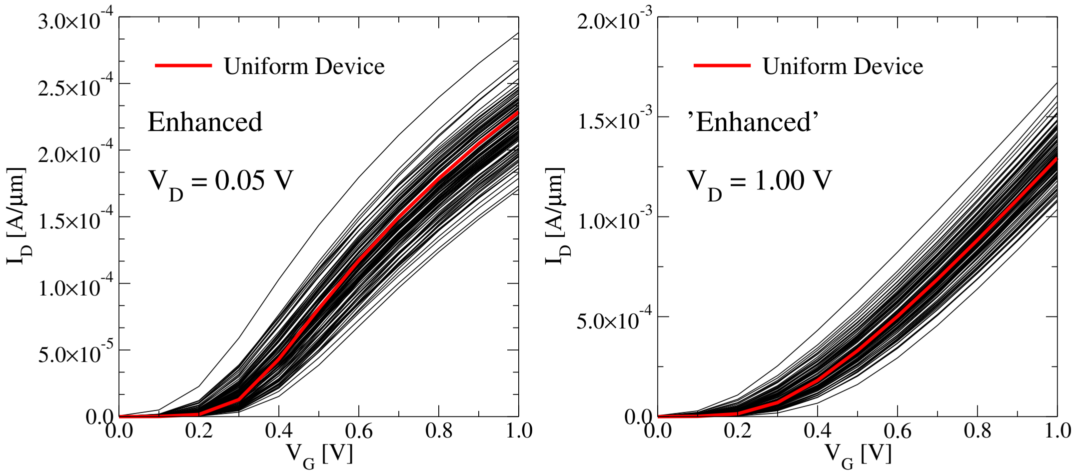

FIGURE 6.8: Enhanced $I_D - V_G$ curves at both low drain bias (left) and high drain bias (right) obtained from quantum corrected DD after calibration to MC simulation at high gate.

Figure 6.10 shows the on-current distribution for both the original and enhanced DD characteristics at high gate bias and both low and high drain bias. At both low and high drain bias the enhanced on-current distribution is flat topped and skewed to lower currents, while the original distributions has the sharper centralised peak. The enhanced on-current distributions at both low and high drain bias have the greater standard

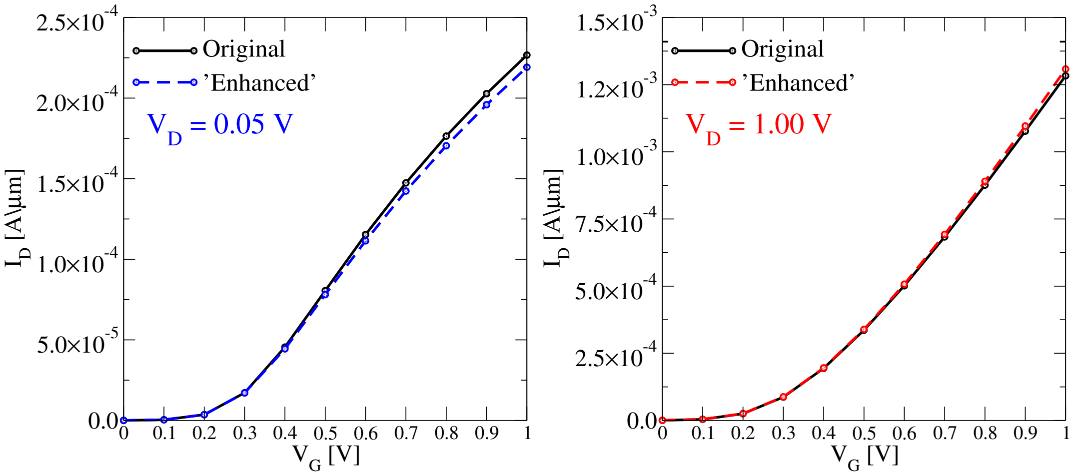

FIGURE 6.9: The mean of original and Enhanced on-current at both low drain bias (left) and high drain bias (right) obtained from original DD simulation and quantum corrected DD after calibration to MC simulation at high gate.

deviation in the on-current distributions due to transferred transport variability into the enhanced mobility models.

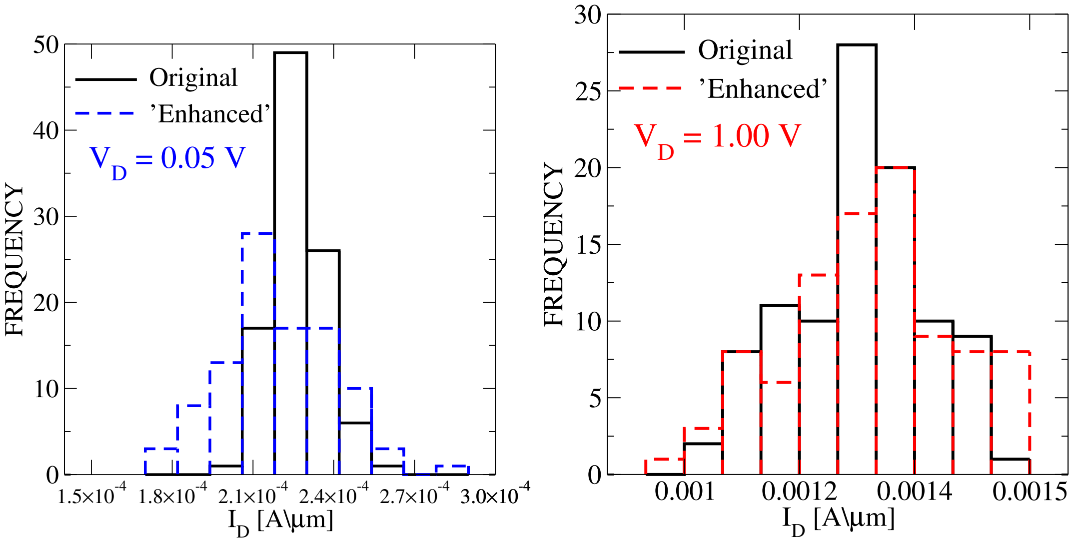

FIGURE 6.10: Distribution of on-current at high gate voltage at both low drain bias (left) and high drain bias (right) obtained from both original quantum corrected DD and after calibration to MC simulation at high gate.

Figures 6.11 and 6.12 compare gate voltage dependence of the absolute and relative standard deviations obtained from DD simulations before and after the calibration in respect of the MC simulations. The increase in current variability due to transport variability, inferred from the difference between the original and enhanced standard deviations, is strongest at drive current conditions but reduces at low gate bias. The reduction at low drain bias is from more than 200% at $V_G = 1V$ to approximately 20% at $V_G = 0.4V$. The reduction is less dramatic at high drain bias.

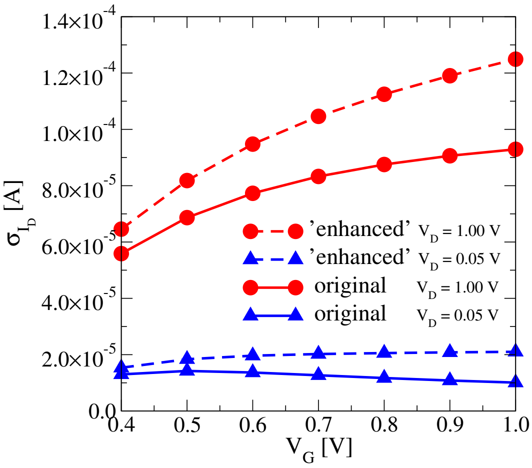

FIGURE 6.11: Standard deviation of drain-current variation as a function of gate voltage at both low and high drain and for both original and enhanced $I_D - V_G$ curves. Agreement is preserved towards the subthreshold regime.

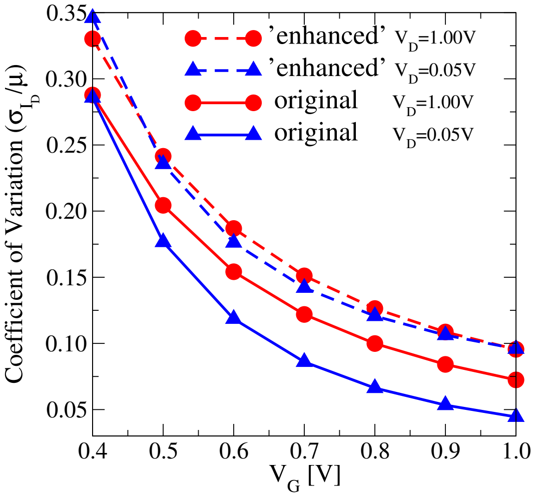

FIGURE 6.12: Coefficient of variation of drain current as a function of gate voltage showing reduced variation at higher gate biases. Also seen is increased variation within enhanced DD simulation..

The sub threshold region is relatively unaltered by the mobility calibration due to the dominance of the electrostatics in device operation in this regime. This validates the use of DD for threshold voltage variability analysis. The reduction in the relative importance of transport variability at high drain bias compared to low drain bias is associated with the reduced impact of ionised impurity scattering at high energies and an increase in ballistic propagation of carriers.

Table 6.1 compares the average values V_T and the standard deviations at high and low drain bias obtained from the DD simulation before and after the mobility calibration to the MC results. The threshold voltage distribution for the original and enhanced characteristics is shown in figure 6.13, illustrating that mobility calibration does not significantly affect V_T variability and again validating the use of DD to estimate V_T variation. This indicates that the enhanced model maintains the shape of the threshold voltage distribution at both low and high drain bias. Further, it highlights the reliability of the proposed hierarchic methodology in the subthreshold region.

	Threshold Voltage			
	Low Drain Bias		High Drain Bias	
	original	enhanced	original	enhanced
μV_T $[mV]$	272	274	160	161
σV_T $[mV]$	37.4	41.3	40.1	42.5

Table 6.1: Mean and standard deviation of the threshold voltage at low and high drain bias for both original and enhanced DD.

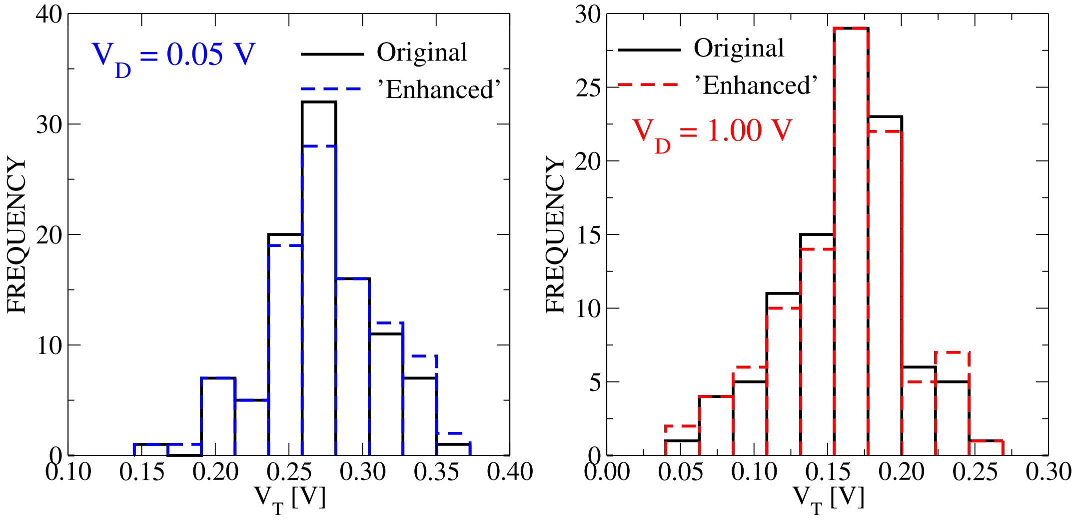

Figure 6.13: Original and enhanced V_T distribution at both low drain bias (left) and high drain bias (right) obtained from both original quantum corrected DD and after calibration to MC simulation at high gate.

The distributions of the key electrical parameters including the off current (I_{off}), subthreshold slope and DIBL obtained from original and enhanced model at both low and high drain bias are shown in figures 6.14, 6.15 and 6.16 respectively. These key figures of merit demonstrate that the distributions of the enhanced model coincide well with the original distributions. This indicates that the proposed hierarchic methodology does not significantly affect the key electrical parameters, supporting its use in statistical compact modelling.

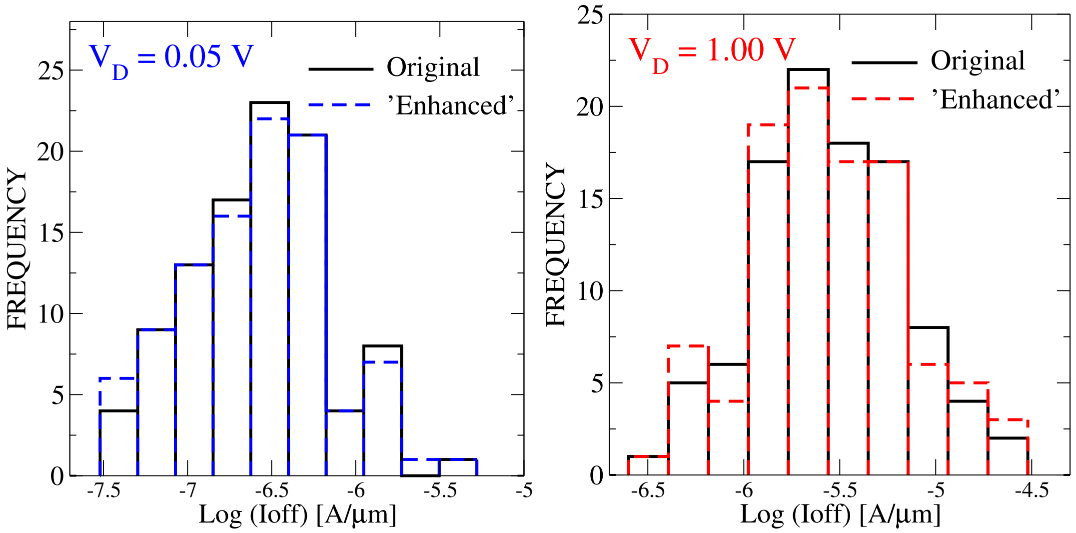

FIGURE 6.14: Original and enhanced Ioff distribution at both low drain bias (left) and high drain bias (right) obtained from both original quantum corrected DD and after calibration to MC simulation at high gate.

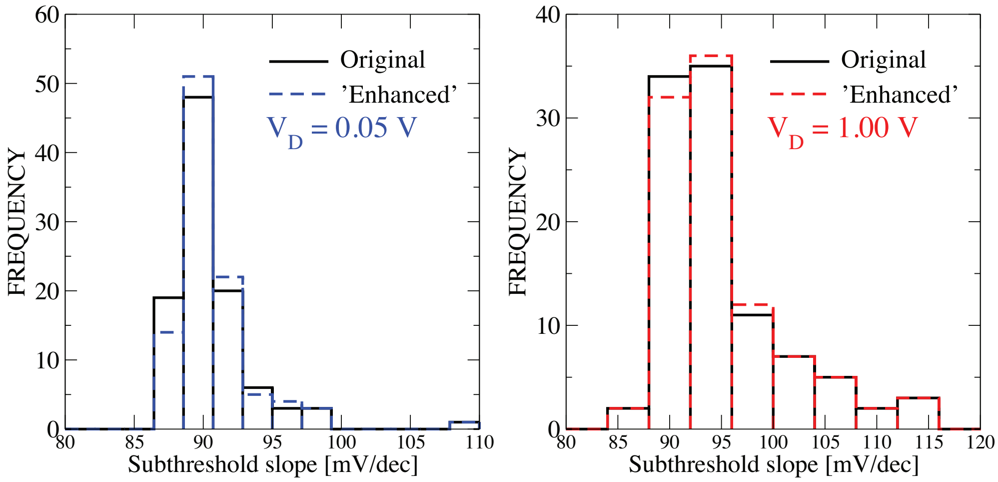

FIGURE 6.15: Original and enhanced subthreshold slope distribution at both low drain bias (left) and high drain bias (right) obtained from both original quantum corrected DD and after calibration to MC simulation at high gate.

6.1.4.3 Third Stage: compact model extraction

Following the methodology described in the previous section, statistical compact models were extracted from the DD simulated statistical set of $I_D - V_G$ characteristics both

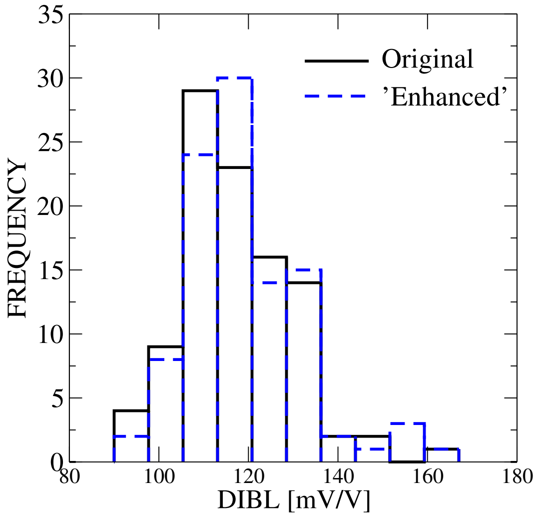

Figure 6.16: Original and enhanced DIBL distribution obtained from both original quantum corrected DD and after calibration to MC simulation at high gate.

before and after the calibration to the MC simulation results. For each compact model, the total relative RMS error of the extraction process was calculated. This was defined as the sum of the squared relative differences between drain current data points obtained by statistical 3D DD simulation and those obtained from Spice extracted compact models across the range of gate biases at both low and high drain bias.

Figure 6.17 shows the distribution of the RMS error from the extraction process for both the original and the enhanced $I_D - V_G$ characteristics. The distribution of the RMS error from compact model extraction for both cases shows similar, minimal error. The average statistical compact model error and its standard deviation are larger when the transport variability is taken into account compared to the reference DD simulations. This is expected when identical compact model parameter sets are used to capture different magnitudes of statistical variability. Still, the relatively tight error distribution of the final statistical compact model set is sufficient not only for digital but also for analogue applications.

The proposed statistical compact modelling approach accurately captures the correlation among the key electrical parameters and BSIM4 parameters while commonly used approaches to statistical compact model usually neglect the correlations among them [209–211]. The left plot in figure 6.18 clearly shows the strong positive correlation between the threshold voltage obtained from physical $I_D - V_G$ charcteristics (V_T) with the extracted compact model parameter (V_{th0}) in both the original and enhanced models.

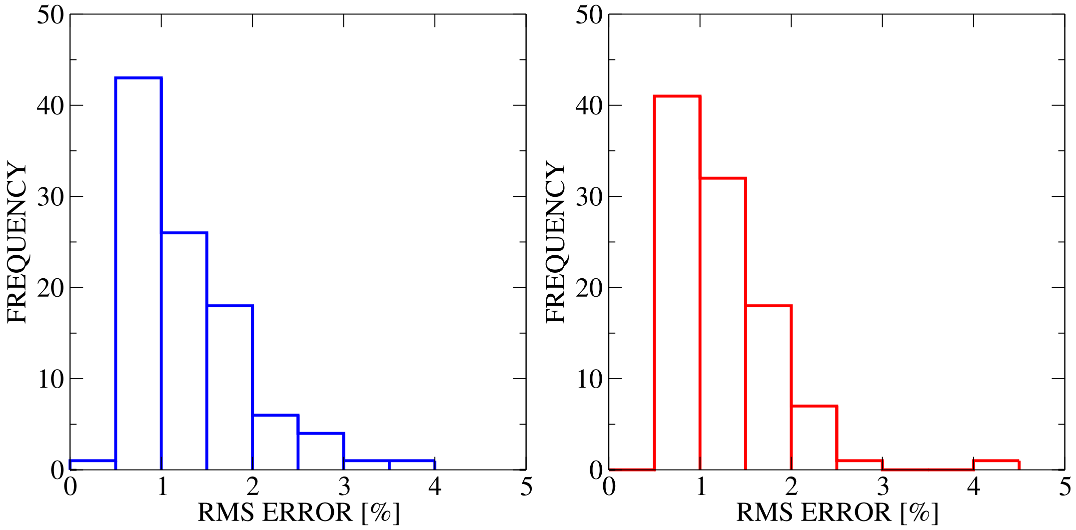

Figure 6.17: Distribution of RMS error associated with compact model extraction based upon the original $I_D - V_G$ curves (left) and the enhanced $I_D - V_G$ curves (right).

Similarly, the right plot in fugue 6.18 shows a strong negative correlation between the key electrical parameter $DIBL$ and the compact model parameter $Dsub$ in both the original and enhanced models. Both strong correlations indicates that the proposed compact model extraction strategy preserves the physical meaning of parameters compared with the results of the physical simulations. The maintenance of the correlation between key electrical parameters and BSIM4 parameters may be employed as a golden standard to generate an accurate statistical compact model based on the physical device characteristics [209, 210].

The correlation matrix (6.3) shows significant correlations between the BSIM4 parameters. The lower-left of the matrix presents the correlation coefficient associated with BSIM4 parameters extracted using the original DD device characteristics, while the upper-right presents similar results based upon extraction from the 'enhanced' characteristics. The strong correlation between certain extracted parameters limits the use of independent statistically generated compact model parameters. Such an independent extraction strategy is based upon the assumption that the distribution of compact model parameters is well approximated by uncorrelated normal distributions [212].

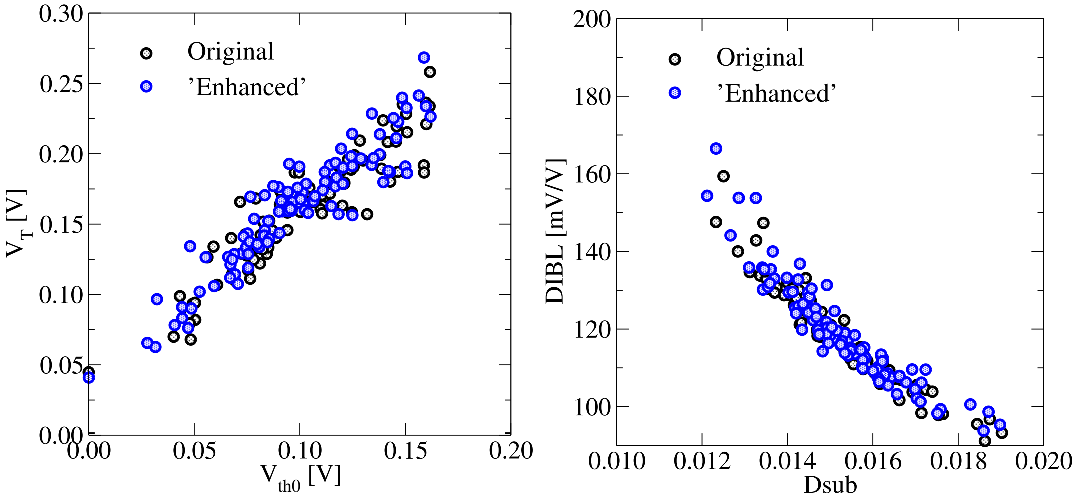

FIGURE 6.18: Correlation between key electrical parameters V_T (left) and $DIBL$ (right) with extracted BSIM4 parameters V_{th0} (left) and $Dsub$ (right) for original and 'enhanced' device characteristics. Correlation coefficient between V_T and V_{th0} are $\rho_{\text{orginal}} = 0.9229$ and $\rho_{\text{enhanced}} = 0.9332$. Correlation coefficients between $DIBL$ and $Dsub$ are $\rho_{\text{orginal}} = -0.9534$ and $\rho_{\text{enhanced}} = -0.9299$.

$$\begin{pmatrix} \mathbf{Vth0} & 0.1634 & -0.6948 & 0.1572 & 0.2605 & -0.3620 & 0.1576 \\ 0.1398 & \mathbf{Rdsw} & 0.2329 & 0.8313 & 0.4904 & 0.6587 & -0.2732 \\ -0.7429 & 0.0167 & \mathbf{Nfactor} & 0.2116 & 0.0835 & 0.5231 & -0.2232 \\ 0.3523 & 0.7941 & -0.1702 & \mathbf{Voff} & 0.3227 & 0.5184 & -0.2980 \\ 0.1343 & -0.0791 & 0.1675 & -0.1423 & \mathbf{Minv} & 0.3981 & -0.2610 \\ 0.0146 & 0.9014 & 0.1871 & 0.6628 & 0.1480 & \mathbf{U0} & -0.3777 \\ 0.1500 & -0.5727 & -0.3807 & -0.3241 & -0.5092 & -0.7851 & \mathbf{Dsub} \end{pmatrix} \tag{6.3}$$

However, the distributions of extracted BSIM4 parameters do not follow this assumption, as shown at the figure 6.19 where the distributions of 7 BSIM4 parameters extracted from both original and enhanced characteristics are seen to deviate from normality. It is evident that the shape of the left tail changes in the case of $Voff$, $Rdsw$, $Nfactor$, $Minv$ and $U0$ BSIM4 parameters, indicating that enhanced parameters are more skewed to the left side of the mean. The enhanced model has an impact on changes in kurtosis of $Rdsw$, $Nfactor$, and $Minv$ distributions. Table 6.2 shows key statistical values for both original and enhanced BSIM4 parameters. These results indicate that the enhanced model significantly change the shapes of the distributions of BSIM4 parameters. This manifests the significance of the proposed hierarchic extraction methodology in order to accurately propagate transport variability effects into statistical compact models since it significantly affects the extracted parameters which transfers, in turn, those effects into circuit simulations.

	Vth0 $[V]$		**Rdsw** $[\Omega/\mu m]$		**Nfactor**	
	original	enhanced	original	enhanced	original	enhanced
μ	0.1018	0.0980	129.8467	124.5187	1.8519	1.7617
σ	0.0327	0.0336	13.0756	18.0452	0.2598	0.2422
γ_1	-0.1750	-0.2119	0.1348	-0.6048	1.4304	1.4058
γ_2	-0.1286	-0.2061	1.1695	2.3448	2.3799	3.2633
	Voff $[V]$		**Minv**		**U0**	
	original	enhanced	original	enhanced	original	enhanced
μ	-0.0957	-0.0978	2.2172	1.8804	114.7911	97.8128
σ	0.0139	0.0128	0.4180	0.3327	19.3366	21.2811
γ_1	0.2371	0.4119	0.5402	-0.6905	0.8527	0.3442
γ_2	-0.2068	0.3618	0.4062	0.9181	1.2219	1.3040
	Dsub					
	original	enhanced				
μ	0.0154	0.0153				
σ	0.0013	0.0014				
γ_1	0.3352	0.2797				
γ_2	0.2739	0.3075				

Table 6.2: Mean (μ), standard deviation (σ), skew (γ_1) and kurtosis (γ_2)of BSIM4 parameters for both original and enhanced statistical compact models.

The above comprehensive analysis of the compact model results indicates that BSIM4 parameters are nonnormally distributed which in turn has a practical impact on circuit simulations. The violated normality assumption limits using the principal component analysis (PCA) approach [210] as a tool for direct generation of BSIM4 parameters used in large scale statistical circuit simulations. PCA provides the reconstruction of BSIM4 parameters within twofold limits. Firstly, the PCA approach limits the shape of distribution of the generated set of parameters which are constrained only to normally distributed shapes with preserving the first and second moment of distributions of original samples. Secondly, PCA does not properly account for the tails of parameter's distributions which can be accurately capture by controlling higher moments of distributions [213]. This necessitates the deployment of the correct statistical tools in order to assess the accuracy in the tails of parameter's distribution which might be captured by the preserving the higher moments. This is not the primary purpose of this work, though a detailed discussion of a statistically accurate reconstruction methodology of statistical compact model parameters is presented in [213].

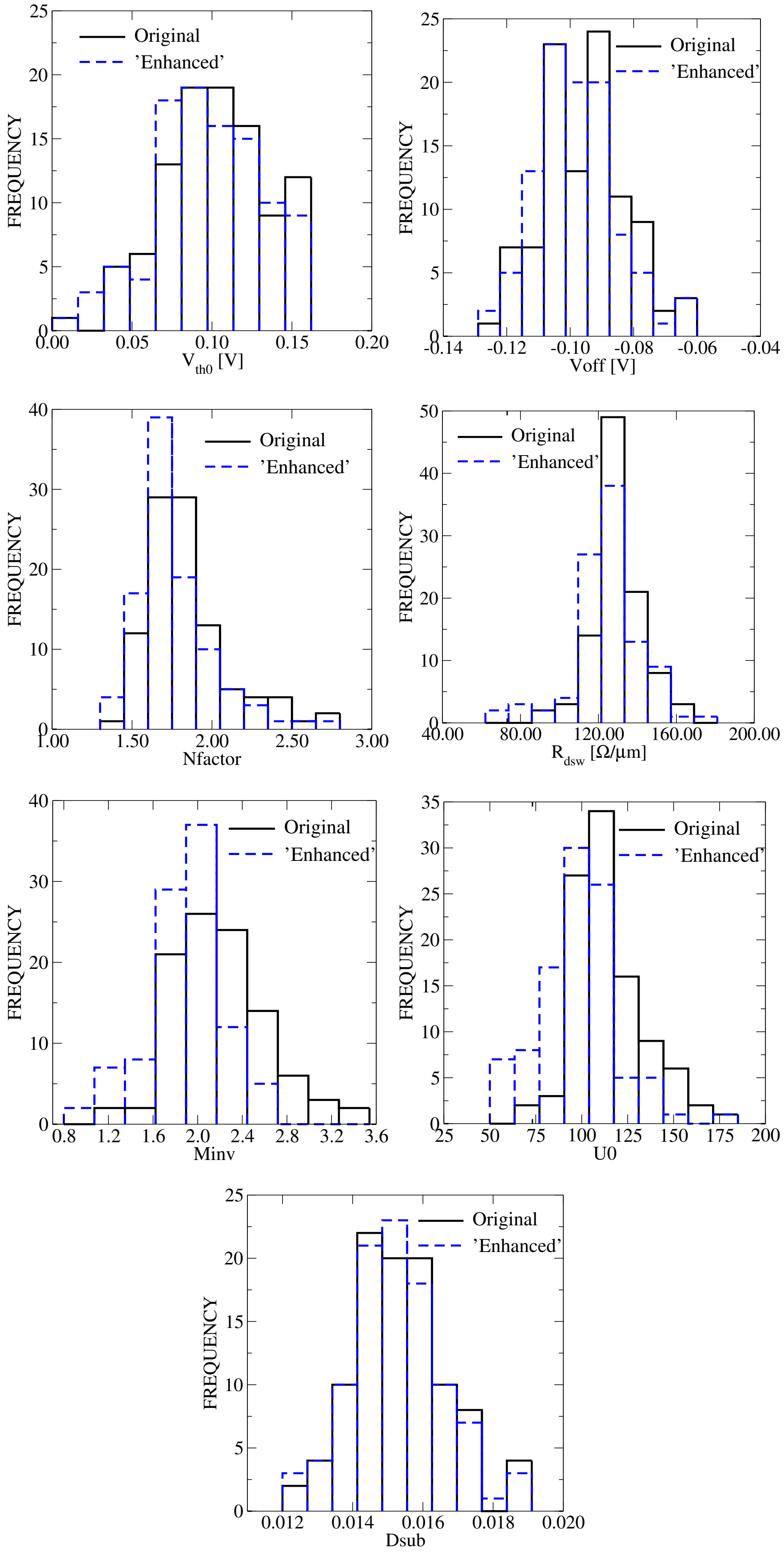

Figure 6.19: Distribution of BSIM parameters associated with compact model extraction based upon the original $I_D - V_G$ curves (black) and the enhanced $I_D - V_G$ curves (blue).

6.1.5 Simulation Strategy of the Variability in NANOCMOS Inverter

In order to determine the influence of the magnitude of the drain current variation on nano CMOS circuit performance, a 45nm technology generation inverter, shown in figure 6.20, is simulated. The inverter circuit simulations can be generally used as an indicator to estimate digital chip performance [214]. The accurate direct statistical compact modelling approach, discussed in the previous section, is used to investigate the effects of input waveform on variation of delay and power dissipation of an inverter simulation in detail under various input signal and load conditions. The input signal slew rate also affects the current trajectories [215] and this is affected by the impact of on-current variations on device characteristics which is strongly bias dependent as has been shown in the previous section.

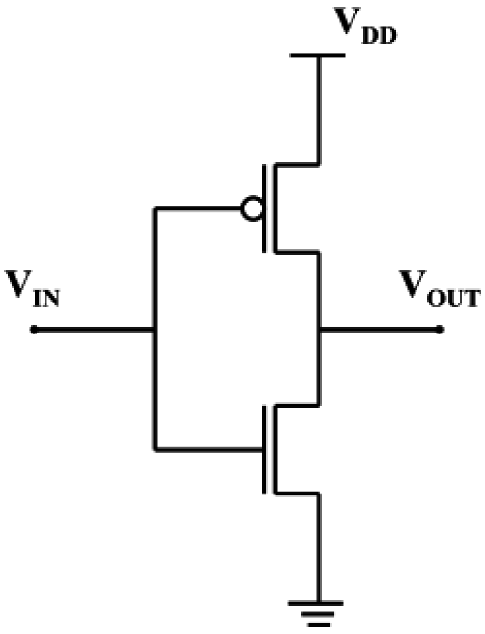

FIGURE 6.20: Schematic inverter circuit.

A minimum size nMOSFET with width ratio of 1 and a pMOSFET with width ratio of 2 are employed in the simulation study to emphasise the statistical variability induced by RDD. The larger width of the pMOSFET is introduced to balance the transfer characteristics of the inverter. The supply voltage is 1V. In order to demonstrate the effect of slew rate on inverter simulations, an ideal 2GHz symmetric clock pulse with various rise/fall times is used. There are two simulation experiments. The first experiment considers the inverter simulations with various slew rates (2, 10, 20 and 50 ps) and with the 1 unit load of $0.105fF$. The effect of various load capacitances (1, 2, 4 and 6 units) on the variation of delay and power dissipation in the inverter simulations at given slew rate 20 ps is investigated in the second simulation experiment.

The information obtained from the compact model extraction of statistical nMOSFET, discussed in the previous section, has been implemented in the HSPICE inverter circuit simulations. The pMOSFET device is defined using the compact model parameters extracted from a uniform pMOSFET device. HSPICE simulations were carried out for a statistical sample of 100 random inverter circuits. Comparison was then made between the simulation of inverters obtained from the original and enhanced compact model cards.

6.1.6 Results and Discussion

In the first inverter study, the effect of different input rise time conditions with load of 1 unit on the variation of the fall time propagation delay t_{dHL} was investigated. The mean values of t_{dHL} as a function of the rise time are plotted in 6.21 for both original and enhanced compact model cards. As expected, the mean values increase almost linearly with the increase of the input rise time. Figure 6.21 shows that the higher slew rate indicates longer delay since the transistor spends less time in strong inversion region during the switching. The mean delays obtained from both original and enhance compact model cards are almost identical. The same is clearly seen for mean values of dissipated energy.

The normalized standard deviation σ/μ of t_{dHL} under different input rise time slopes with load of 1 unit are shown in figure 6.22. The values of σ/μ increases with increasing input rise time, with the variation at 50 ps more than twice that at 2 ps. The difference between the variation from original and enhanced models is seen to slightly fan out with increasing input rise time.

The normalized standard deviation σ/μ of t_{dHL} and E versus different loads under a 20 ps input rise time slope is illustrated in figure 6.23. The normalized standard deviation decreases with increasing load. Loads of 4 and 6 units are almost identical, inidcating that σ/μ is almost saturated for higher loads. This indicates that increasing load capacitance will improve the variability behavior since it will push the switch trajectory

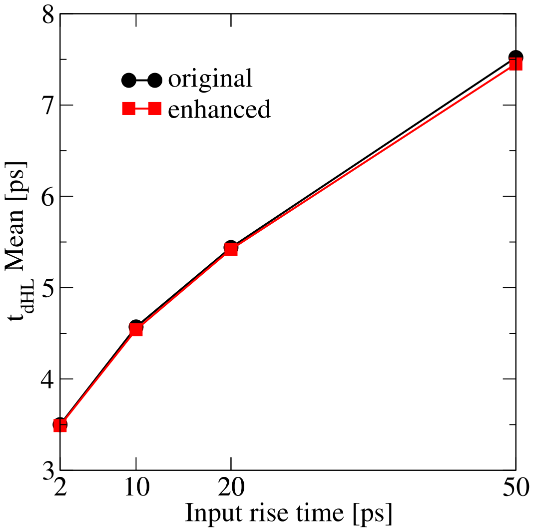

FIGURE 6.21: Statistical analysis of mean values of t_{dHL} (left) and dissipated energy E (right) versus different input rise times.Mean values of both original and enhanced compact model cards are compared.

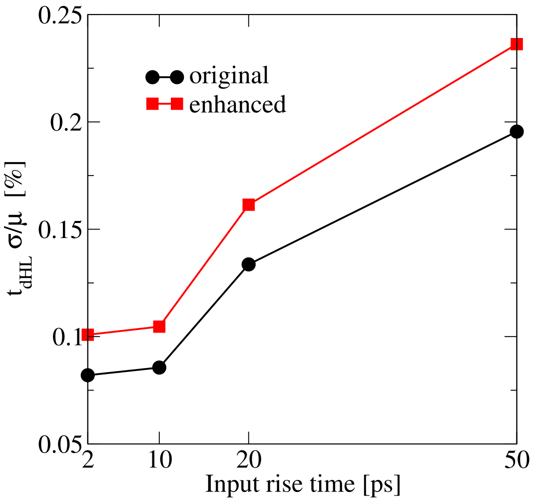

FIGURE 6.22: Statistical analysis of Normalized values of σ/μ of t_{dHL} versus different input rise times.Mean values of both original and enhanced compact model cards are compared.

up to the high gate bias regime. Using a load of 1 unit as an example, the normalized standard deviation of t_{dHL} of the enhanced model is reduced from 16% to roughly 13% for the original model. The spread between σ/μ of t_{dHL} of the enhanced and original models is approximately 30% for all load capacitances. This inidicates that the enhanced model shows 30% higher variability than original. This proves that statical variability of on-current plays crucial role in changes of device switch trajectory.

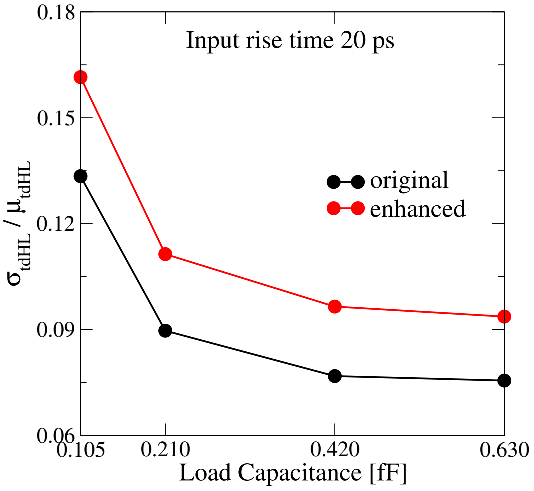

FIGURE 6.23: Statistical analysis of Normalized values of σ/μ of t_{dHL} various load capacitances for 20 ps input rise time. Normalized values of σ/μ of both original and enhanced compact model cards are compared.

Generally, the power dissipation in digital circuits can be divided into static, dynamic and short circuit [216] dissipation. Static dissipation is calculated in off condition in which the subthreshold and gate leakage current flow through the supply. Dynamic dissipation depends on the size of the capacitive component of the load while the short circuit dissipation is caused by existence of a DC path for the current flowing from supply to ground during the switching. Since the input rise time determines the amount of time in which the inverter stays at short circuit state, it significantly affects the on power dissipation variation. Variation in the energy dissipation in our case is mostly introduced by short-circuit and dynamic dissipation since subthreshold and gate leakage dissipation is negligible.

Figure 6.24 shows the mean values of total energy dissipation during a full input cycle under different input rise time slopes with a load of 1 at both original and enhanced compact model cards. The average energy dissipation is practically the same for both cases and increase with increasing input rise time.

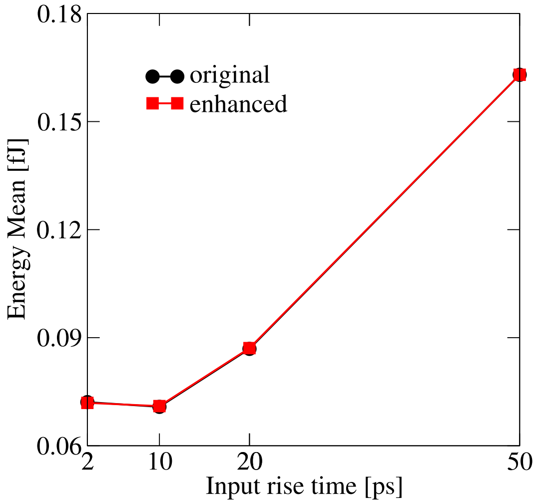

FIGURE 6.24: Statistical analysis of mean values of dissipated energy E versus different input rise times.Mean values of both original and enhanced compact model cards are compared.

The normalized standard deviation σ/μ of the energy dissipation from both the original and the enhanced model versus different input rise time slopes with load of 1 is illustrated in figure 6.25. The σ/μ increases with increasing input rise time for both the original and enhanced models. The difference between values of σ/μ for both original and enhanced models increases with increasing input rise time.

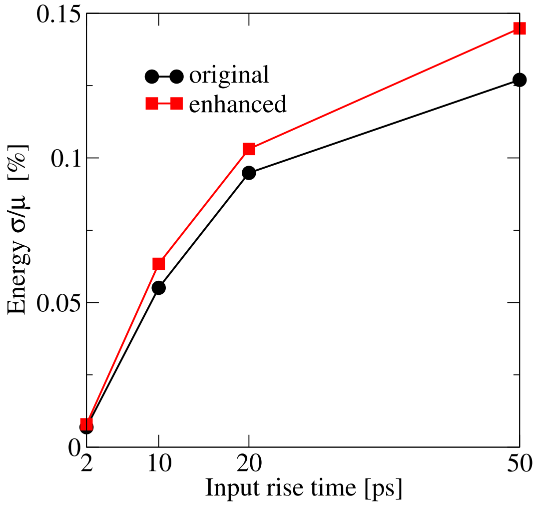

FIGURE 6.25: Statistical analysis of Normalized values of σ/μ of dissipated energy E versus different input rise times.Mean values of both original and enhanced compact model cards are compared.

The normalized standard deviation σ/μ of the energy dissipation versus different loads under 20 ps input rise time slope are illustrated in figure 6.26. As expected, the maximum

σ/μ of energy dissipation in both cases occurred at the lowest load of 1 unit which represents the worst-case energy variation in reality. Higher variations can be clearly seen in lower loads, while in higher loads variations becomes almost load independent.

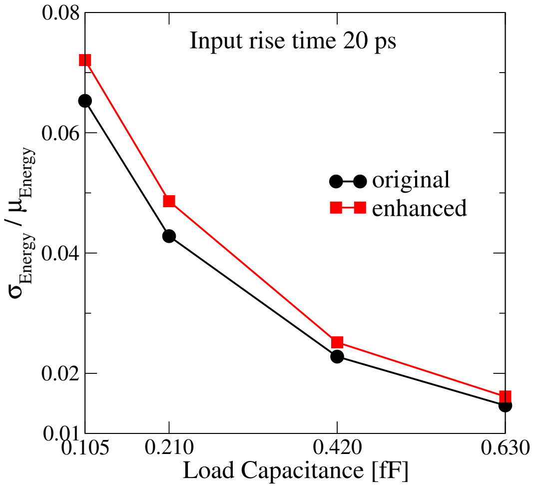

FIGURE 6.26: Statistical analysis of Normalized values of σ/μ of E various load capacitances for 20 ps input rise time. Normalized values of σ/μ of both original and enhanced compact model cards are compared.

6.2 Conclusions

Significantly larger RDD induced drain current variability was observed in the simulation of a 35-nm bulk nMOSFET using quantum corrected MC when compared with equivalent DD simulation. The increased transport related variability was successfully transferred to DD simulations by a self-consistent calibration of the mobility models at low and high drain bias. This enabled the efficient simulation of enhanced target device characteristics for the statistical ensemble from which accurate statistical compact models were extracted.

This provides an accurate compact models extraction methodology transferring results from accurate physical variability simulation into statistical compact models suitable for statistical circuit simulation. This hierarchic strategy can be used for reliable statistical standard cell characterisation that is still a research hotspot.

Chapter 7

Conlucsion

An efficient hierarchic simulation methodology that accurately models MOSFETs, subject to intrinsic parameter variations, over a complete range of bias conditions and enables the transfer of statistical parameter distributions to compact models and subsequent statistical circuit analysis has been developed and demonstrated.

The proposed methodology combines for the first time the accuracy of Monte Carlo (MC) simulation at high gate bias with the efficiency of Drift Diffusion (DD) simulation at low gate bias. It has been shown that quantum corrected 'atomistic' MC simulations with the inclusion of *ab initio* scattering from discrete random dopants, capture significant additional on-current variation compared with DD. This is due to the inclusion of transport variation from position dependent scattering not captured in DD simulation, which resolves well only the electrostatic operation of devices and accurately models the sub-threshold regime. Self consistent recalibration of DD mobility models on an individual device basis to match the MC results allows this increased on-current variations to be incorporated in DD. It was shown that such recalibration have little impact on the subthreshold distribution, highlighting the success of our approach to incorporate transport variation effects in DD. Complete sets of 'enhanced' DD $I_D - V_G$ characteristics were then simulated from which compact model extraction was performed. The incorporation of additional, physically based, on-current variation in industry standard compact models and subsequent statistical circuit analysis was the major motivation and success of this work.

This work focused on random discrete dopant (RDD) induced drain current variation as this is currently the major source of intrinsic device variability in conventional MOSFETs. RDD induced transport variation may be introduced in *ab initio* MC directly via the carrier-impurity interaction resolved through the real space trajectories of the MC carriers in the Coulomb potential landscape of the individual impurities. This has been described in the past but was reliant upon an analytical short range correction to the mesh resolved force and had not been applied to quantum corrected MC simulation using the density gradient algorithm. Here, the use of the density gradient (DG) effective quantum potential to include both quantum confinement effects and the carrier-impurity interaction in a consistent and efficient manner was presented. The introduction of the carrier-impurity interaction mediated via the mesh resolved DG quantum potential was introduced in chapter 4 and validated by comparison with Rutherford scattering. The simulated scattering angle dependence upon impact parameter showed good agreement with the analytical Rutherford result and with simulated scattering using the previously used short-range correction model. The comparison in both cases strongly suggested the suitability of the DG resolved interaction in self-consistent *ab initio* MC simulation. Further validation was provided through simulation of the doping concentration dependence of bulk mobility.

Having successfully demonstrated the accuracy of utilising the DG effective quantum potential for *ab initio* ionised impurity scattering, the effects of random discrete dopant fluctuation on on-current variation in a series of well scaled contemporary n-MOSFETs were comprehensively studied following a series of statistical simulations at both low and high drain bias. In all cases, increased on-current variation associated with additional transport variation in MC was observed compared with DD. Additional variation in comparison to classical MC, due to reduced screening when quantum effects are taken into account, was highlighted. The relative importance of transport and electrostatic variation at each device dimension was inferred, highlighting the importance of transport variation at low drain bias and the electrostatic influence in the near-ballistic regime at high drain bias.

A comprehensive statistical analysis of the on-current distributions obtained from MC and DD was described in Chapter 5 and applied separately to the above results obtained at low and high drain bias for each of the device dimensions. In addition to basic statistical measures, such as the mean, standard deviation, skew and kurtosis, the statistical confidence intervals were introduced to assess the simulation accuracy. Results were scrutinised using one graphical and two analytical normality tests. The statistical confidence intervals indicated moderate departure from normality. The normal behaviour of both DD and MC simulation results was confirmed for each of the scaled device. It should be noted that the Jarque-Bera test has two significant drawbacks that may affect results. Firstly, the asymptotic distribution of Jarque-Bera test statistics holds only for very large samples, clearly not the case for the sample sizes of 50 used here. Secondly, the test uses the empirical skewness and kurtosis which are subjected to sampling errors. With respect to this, we have applied Shapiro-Wilk test which belongs among the most reliable test for normality of small and medium sample size. Both tests provided only one of piece of evidence of normality test. Additional simulation results would be needed for more accurate analysis.

Two statistical models were constructed based on a regression analysis in order to accurately classify and assess the effects of the random discrete dopants on drain current fluctuations into their relative electrostatic and transport contributions. It was assumed that DD simulation accounts for the entire electrostatic variation and that this is identically recovered within MC. The analysis also took into account the statistical dependence of DD and MC results. The proposed models were specifically designed to distinguish the electrostatic and transport variability contributions from simulation results. Both models highlighted the ratio of transport variability to the overall on-current variability. They both showed that the ratio of transport variability decreases with decreasing channel length. Both models indicated that the presence of quantum corrections had a significant impact on the transport variability in longer channel devices, while the electrostatic effects were dominant at smaller channel lengths.

The novel incorporation of the additional transport variation observed in MC into efficient DD simulation was discussed in Chaper 6. This was achieved through a self-consistent calibration of the DD mobility models, on an individual device basis, at low and high drain bias but at a single, high, gate bias. This then allowed the efficient simulation of accurate 'enhanced' device characteristic followed by the extraction of statistical compact models. This forms the three-stage hierarchic simulation strategy adopted for the remainder of the work presented.

Again, RDD induced drain current variation within a realistic 35nm nMOSFET was used to illustrate the developed technique. Simulations were performed for an ensemble of 100 randomly generated devices at a high gate bias of 1.0 V and low and high drain biases of 0.05 V and 1.0 V respectively. Following DD mobility calibration, the enhanced $I_D - V_G$ curves resulted in increased drain current variability compared with the original DD results, as expected. The threshold voltage distribution for the original and enhanced characteristics however remained unchanged, indicating that mobility calibration did not significantly affect V_T variability and validating the use of DD to estimate V_T variation. The BSIM4 statistical compact modelling approach was presented and used to extract compact model parameters obtained from the enhanced I_D-V_G characteristics. A strong correlation between the key electrical parameters and compact model parameters in both the original and enhanced models indicated that the proposed compact model extraction strategy preserves the physical meaning of those parameters. It was found, however, that the enhanced model significantly altered the shapes of the distributions of BSIM4 parameters due to the inclusion of transport variability. This highlights the fundamental importance of this hierarchic extraction methodology. The propagation of transport variability into statistical compact models significantly affects the extracted parameters which transfers, in turn, those effects into circuit simulations. This methodology provides an accurate framework allowing to transfer transport variability from the level of physical simulations via compact model extraction to transistor-level circuit simulation.

7.1 Future Work

Extension of this work to include other sources of *ab initio* scattering and the continued investigation of parameter fluctuation would be useful in order to further establish the relative importance of transport and electrostatic variation in each case. Within this work *ab initio* ionised impurity scattering has been successfully implemented using the density gradient effective quantum potential. A natural extension would be the inclusion of *ab initio* surface roughness scattering in order to account for transport variations associated with the random pattern of the interface in individual transistors. Additionally, the employment of high-κ metal gate might be useful extension of this work, since its variations in the local dielectric value introduces the surface potential variation which can make the certain impact on carrier's transport through channel.

Appendix A

Statistical Analysis of Drain Current Variability : 25 nm MOSFET

A.1 Descriptive Statistical Results at Low Drain Bias

The basic measures of descriptive statistics for the drain current variation obtained from DD and MC simulations at low drain bias and for the scaled 25nm device are presented in table A.2. In all cases the DD simulations result in larger currents when compared with the equivalent MC results, the mean DD current being approximately twice that of MC. However, a higher standard deviation from MC simulation is evident and indicates that data are more spread out than DD results.

	25 nm Device : Simulations at Low Drain Bias	
	DD	MC
$\mu\ [A\mu m^{-1}]$	$(1.60 \pm 0.01) \times 10^{-4}$	$(8.2 \pm 0.2) \times 10^{-5}$
$\sigma\ [A\mu m^{-1}]$	$(1.0 \pm 0.1) \times 10^{-5}$	$(1.6 \pm 0.2) \times 10^{-5}$
γ_1	-0.16	0.00
γ_2	-0.53	0.41

Table A.1: The values of the mean, standard deviation, skewness and kurtosis of drain currents results obtained from both DD and MC simulations at low drain bias of 25 nm device.

31 and 37 of the 50 devices from DD and MC simulations respectively have drain current values within the range of σ from the mean. Almost all devices from both DD and MC simulations lie within the range of 2σ, with only two from DD and one from MC falling far outside that range. Thus, both DD and MC results at low drain bias show fair variability across the sample.

The coefficient of variation for MC is obtained as $CV = 19.3\%$, while DD only has $CV = 6.5\%$. CV coefficient indicates the higher variations in MC results than in DD.

Both DD and MC results are negatively skewed. DD results are platykurtic, while MC results are leptokurtic. The skewness indicates little departure from symmetry in both DD and MC results. The distribution of DD results has moderate flat-topped shape, while the distribution of MC results shows a sharper peak than normal distribution.

Table A.2 presents the confidence intervals of the above estimated statistical parameters. The confidence intervals of $\langle I_{D\ MC} \rangle$ and $\langle I_{D\ DD} \rangle$ indicate almost coincidence with a symmetric standard normal approximation since $R \backslash L$ ratio values are almost one. The confidence intervals of $\sigma I_{D\ MC}$ and $\sigma I_{D\ DD}$ indicate moderate departure from the asymmetry compared with the standard normal approximation since $R \backslash L$ ratios are moderately higher than one.

	25 nm Device : Simulations at Low Drain Bias			
	DD		MC	
	95% Confidence Interval	$R \backslash L$	95% Confidence Interval	$R \backslash L$
μ $[A\mu m^{-1}]$	$[1.57, 1.63] \times 10^{-4}$	0.97	$[7.74, 8.60] \times 10^{-5}$	0.99
σ $[A\mu m^{-1}]$	$[0.88, 1.23] \times 10^{-5}$	1.30	$[1.27, 1.93] \times 10^{-5}$	1.32
γ_1	$[-0.96, 0.60]$	0.94	$[-1.09, 1.10]$	1.01
γ_2	$[-1.07, 0.19]$	1.65	$[-0.44, 1.48]$	1.79

Table A.2: 95% nonparameric ABC confidence interval of mean value, standard deviation, skewness and kurtosis compute for 25 nm device at low drain bias.

Further, table A.2 shows that the zero values of skewness and kurtosis of DD and MC simulation results lie within the range of the 95% confidence interval. This leads to acceptance of the null hypothesis of the confidence interval normality test for both skewness and kurtosis which means that data might be drawn from normal distributed population.

Additionally, Q-Q plots of the simulation results, shown for both DD and MC in figure A.1, are approximating linear, supporting the suggestion that the data are normally distributed. In the DD (left) plot, two outliers are evident at the low end of the range with one at the high end. In the MC (right) plot, two outliers are evident at the low end of the range while two are seen at the high end.

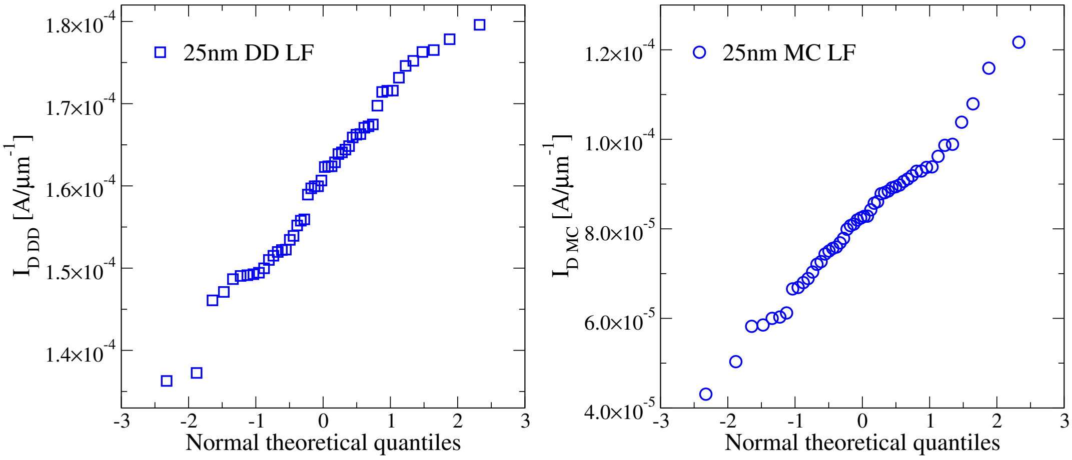

Figure A.1: Q-Q plot for DD (left) and MC (right) simulation results at low drain bias of 25 nm device.

Table A.3 presents the normality test results. For all cases, the p-values are greater than the chosen significance level $\alpha = 0.05$ so the null hypothesis that DD and MC simulations results come from a normally distributed population is accepted.

	25 nm Device : Simulations at Low Drain Bias			
	Normality test			
	DD		MC	
	Test Statistics	p-value	Test Statistics	p-value
Shapiro-Wilk	0.98	0.37	0.99	0.91
Jarque-Bera	0.94	0.63	0.13	0.94

Table A.3: Normality test for 25 nm device at low drain bias.

A.2 Descriptive Statistical Results at High Drain Bias

The basic statistic of drain current values obtained from DD and MC simulations at high drain bias are presented in table A.4 For all devices, the DD simulations at high drain bias result in larger currents when compared with the equivalent MC results, and the mean current over the 50 devices is an additional approximately 4.5 times over the mean from MC.

	25 nm Device : Simulations at High Drain Bias	
	DD	MC
μ $[A\mu m^{-1}]$	$(6.05 \pm 0.09) \times 10^{-3}$	$(1.32 \pm 0.03) \times 10^{-3}$
σ $[A\mu m^{-1}]$	$(6.8 \pm 0.7) \times 10^{-4}$	$(2.1 \pm 0.2) \times 10^{-4}$
γ_1	-0.04	0.01
γ_2	-0.57	-0.10

Table A.4: The values of the mean, standard deviation, skewness and kurtosis of drain currents results obtained from both DD and MC simulations at high drain bias of 25 nm device.

33 and 34 of the 50 devices from DD and MC have the drain current value within σ of the mean. Almost all devices in each case lie within the range of 2σ, while only three from DD simulations and one from MC simulations fall far outside this range. Thus, both DD and MC results at high drain bias show moderate variability across the sample.

The values of standard deviation are presented in table A.4.The coefficient of variation for MC is obtained as $CV = 15.7\%$, while DD only has $CV = 11.1\%$. Despite the fact that the standard deviation of DD results is larger than MC results the CV coefficient indicates the higher variations in MC results than in DD.

Further, table A.4 shows that the DD results are negatively skewed while MC results showsa positive value of skew. Both DD and MC results are platykurtic. The skewness indicates almost the same symmetry as normal distribution. The distribution of DD results has a moderate flat-topped shape while the distribution of MC results shows very little departure of the peak shape from a normal distribution.

Table A.5 presented the confidence intervals of the above estimated statistical parameters. The confidence intervals of $\langle I_{D\ MC} \rangle$ and $\langle I_{D\ DD} \rangle$ are almost identical with a standard normal approximation since $R \backslash L$ ratio values is nearly one. The confidence intervals of $\sigma I_{D\ MC}$ and $\sigma I_{D\ DD}$ indicate moderate departure from the asymmetry compared with the standard normal approximation since $R \backslash L$ ratios are moderately higher than one.

Further, the table A.5 shows that the zero values of skewness and kurtosis of DD and MC simulation results lie within the range of the 95% confidence interval. The null hypothesis of the confidence interval normality test for both skewness and kurtosis is then again accepted. Therefore, as with previous observations, the data might be drawn from normally distributed population.

	25 nm Device : Simulations at High Drain Bias			
	DD		MC	
	95% Confidence Interval	$R\backslash L$	95% Confidence Interval	$R\backslash L$
μ $[A\mu m^{-1}]$	$[5.86, 6.24] \times 10^{-3}$	0.99	$[1.27, 1.38] \times 10^{-3}$	1.00
σ $[A\mu m^{-1}]$	$[5.71, 7.91] \times 10^{-4}$	1.21	$[1.71, 2.48] \times 10^{-4}$	1.20
γ_1	$[-0.83, 0.73]$	0.96	$[-0.95, 0.86]$	0.89
γ_2	$[-1.04, 0.08]$	0.96	$[-0.76, 0.75]$	1.74

Table A.5: 95% nonparameric ABC confidence interval of mean value, standard deviation, skewness and kurtosis compute for 25 nm device at high drain bias.

Q-Q plots for simulation results at high drain bias are plotted in figure A.2. In the DD (left) plot, one outlier is evident at the high end of the range and two are at the low end. In the MC (right) plot, five outliers are evident at the high end of the range and three are at the low end of the range. Both plots are approximating linear, suggesting that the data are normally distributed. The plots are not completely linear due to small sample size.

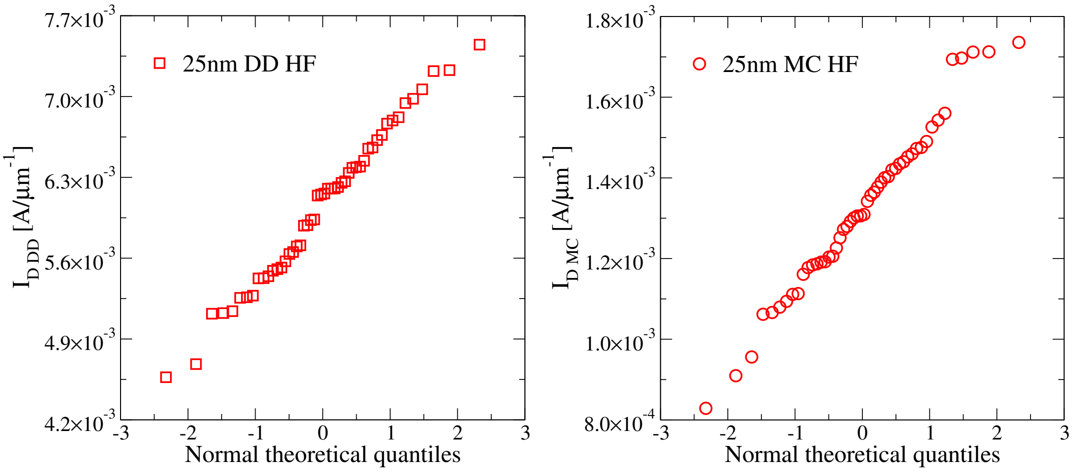

Figure A.2: Q-Q plot for DD (left) and MC (right) simulation results at high drain bias of 35nm device.

Table A.6 finally presents results for the normality test. For all cases, the p-values are greater than the chosen significance level $\alpha = 0.05$ so, again, the null hypothesis that DD and MC simulations results come from a normally distributed population is accepted.

	25 nm Device : Simulations at High Drain Bias			
	Normality test			
	DD		MC	
	Test Statistics	p-value	Test Statistics	p-value
Shapiro-Wilk	0.99	0.78	0.98	0.66
Jarque-Bera	0.83	0.66	0.09	0.96

Table A.6: Normality test for 25 nm device at high drain bias.

A.3 DD versus MC : Percentage Change in Current

The uniform drain current values are presented in table A.7. From this it can be seen that both atomistic DD and MC simulations result in a reduction in average current compared with uniform cases.

	25 nm Device	
	Uniform Drain Currents	
	Low Drain Bias	High Drain Bias
$I^u_{D\ DD}$ $[A\mu m^{-1}]$	1.65×10^{-4}	6.28×10^{-3}
$I^u_{D\ MC}$ $[A\mu m^{-1}]$	9.07×10^{-5}	1.38×10^{-3}

Table A.7: Uniform currents obtained from DD and MC simulations of 25 nm device.

Scatter plots of the percentage change in current for both DD and MC at both low and high drain bias and for all 50 devices are presented in figure A.3. Higher correlation ($\rho = 0.90$) at high drain highlights the importance of electrostatic effects, while at low drain the lesser correlation ($\rho = 0.76$) stress the increased relative importance of transport variations.

37 of the 50 devices from MC simulation at low drain bias show reduced current while the number of devices slightly decrease to 32 in DD simulation at low drain bias. 20 of the 50 devices from MC simulation at low drain bias show greater or approximately similar reduction in current as the device with maximum reduction in current from DD simulation at low drain bias. 6 of the 50 devices from MC simulation at low drain bias show greater or approximately similar increase in current as the device with maximum increase in current from DD simulation at low drain bias. The absolute value of the largest increase in current in MC at low drain bias is seen to be fairly lesser (approximetly 53%) than the absolute value of the largest reductions in current seen in MC. The highest reductions in current in DD is moderately larger (approximetly 90%) than the largest increase in current seen in DD.

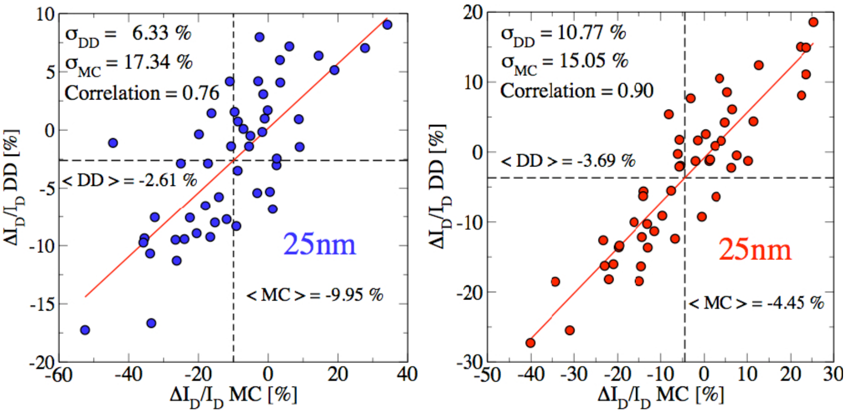

FIGURE A.3: Scatter plots of percentage drain-current variation from MC simulation against DD simulation, both including quantum corrections.The statistical ensemble is shown along with a linear regression line.The correlation at high (red) and low (blue) drain is seen.

Further, the standard deviation of the percentage change in current variation calculated from DD at low drain bias is $\sigma\Delta I_{D\ DD} = 6.33\%$, while standard deviation from MC is $\sigma\Delta I_{D\ MC} = 17.34\%$, as illustrated in figure A.3.

30 of the 50 devices from MC simulation at high drain bias show reduced current while the number of devices fairly increases to 32 devices from DD at high drain bias. 4 of the 50 devices from MC simulation at high drain bias show greater or approximately similar reduction in current as the device with maximum reduction in current from DD simulation at high drain bias. 4 of the 50 devices from MC simulation at high drain bias show greater or approximately similar increase in current as the device with maximum increase in current from DD simulation at high drain bias. The absolute value of the largest reductions in current in MC at high drain bias is seen to be fairly larger (approximately 58%) than the absolute value of the largest increase in current seen in MC. The highest reductions in current in DD at high drain bias is moderate larger (approximetly 47%) than the largest increase in current seen in DD. The higher variations in MC over DD can again be clearly seen.

The standard deviation of the percentage change in current variation calculated from DD at high drain bias is $\sigma\Delta I_{D\ DD} = 10.77\%$ while standard deviation from MC is $\sigma\Delta I_{D\ MC} = 15.05\%$, as presented in figure A.3.

The magnitude of the MC percentage change in current variations is larger than compared with DD at both low drain and high drain biases. The percentage current variation in MC simulation at low drain bias is almost three times larger than in DD, while at high drain bias MC percentage current variation is only approximately 50% larger than in DD.

Appendix B

Statistical Analysis of Drain Current Variability : 18 nm MOSFET

B.1 Descriptive Statistical Results at Low Drain Bias

The basic measures of descriptive statistics for the drain current variation obtained from DD and MC simulations at low drain bias and for the scaled 18nm device are presented in table B.1. In all cases the DD simulations at low drain bias result in larger currents when compared with the equivalent MC results, the mean DD current being approximately 2.5 times that of MC.

	18 nm Device : Simulations at Low Drain Bias	
	DD	MC
$\mu\ [A\mu m^{-1}]$	$(2.37 \pm 0.03) \times 10^{-4}$	$(9.1 \pm 0.3) \times 10^{-5}$
$\sigma\ [A\mu m^{-1}]$	$(2.3 \pm 0.2) \times 10^{-5}$	$(2.2 \pm 0.2) \times 10^{-5}$
γ_1	-0.51	-0.03
γ_2	0.72	-0.05

TABLE B.1: The values of the mean, standard deviation, skewness and kurtosis of drain currents results obtained from both DD and MC simulations at low drain bias of 18 nm device.

33 and 37 of the 50 devices from DD and MC simulations respectively have drain current values within σ of the mean. Almost all devices from both DD and MC simulations

lie within the range of 2σ, while only three from DD simulations and two from MC simulations fall far outside the range of 2σ. Thus, both DD and MC results at low drain bias show fair variability across the sample.

The values of standard deviation are also presented in table B.1. The coefficient of variation of MC results is $CV = 24.6\%$, while for DD results it is have $CV = 9.6\%$. Despite the fact that the standard deviation of DD results is larger than MC results, the CV coefficient indicates that again there are higher variations in MC results than in DD.

Both DD and MC results are negatively skewed. DD results are leptokurtic while MC results are platykurtic. The skew of MC results indicates little departure from symmetry, while DD results shows modest asymmetry from the normal distribution. The distribution of DD results has a moderately sharper peak than normal distribution, while MC results shows a peak with similar shape as normal distribution.

Table B.2 presents the confidence intervals of the above estimated statistical parameters. The confidence intervals of $\langle I_{D\ MC} \rangle$ indicate almost coincidence with the symmetric standard normal approximation since $R\backslash L$ ratio values are almost one, while $\langle I_{D\ DD} \rangle$ confidence interval indicate modest asymmetry from standard normal approximation since $R\backslash L$ ratio values is less than one. The confidence interval of $\sigma I_{D\ MC}$ shows modest asymmetry, while the interval of $\sigma I_{D\ DD}$ indicates moderate departure from the asymmetry compared with the standard normal approximation.

	18 nm Device : Simulations at Low Drain Bias			
	DD		MC	
	95% Confidence Interval	$R\backslash L$	95% Confidence Interval	$R\backslash L$
$\mu\ [A\mu m^{-1}]$	$[2.30, 2.43] \times 10^{-4}$	0.90	$[8.43, 9.66] \times 10^{-5}$	0.99
$\sigma\ [A\mu m^{-1}]$	$[1.86, 2.90] \times 10^{-5}$	1.64	$[1.82, 2.66] \times 10^{-5}$	1.17
γ_1	$[-1.55, 0.64]$	1.06	$[-0.94, 0.86]$	0.98
γ_2	$[-0.63, 2.35]$	1.56	$[-0.76, 0.82]$	1.65

Table B.2: 95% nonparameric ABC confidence interval of mean value, standard deviation, skewness and kurtosis compute for 18 nm device at low drain bias.

Table B.2 also shows that all zero values of skewness and kurtosis lie within the range of the 95% confidence interval. The null hypothesis of the confidence interval normality test is therefore accepted for both simulated distributions.

Further, Q-Q plots relevant to the above data are shown in figure B.1. In DD (left) plot, one outlier is evident at both the low and high end of the range. In the MC (right) plot, five outliers are evident at the high end of the range, while only two are at the low end. Both plots are approximating linear, suggesting that the data are normally distributed.

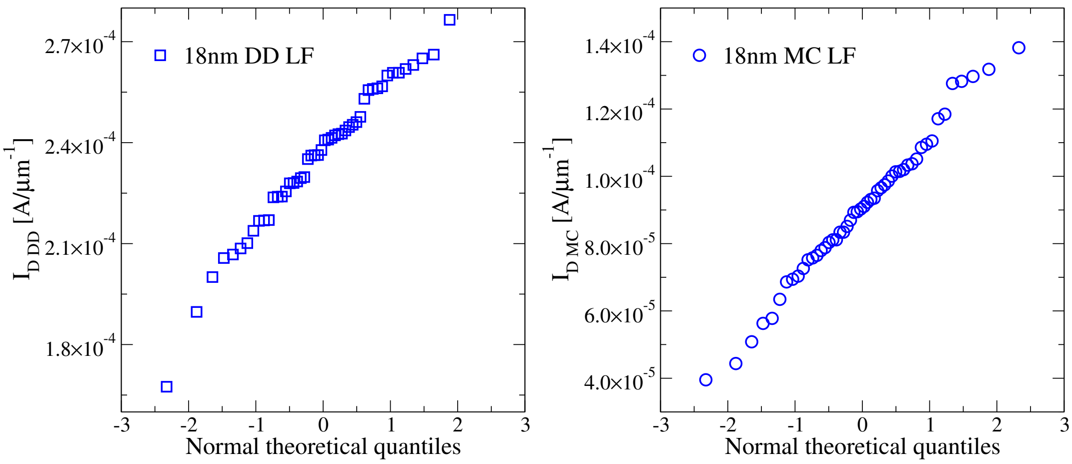

FIGURE B.1: Q-Q plot for DD (left) and MC (right) simulation results at low drain bias of 18 nm device.

Table B.3 presents the normality test results. For all cases, the p-values are greater than the chosen significance level $\alpha = 0.05$ so the null hypothesis that DD and MC simulations results come from a normally distributed population is accepted.

	18 nm Device : Simulations at Low Drain Bias			
	Normality test			
	DD		MC	
	Test Statistics	p-value	Test Statistics	p-value
Shapiro-Wilk	0.98	0.58	0.99	0.90
Jarque-Bera	2.62	0.27	0.064	0.97

TABLE B.3: Normality test for 18 nm device at low drain bias.

B.2 Descriptive Statistical Results at High Drain Bias

The mean, standard deviation, skew and kurtosis of both DD and MC simulated distributions are presented again for the 18nm device, but this time for high drain bias, in table B.4 For all devices, the DD simulations at high drain bias result in larger currents compared with equivalent MC results, the DD mean being approximately 4.5 times that of MC.

	18 nm Device : Simulations at High Drain Bias	
	DD	MC
$\mu\ [A\mu m^{-1}]$	$(8.5 \pm 0.2) \times 10^{-3}$	$(1.80 \pm 0.07) \times 10^{-3}$
$\sigma\ [A\mu m^{-1}]$	$(1.4 \pm 0.1) \times 10^{-3}$	$(4.6 \pm 0.5) \times 10^{-4}$
γ_1	-0.19	-0.13
γ_2	0.39	0.09

TABLE B.4: The values of the mean, standard deviation, skewness and kurtosis of drain currents results obtained from both DD and MC simulations at high drain bias of 18 nm device.

33 and 34 of the 50 devices from DD and MC simulations, respectively, have the drain current value within the range of σ from the mean. Almost all devices from both DD and MC simulations lie within the range of 2σ, while only two from both DD and MC simulations fall far outside the 2σ range.

Assessing the standard deviation, MC results are distributed with a coefficient of variation $CV = 25.8\%$, while DD only has $CV = 15.9\%$. This implies that MC results shows approximately 1.6 times higher variations than DD.

Further, table B.4 shows both DD and MC results are negatively skewed. The skew indicates modest asymmetry compared with normal distribution. Both DD and MC results are leptokurtic. The distribution of DD results has sharper peak than the normal distribution, while the distribution of MC results shows nearly the same shape of peak compared with normal.

Table B.5 presents the confidence intervals associated with the above estimates. The confidence intervals of $\langle I_{D\ MC} \rangle$ and $\langle I_{D\ DD} \rangle$ are nearly symmetric. The confidence intervals of $\sigma I_{D\ MC}$ and $\sigma I_{D\ DD}$ indicate moderate departure from the asymmetry compared with the standard normal approximation since $R \backslash L$ ratios are moderately higher than one.

	18 nm Device : Simulations at High Drain Bias			
	DD		MC	
	95% Confidence Interval	$R \backslash L$	95% Confidence Interval	$R \backslash L$
$\mu\ [A\mu m^{-1}]$	$[8.16, 8.90] \times 10^{-3}$	0.96	$[1.67, 1.92] \times 10^{-3}$	0.97
$\sigma\ [A\mu m^{-1}]$	$[1.11, 1.68] \times 10^{-3}$	1.44	$[3.78, 5.59] \times 10^{-4}$	1.25
γ_1	$[-1.31, 0.90]$	0.96	$[-1.03, 0.92]$	1.16
γ_2	$[-0.57, 1.72]$	1.83	$[-0.66, 1.07]$	1.75

TABLE B.5: 95% nonparameric ABC confidence interval of mean value, standard deviation, skewness and kurtosis compute for 18 nm device at high drain bias.

Further, table B.5 shows that the zero values of skewness and kurtosis of DD and MC simulation results lie within the range of the 95% confidence interval. This implies the acceptance of the null hypothesis, and therefore, data might be drawn from normal distributed population.

Q-Q plots for both DD and MC simulation results at high drain bias are plotted in figure B.2. The DD (left) plot shows one outlier at the low end of the range, while two lie at the high end. In the MC (right) plot, two outliers are evident at the low end while only one is seen at the high end. Both plots are approximately linear, suggesting that the data are normally distributed.

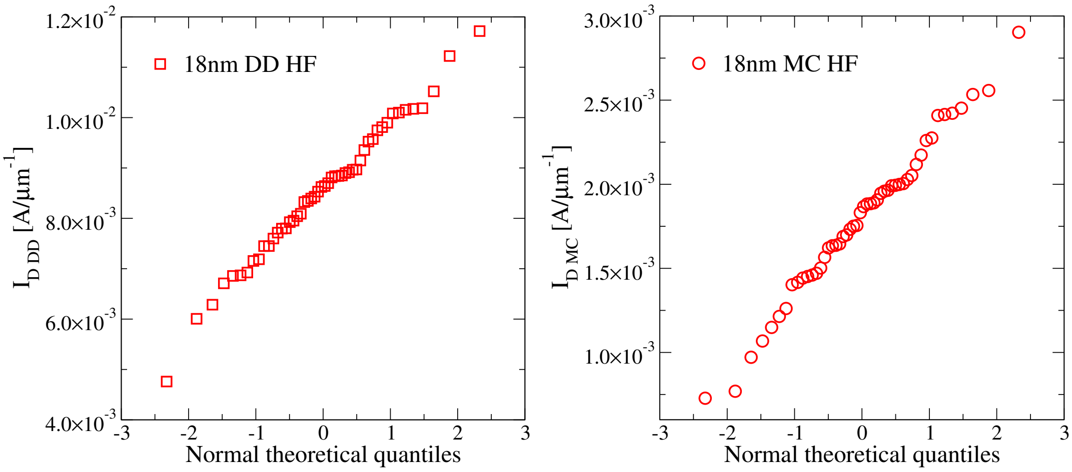

FIGURE B.2: Q-Q plot for DD (left) and MC (right) simulation results at high drain bias of 18nm device.

Table B.6 presents results of the normality test and implies that in all cases the null hypothesis is accepted. This means that simulation results come from a normally distributed population.

	18 nm Device : Simulations at High Drain Bias			
	Normality test			
	DD		MC	
	Test Statistics	p-value	Test Statistics	p-value
Shapiro-Wilk	0.99	0.97	0.99	0.90
Jarque-Bera	0.39	0.82	0.13	0.94

TABLE B.6: Normality test for 18 nm device at high drain bias.

B.3 DD versus MC : Percentage Change in Current

The uniform drain current values are presented in table B.7. From this it can be seen that atomistic DD simulations result in an average currents that is less than the uniform cases at both low and high drain bias. The average atomistic current over MC simulation is slightly less than the uniform case at high drain bias. This contrasts with the low drain case where the average current in atomistic MC is larger than uniform case.

	18 nm Device	
	Uniform Drain Currents	
	Low Drain Bias	High Drain Bias
$I^u_{D\ DD}$ $[A\mu m^{-1}]$	2.42×10^{-4}	8.67×10^{-3}
$I^u_{D\ MC}$ $[A\mu m^{-1}]$	8.40×10^{-5}	1.83×10^{-3}

TABLE B.7: Uniform currents obtained from DD and MC simulations of 18 nm device.

Scatter plots of the percentage change in current from the uniform device for both DD and MC at both low and high drain bias for all 50 devices are presented in figure B.3. Higher correlation ($\rho = 0.87$) at high drain highlights the importance of electrostatic effects, while at low drain the lesser correlation ($\rho = 0.78$) highlights the importance of transport variations.

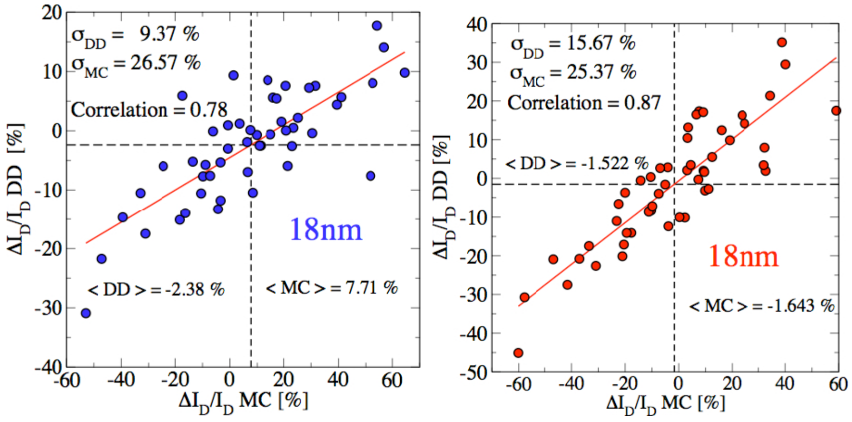

FIGURE B.3: Scatter plots of percentage drain-current variation from MC simulation against DD simulation, both including quantum corrections.The statistical ensemble is shown along with a linear regression line.The correlation at high (red) and low (blue) drain is seen.

20 of the 50 devices from MC simulation at low drain bias show reduced current while the number of devices increases to 29 in DD simulation at low drain bias. 5 of the 50 devices from MC simulation at low drain bias show greater or approximately similar reduction

in current as the device with maximum reduction in current from DD simulation at low drain bias. 20 of the 50 devices from MC simulation at low drain bias show greater or approximately similar increase in current as the device with maximum increase in current from DD simulation at low drain bias. The absolute value of the largest increase in current in MC at low drain bias is seen to be modestly larger (approximetly 21%) than the absolute value of the largest reductions in current seen in MC. The highest reductions in current in DD is moderately larger (approximetly 74%) than he largest increase in current seen in DD.

Further, the standard deviation of the percentage change in current variation calculated from DD at low drain bias is $\sigma \Delta I_{D\ DD} = 9.38\%$, while standard deviation from MC is $\sigma \Delta I_{D\ MC} = 26.57\%$, as illustrated in figure B.3.

24 of the 50 devices from MC simulation at high drain bias show reduced current while the number of devices fairly increases to 26 devices from DD at high drain bias. 4 of the 50 devices from MC simulation at high drain bias show greater or approximately similar reduction in current as the device with maximum reduction in current from DD simulation at high drain bias. 7 of the 50 devices from MC simulation at high drain bias show greater or approximately similar increase in current as the device with maximum increase in current from DD simulation at high drain bias. The absolute value of the largest reductions in current in MC at high drain bias is seen to be almost the same as the absolute value of the largest increase in current seen in MC. The highest reductions in current in DD at high drain bias is modestly larger (approximetly 28%) than the largest increase in current seen in DD.

The standard deviation of the percentage change in current variation calculated from DD at high drain bias is $\sigma \Delta I_{D\ DD} = 15.68\%$ while standard deviation from MC is $\sigma \Delta I_{D\ MC} = 25.37\%$, as presented in figure B.3.

The magnitude of the MC percentage change in current variations is larger than compared to DD at both low drain and high drain biases. The MC percentage current variation in current at low drain bias is almost three times larger than in DD, while at high drain bias MC percentage current variation is only approximately 61% larger than in DD.

Appendix C

Statistical Analysis of Drain Current Variability : 13 nm MOSFET

C.1 Descriptive Statistical Results at Low Drain Bias

The basic measures of descriptive statistics for the drain current variation obtained from DD and MC simulations at low drain bias and for the scaled 13nm device are presented in table C.1. In all cases the DD simulations at low drain bias result in larger currents when compared with the equivalent MC results, the mean current being approximately 4 times of MC.

	13 nm Device : Simulations at Low Drain Bias	
	DD	MC
μ $[A\mu m^{-1}]$	$(3.05 \pm 0.06) \times 10^{-4}$	$(7.7 \pm 0.3) \times 10^{-5}$
σ $[A\mu m^{-1}]$	$(3.9 \pm 0.4) \times 10^{-5}$	$(2.2 \pm 0.2) \times 10^{-5}$
γ_1	-0.40	0.22
γ_2	-0.34	-0.07

Table C.1: The values of the mean, standard deviation, skewness and kurtosis of drain currents results obtained from both DD and MC simulations at low drain bias of 13 nm device.

32 and 34 of the 50 devices from DD and MC simulations, respectively, have drain current values within σ of the mean. Almost all devices from both DD and MC simulations lie

within the range of 2σ, while only two from both DD and MC simulations fall far outside this range.

The standard deviation of the drain current variation is presented in table C.1. The coefficient of variation of MC results is $CV = 28.9\%$, while DD results only have $CV = 12.8\%$. Despite the fact that the standard deviation of DD results is larger than MC results, the CV coefficient of MC results is more than 2 times than of DD. This implies significantly higher variability in MC results than in DD.

DD results are shifted to the left of the mean, while MC results are skewed to the right. The skewness indicates modest departure from symmetry in both DD and MC results. Both DD and MC results are platykurtic. The distribution of DD results has a moderately flat-topped shape, while the distribution of MC results shows a similarly shaped peak as a normal distribution.

Table C.2 presents the confidence intervals of the above estimated statistical parameters. The confidence intervals of $\langle I_{D\ MC}\rangle$ and $\langle I_{D\ DD}\rangle$ are almost symmetric while those of $\sigma I_{D\ MC}$ and $\sigma I_{D\ DD}$ indicate moderate departure from the asymmetry compared with the standard normal approximation since $R\backslash L$ ratios are moderately higher than one.

	13 nm Device : Simulations at Low Drain Bias			
	DD		MC	
	95% Confidence Interval	$R\backslash L$	95% Confidence Interval	$R\backslash L$
$\mu\ [A\mu m^{-1}]$	$[2.94, 3.16] \times 10^{-4}$	0.92	$[7.10, 8.32] \times 10^{-5}$	1.05
$\sigma\ [A\mu m^{-1}]$	$[3.29, 4.66] \times 10^{-5}$	1.26	$[1.85, 2.70] \times 10^{-5}$	1.41
γ_1	$[-1.10, 0.43]$	1.14	$[-0.72, 1.17]$	1.03
γ_2	$[-0.96, 0.56]$	1.85	$[-0.81, 1.07]$	1.80

TABLE C.2: 95% nonparameric ABC confidence interval of mean value, standard deviation, skewness and kurtosis compute for 13 nm device at low drain bias.

Further, table C.2 shows that the zero values of skewness and kurtosis lie within the range of the 95% confidence interval. The null hypothesis of the confidence interval normality test is therefor accepted. This implies that the results might be drawn from normally distributed population.

Q-Q plots of both DD and MC simulation results at low drain bias are plotted in figure C.1. In the DD (left) plot, two outliers are evident at the low end of the range while three lie at the high end. In the MC (right) plot, two outliers are evident at the high end of the range while only one lies at the low end. Both plots are approximately linear, suggesting that the data are normally distributed.

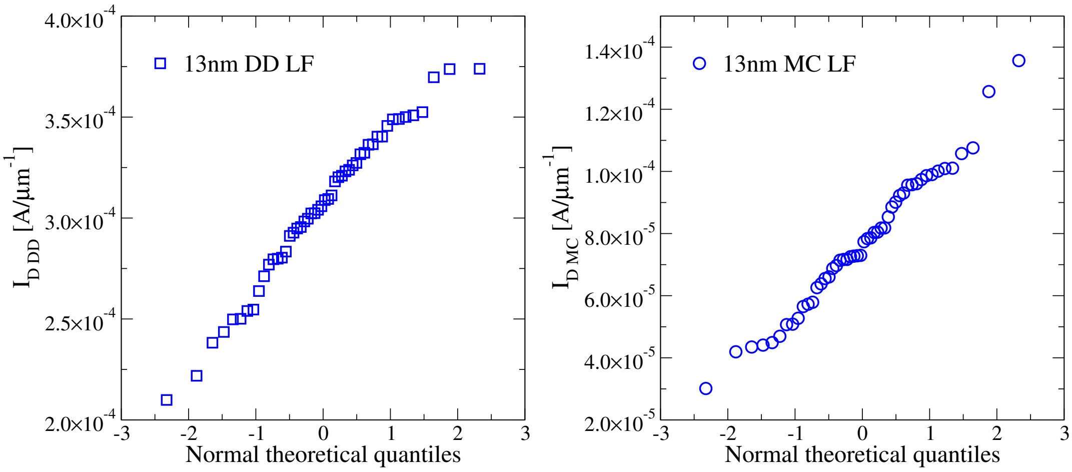

FIGURE C.1: Q-Q plot for DD (left) and MC (right) simulation results at low drain bias of 13nm device.

Table C.3 presents the normality test results. For all cases, the p-values are greater than the chosen significance level $\alpha = 0.05$ so the null hypothesis that DD and MC simulations results come from a normally distributed population is accepted.

	13 nm Device : Simulations at Low Drain Bias			
	Normality test			
	DD		MC	
	Test Statistics	p-value	Test Statistics	p-value
Shapiro-Wilk	0.98	0.44	0.98	0.71
Jarque-Bera	1.60	0.45	0.41	0.82

TABLE C.3: Normality test for 13 nm device at low drain bias.

C.2 Descriptive Statistical Results at High Drain Bias

Similarly, statistical estimators of the variation at high drain bias is presented in table C.4. In all cases the DD simulations result in larger currents when compared with equivalent MC results, the DD mean being approximately 4.5 times that of MC.

33 and 35 of the 50 devices from DD and MC simulations, respectively, have drain current values within σ of the mean. Almost all devices from both DD and MC simulations lie within the range of 2σ, while only one from DD fall far outside this range.

	13 nm Device : Simulations at High Drain Bias	
	DD	MC
μ $[A\mu m^{-1}]$	$(1.11 \pm 0.03) \times 10^{-2}$	$(1.70 \pm 0.07) \times 10^{-3}$
σ $[A\mu m^{-1}]$	$(2.0 \pm 0.2) \times 10^{-3}$	$(4.6 \pm 0.5) \times 10^{-4}$
γ_1	-0.25	-0.08
γ_2	-0.67	-0.68

Table C.4: The values of the mean, standard deviation, skewness and kurtosis of drain currents results obtained from both DD and MC simulations at high drain bias of 13 nm device.

The values of the coefficient of variation are presented in table C.4. MC results in $CV = 27.4\%$, while DD only has $CV = 18.5\%$. MC results indicates almost 50% higher variability than in DD.

Further, table C.4 shows that both DD and MC results are shifted to the left of the mean. The skewness indicates modest departure from symmetry compared with a normal distribution. Both DD and MC results are platykurtic showing moderate flat-topped shape compared with a normal distribution.

Table C.5 presented the confidence intervals for the above statistical parameters. The confidence intervals of $\langle I_{D\ MC} \rangle$ and $\langle I_{D\ DD} \rangle$ are almost identical with the standard normal approximation since $R \backslash L$ ratio values are nearly one. The confidence intervals of $\sigma I_{D\ MC}$ and $\sigma I_{D\ DD}$ indicate modest departure from the asymmetry compared with the standard normal approximation.

	13 nm Device : Simulations at High Drain Bias			
	DD		MC	
	95% Confidence Interval	$R \backslash L$	95% Confidence Interval	$R \backslash L$
μ $[A\mu m^{-1}]$	$[1.05, 1.16] \times 10^{-2}$	0.95	$[1.57, 1.82] \times 10^{-3}$	0.98
σ $[A\mu m^{-1}]$	$[1.73, 2.37] \times 10^{-3}$	1.18	$[3.92, 5.36] \times 10^{-4}$	1.14
γ_1	$[-0.90, 0.52]$	1.15	$[-0.78, 0.66]$	1.04
γ_2	$[-1.12, -0.05]$	1.73	$[-1.11, -0.13]$	1.63

Table C.5: 95% nonparameric ABC confidence interval of mean value, standard deviation, skewness and kurtosis compute for 13 nm device at high drain bias.

Table C.5 shows that the zero values of skewness from DD and MC results lie within the range of the 95% confidence interval, while the zero value of kurtosis falls outside this interval. We only accept the null hypothesis of the confidence interval normality test for skewness, while for kurtosis the null hypothesis is rejected. Further analysis is necessary to verify if simulation results are drawn from normal distributed population.

Q-Q plots for DD and MC results are plotted in figure C.2. In the DD (left) plot, one outlier is evident at the low end of the range, while two lie at the high end. In the MC (right) plot, three outliers are evident at the high end of the range, while two are at the low. Both plots are approximating linear, suggesting that the data are normally distributed.

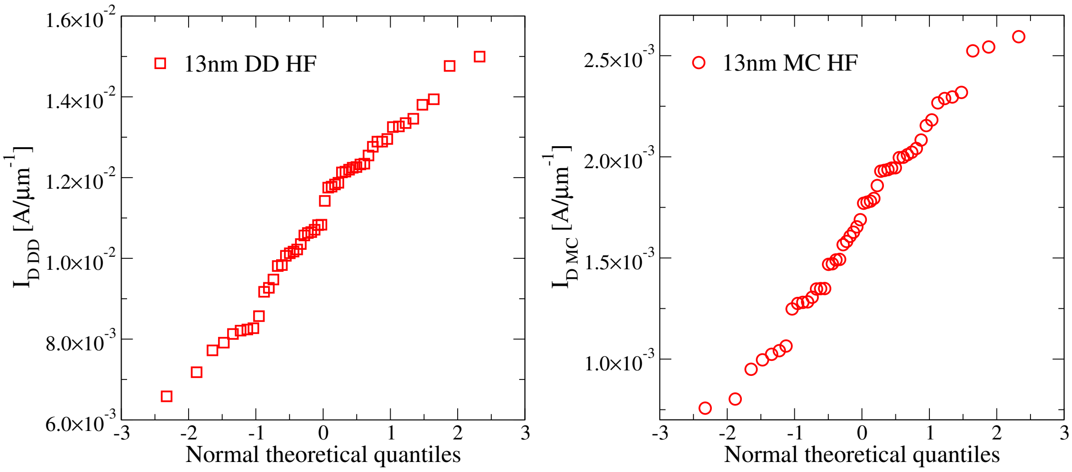

FIGURE C.2: Q-Q plot for DD (left) and MC (right) simulation results at high drain bias of 13nm device.

Table C.6 presents the normality test results for the above statistical parameters. The results indicate that DD and MC results may be drawn from normally distributed population.

	13 nm Device : Simulations at High Drain Bias			
	Normality test			
	DD		MC	
	Test Statistics	p-value	Test Statistics	p-value
Shapiro-Wilk	0.98	0.39	0.98	0.59
Jarque-Bera	1.59	0.45	1.17	0.56

TABLE C.6: Normality test for 13 nm device at high drain bias.

C.3 DD versus MC : Percentage Change in Current

The uniform drain current values are presented in table C.7. The atomistic DD simulations at low drain bias result in an average current lesser than the uniform case, while at high drain bias they result in an average current larger than uniform. Similarly, the atomistic MC simulations at low drain result in an average currents lesser than the uniform, while at high drain bias they result in an average current larger than uniform.

	13 nm Device	
	Uniform Drain Currents	
	Low Drain Bias	High Drain Bias
$I^u_{D\ DD}$ $[A\mu m^{-1}]$	3.10×10^{-4}	1.09×10^{-2}
$I^u_{D\ MC}$ $[A\mu m^{-1}]$	9.08×10^{-5}	1.57×10^{-3}

TABLE C.7: Uniform currents obtained from DD and MC simulations of 13 nm device.

Scatter plots of the percentage change in current relative to the uniform device for both DD and MC at both low and high drain bias for all 50 devices are presented in figure C.3. Higher correlation ($\rho = 0.91$) at high drain highlights the importance of electrostatic effects. The value of the correlation at low drain ($\rho = 0.83$) is nearly equal to the value at high drain bias which shows that the ballistic transport becomes more apparent in a smaller devices.

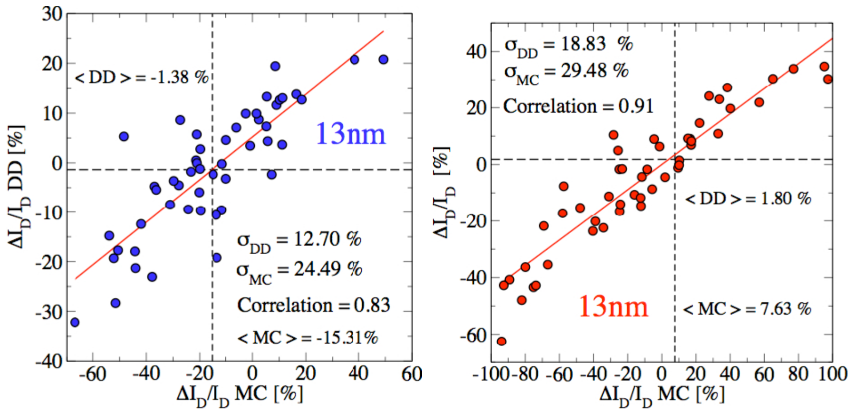

FIGURE C.3: Scatter plots of percentage drain-current variation from MC simulation against DD simulation, both including quantum corrections.The statistical ensemble is shown along with a linear regression line.The correlation at high (red) and low (blue) drain is seen.

35 of the 50 devices from MC simulation at low drain bias show reduced current while the number of devices slightly decreases to 27 in DD simulation at low drain bias. 13 of the 50 devices from MC simulation at low drain bias show greater or approximately similar reduction in current as the device with maximum reduction in current from DD simulation. 3 of the 50 devices from MC simulation at low drain bias show greater or approximately similar increase in current as the device with maximum increase in current from DD. The absolute value of the largest reduction in current in MC at low

drain bias is seen to be moderately larger (approximetly 35%) than the absolute value of the largest increase in current seen in MC. The highest reductions in current in DD is moderately larger (approximetly 55%) than he largest increase in current seen in DD.

Further, the standard deviation of the percentage change in current calculated from DD at low drain bias is $\sigma \Delta I_{D\ DD} = 12.71\%$, while standard deviation from MC is $\sigma \Delta I_{D\ MC} = 24.49\%$, as illustrated in figure C.3.

20 of the 50 devices from MC simulation at high drain bias show reduced current while the number of devices modestly increases to 25 devices from DD at high drain bias. 4 of the 50 devices from MC simulation at high drain bias show greater or approximately similar reduction in current as the device with maximum reduction in current from DD simulation at high drain bias. 9 of the 50 devices from MC simulation at high drain bias show greater or approximately similar increase in current as the device with the maximum increase in current from DD simulation. The absolute value of the largest reduction in current in MC at high drain bias is seen to be modestly lesser (approximately 20%) than the absolute value of the largest increase in current seen in MC. The highest reductions in current in DD at high drain bias is comparable to the largest increase in current seen in DD. IThe higher variations in MC compared with DD can again clearly be seen.

The standard deviation of the percentage change in current variation calculated from DD at high drain bias is $\sigma \Delta I_{D\ DD} = 18.84\%$ while standard deviation from MC is $\sigma \Delta I_{D\ MC} = 29.49\%$, as presented in figure C.3.

The magnitude of the MC current variations is larger than DD at both low drain and high drain biases, almost two times larger than in DD at low drain, while approximately only 56% larger than DD at high drain.

Appendix D

Statistical Analysis of Drain Current Variability : 9 nm MOSFET

D.1 Descriptive Statistical Results at Low Drain Bias

The basic measures of descriptive statistics for the drain current variation obtained from DD and MC simulations at low drain bias and for the 9nm device are presented in table D.1. In all cases the DD simulations result in larger currents when compared with the equivalent MC results, with the mean current being approximately 5 times that of MC.

	9 nm Device : Simulations at Low Drain Bias	
	DD	MC
μ $[A\mu m^{-1}]$	$(3.0 \pm 0.1) \times 10^{-4}$	$(5.6 \pm 0.4) \times 10^{-5}$
σ $[A\mu m^{-1}]$	$(7.5 \pm 0.8) \times 10^{-5}$	$(3.1 \pm 0.3) \times 10^{-5}$
γ_1	-0.27	0.35
γ_2	-0.33	-0.21

Table D.1: The values of the mean, standard deviation, skewness and kurtosis of drain currents results obtained from both DD and MC simulations at low drain bias of 9 nm device.

33 and 35 of the 50 devices from DD and MC simulations, respectively, have drain current values within the range of σ from the mean. Almost all devices from both DD and MC simulations lie within the range of 2σ, with only one from DD simulations

and three from MC simulations falling far outside that range. Thus, both DD and MC results at low drain bias show fair variability across the sample.

The values of standard deviation are presented in table B.1. The coefficient of variation of MC results is $CV = 55.7\%$, while DD results only have $CV = 25.1\%$. The CV coefficient of MC results is thus 2 times greater than DD which means MC results show significantly greater variability.

DD results are shifted to the left of the mean, while MC results are skewed to the right. The skewness indicates modest departure from symmetry in both DD and MC results while both DD and MC results are also platykurtic.

Table D.2 presents the associated confidence intervals. The confidence intervals of $\langle I_{D\ MC} \rangle$ and $\langle I_{D\ DD} \rangle$ show nearly coincidence with symmetric standard normal approximation, while for $\sigma I_{D\ MC}$ and $\sigma I_{D\ DD}$ they indicate moderate departure.

	9 nm Device : Simulations at Low Drain Bias			
	DD		MC	
	95% Confidence Interval	$R\backslash L$	95% Confidence Interval	$R\backslash L$
$\mu\ [A\mu m^{-1}]$	$[2.79, 3.20] \times 10^{-4}$	0.95	$[4.78, 6.50] \times 10^{-5}$	1.07
$\sigma\ [A\mu m^{-1}]$	$[6.28, 8.91] \times 10^{-5}$	1.21	$[2.59, 3.71] \times 10^{-5}$	1.20
γ_1	$[-1.03, 0.55]$	1.05	$[-0.49, 1.07]$	0.87
γ_2	$[-0.98, 0.64]$	1.88	$[-0.87, 0.68]$	1.78

Table D.2: 95% nonparameric ABC confidence interval of mean value, standard deviation, skewness and kurtosis compute for 9 nm device at low drain bias.

Further, the table D.2 shows that the zero values of skewness and kurtosis of DD and MC simulation results lie within the range of the 95% confidence interval. This implies that the null hypothesis of normality test is accepted. Results at low drain bias simulation of 9 nm device might be drawn from normal distribution.

Q-Q plots for the simulation results at low drain bias are plotted in figure D.1. In the DD (left) plot, one outlier is evident at both the low and high end of the range. In the MC (right) plot, three outliers are evident at the high end. Both plots are once again approximately linear, suggesting that the data are normally distributed.

Table D.3 present results of the normality test. In all cases, the p-values are greater than the chosen significance level $\alpha = 0.05$ so the null hypothesis that DD and MC simulations results come from a normally distributed population is accepted.

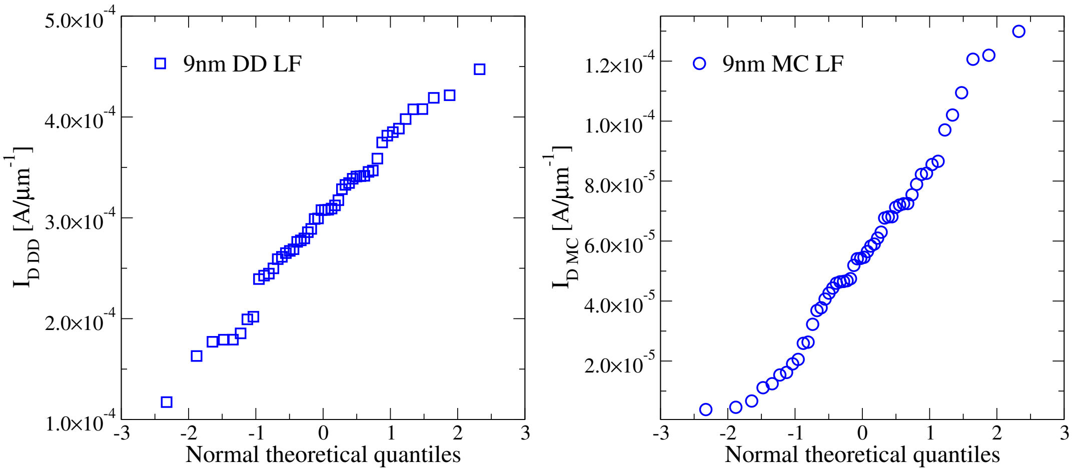

FIGURE D.1: Q-Q plot for DD (left) and MC (right) simulation results at low drain bias of 9nm device.

	9 nm Device : Simulations at Low Drain Bias			
	Normality test			
	DD		MC	
	Test Statistics	p-value	Test Statistics	p-value
Shapiro-Wilk	0.98	0.64	0.97	0.32
Jarque-Bera	0.95	0.62	1.16	0.56

TABLE D.3: Normality test for 9 nm device at low drain bias.

D.2 Descriptive Statistical Results at High Drain Bias

The basic statistics of drain current variation from both DD and MC simulation at high drain bias are presented in table D.4 In all cases the DD simulations result in larger currents when compared with the equivalent MC results, with the mean current approximately 7.5 times that of MC.

	9 nm Device : Simulations at High Drain Bias	
	DD	MC
$\mu\ [A\mu m^{-1}]$	$(1.20 \pm 0.05) \times 10^{-2}$	$(1.6 \pm 0.1) \times 10^{-3}$
$\sigma\ [A\mu m^{-1}]$	$(3.6 \pm 0.4) \times 10^{-3}$	$(6.9 \pm 0.7) \times 10^{-4}$
γ_1	-0.08	0.19
γ_2	-0.38	-0.72

TABLE D.4: The values of the mean, standard deviation, skewness and kurtosis of drain currents results obtained from both DD and MC simulations at high drain bias of 9 nm device.

33 and 34 of the 50 devices from DD and MC, respectively, have drain current values within σ of the mean. Almost all devices from DD and MC simulations lie within the range of 2σ, with only one from DD simulations falling far outside this range.

The standard deviation of the device distribution are presented in table D.4. MC results have a coefficient of variation of $CV = 42.8\%$, while DD only has $CV = 29.9\%$. MC results thus show significantly higher variation.

Further, table D.4 shows that DD results are negatively skewed, while MC results are shifted to the right of the mean. The skewness indicates almost the same symmetry as normal distribution. Both DD and MC results are platykurtic showing moderate flat-topped shape compared with a normal distribution.

Table D.5 presents the confidence intervals. The confidence intervals of $\langle I_{D\ MC}\rangle$ and $\langle I_{D\ DD}\rangle$ are nearly the same as the standard normal approximation since $R\backslash L$ ratio values are almost one. The confidence intervals of $\sigma I_{D\ MC}$ and $\sigma I_{D\ DD}$ indicate moderate departure from the asymmetry compared with the standard normal approximation.

	9 nm Device : Simulations at High Drain Bias			
	DD		MC	
	95% Confidence Interval	$R\backslash L$	95% Confidence Interval	$R\backslash L$
$\mu\ [A\mu m^{-1}]$	$[1.10, 1.29] \times 10^{-2}$	0.98	$[1.43, 1.81] \times 10^{-3}$	1.04
$\sigma\ [A\mu m^{-1}]$	$[3.02, 4.26] \times 10^{-3}$	1.33	$[5.87, 7.99] \times 10^{-4}$	1.16
γ_1	$[-1.02, 0.68]$	0.79	$[-0.63, 0.81]$	0.77
γ_2	$[-1.07, 0.72]$	1.95	$[-1.14, -0.10]$	1.77

TABLE D.5: 95% nonparameric ABC confidence interval of mean value, standard deviation, skewness and kurtosis compute for 9 nm device at high drain bias.

Further, the table D.5 shows that the zero values of skewness of DD and MC simulation results lie within the range of the 95% confidence interval, while the zero value of kurtosis lies within the range only for DD results. The null hypothesis of the confidence interval normality test is therefore accepted for skewness, while the null hypothesis of kurtosis is only accepted for DD results. This implies that further analysis is needed.

Q-Q plots for DD and MC simulation results are plotted in figure D.2. In the DD (left) plot no outliers are evident. In the MC (right) plot one outlier is evident at the low end of the range. Both plots are approximately linear, suggesting that the data is normally distributed.

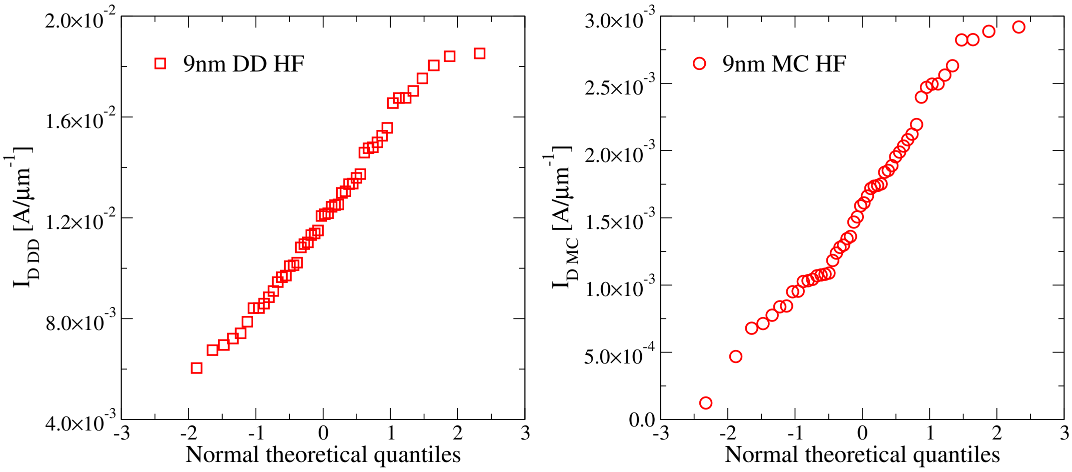

Figure D.2: Q-Q plot for DD (left) and MC (right) simulation results at high drain bias of 9nm device.

Table D.6 presents the normality test results for the above statistical properties. In all cases, the p-values are greater than the chosen significance level $\alpha = 0.05$ so the null hypothesis that DD and MC simulations results come from a normally distributed population is accepted.

	9 nm Device : Simulations at High Drain Bias			
	Normality test			
	DD		MC	
	Test Statistics	p-value	Test Statistics	p-value
Shapiro-Wilk	0.98	0.76	0.97	0.29
Jarque-Bera	0.49	0.78	1.50	0.47

Table D.6: Normality test for 9 nm device at high drain bias.

D.3 DD versus MC : Percentage Change in Current

The uniform drain current values are presented in table D.7. The atomistic DD simulations at low drain bias result in an average current lesser than the uniform case, while at high drain bias they result in an average current larger than uniform. The atomistic MC simulations at low drain result in an average currents less than the uniform cases, while at high drain bias they result in an average current larger than uniform.

Scatter plots of the percentage change in current relative to the uniform device at both low and high drain bias for all 50 devices are presented in figure A.3. Higher correlation

	9 nm Device	
	Uniform Drain Currents	
	Low Drain Bias	High Drain Bias
$I^u_{D\ DD}$ $[A\mu m^{-1}]$	3.13×10^{-4}	1.19×10^{-2}
$I^u_{D\ MC}$ $[A\mu m^{-1}]$	6.18×10^{-5}	1.50×10^{-3}

Table D.7: Uniform currents obtained from DD and MC simulations of 9 nm device.

($\rho = 0.96$) at high drain highlights the importance of electrostatic effects. The value of the correlation at low drain ($\rho = 0.94$) is almost the same as the value at high drain bias. This implies the importance of ballistic transport in such small devices.

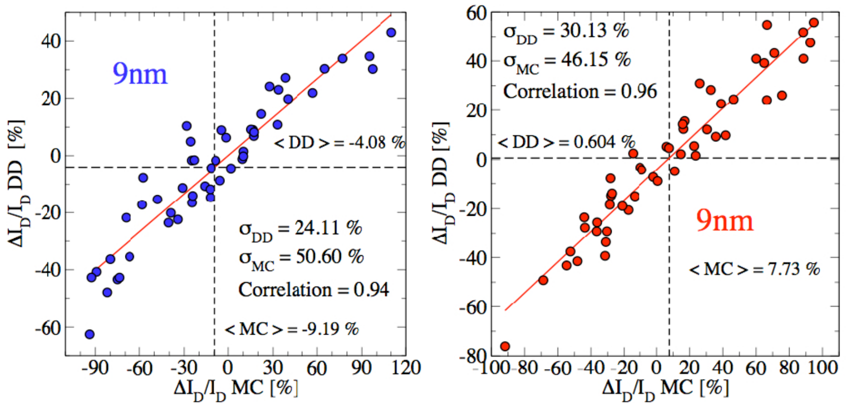

Figure D.3: Scatter plots of percentage drain-current variation from MC simulation against DD simulation, both including quantum corrections.The statistical ensemble is shown along with a linear regression line.The correlation at high (red) and low (blue) drain is seen.

30 of the 50 devices from MC simulation at low drain bias show reduced current while the number of devices slightly decrease to 29 in DD simulation at low drain bias. 9 of the 50 devices from MC simulation at low drain bias show greater or approximately similar reduction in current as the device with maximum reduction in current from DD simulation at low drain bias. 7 of the 50 devices from MC simulation at low drain bias show greater or approximately similar increase in current as the device with maximum increase in current from DD simulation at low drain bias. The absolute value of the largest increase in current in MC at low drain bias is seen to be modestly larger (approximetly 17%) than the absolute value of the largest reductions in current seen in MC. The highest reductions in current in DD is moderately larger (approximetly 45%) than he largest increase in current seen in DD.

Further, the standard deviation of the percentage change in current variation calculated from DD at low drain bias is $\sigma\Delta I_{D\ DD} = 24.11\%$, while standard deviation from MC is $\sigma\Delta I_{D\ MC} = 50.16\%$, as illustrated in figure D.3.

23 of the 50 devices from MC simulation at high drain bias show reduced current while the number of devices fairly increases to 24 devices from DD at high drain bias. 2 of the 50 devices from MC simulation at high drain bias show greater or approximately similar reduction in current as the device with maximum reduction in current from DD simulation at high drain bias. 10 of the 50 devices from MC simulation at high drain bias show greater or approximately similar increase in current as the device with maximum increase in current from DD simulation at high drain bias. The absolute value of the largest reductions in current in MC at high drain bias is seen to be almost the same as the absolute value of the largest increase in current seen in MC. The highest reductions in current in DD at high drain bias is moderate larger (approximetly 36%) than the largest increase in current seen in DD.

The standard deviation of the percentage change in current variation calculated from DD at high drain bias is $\sigma\Delta I_{D\ DD} = 30.14\%$ while standard deviation from MC is $\sigma\Delta I_{D\ MC} = 46.16\%$, as presented in figure D.3.

The magnitude of the MC percentage change in current variations is larger than compared to DD at both low drain and high drain biases. The MC percentage current variation in current at low drain bias is almost two times larger than in DD, while at high drain bias MC percentage current variation is only approximately 50% larger than in DD.

Bibliography

[1] Mistry, K., et.al., " A 45nm Logic Technology with High-k+Metal Gate Transistors, Strained Silicon, 9 Cu Interconnect Layers, 193nm Dry Patterning, and 100% Pb-free Packaging", In IEDM Digest of Technical Papers, pages 247250, 2007.

[2] G. E. Moore, "Cramming More Components onto Integrated Circuits," Electronics, 38:114-117, 1965.

[3] G. E. Moore, "Progress in Digital Integrated Electronics," IEDM Tech. Digest, pages 1113, 1975.

[4] The International Technology Roadmap for Semiconductor (2009 Edition), San Jose, CA: Semiconductor Industry Association. [Online]. Available: http://www.itrs.net

[5] Asenov A., "Random dopant induced threshold voltage lowering and fluctuations in sub-0.1 lm MOSFETs: A 3-D atomistic simulation study," IEEE Trans Electron Dev;45(12):2505-13, 1998.

[6] K. Bernstein, D. Frank, A. Gattiker, W. Haensch, B. Ji, S. Nassif, E. Nowak, D. Pearson, and N. Rohrer, "High-performance CMOS variability in the 65-nm regime and beyond," IBM Journal Research Development, vol. 50, p. 433, 2006.

[7] A. R. Brown, G. Roy and A. Asenov, "Poly-Si Gate Related Variability in Decananometre MOSFETs with Conventional Architecture," IEEE Trans. on Electron Devices, Vol.54, No.11, pp.3056-3063, 2007.

[8] T. Mizuno, J. Okamura, and A. Toriumi, "Experimental study of threshold voltage fluctuation due to statistical variation of channel dopant number in MOSFETs," IEEE Trans. on Electron Devices, vol. 41, no. 11, pp. 2216-2221, Nov. 1994.

[9] Stolk P.A., Klaasen D.B.M.,"The effect of statistical dopant fluctuations on MOS device performance," In: IEDM Tech Dig; pp. 627-30,1996.

[10] A. Asenov, S. Kaya, and A. R. Brown, " Intrinsic Parameter Fluctuations in Decananometer MOSFETs Introduced by Gate Line Edge Roughness," IEEE Transactions on Electron Devices, 50, pp. 1254-1260, May 2003.

[11] D. Reid, C. Millar, G. Roy, S. Roy, and A. Asenov, "Understanding LER-induced Statistical Variability: A 35,000 Sample 3D Simulation Study," Proc. ESSDERC 2009: Sept. 14-18, 2009.

[12] S. Goodnick, D. Ferry, and C. Wilmsen, "Surface roughness at the Si(100)-SiO2 interface," Physical Review B, vol. 32, p. 8171, 1985.

[13] A. Asenov, S. Kaya, and J. H. Davies, "ntrinsic threshold voltage fluctuations in decanano MOSFETs due to local oxide thickness variations," IEEE Transactions on Electron Devices, vol. 49, pp. 112-119, 2002.

[14] P. Andrei and I. Mayergoyz, "Quantum mechanical effects on random oxide thickness and random dopant induced fluctuations in ultrasmall semiconductor devices," J. Appl. Phys., vol. 94, no. 11, pp. 7163-7172, Dec. 2003.

[15] Tuinhout, H.P., "Impact of parametric mismatch and fluctuations on performance and yield of deep-submicron CMOS technologies, " In: Proc. 32nd European Solid-State Device Research Conference (ESSDERC), Firenze, Italy, pp. 95-101,2002.

[16] Asenov, A., Saini, S., "Polysilicon gate enhancement of the random dopant induced threshold voltage fluctuations in sub 100 nm MOSFETs with ultrathin gate oxide," IEEE Trans. Electron Devices 47(4), pp. 805-812, 2000.

[17] A. R. Brown, J. R. Watling, and A. Asenov, "Intrinsic parameter fluctuations due to random grain orientations in high-k gate stacks," J. Comput. Electron., vol. 5, no. 4, pp. 333-336, Dec. 2006.

[18] Watling, J.R., Brown, A.R., Ferrari, G., Babiker, J.R., Bersuker, G., Zeitzoff, P., Asenov, A., "Impact of High-k Gate Stacks on Transport and Variability in Nano-CMOS Devices, " J. Comput. Theor. Nanosci. 5, pp. 1072-1088,2008.

[19] K. Ohmori, T. Matsuki, D. Ishikawa, T. Morooka, T. Aminaka, et al., "Impact of Additional Factors in Threshold Voltage Variability of Metal/High-k Gate Stacks

and Its Reduction by Controlling Crystalline Structure and Grain Size in the Metal Gates," IEDM Digest. Tech. Papers, pp.409-412, 2008

[20] H. Dadgour, K. Endo, V. De, and K. Banerjee, "Modeling and Analysis of Grain-Orientation Effects in Emerging Metal-Gate Devices and Implications for SRAM Reliability," IEDM Digest. Tech. Papers, pp.705-708, 2008

[21] C.-H. Hwang, T.-Y. Li, M.-H. Han, K.-F. Lee, H.-W. Cheng, Y. Li, "Statistical Analysis of Metal Gate Workfunction Variability, Process Variation, and Random Dopant Fluctuation in Nano-CMOS Circuits," Proc. SISPAD, pp.99-102, 2009

[22] A. Asenov, A. R. Brown, J. H. Davies, S. Kaya, and G. Slavcheva, "Simulation of intrinsic parameter fluctuations in decananometre and nanometre scale MOSFETs," IEEE Trans. Electron Devices, vol. 50, no. 9, pp. 1837-1852, Sep. 2003.

[23] H. S. Wong and Y. Taur, "Three-dimensional atomistic simulation of discrete random dopant distribution effects in sub-0.1 m MOSFETs," in Proc. IEEE Int. Electron Devices Meeting (IEDM), pp. 29.2.1-29.2.4, 1993.

[24] W. J. Gross, D. Vasileska and D, K, Ferry, "Three-Dimensional Simulations of Ultrasmall Metal-Oxide-Semiconductor-Field-Effect-Transistors: The Role of Discrete Impurities on the Device Terminal Characteristics," J. Appl. Phys., 91, pp.3737-3740, 2002

[25] Frank DJ, Taur Y, Ieong M, Wong H-SP, "Monte Carlo modeling of threshold variation due to dopant fluctuations," In: VLSI symp tech dig; p. 169-170.1999.

[26] G. Roy, A. R. Brown, F. Adamu-Lema, S. Roy, and A. Asenov, "Simulation study of individual and combined sources of intrinsic parameter fluctuations in conventional nano-MOSFETs," IEEE Trans. Electron Devices, vol. 53, no. 12, pp. 3063-3070, Dec. 2006

[27] S. Markov, A. R. Brown, B. Cheng, G. Roy, S. Roy and A. Asenov, "Three-Dimensional statistical simulation of gate leakage fluctuations due to combined interface roughness and random dopants," Japanese Journal of Applied Physics, Vol. 46, Issue 4B, pp. 2112 (2007).

[28] R. Rodrguez, J. H. Stathis, B. P. Linder, S. Kowalczyk, C. T. Chuang, R. V. Joshi, G. Northrop, K. Bernstein, A. J. Bhavnagarwala, and S. Lombardo, "The Impact

of Gate-Oxide Breakdown on SRAM Stability," IEEE Electron Dev. Lett, Vol 23, p. 559 (2002).

[29] A. Asenov, A.R. Brown and J.R. Watling, "Quantum corrections in the simulation of decanano MOSFETs" Solid-State Electronics 47, pp 1141-1145, 2003.

[30] G. Roy, A. R. Brown, A. Asenov, and S. Roy, "Bipolar quantum corrections in resolving individual dopants in atomistic device simulations," Superlattices Microstruct., vol. 34, no. 36, pp. 327-334, Sep./Dec. 2004.

[31] S. E. Laux and M. V. Fischetti, "Issues in Modeling Small Devices," International Electron Devices Meeting (IEDM) Technical Digest, pp.523-526, 1999.

[32] C. Riddet, A. R. Brown, C. L. Alexander, J. R. Watling, S. Roy, and A. Asenov, "3-D Monte Carlo simulation of the impact of quantum confinement scattering on the magnitude of current fluctuations in double gate MOSFETs," IEEE Transactions on Nanotechnology, vol. 6, iss. 1, pp. 48-55, 2007.

[33] C. L. Alexander, G. Roy, and A. Asenov, "Random-Dopant-Induced Drain Current Variation in Nano-MOSFETs: A Three-Dimensional Self-Consistent Monte Carlo Simulation Study Using Ab Initio Ionized Impurity Scattering," IEEE Trans. Electron Dev., vol. 55, iss.11, pp.3251-3258, 2008.

[34] C. L. Alexander, G. Roy, and A. Asenov, "Increased intrinsic parameter fluctuations through ab initio Monte Carlo simulations in nano-scaled MOSFETs," in International Electron Devices Meeting (IEDM), Tech. Dig., 2006, pp.1-4.

[35] W. Haensch, E. Nowak, R. Dennard, P. Solomon, A. Bryant, O. Dokumaci, A. Kumar, X. Wang, J. Johnson, and M. Fischetti, "Silicon CMOS devices beyond scaling," IBM Journal Research Development, vol. 50, p. 339, 2006.

[36] A. Asenov, A. R. Brown, Gareth Roy, B. Cheng, C. Alexander, C. Riddet, U. Kovac, A. Martinez, N. Seoane, S. Roy, "Simulation of statistical variability in nano-CMOS transistors using drift-diffusion, Monte Carlo and non-equilibrium Greens function techniques", J Comput Electron Vol. 8, pp. 349-373 (2009).

[37] Gilbert Declerck, "A look into the future of nanoelectronics", In VLSI Symposium Technical Digest, pages 67, 2005.

[38] E. P. Gusev, V. Narayanan, M. M. Frank, "Advanced high-k dielectric stacks with polySi and metal gates: recent progress and current challenges", IBM Journal of Research and Development, Volume 50 , Issue 4/5 (July 2006),Pages: 387 - 410, ISSN:0018-8646

[39] Henson, K.; et.al., " Gate length scaling and high drive currents enabled for high performance SOI technology using high-k/metal gate", Electron Devices Meeting, 2008. IEDM 2008, Page(s): 1 - 4

[40] J. R. Watling, L. Yang, A. Asenov, J. R. Barker, and S. Roy, "Impact of high-k dielectric HfO2 on the mobility and device performance of sub-100-nm nMOSFETs," IEEE Transactions on Device and Materials Reliability, vol. 5, iss. 1, pp. 103-108, 2005.

[41] Hasegawa, S.; et.al.;" A cost-conscious 32nm CMOS platform technology with advanced single exposure lithography and gate-first metal gate/high-k process", Electron Devices Meeting, 2008. IEDM 2008. Page(s): 1 - 3.

[42] Arnaud, F.; et. al.; " 32nm general purpose bulk CMOS technology for high performance applications at low voltage", Electron Devices Meeting, 2008. IEDM 2008. Page(s): 1 - 4.

[43] Natarajan, S.; et. al.; "A 32nm logic technology featuring 2nd-generation high-k + metal-gate transistors, enhanced channel strain and 0.171?m2 sram cell size in a 291mb array" In IEDM Digest of Technical Papers.

[44] K. Mistry et al., "Delaying Forever: Uniaxial Strained Silicon Transistors in a 90nm CMOS Technology," 2004 VLSI Technology Symposium, pp. 50-51.

[45] B. Cheng, S. Roy, G. Roy, F. Adamu-Lema, and A. Asenov, "Impact of intrinsic parameter fluctuations in decanano MOSFETs on yield and functionality of SRAM cells," Solid-State Electronics, vol. 49, no. 5, pp. 740-746, May 2005.

[46] B. Cheng, S. Roy and A. Asenov, "The impact of random dopant effects on SRAM cells," Proc. 30th European Solid-State Circuits Conference (ESSCIRC), Leuven, 219 (2004).

[47] Agarwal, A., Chopra, K., Zolotov, V., Blaauw, D,"Circuit optimization using statistical static timing analysis", In: Proc. 42nd Design Automation Conference, Anaheim, p. 321 (2005)

[48] H. Aikawa,"Variability aware modeling and characterization in standard cell in 45 nm cmos with stress enhancement technique", In VLSI Technology Symposium, pages 90-91, 2008.

[49] A. Cathignol, B. Cheng, et al, "Quantitative evaluation of statistical variability sources in a 45-nm technological node lp n-mosfet", Electron Device Letters, 29(6):609-611, June 2008.

[50] K. Ishimaru, "45nm/32nm cmos - challenge and perspective", Solid State Electronics, 52(9):1266-1273, September 2008.

[51] H. P. Tuinhout, "Impact of parametric mismatch and fluctuations on performance and yield of deep-submicron cmos technologies", In Proceedings of ESSDERC, pages 95-101, 2002.

[52] D. Reid, C. Millar, G. Roy, S. Roy, and A. Asenov, "Statistical enhancement of combined simulations of RDD and LER variability: What can simulation of a 10^5 sample teach us?" International Electron Devices Meeting 2009: Dec. 7-9, 2009.

[53] H. Dadgour, D. Vivek and K. Banerjee, "Statistical modeling of metal-gate Work-Function Variability in emerging device technologies and implications for circuit design," IEEE/ACM International Conference on Computer-Aided Design, pp.270-277, 2008

[54] K. J. Kuhn, "Reducing variation in advanced logic technologies: Approaches to process and design for manufacturability of nanoscale CMOS," In IEDM Digest of Technical Papers, pages 471-474, 2007.

[55] R. W. Keyes, "Physical limits in digital electronics," Proc. IEEE, vol. 63, pp. 740-766, 1975.

[56] K. R. Lakshmikumar, R. A. Hadaway, and M. A. Copeland, "Characterization and Modeling of Mismatch in MOS Transistors for Precision Analog Design," IEEE J.Solid-State Circuits, vol. 21, pp. 1057-1066, 1986.

[57] Asenov,A., Balasubramaniam, R., Brown,A.R., and Davies,J.H., "RTS Amplitudes in Decananometer MOSFETs: 3-D Simulation Study," IEEE Transaction on Electron Devices, Vol. 50, No. 3, March 2003.

[58] M. Faiz. Bukhori, S. Roy and A. Asenov, "Simulation of Statistical Aspects of Charge Trapping and Related Degradation in Bulk MOSFETs in the Presence of Random Discrete Dopants," IEEE Trans. Electron Dev. vol. 57, iss. 4, pp. 795-803, Apr. 2010.

[59] B. Hoeneisen and C. A. Mead, "Fundemental limitations in micro-electronics IMOS technology," Solid State Electron., vol. 15, pp. 819-829, 1972.

[60] M. Steyaert, J. Bastos, R. Roovers, P. Kinget, W. Sansen, B. Graindourse, A. Pergot, and E. Janssens, "Threshold mismatch in short-channel MOS transistors," Electron Lett., 30, pp. 1546-1548, 1994.

[61] J. T. Horstmann, U. Hilleringmann, and K. F. Goser,"Matching analysis of deposition dened 50-nm MOSFETs," IEEE Trans. Elec. Dev., 45, pp. 299-306, 1998.

[62] K. Takeuchi, T. Tatsumi, and A. Furukawa, "Channel engineering for the reduction of random-dopant-placement-induced threshold voltage fluctuation," In IEDM Digest of Technical Papers, pages 841-844, 1997.

[63] Andrei, P.," On the analysis of random doping induced fluctuations in ultra small semiconductor devices by linearization", International Conference on Simulation of Semiconductor Processes and Devices, SISPAD, pp. 256 - 259,2006.

[64] T. Hagiwara, K. Yamaguchi, and S. Asai, "Threshold voltage deviation in very small mos transistors due to local impurity fluctuations", In VLSI Technology Symposium Technical Digest, pp. 46-47, 1982.

[65] Y. Taur, D. Buchanan, W. Chen, D. Frank, K. Ismail, S. H. Lo, G. Sai-Halasz, R. Viswanathan, H. J. C. Wann, S. Wind, and H. S. Wong,'"CMOS Scaling into the Nanometer Regime", Proc. IEEE, pp. 85-486, 1997.

[66] K. Nishiohara, N. Shiguo, and T. Wada." Effects of mesoscopic fluctuations in dopant distributions on MOSFETs threshold voltage," IEEE Trans. Elec. Dev., 39, pp. 634-639, 1992.

[67] P. A. Stolk, F. P. Widdershoven, and D. B. M. Klaasen,"Device modeling of statistical dopant fluctuations in mos transistors," In Proc. of SISPAD, pp. 153-156, 1997.

[68] A. Asenov, G. Slavcheva, A. R. Brown, J. H. Davies, and S. Saini, "Increase in the random dopant induced threshold fluctuations and lowering in sub 100 nm MOSFETs due to quantum effects: A 3-D density gradient simulation study," IEEE Trans. Electron Devices, vol. 48, no. 4, pp. 722-729, Apr. 2001.

[69] M. Hane, T. Ikezawa, and T. Ezaki,"Atomistic 3-d process/device simulation considering gate line edge roughness and poly-si random crystal orientation effects," IEDM Tech. Dig., pp. 241-244, 2003.

[70] D. Reid, C. Millar, G. Roy, S. Roy, and A. Asenov, "Analysis of Threshold Voltage Distribution due to Random Dopants: A 100,000 Sample 3D Simulation Study," IEEE Transactions on Electron Devices, Volume 56, Issue 10,pp.2255-2263 Oct. 2009.

[71] G. Slavcheva, J. H. Davies, A. R. Brown, and A. Asenov, "Potential Fluctuations in MOSFETs generated by randomly distributed impurites in the depletion layer", J. Appl. Phys, pp. 4326- 4334, 2002.

[72] O. Weber, O. Faynot, et al,"High immunity to threshold voltage variability in undoped ultra-thin fdsoi mosfets and its physical understanding," In IEDM Digest of Technical Papers, 2008.

[73] E. Baravelli, A. Dixit, R. Rooyackers, M. Jurczak, N. Speciale, and K. De Meyer,"Impact of line-edge roughness on finfet matching performance," IEEE Transactions on Electron Devices, 54(9), pp. 2466-2474, 2007.

[74] D. Reid, C. Millar, S. Roy, R. O. Sinnott, G. Stewart, G. Stewart, and A. Asenov, "Prediction of Random Dopant Induced Threshold Voltage Fluctuations in NanoCMOS Transistors," Simulation of Semiconductor Processes and Devices 2008: Sept. 9-11, 2008.

[75] D. Reid, C. Millar, S. Roy, G. Roy, R. O. Sinnott, G. Stewart, G. Stewart, and A. Asenov, "An Accurate Statistical Analysis of Random Dopant Induced Variability in 140,000 13nm MOSFETs," Silicon Nanoelectronics Workshop 2008: June 15-16, 2008.

[76] C. Millar, D. Reid, G. Roy, S. Roy, and A. Asenov, "Accurate Statistical Description of Random Dopant Induced Threshold Voltage Variability," IEEE Electron Device Letters, vol. 29, iss. 8, pp. 946-948, Aug. 2008.

[77] U. Kovac, D. Reid, C. Millar, G. Roy, S. Roy, and A. Asenov, "Statistical simulation of random dopant induced threshold voltage fluctuations for 35 nm channel length MOSFET," Microelectronics Reliability, vol. 48, iss. 8-9, pp. 1572-1575, 2008.

[78] Saitoh, M.; Yasutake, N.; Nakabayashi, Y.; Uchida, K.; Numata, T., "Physical understanding of Vth and Idsat variations in (110) CMOSFETs", VLSI Technology, 2009 Symposium on, 2006 , Page(s): 114 - 115

[79] W. J. Gross, D. Vasileska, and D. K. Ferry, "A Novel Approach for Introducing the Electron-Electron and Electron-Impurity Interactions in Particle Based Simulations," IEEE Trans. Elec. Dev. Lett., vol. 20, pp. 463-465, 1999.

[80] S. Barraud, P. Dollfus, S. Galdin and P. Hesto, "Short-range and long-range Coulomb interactions for 3D Monte Carlo device simulation with discrete impurity distribution," J. Solid-State Elec., 46, pp.1061-1067, 2002

[81] P. Dollfus, A. Bournel, S. Galdin, S. Barraud and P. Hesto, "Effect of Discrete Impurities on Electron Transport in Ultrashort MOSFETs Using 3-D MC Simulation," IEEE Trans. Elec. Dev., 51, pp.749-756, 2004

[82] De, V.K.; Xinghai Tang; Meindl, J.D.,"Random MOSFET parameter fluctuation limits to gigascale integration (GSI)",Symposium on VLSI Technology, 1996, Digest of Technical Papers,Page(s): 198 - 199.

[83] C. Riddet , A. R. Brown, C. Alexander, J. R. Watling, S. Roy and A. Asenov, "Scattering from Body Thickness Fluctuations in Double Gate MOSFETs: An *ab initio* Monte Carlo Simulation Study," Journal of Computational Electronics, Volume 3, Numbers 3-4, pp.341-345, October, 2004.

[84] Cathignol, A., Rochereau, K., Ghibaudo, G.,"Impact of a single grain boundary in the polycrystalline silicon gate on sub 100 nm bulk MOSFET characteristicsimplication on matching properties," In: Proc. 7th European Workshop on Ultimate Integration of Silicon (ULIS), Grenoble, France, pp. 145-148, 2006.

[85] A. R. Brown, A. Asenov and J. R. Watling, "Intrinsic Fluctuations in Sub 10 nm Double-Gate MOSFETs Introduced by Discreteness of Charge and Matter," IEEE Trans. on Nanotechnology, Vol.1, pp.195-200, 2002.

[86] Asenov, A., Brown, A.R., Davies, J.H., Saini, S.,"Hierarchical approach to atomistic 3D MOSFET simulation", IEEE Trans. Comput.-Aided Des. Integr. Circuits Syst. 18(11), 1558-1565, 1999.

[87] G. Roy, Simulation of intrinsic parameter fluctuations in nano-CMOS devices, Ph.D. dissertation, University of Glasgow, EEE Dept., 2005.

[88] U. Ravaioli, " Hierarchy of simulation approaches for hot carrier transport in deep submicron devices," Semicond. Sci. Technol.13, pp. 1-10, 1998.

[89] P. G. Drennan, C. C. McAndrew, "Understanding MOSFET mismatch for analog design," IEEE J. Solid-State Circuits, vol. 38, pp. 450-456, 2003.

[90] B. Kaczer, R. Dcgracvc, M. Rasras, K. Van de Mieroop, P. J. Roussel, G. Groeseneken, "Impact of MOSFET gate oxide breakdown on digital circuit operation and reliability," IEEE Trans. Electron Devices, vol49, p. 500, 2002

[91] J. A. Power, B. Donellan, A. Mathewson and W. A. Lane, "Relating statistical MOSFET model parameter variabilities to ICmanufacturing process fluctuations enabling realistic worst case design," IEEE Trans. Semicond. Manufact. Vol. 7 p. 306, 1994.

[92] X. Li, C. C. McAndrew, W. Wu, S. Chaudhry, J. Victory and G. Gildenblat, "Statistical Modeling with the PSP MOSFET Model," IEEE Transactions on Computer-Aided Design of Integrated Circuits and Systems, Von. 29, No. 4, p.599, April 2010.

[93] S. Roy, B. Cheng, G. Roy, and A. Asenov, "A methodology for introducing atomistic parameter fluctuations into compact device models for circuit simulation," Journal of Computational Electronics, vol. 2, pp. 427-431, 2003.

[94] B. Cheng, S. Roy, A. Asenov, "The Scalability of 8T-SRAM Cells under the influence of Intrinsic Parameter Fluctuations," Proc. 33th European Solid-State Circuits Conference (ESSCIRC), p. 93, 2007.

[95] A. Bhavnagarwala, S. Kosonocky, C. Radens, K. Stawiasz, R. Mann, Q. Ye, K. Chin, "Fluctuation limits scaling opportunities for CMOS SRAM cells," Tech. Digest of IEDM, pp. 659-662, 2005.

[96] W. VanRoosbroeck, "Theory of Flow of Electrons and Holes in Germanium and Other Semiconductors," Bell Syst.Techn.J., vol. 29, pp. 560-607, 1950.

[97] B. Meinerzhagen and W. Engl, "The Influence of the Thermal Equilibrium Approximation on the Accuracy of Classical Two-Dimensional Numerical Modeling of Silicon Submicrometer MOS Transistors," IEEE Trans.Electron Devices, vol. ED-35, no. 5, pp. 689-697, 1988.

[98] Y. Taur and T. Ning, Fundamentals of Modern VLSI Devices. Cambridge University Press, 1998.

[99] M. G. Ancona, "Equations of State for Silicon Inversion Layers," IEEE Transactions on Electron Devices, vol. 47, no. 7, pp. 1449-1456, July 2000.

[100] M. G. Ancona and G. J. Iafrate, "Quantum correction to the equation of state of an electron gas in a semiconductor," Physical Review B, vol. 39, no. 13, pp. 9536-9540, May 1989.

[101] D. Bohm, "A Suggested Interpretation of the Quantum Theory In Terms of Hidden Variables. I," Physical Review, vol. 85, no. 2, pp. 166-179, January 1952.

[102] A. R. Brown, A. Martinez, N. Seoane and A. Asenov, "Comparison of Density Gradient and NEGF for 3D Simulation of a Nanowire MOSFET, " Proc. Spanish Conference on Electron Devices (CDE), Feb 11-13, Santiago de Compostela, Spain, pp.140-143 (2009)

[103] J. R. Watling, A. R. Brown, A. Asenov, A. Svizhenko, and M. P.Anantram, "Simulation of direct source-to-drain tunnelling using the density gradient formalism: Non-equilibrium Greens function calibration," International Conference on Simulation of Semiconductor Processes and Devices (SISPAD), pp. 267-270, 2002.

[104] A. Asenov, J. R. Watling, A. R. Brown, and D. K. Ferry, "The Use of Quantum Potentials for Confinement and Tunnelling in Semiconductor Devices," Journal of Computational Electronics, vol. 1, no. 4, pp. 503-513, 2002.

[105] D. K. Ferry, R. Akis, and D. Vasileska, ”Quantum Effects in MOSFETs: Use of an Effective Potential in 3D Monte Carlo Simulation of Ultra-Short Channel Devices,” International Electron Devices Meeting (IEDM) Technical Digest, pp. 287-290, 10-13 December 2000.

[106] R. P. Feynman and A. R. Hibbs, Quantum Mechanics and Path Integrals. McGraw-Hill Companies, New York, 1965.

[107] M. Aldegunde, Natalia Seoane, A.J. Garcia-Loureiro, K. Kalna, ”Reduction of the self-forces in Monte Carlo simulations of semiconductor devices on unstructured meshes”, Computer Physics Communications, Volume 181, Issue 1, , Pages 24-34, January 2010.

[108] Laux, S.E., ”On particle-mesh coupling in Monte Carlo semiconductor device simulation,” IEEE Transactions on Computer-Aided Design of Integrated Circuits and Systems, vol.15, no.10, pp.1266-1277, October 1996.

[109] R. W. Hockney and J. W. Eastwood, Computer Simulation Using Particles. New York: McGraw-Hill, 1981.

[110] S. Selberherr, Analysis and Simulation of Semiconductor Devices. Springer-Verlag Wien New York, 1984.

[111] D. Scharfetter and H. Gummel, ”Large-signal analysis of a silicon read diode oscillator,” IEEE Transactions on Electron Devices, vol. 16, p. 64, 1969.

[112] M. Ancona, D. Yergeau, Z. Yu, and B. Biegel, ”On Ohmic boundary conditions for density-gradient theory,” Journal of Computational Electronics, vol. 1, p. 103, 2002.

[113] A. Asenov, ”Modeling end-of-the roadmap transistors,” ser. 203rd Electrochemical Society (ECS) Meeting, p. 974.

[114] D. M. Caughey and R. E. Tomas, ”Carrier Mobilities in Silicon Empirically Related to Doping and Field,” Proceedings of the IEEE, pages 2192-2193, December 1967.

[115] W. R. Thurber, R. L. Mattis, and Y. M. Liu, Resistivity-Dopant density Relationship for Phosphorus Doped Silicon, J. Electrochem. Soc.: Solid State Sci. & Technol., vol. 127, pp. 1807-1812, 1980.

[116] Chee Wee; Maikop, S.; Yu, C.-Y.; , "Mobility-enhancement technologies," Circuits and Devices Magazine, IEEE , vol.21, no.3, pp. 21- 36, May-June 2005.

[117] Fischetti, M.V., Laux,S.E., Band structure, deformation potentials, and carrier mobility in strained Si, Ge, and SiGe alloys, Journal of Applied Physics, Volume 80, Issue 4, pp.2234-2252,August 15, 1996.

[118] C. Alexander, "Ab initio Scattering From Random Discrete Charges and its Impact on the Intrinsic Parameter Fluctuations in Nano-CMOS Devices", PhD. thesis, University of Glasgow, 2005.

[119] R L Liboff, Introduction to the Theory of Kinetic Equations,Wiley, N.Y., 1969.

[120] M. Lundstrom, Fundamentals of Carrier Transport. Cambridge University Press, 2nd edition ed., 2000.

[121] C. Kittel, Introduction to solid state physics, John Wiley & Sons, 7 edition, 1996.

[122] K. Tomizawa, Numerical Simulation of Submicron Semiconductor Devices, Artech House, 1993.

[123] J. M. Higman, K. Hess, C. G. Hwang, and R. W. Dutton, "Coupled Monte Carlo-Drift Diffusion Analysis of Hot-Electron Effects in MOSFETs," IEEE Transactions on Electron Devices, vol. 36, no. 5, pp. 930-937, 1989.

[124] F. M. Bufler, A. Schenk, and W. Fichtner, "Efficient Monte Carlo Device Modeling," IEEE Transactions on Electron Devices, vol. 47, no. 10, pp.1891-1897, October 2000.

[125] C. Jungemann and B. Meinerzhagen, "On the applicability of nonselfconsistent Monte Carlo device simulations," IEEE Transactions on Electron Devices, vol. 49, no. 6, pp. 1072-1074, June 2002.

[126] S. E. Laux and M. V. Fischetti, "Issues in Modeling Small Devices," International Electron Devices Meeting (IEDM) Technical Digest, pp.523-526, 1999.

[127] F. Venturi, R. K. Smith, E. C. Sangiorgi, M. R. Pinto, and B. Ricco, "A General Purpose Device Simulator Coupling Poisson and Monte Carlo Transport with Applications to Deep Submicron MOSFETs," IEEE Transactions on Computer-Aided Design, vol. 8, no. 4, pp. 360-369, April 1989.

[128] C. Moglestue, "Self-consistent Monte Carlo particle modelling of small semiconductor elements," Reports on Progress in Physics, vol. 53, pp. 1333-1353, 1990.

[129] C. Jacoboni and L. Reggiani, "The Monte Carlo method for the solution of charge transport in semiconductors with application to covalent materials," Rev. Mod. Phys., vol. 55, pp. 645-705, 1983.

[130] W. Fawcett, D. A. Boardman, and S. Swain, "Monte Carlo determination of electron transport properties in gallium arsenide," J. Phys. Chem. Solids, vol. 31, pp. 1963-1990, 1970.

[131] J.H. Davies, The Physics of Low-dimensional Semiconductors: An Introduction,Cambridge University Press, 1998.

[132] P. Yu, and M. Cardona, Fundamentals of Semiconductors, Springer, 2003.

[133] D. K. Ferry, Semiconductor Transport. Taylor & Francis, 2000.

[134] C. Moglestue, "A Self-Consistent Monte Carlo Particle Model to Analyze Semiconductor Microcomponents of any Geometry, IEEE Trans. Computer-Aided Design, vol. 5, pp. 326-345, 1986.

[135] C. Moglestue, Monte Carlo Simulations of Semiconductor Devices.Chapman and Hall, 1993.

[136] M. Cardona, and F.H. Pollak, "Energy-Band Structure of Germanium and Silicon: The Method," Phys.Rev., vol. 142, no. 2, pp. 530-543, 1966.

[137] J. M. Luttinger, and W. Kohn, "Motion of electrons and holes in perturbed periodic fields," Physical Review, vol. 97, no. 4, pp. 869-883, Feb 1955.

[138] E.O. Kane, "Energy band structure in p-type germanium and silicon," J.Phys.Chem.Solids, vol. 1, no. 1-2, pp. 82-99, 1956.

[139] T. B. Bahder, "Eight-Band $k \cdot p$ Model of Strained Zinc-Blende Crystals," Physical Review B, vol. 41, pp. 11992 - 12001, 1990.

[140] J.R. Chelikowsky, and M.L. Cohen, "Nonlocal Pseudopotential Calculations for the Electronic Structure of Eleven Diamond and Zinc-Blende Semiconductors," Phys.Rev.B, vol. 14, no. 2, pp. 556-582, 1976.

[141] M. L. Cohen, and J. Chelikowsky, ”Electronic structure and optical properties of semiconductors,” volume 75 of Springer Ser. Solid-State Sci. Springer, Berlin, Heidelberg, 1989.

[142] M.V. Fischetti, and S.E. Laux, ”Band Structure, Deformation Potentials, and Carrier Mobility in Strained Si, Ge, and SiGe Alloys,” J.Appl.Phys., vol. 80, no. 4, pp. 2234-2252, 1996.

[143] C. Jungemann, and B. Meinerzhagen, ”Hierarchical Device Simulation: The Monte Carlo Perspective,” Computational Microelectronics. Springer, 2003.

[144] D. Porezag, Th. Frauenheim, Th. Khler, G. Seifert, and R. Kaschner, ”Construction of tight-binding-like potentials on the basis of density-functional theory: Application to carbon,” Phys. Rev. B 51, pp.12947-12957,1995.

[145] M. Elstner, D. Porezag, G. Jungnickel, J. Elsner, M. Haugk, Th. Frauenheim, S. Suhai, and G. Seifert, ”Self-consistent-charge density-functional tight-binding method for simulations of complex materials properties,” Phys. Rev. B 58, pp.7260-7268, 1998.

[146] R.C. Chaney, C.C. Lin, and E.E. Lafon, ”Application of the Method of Tight Binding to the Calculation of the Energy Band Structures of Diamond, Silicon, and Sodium Crystals,” Phys.Rev.B, vol. 3, no. 2, pp. 459-472, 1971.

[147] C. Jacoboni and P. Lugli, The Monte Carlo Method for Semiconductor Device Simulation. Springer-Verlag Wien New York, 1989.

[148] C. Canali, C. Jacoboni, F. Nava, G. Ottaviani, and A. Alerigi-Quaranta, ”Electron Drift Velocity in Silicon,” Phys. Rev. B, vol. 12, pp. 2265-2284, 1975.

[149] C. Herring, and E. Vogt, ”Transport and Deformation-Potential Theory for Many-Valley Semiconductors with Anisotropic Scattering,” Phys.Rev., vol. 101, no. 3, pp.944-961, 1956.

[150] E. M. Conwell and M. 0. Vassell, ”High field transport in n-type. GaAs, Phys. Rev., vol. 166, no. 3, pp. 797-821, 1968.

[151] R. Clerc, , F. Dauge, R. Hude, and G. Ghibaudo, ”Quantum Confinement in NMOS Double Gate Devices: Impact of Conduction Band Non Parabolicity,” Proc. ULIS 2004, 2004.

[152] M. V. Fischetti and S. E. Laux,"Monte Carlo analysis of electron transport in small semiconductor devices including band-structure and space-charge effects," Phys. Rev. E, vol. 38, pp. 9721-9745, 1988.

[153] H. Brooks and C. Herring, "Scattering by Ionized Impurieties in Semiconductors," Phys. Rev. 83, 879-879,1951.

[154] B. K. Ridley, "Reconciliation of the Conwell-Weisskopf and Brooks-Herring formulae for charged-impurity scatterign in semiconductors: Third-body interference," J. Phys. C, vol. 10, pp. 1589-1593, 1977.

[155] B. K. Ridley, Quantum Processes in Semiconductors. Oxford University Press, 4th edition ed., 1999.

[156] E. Conwell and V. F. Weisskopf, "Theory of Impurity Scattering in Semiconductors," Phys. Rev. 77, pp. 388-390 ,1950

[157] H. Rees, "Calculation of steady state distribution functions by exploiting stability," Volume 26, Issue 9, pp. 416-417, 1968

[158] H. Rees, "Calculation of distribution functions by exploiting the stability of the steady state," J. Phys. Chem. Solids, vol. 30, pp. 643-655,. 1969.

[159] F. M. Bufler, Full-Band Monte Carlo Simulation of Electrons and Holes in Strained Si and SiGe. Herbert Utz Verlag, 1998.

[160] R. P. Joshi and D. K. Ferry, "Effect of multi-ion screening on the electronic transport in deoped semiconductors: A molecular dynamics ananalysis," Phys. Rev. B, vol. 43, pp. 9734-9739, 1991.

[161] C. J. Wordelman and U. Ravaioli, "Intergration of a Particle-Particle-Particle-Mesh Algorithm with the Ensemble Monte Carlo Method for the Simulation of Ultra-Small Semiconductor Devices," IEEE Transactions on Electron Devices, vol. 47, no. 2, pp. 410-416, February 2000.

[162] C. L. Alexander, J. R.Watling, A. R. Brown and A. Asenov, "Artificial carrier heating due to the introduction of ab initio Coulomb scattering in Monte Carlo simulations," Superlattices and Microstructures, vol. 34, pp. 319-326, 2003.

[163] Gross, W.J.; Vasileska, D.; Ferry, D.K., "Ultrasmall MOSFETs: the importance of the full Coulomb interaction on device characteristics", IEEE Transactions on Electron Devices, Volume 47, Issue 10, pp.1831 - 1837,Oct. 2000.

[164] H. Tsuchiya and T. Miyoshi, "Quantum transport modeling of ultrasmall semiconductor devices," IEICE Trans. Electron., vol. E82-C, no. 6, pp. 880-887, 1999.

[165] H. Tsuchiya, M. Horino, M. Ogawa, and T. Miyoshi, "Quantum Transport Simulation of Ultrathin and Ultrashort Silicon-On-Insulator Metal-Oxide-Semiconductor Field Effect Transistors," Japanese Journal of Applied Physics, vol. 42, no. 12, pp. 7238-7243, December 2003.

[166] B. Wu and T. wei Tang, "Quantum Corrected Boltzmann Transport Model for Tunneling Effects," International Conference on Simulation of Semiconductor Processes and Devices (SISPAD), pp. 279-282, 3-5 Sept 2003.

[167] B. Winstead and U. Ravaioli, "A Quantum Correction Based on Schrodinger Equation Applied to Monte Carlo Device Simulation," IEEE Transactions on Electron Devices, vol. 50, no. 2, pp. 440-446, February 2003.

[168] H. Tsuchiya and U. Ravaioli, "Particle Monte Carlo simulation of quantum phenomena in semiconductor nanostructures," Journal of Applied Physics, vol. 89, no. 7, pp. 4023-4029, April 2001.

[169] M. Ogawa, H. Tsuchiya, and T. Miyoshi, "Quantum Transport Modeling in Nano-Scale Devices," International Conference on Simulation of Semiconductor Processes and Devices (SISPAD), pp. 261-266, 2002.

[170] H. Tsuchiya, M. Horino, and T. Miyoshi, "Quantum Monte Carlo Device Simulation of Nano-Scaled SOI-MOSFETs," Journal of Computational Electronics, vol. 2, pp. 91-95, 2003.

[171] H. Tsuchiya, A. Svizhenko, M. P. Anantram, M. Ogawa, and T. Miyoshi, "Comparison of Non-Equilibrium Greens Function and Quantum-Corrected Monte Carlo Approaches in Nano MOS Simulation," Journal of Computational Electronics, vol. 4, pp. 35-38, 2005.

[172] T. wei Tang and B. Wu, "Quantum Corrected Monte Carlo Simulation of Semiconductor Devices Using the Effective Conduction-Band Edge Method," Journal of Computational Electronics, vol. 2, no. 2-4, pp. 131-135, 2003.

[173] B. Wu and T. wei Tang, "The Effective Conduction Band Edge Method of Quantum Correction to the Monte Carlo Device Simulation," Journal of Computational Electronics, vol. 3, no. 3/4, pp. 347-350, October 2004.

[174] D. Vasileska and S. S. Ahmed, "Narrow-Width SOI Devices: The Role of Quantum-Mechanical Size Quantization Effect and Unintentional Doping on the Device Operation," IEEE Transactions on Electron Devices, vol. 52, no. 2, pp. 227-236, February 2005.

[175] K. Kalna and A. Asenov, "Quantum Corrections in the Monte Carlo Simulations of Scaled PHEMTs with Multiple Delta Doping," Journal of Computational Electronics, vol. 1, pp. 257-261, 2002.

[176] M.-A. Jaud, S. Barraud, P. Dollfus, H. Jaouen, and G. L. Carval, "Pearson versus gaussian effective potentials for quantumcorrected Monte-Carlo simulation," Journal of Computational Electronics, vol. 6, no. 1-3, pp. 19-22, 2007.

[177] Trellakis, A.; Galick, A. T.; Pacelli, A.; Ravaioli, U., "Iteration scheme for the solution of the two-dimensional Schrdinger-Poisson equations in quantum structures", Journal of Applied Physics, Volume 81, Issue 12, June 15, 1997, pp.7880-7884.

[178] X.-F. Fan, X. Wang, B. Winstead, L. F. Register, U. Ravaioli, and S. K. Banerjee, "MC Simulation of Straind-Si MOSFET With Full-Band Structure and Quantum Correction," IEEE Transactions on Electron Devices, vol. 51, no. 6, pp. 962-970, June 2004.

[179] G. A. Kathawala and U. Ravaioli, "3-D Monte Carlo simulations of Fin-FETs," International Electron Devices Meeting (IEDM) Technical Digest,pp. 29.2.1-29.2.4, December 2003.

[180] B. Winstead, H. Tsuchiya, and U. Ravaioli, "Comparison of Quantum Corrections for Monte Carlo Simulations," Journal of ComputationalElectronics, vol. 1, no. 1, pp. 201-207, 2002.

[181] S. Datta, "Nanoscale device modeling: The Greens function method," Superlattices and Microstructures, vol. 28, no. 4, pp. 253-278, 2000.

[182] S. Datta, "The Non-Equilibrium Greens Function (NEGF) Formalism: An Elementary Introduction," International Electron Devices Meeting (IEDM) Technical Digest, no. 703-706, 2002.

[183] A. Svizhenko, M. P. Anantram, T. R. Govindan, B. Biegel, and R. Venugopal,"Two-dimensional quantum mechanical modeling of nanotransistors," Journal of Applied Physics, vol. 91, no. 4, pp. 2343-2354, February 2002.

[184] S. Datta, Electronic Transport in Mesoscopic Systems, ser. Cambudge Studies in Semiconductor Physics and Mircoelectronic Engineering. Cambridge University Press, Cambridge, 1997.

[185] A. Martinez, J.R. Barker, A.R. Brown, A. Asenov, N. Seoane, "Simulation of Impurities with an Attractive Potential in Fully 3D Real-Space Non-Equilibrium Greens Function Quantum Transport Simulations"; Conference, Hakone, Japan; in: "Proc. of SISPAD", pp. 341 - 344, 2008.

[186] L. Lucci, P. Palestri, D. Esseni, and L. Selmi, "Multi-subband Monte Carlo modeling of nano-MOSFETs with strong vertical quantization and electron gas degeneration," International Electron Devices Meeting (IEDM) Technical Digest, pp. 631-634, 2005.

[187] Rafferty, C.S., Biegel, B., Yu, Z., Ancona, M.G., Bude, J., Dutton, R.W.,"Multidimensional quantum effect simulation using a density-gradient model and script-level programming techniques," In: International Conference on Simulation of Semiconductor Processes and Devices (SISPAD), pp. 137-140, September 24 1998.

[188] C. Riddet, A. R. Brown, S. Roy, and A. Asenov, "Boundary Conditions for Density Gradient Corrections in 3D Monte Carlo Simulations," Journal of Computational Electronics, vol. 7, pp. 231-235, 2008.

[189] S. Jin, Y. J. Park, and H. S. Min, "Simulation of Quantum Effects in the Nanoscale Semiconductor Device," Journal of Semiconductor Technology and Science, vol. 4, pp. 32-40, March 2004.

[190] Bude, J.D., "MOSFET modeling into the ballistic regime," In: International Conference on Simulation of Semiconductor Processes and Devices (SISPAD), pp. 23-26, September 2000.

[191] S. Inaba, et. al., "High performance 35 nm gate length CMOS with NO oxynitride gate dielectric and Ni salicide," IEEE Trans. Electron Devices, vol. 49, no. 12, pp. 2263-2270, Dec. 2002.

[192] Taurus User Guide Version W-2004.09, Synopsis, Mountain View, CA,Sep. 2004.

[193] The International Technology Roadmap for Semiconductors, Semiconductor Industry Assoc., San Jose, CA, 2003. [Online]. *Available* : *http* : //*www.itrs.net*

[194] D. Vasileska and S. S. Ahmed, "Narrow-width SOI devices: The role of quantum-mechanical size quantization effect and unintentional doping on the device operation," IEEE Trans. Electron Device, vol. 52, no. 2, pp. 227-236, Feb. 2005.

[195] Kendall and Stuart, The advanced theory of statistics, Volume 1, The fourth edition,1977.

[196] Kendall and Stuart, The advanced theory of statistics, Volume 2, The fourth edition,1977.

[197] T. J. DiCiccio and B. Efron, "Bootstrap Cofidence Intervals," Statistical Science, Vol. 11, No. 3, 189-228, 1996.

[198] B. Efron, "Better Bootstrap Confidence Intervals," Journal of the American Statistical Association, Vol. 82, No. 397, pp. 171-185, Mar. 1987.

[199] B. Efron, "Bootstrap Methods. Another Look at the Jackknife", TheAnnals of Statistics, 7: 1-26, 1979.

[200] B. Efron and R. Gong,"A Leisurely Look at the Bootstrap, the Jackknife, and Cross-Validation", Amer. Statist. 37:3648, 1983.

[201] B. Efron and B. Tibshirani, An Introduction to the Bootstrap. Chapman and Hall, 1993.

[202] Kotlyar, R., Giles, M., Cea, S., Linton, T., Shifren, L., Weber, C., and Stettler, M., "Modeling the effects of applied stress and wafer orientation in silicon devices:

from long channel mobility physics to short channel performance", Journal of Computational Electronics , pp. 110 123, 2009.

[203] Shapiro, S. S. and Wilk, M. B., "An analysis of variance test for normality (complete samples)", Biometrika, Vol. 52, No. 3/4, pp. 591-611, 1965.

[204] Jarque, Carlos M.; Anil K. Bera (1980). "Efficient tests for normality, homoscedasticity and serial independence of regression residuals". Economics Letters 6 (3): 255-259.

[205] C. L. Alexander, A. R. Brown, J. R. Watling, and A. Asenov, "Impact of scattering in 'atomistic' device simulations," Solid-State Electronics, vol. 49, no. 5, pp. 733-739, 2005.

[206] BSIM4v4 manual. Available from: $http : //www - device.eecs.berkeley.edu/\ bsim3/bsim4\_get.html$.

[207] Aurora Users manual. Synopsys. 2002.

[208] R. O. Sinnott, A. Asenov, A. R. Brown, C. Millar, S. Roy, G. Roy, and G. Stewart, "Grid Infrastructures for the Electronics Domain: Requirements and Early Prototypes from an EPSRC Pilot Project," in Proc. UK e-Science All Hands Meeting, Nottingham, UK, pp. 509-516,2007.

[209] B. Bindu, B. Cheng, G. Roy, X. Wang, S. Roy, A. Asenov, "Parameter set aand data sampling strategy for accurate yet efficient statistical MOSFET compact model extraction," Solid-State Electronics, Vol. 53 web punlished first (2009)

[210] B. Cheng, N. Moezi, D. Dideban, G. Roy, S. Roy, A. Asenov, "Benchmarking the Accuracy of PCA Generated Statistical Compact Model Parameters Against Physical Device Simulation and Directly Extracted Statistical Parameters," Proc. of SISPAD, pp. 143-146, 2009.

[211] B. Cheng, D.Dideban, N.Moezi, C.Millar, G.Roy, X.Wang, S.Roy, A. Asenov, "Statistical Variability Compact Modeling Strategies for BSIM4 and PSP", IEEE Design and Test of Computers, vol. 27, iss. 2,pp.26-35, Mar./Apr. 2010.

[212] HSPICE users manual. Synopsys; 2007.

[213] Urban Kovac, D. Dideban, B. Cheng, N. Moezi, G. Roy and A. Asenov, ”A Novel Approach to the Statistical Generation of Non-normal Distributed PSP Compact Model Parameters using a Nonlinear Power Method,” in Proc. Simulation of Semiconductor Processes and Devices, Sept. 5-8, 2010, accepted.

[214] Narain D. Arora, Rafael Rios, and Cheng-Liang Huang, ” Modeling the Poly silicon Depletion Effect and Its Impact on Submicrometer CMOS Circuit Performance”, IEEE Trans. Electron Devices, vol. 42, no. 5, pp. 935-943, May. 1995.

[215] M. H. Na, E. J. Nowak, W. Haensch and J. Cai, ”The effective drive current in CMOS inverters,” IEDM Tech. Digest. 2002

[216] V.Adler, E.G.Friedman, ”Delay and Power Expressions for Short Channel CMOS Inverter Driving Resistive Interconnect”, Analog Integrated Circuits and Signal Processing, Vol 14., no 1-2, Sep.1997.